Ondes internes divergentes et convergentes : étude expérimentale de la marée interne

Natalia Shmakova

To cite this version:

Natalia Shmakova. Ondes internes divergentes et convergentes : étude expérimentale de la marée interne. Sciences de la Terre. Université Grenoble Alpes, 2016. Français. NNT : 2016GREAU040 . tel-01562044

HAL Id: tel-01562044
https://theses.hal.science/tel-01562044v1

Submitted on 13 Jul 2017

Communauté
UNIVERSITÉ Grenoble Alpes

THÈSE

Pour obtenir le grade de

DOCTEUR DE LA COMMUNAUTÉ UNIVERSITÉ GRENOBLE ALPES

Spécialité : **Océan, Atmosphère, Hydrologie**

Arrêté ministériel : 30 septembre 2016

Présentée par

Natalia SHMAKOVA

Thèse dirigée par **Jan-Bert Flór** et
codirigée par **Bruno Voisin**

préparée au sein du **Laboratoire des Écoulements Géophysiques et Industriels**
dans **l'École Doctorale Terre, Univers, Environnement**

Ondes internes divergentes et convergentes :
étude expérimentale de la marée interne

Thèse soutenue publiquement le **15 décembre 2016**,
devant le jury composé de :

M. Nicolas MORDANT
Professeur à l'université Grenoble Alpes, Président
M. Thomas PEACOCK
Professeur au MIT, Rapporteur
M. Leo MAAS
Professeur à l'université d'Utrecht, Rapporteur
M. Thierry DAUXOIS
Directeur de recherche à l'ENS de Lyon, Examinateur
M. Jean-Marc CHOMAZ
Directeur de recherche à l'École Polytechnique, Examinateur
M. Jan-Bert FLÓR
Directeur de recherche à l'université Grenoble Alpes, Directeur de thèse
M. Bruno VOISIN
Chargé de recherche à l'université Grenoble Alpes, Co-Directeur de thèse

Contents

Abstract

The Earth's oceans are stratified in density by temperature and salinity gradients. The interaction of tidal currents with ocean bottom topography results therefore in the radiation of internal gravity waves into the ocean interior. These waves are called internal tides and their dissipation owing to nonlinear wave breaking plays an important role in the mixing of the abyssal ocean, and hence in the large-scale ocean circulation.

In this context we investigate the generation of internal waves by oscillating objects of different idealized geometries as a model of barotropic flow over ocean topography, and consider linear as well as nonlinear effects on these waves resulting from interactions with the object and from wave–wave interactions. The relatively novel contribution of this thesis is the investigation of three-dimensional flow aspects that were accessible with our experimental approach, and are generally difficult to investigate by numerical and analytical modelling.

First we investigate the wave structure of the first and higher harmonics for an oscillating spheroid, emitting *diverging* waves. Higher harmonics are generated by nonlinear instability at the surface of the object together with nonlinear effects in the zone of intersection of the primary beams. They may intersect and focus, therefore increase in energy, and become dominant over the first harmonic. The horizontal structures of both, first and higher harmonics are determined.

We then consider waves generated by an oscillating torus, that are *converging* to a focal point. Outside this focal region experimental results and theoretical predictions are in good agreement, but in the focal region the wave amplitude is twice as large as it is close to the torus, leading to local nonlinear wave amplification and incipient wave breaking for large oscillation amplitudes. As a result, the propagation of the first harmonic waves is found to be hindered in the focal region. A standing pattern forms, while new waves are generated and emitted away from this focal region.

A larger torus has been tested at the Coriolis platform to compare the focusing of internal gravity, inertia–gravity and inertial waves in a low viscous regime. Owing to the complexity of the focal region, a second harmonic is observed even at low oscillation amplitude. The vertical vorticity field of internal gravity waves exhibits a dipolar structure in the focal zone, which transforms in the rotating case into a "Yin–Yang-shaped" monopolar vortex structure. The overall structure of the inertial wave beams is close to that for internal gravity waves, though relatively more intense.

Résumé

Les océans de la Terre sont stratifiés en densité par les gradients de température et de salinité. L'interaction des courants de marée avec la topographie du fond océanique entraîne donc le rayonnement des ondes de gravité interne dans l'intérieur de l'océan. Ces ondes sont appelées marées internes et leur dissipation due à le déferlement des ondes nonlinéaires joue un rôle important dans le mélange de l'océan abyssal, et donc dans la circulation océanique à la grande échelle.

Dans ce contexte, nous étudions la génération des ondes internes par l'oscillation d'objet de différentes géométries simplifiées afin de modéliser le marée barotropique sur la topographie océanique et considérons les effets linéaires et nonlinéaires sur ces ondes résultant d'interactions avec l'objet et entre ces ondes. La contribution relativement nouvelle de cette thèse est l'étude des aspects de flux tridimensionnels qui étaient accessibles avec notre approche expérimentale, et sont généralement difficiles à étudier par modélisation numque et analytique.

Nous étudions d'abord la structure des ondes fundamentale et des harmoniques supérieur pour un sphéroïde oscillant, émettant des ondes divergentes. Les harmoniques supérieures sont générées par l'instabilité non linéaire à la surface de l'objet avec des effets nonlinéaires dans la zone d'intersection des faisceaux fundamentales. Ils peuvent se croiser et se concentrer, donc augmenter d'énergie, et devenir dominant sur les ondes fundamentales. On détermine les structures horizontales des ondes fundamentale et des harmoniques supérieures.

Subséquemment, nous considérons les ondes générées par un tore oscillant, qui convergent vers un point focal. En dehors de cette région focale, les résultats expérimentaux et les prédictions théoriques sont en bon accord, mais dans la région focale, l'amplitude de l'onde est deux fois plus grande que près du tore, conduisant à une amplification locale nonlinéaire et à un déferlement des onde pour les grandes amplitudes d'oscillations. En conséquence, la propagation des ondes fundamentales se trouve entravée dans la région focale. L'onde stationnaire se forme alors que de nouvelles ondes sont générées et émises de cette région focale.

Un tore plus grand a été testé sur la plate-forme Coriolis pour comparer la focalisation des ondes de gravité internes, inertie–gravité et des ondes inertielles dans un régime faiblement visqueux. En raison de la complexité de la zone focale, une seconde harmonique est observée même quand l'amplitude d'oscillation est faible. Le champ de vorticité verticale des ondes de gravité interne présente une structure dipolaire dans la zone focale, qui se transforme dans le cas tournant en une structure de vortex "Yin–Yang". La structure globale des faisceaux des ondes inertiels est proche de celle pour des ondes de gravité internes, bien q'elle est relativement plus intense.

Acknowledgements

Three years that ended up with this thesis were full of hard work, scientific and practical problems, but also they were full of new acquaintances, smiles and good times. It would be impossible for me to overcome all the obstacles without the scientific and psychological support of number of people who I would like to mention here.

I would like to thank my thesis directors Jan-Bert Flór and Bruno Voisin for the scientific discussions and advices, availability even without setting the meeting hour and for the freedom they gave me in the laboratory to consider experimentally different aspects of the study. In particular, thanks to Jan-Bert for keeping a positive attitude in any difficult situation and for the confidence when leaving me as a boss in the experimental room, and thanks to Bruno for being always precised and pedantic, and ready to help with not only scientific, but also with bureaucratic and administrative problems. I have learnt a lot from working with both of them and I will keep all advices in mind for my future scientific career and life.

I thank Leo Maas and Thomas Peacock, the referees of this thesis for their comments and questions, which are highly appreciated. I also thank both referees for responsiveness and for making the report in a very short period of time. I thank Nicolas Mordant, Thierry Dauxois and Jean-Marc Chomaz for accepting to be members of the jury for the thesis defense. Apart from the these, I would like to thank Leo for discussions at the conferences, Thierry for showing me the Laboratoire de Physique of the ENS Lyon, Jean-Marc for the great art and science performances and Nicolas for the possibility to present my work at the APS.

During the last year, I had a chance to make experiments at the Coriolis platform, which was a great experience and could not be possible without contribution of Joel Sommeria and Samuel Viboud. I would like to thank Joel for participation in my thesis, especially in the part related to data processing and Samuel for technical help at the platform and advices on experimental procedure. I also thank Stéphane Mercier for his help on reconstruction of the experimental setup and Jean-Marc Barnoud for fast modifications of oscillating objects and creation of supports for them.

Computer, even more than one, was the very necessary device for image recording and data processing. Merci les informaticiens Gabriel Moreau, Olivier de Marchi et Cyrille Bonamy pour votre support permanent du serveur.

Starting from the master program, Achim Wirth and Chantal Staquet were always interested in my life in the laboratory and were always giving good advises, especially in the end of the thesis, for that I thank them.

I would like to give special thanks to Evgeny Ermanyuk who proposed me as a candidate for master and Ph.D in Laboratoire des Écoulements Géophysiques et Industriels (LEGI), who was always watched my progress and participated in number of discussions and through whom I met Bruno, Jan-Bert and other scientists in LEGI. I also thank Evgeny for a brief "how to live in France" introduction and to his family for being always very welcoming.

I was able to visit several conferences, participate in the summer school in Cambridge and even to take part in the organization of the colloquium in LEGI. All this was possible thanks to financial support of the LabEx OSUG@2020.

The last three years path in the LEGI was not only dedicated to an academic experience but was also a way to meet new adorable people inside and outside the laboratory. I thank Gabriele, my first office mate and a good friend for working with me in the laboratory until midnight and cooking italian dinners, and also his mother for giving me an opportunity to stay in sunny Italy at the seaside every August. Grazie mille per tutto, mio caro amico. For an endless supply of optimism I thank Lucas. Thanks to my present office mates Keshav and Julian for having long discussions about everything what is happening around or happened before. I am very thankful for the contribution of Jean-Bastien during the last months of my thesis, for his care and concern and for the willingness to support me when I was ready to give up. I mention here Caroline who has nothing to do with science, but was always so happy to hear good news from me even without understanding what am I talking about.

At last but not least, I thank my parents who were 9000 km away during my four years of study in France, but who were always ready to talk, to share, to cheer me up. I have always felt their presence. Thanks to my grandmother for the particular support and to my aunt, who is now not the only scientist in the family.

Chapter 1

Introduction

> *Voyez cet océan,*
> *monsieur le professeur,*
> *n'est-il pas doué d'une vie réelle?*
>
> J. Verne, *Vingt mille lieues sous les mers*

1.1 Waves in the ocean and atmosphere

The investigation of internal waves in stratified and/or rotating fluids is relevant to geophysics, climatology and technical physics, among others. It is not only important for the general knowledge of the atmosphere and the ocean, but also for practical problems related to shipping and aeronautics. The history of internal wave studies goes back to 250 years, if one takes into account the notes of Franklin (1769) describing waves at the oil–water interface. One of the first dynamical effects of internal waves that has been observed is the so-called "dead water" phenomenon: the transport of energy and momentum from a ship propeller to nonlinear interfacial waves between two water layers. The dead water effect slowed down or stopped the ships driven at those time by direct thrust with small power, in particular Norwegian fisher boats in fjords. At the end of the nineteenth century the famous Norwegian polar explorer F. Nansen described his observations of the dead water phenomenon during the oceanographic expedition of the ship *Fram* in the North Atlantic in 1893–1896 (Nansen, 1897). He noted that this effect takes place when a fresh water layer is on top of a salt water layer. The famous meteorologist V. F. K. Bjerknes made the hypothesis that the loss of ship velocity described by Nansen might be caused by wave generation at the interface between the two water layers. Later, this hypothesis has been proved by V. W. Ekman, who made experiments in a density-stratified fluid (Ekman, 1906). Ekman showed that a self-propelled object moving with a small speed close to the interface of two layers of different densities generates internal waves which neutralize most of the engine power. In the ocean, as a rule, internal waves are always generated by some natural phenomenon whenever

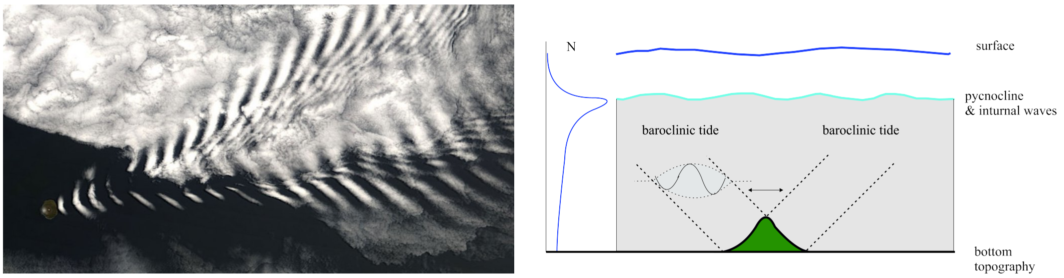

(a) (b)

Figure 1.1: Internal wave generation in the ocean and atmosphere: (a) lee waves generated by wind over Amsterdam Island (Indian ocean), image from the NASA Earth Observatory (`http://earthobservatory.nasa.gov/IOTD/view.php?id=6151`), (b) the internal tide generated by the interaction of the barotropic tide with ocean bottom topography.

there are two layers of fluid with different densities, and they usually have impressive characteristics: amplitudes of tens of meters, wavelengths from a few meters to several kilometers, and periods from minutes to hours. These are special types of waves, called interfacial waves, between two layers of different density. Below we consider the waves which propagate through the continuously stratified fluid interior and owe their existence to the effects of rotation and/or density stratification. This wider class of waves is called internal waves, in contrast to waves at the water surface, and can be generated by perturbations in stratified fluids (internal gravity waves), rotating fluids (inertial waves) and in rotating stratified (inertia-gravity waves).

For a very long time the structure of the abyssal ocean could not be investigated: electromagnetic waves do not propagate through the water and the visualisation of the ocean interior via classical techniques (such as optical Doppler) is not possible. As a result, the first internal waves were observed in the atmosphere. A well-known example is the lee waves generated by wind over hills or mountain ranges (see Figure 1.1a). Lee waves propagate through the atmosphere to distances of hundreds of kilometers and can be observed from space due to cloud formation at the wave crests. Three important characteristics for their generation are the stratification of the atmosphere (in temperature), the flow speed and the obstacle (mountain or island) size. Intersections of lee waves generated behind islands due to strong continuous wind current form complicated atmospheric structures. In the case when the obstacle has nearly equal dimensions perpendicular and parallel to the flow, lee waves form a horseshoe or wedge-like shape.

In the 1950s, technical progress allowed to make the first qualitative measurements of internal waves, showing the input of internal waves into the ocean dynamics and leading the way to modern oceanography. Before that, the ocean was believed to be slowly and weakly changing in time and space, while in practice it is a complicated combination of space and time scales. Understanding of the role of internal waves in the changing ocean leads to different view of its dynamics and physics, such as the connection between internal waves and turbulence in view of ocean mixing.

As a whole, it gradually has been recognized (see e.g. Turner, 1973) that internal gravity waves play an important role in the dynamics of both, the atmosphere and oceans, being responsible for significant transport of momentum and energy through density-stratified fluids.

1.2 Stratification and mixing in the ocean

In the world's oceans the vertical and horizontal distributions of temperature, salinity and pressure are constantly changing, with some processes increasing the density gradients while others are continuously mixing them. Figure 1.2 shows the main processes that are responsible for the ocean stratification, including solar radiation and heat transport, precipitation and evaporation, ice melting and freezing, fresh water income from rivers, all contributing to stratify the ocean.

Precipitation and evaporation affect the salinity of the ocean, as well as fresh water input from rivers and melting ice in the Northern and Southern Poles. Cold water from the poles also changes the ocean temperature and together with heating from the sun form the temperature gradient. These processes are not equally performing in different parts of oceans and at different depths, and cause different water masses with in between them strong gradients in temperature and salinity. Gradients can be positive (so that the density increases with height) or negative, and the stratification is respectively stable and unstable. The formation of density gradients is opposed by mixing processes that homogenize these gradients. Mixing can be molecular, turbulent and convective. The main mixing processes are represented in Figure 1.2 and are briefly discussed below.

Molecular mixing is due to diffusion processes. Local instabilities can occur because salt diffuses slower than heat, leading to mixing over layer depths of tens of meters (double diffusion). In the particular case when the layer of cold fresh water lies below the warmer salty layer, so-called salt fingering can be observed. Salt fingering processes occur in the upper ocean central waters, like below the Mediterranean salt tongue or east of Barbados (see e.g. Kunze, 1990).

Convection occurs in the ocean when the surface layer becomes denser than the water below due to its cooling or salinity increase (by evaporation or ice formation). It can be observed together with turbulent mixing or without it, affecting the circulation and properties of water masses. Convective mixing affects the ocean in the vertical direction. The most intensive convection takes place in winter, when surface cooling leads to mixing of an isothermal surface layer with a depth of about a hundred meters (see e.g. Killworth, 1983).

In view of large-size ocean currents, even at low velocity, most currents have a high Reynolds number and are therefore rather turbulent. Kilometers-wide ocean currents have a large effect on ocean mixing. Currents transport cold water from the Pole to the Equator and warm water the other way round, and thus help to stabilise the Earth's temperature. Due to instabilities, water masses may break off from the ocean current and result in eddies drifting across the ocean basin with a

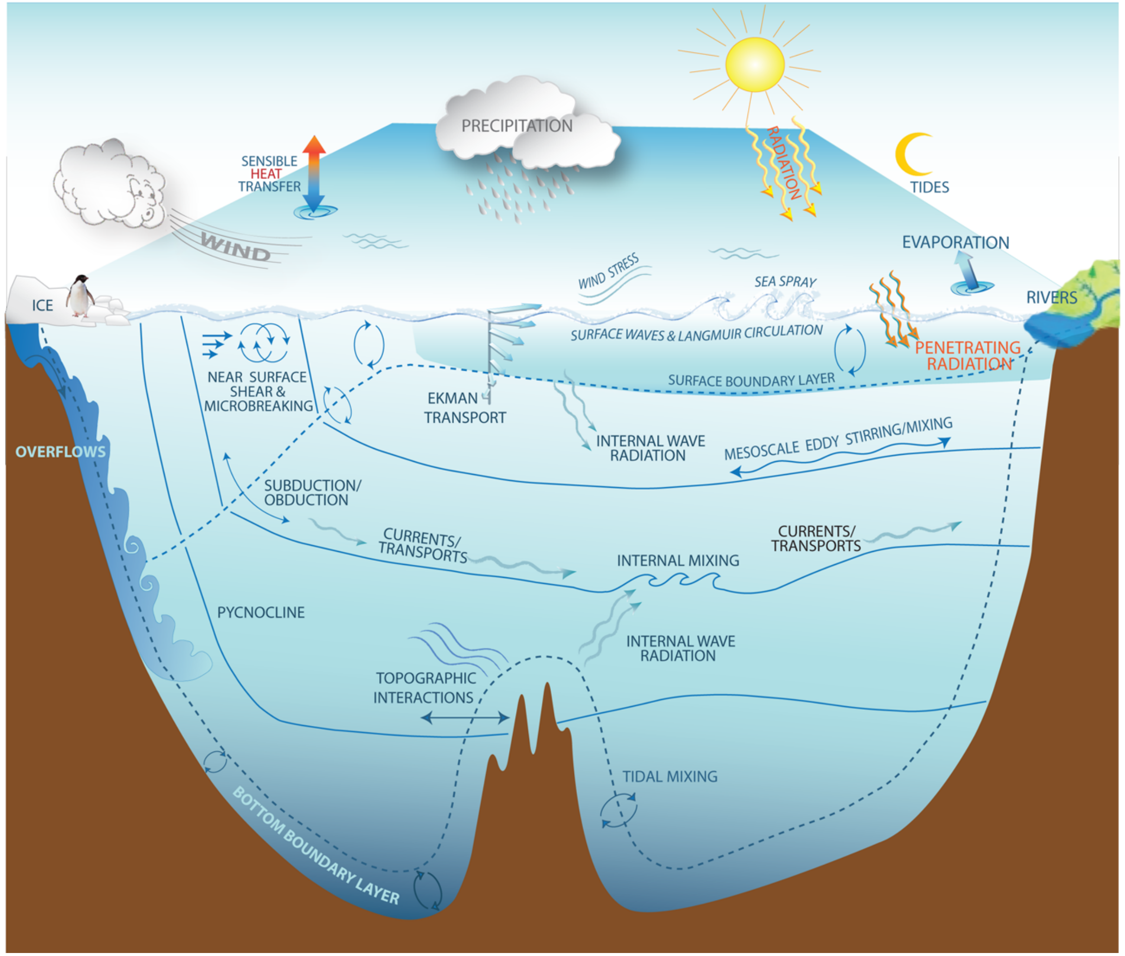

Figure 1.2: Schematic picture of processes in the ocean (image from `https://www.gfdl.noaa.gov/ocean-mixing/`).

speed of about 4 kilometers per day. They are visible at the ocean surface from the satellite data but their structure is three-dimensional and reaches the pycnocline. These eddies contain water of different salinity or temperature which mixes into their surroundings. This mixing is generally horizontal. Mesoscale eddies result from boundary currents like the Gulf Stream due to instability of sheared motion.

Large scale turbulent motions occur in the ocean upper layer due to the wind stress. The resulting surface waves have sizes that range from small ripples to tsunamis. Surface waves can propagate and transport energy over large distances, and their breaking causes mixing of the ocean surface layer. Frictional coupling of wind and ocean surface water, called Ekman transport, together with Earth's rotation effect (through the Coriolis force), generates net motion of the surface fluid perpendicular to the wind direction In combination with the restriction on lateral movement caused by bottom Ekman transport generates up- or down-welling. Ekman up- and down-walling occur close to coasts as well as in the open ocean. An example of the latter is equatorial upwelling, with the cold water rising to the surface and thus destabilising the stratification (Wyrtki, 1981).

A thin surface layer of about 100 m depth is well-mixed by the precesses mentioned above. This layer is separated from the deep ocean by a salinity or temperature jump, called pycnocline or thermocline. Significant change in density is caused by dense gravity currents generated at the continental shelves or semi-enclosed basins. Instability caused by the large density difference in the Antarctic continental slope results in Kelvin-Helmholtz structures and thus into intensive mixing. The rest of the ocean is stratified by temperature and salinity. Internal waves, that transport energy from the surface to the ocean interior, can be generated by perturbations at the surface boundary layer. These waves can break, transforming energy to small scales.

1.3 The internal tide

1.3.1 Importance

Recent estimations have indicated, though, that the most important generation of internal waves and relevant mixing comes from tidal forcing. The global energy rate of lunar and solar tides is 3.7 TW. In the deep ocean internal gravity waves of a special type known as internal or baroclinic tides are generated by the interaction of the barotropic tidal currents with bottom topography (oceanic ridges and mountains, see Figure 1.1*b*). The most accurately known tide is the principal lunar semi-diurnal M_2 tide which is noticeable almost everywhere in all oceans. Calculations of the internal tidal generation were performed for continental slopes (Baines, 1982) and deep bottom topography (Bell, 1975*b*). The transfer of barotropic tidal energy into internal tidal energy was estimated as less then 1% for continental slopes (Baines, 1982) and as 10% for bottom relief in the deep ocean (Bell, 1975*b*). This estimation has been later corrected. Based on the model of Baines (1982) the amplitude of the semi-diurnal internal tide was calculated from energy flux estimations by Morozov (1995) for most underwater ridges and compared with measurement results, collected with moored current and temperature meters giving the possibility to calculate the M_2 amplitude by dividing the semi-diurnal temperature amplitude by the temperature gradient. Large internal wave amplitudes were found when the barotropic tide was perpendicular to the ridge. The resulting map, presenting the M_2 amplitudes in the world's oceans, is presented in Figure 1.3(a). Calculations from these amplitude estimations suggested that the total rate of energy dissipation by the baroclinic tide is about 1.1 TW. This value is overestimated since it is calculated using the entire water depth for mass flux calculation (Munk & Wunsch, 1997). Refined theoretical estimations have been presented by Nycander (2005) and Melet *et al.* (2013). Egbert & Ray (2000) empirically estimated the tidal energy dissipation using satellite altimetry data, which gives direct access to tidal elevations. The resulting map is presented in Figure 1.3(b) and the global rate of energy dissipation from the barotropic to the baroclinic tide is estimated to be 0.9 TW. This is nevertheless 30% of the total dissipation of the barotropic tide. In turn this 0.9 TW energy is converted and dissipated. Munk & Wunsch (1998) estimate that 0.2 TW of energy dissipation is due to the generation of secondary internal waves and 0.7 TW due to turbulence. Later Wunsch & Ferrari (2004) noted once again that the majority of energy dissipates due to internal waves. These values clearly indicate that the transfer of tidal energy into mixing is relevant to the general circulation in the oceans, and since it may affect the temperature of global currents also of interest to climate modelling (Wunsch & Ferrari, 2004; Ferrari & Wunsch, 2008).

Another form of oceanic internal wave that has recently received some attention is the lee waves generated by the interaction of geostrophic flows, such as the Atlantic Circumpolar Current, with bottom topography (see Nikurashin & Ferrari, 2011; Scott *et al.*, 2011). The global energy content of these waves, hence their contribution to mixing, is however smaller, of about 0.2 to 0.4 TW. Accordingly these waves were not taken into account in the present work.

Garrett & Kunze (2007) considered the processes of internal tidal generation and propagation for different topographies and fluid depths. It was shown that wave breaking can occur close to regions of internal wave generation as well as far away from obstacles, where internal tides interact with continental shelves or other waves. Compared to the processes mentioned in section 1.2, tidal mixing is the major mixing process in the ocean, which is why it is one of the main interest in ocean dynamics at present.

1.3.2 Modelling

Much of our knowledge of the underlying physics of internal wave generation, propagation, decay and interaction with the topography comes from theoretical and experimental studies of simplified generic problems. In laboratory experiments we study internal tides either in the reference frame of the bottom topography, so the barotropic tude oscillates back and forth over it, or in the reference frame of the barotropic tide, so the bottom topography plays the role of an oscillating wave gen-

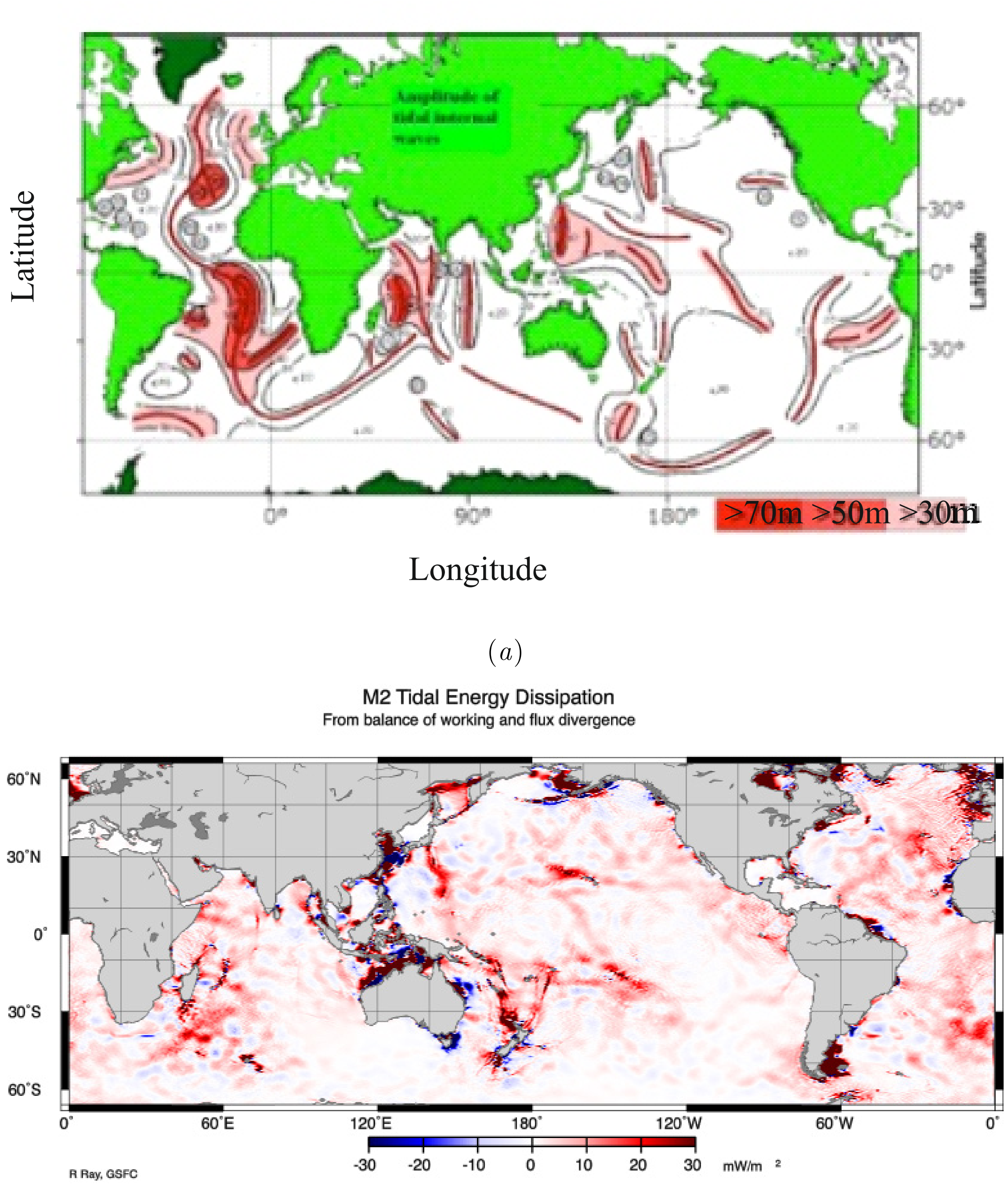

(*a*)

M2 Tidal Energy Dissipation
From balance of working and flux divergence

(*b*)

Figure 1.3: Internal tides in the world's ocean: (*a*) amplitudes of internal waves calculated from the linear model of Baines (1982), image from Morozov (1995); (*b*) energy loss rate estimated from satellite altimeter data, Egbert & Ray (2001); Garrett & Kunze (2007).

erator. The equivalence between the two setups has been considered by Boyer & Zhang (1990*a*,*b*), who showed that it holds to lowest order in an expansion with the topography as a perturbation. The topography can be modelled with obstacles of simplified geometry. Continental slopes either fixed in a barotropic current (Baines & Fung, 1985; Gostiaux *et al.*, 2007; Pairaud *et al.*, 2010; Lim *et al.*, 2010) or oscillating in a fluid at rest (Guo & Davies, 2003; Zhang *et al.*, 2008) have been used, together with oscillating ridges (Matsuura & Hibiya, 1990; Peacock *et al.*, 2008; Echeverri *et al.*, 2009; Dossmann *et al.*, 2011). Depending on the relation between the topographic slope and the wave slope, the topography can be subcritical or supercritical (Baines & Fung, 1985), namely have a slope smaller or larger than the slope of the wave, which depends on the frequency of barotropic oscillations. The generation of internal tide is particularly effective around the critical points, where the wave rays are tangent to the topography (Baines, 1986), as verified experimentally in the above investigations.

Bell (1975*a*,*b*) described theoretically the internal tide as a linear monochromatic internal wave by considering small topographic slope and height, and a fluid of infinite depth and uniform buoyancy frequency N. An analytical estimate was made of the barotropic to baroclinic energy conversion rate. Llewellyn Smith & Young (2002) extended this estimate to finite depth, and applied it to ridges of Gaussian, exponential, or witch-of-Agnesi shape, finding that the conversion rate is higher for larger seamounts and about 10^4 W for an average seamount. Later the estimate was extended to finite topographic slope by series expansion (Khatiwala, 2003), Fourier expansion (Balmforth *et al.*, 2002) or Green's function approach (Pétrélis *et al.*, 2006; Balmforth & Peacock, 2009; Echeverri & Peacock, 2010), and to a vertical barrier (Llewellyn Smith & Young, 2003). Finally it has recently been found that, at given oscillation frequency and fluid depth, specific topographies can prevent conversion to take place (Maas, 2011).

1.4 Waves in rotating and/or stratified fluids

Ocean processes take place in particular physical and geographical conditions, too complex to be analytically described by any existing mathematical apparatus. Instead we introduce approximations, to understand the current state of the ocean and predict its future behavior. Here we investigate the general properties of internal waves in the presence of both rotation and stratification, based on §4.4 and Part I of the Epilogue of Lighthill (1978) and §§10.4 and 11.1 of Brekhovskikh & Goncharov (1994). We start by linearizing the equations of motion of an incompressible inviscid non-diffusive fluid, for small perturbations of the velocity, pressure and density, in the form

$$\frac{\partial u}{\partial t} = -\frac{1}{\bar{\rho}_0}\frac{\partial P}{\partial x} + fv, \tag{1.1}$$

$$\frac{\partial v}{\partial t} = -\frac{1}{\bar{\rho}_0}\frac{\partial P}{\partial y} - fu, \tag{1.2}$$

$$\frac{\partial w}{\partial t} = -\frac{1}{\bar{\rho}_0}\frac{\partial P}{\partial z} - \frac{\rho}{\bar{\rho}_0}g, \tag{1.3}$$

$$\frac{\partial u}{\partial x} + \frac{\partial v}{\partial y} + \frac{\partial w}{\partial z} = 0, \tag{1.4}$$

and

$$\frac{\partial \rho}{\partial t} = \frac{\bar{\rho}_0}{g}N^2 w. \tag{1.5}$$

Equations (1.1)-(1.3) are the momentum equations, (1.4) the continuity equation and (1.5) the incompressible equation of state, for the components (u, v, w) of the velocity in a system of Caresian coordinates (x, y, z) of vertical z-axis, the pressure disturbance P and the density disturbance ρ, with $\rho_0(z)$ the background density of mean value $\bar{\rho}_0$. For simplicity the Boussinesq approximation has been used (see Boussinesq, 1903) so that the variations of density are ignored everywhere except in equation (1.3) where they are multiplied by the acceleration of gravity g. Physically this corresponds to neglecting the inertial effects of the density variations compared to the buoyancy forces that they create. In these conditions the background density arises through the Brunt-Väisälä or buoyancy frequency

$$N = \sqrt{-\frac{g}{\bar{\rho}_0}\frac{\partial \rho_0(z)}{\partial z}}$$

in equation (1.5), which is the frequency of oscillation of a fluid particle, displaced from its equilibrium position where its weight is balanced by the Archimede's force exerted by the surrounding fluid. In the following N will be assumed constant, corresponding to a linear stratification.

From equations (1.3) and (1.5) we obtain

$$\frac{\partial^2 w}{\partial^2 t} = -\frac{1}{\bar{\rho}_0}\frac{\partial^2 P}{\partial z \partial t} - N^2 w, \tag{1.6}$$

which together with equations (1.1), (1.2) and (1.4) provide the governing equations for inertia–gravity waves. Assuming an infinite domain in all directions, the solutions of these linear system with constant coefficients may be sought in the form of plane waves:

$$u = u' \exp^{i(kx+ly+mz-\omega t)},$$

$$v = v' \exp^{i(kx+ly+mz-\omega t)},$$

$$w = w' \exp^{i(kx+ly+mz-\omega t)},$$

$$P = P' \exp^{i(kx+ly+mz-\omega t)},$$

where (k, l, m) are the components of the wave vector $\vec{k}$ and ω is the oscillation frequency. Substituting these expressions into the governing equations we obtain

$$i\omega u' + fv' - \frac{ik}{\bar{\rho}_0}P' = 0, \tag{1.7}$$

$$fu' - i\omega v' + \frac{il}{\bar{\rho}_0}P' = 0, \tag{1.8}$$

$$ku' + lv' + mw' = 0, \tag{1.9}$$

$$(\omega^2 - N^2)w' - \frac{m\omega}{\bar{\rho}_0}P' = 0. \tag{1.10}$$

The contribution of (1.7), (1.8) and (1.10) gives

$$u' = \frac{\omega k + ifl}{\omega^2 - f^2}\frac{P'}{\bar{\rho}_0},$$

$$v' = \frac{\omega l - ifk}{\omega^2 - f^2}\frac{P'}{\bar{\rho}_0},$$

$$w' = \frac{\omega m}{\omega^2 - N^2}\frac{P'}{\bar{\rho}_0}.$$

The remaining (1.9) becomes

$$\omega^2(k^2 + l^2 + m^2) = N^2(k^2 + l^2) + f^2m^2,$$

and provides the dispersion relation for inertia–gravity waves

$$\omega = \sqrt{f^2\frac{m^2}{\kappa^2} + N^2\frac{\kappa_H^2}{\kappa^2}}, \tag{1.11}$$

with $\kappa = \sqrt{k^2 + l^2 + m^2}$ and $\kappa_H = \sqrt{k^2 + l^2}$ the moduli of the wave vector $\vec{k}$ and its horizontal projection $\vec{k}_H$, respectively. If we introduce the angle θ of the wave vector to the horizontal by

$$m = \kappa \sin\theta,$$

$$\kappa_H = \kappa \cos\theta,$$

the dispersion relation can be written in the form

$$\omega = \sqrt{f^2 \sin^2\theta + N^2 \cos^2\theta}. \tag{1.12}$$

and defines the range of frequencies in which internal waves can propagate: $0 < \omega < N$ for pure internal gravity waves (when $f = 0$), $0 < \omega < f$ for pure inertial waves (when $N = 0$) and $min(f, N) < \omega < max(f, N)$ for inertia–gravity waves.

From equation (1.9) it follows that the wave vector is perpendicular to the fluid velocity vector, so that internal waves are transverse.

The same is true of the energy propagation velocity, as is seen by calculating the phase velocity $\vec{c}_p$ and group velocity $\vec{c}_g$, defined by

$$\vec{c}_p = \frac{\omega}{\kappa}\frac{\vec{k}}{\kappa},$$

$$\vec{c}_g = \vec{\boldsymbol{\nabla}}_k \omega,$$

respectively. These follow from (1.11) as

$$\vec{c}_p = \frac{\sqrt{N^2\kappa_H^2 + f^2m^2}}{\kappa^2}\frac{(k,l,m)}{\kappa},$$

$$\vec{c}_g = \frac{N^2 - f^2}{\kappa^2}\frac{\kappa_H m}{\sqrt{N^2\kappa_H^2 + f^2m^2}}\frac{(km, lm, -\kappa_H^2)}{\kappa_H\kappa}.$$

Phase and group velocities are orthogonal, namely $\vec{c}_p \cdot \vec{c}_g = 0$. Since $\vec{c}_g$ is the energy propagation velocity, we conclude that the waves propagate along rays parallel to the planes of constant phase and inclined at the angle

$$\theta = \arccos\sqrt{\frac{\omega^2 - f^2}{N^2 - f^2}}$$

to the vertical. For pure internal gravity waves ($f = 0$) the phase and group velocities have horizontal components of the same sign and vertical components of opposite signs, for pure inertial waves ($N = 0$) the vertical components have identical signs and the horizontal components opposite signs, and for inertia–gravity waves the situation is as for internal gravity waves when $f < N$ and as for inertial waves when $N < f$.

The relative importance of the effects of rotation and gravity can be quantified by introducing the Rossby radius of deformation

$$R_o = (Nh)/f,$$

with h the typical vertical scale. This number characterizes the horizontal scale at which rotation and buoyancy play equally important roles in the evolution of waves generated by some disturbance. In thed following, except for experiments taking place at the Coriolis platform in section 2.4 and chapter 6, R_o will be much larger than the horizontal scale of the experiments. Accordingly the waves will be pure internal gravity waves, simply called internal waves below.

1.5 Generation of internal waves by oscillating objects

1.5.1 Two-dimensional waves

Over the past decades, the mechanisms of internal wave generation have been studied in detail for oscillating objects of various idealised geometries. Oscillations of a body at the frequency ω in a linearly stratified fluid of buoyancy frequency N, with $\omega < N$, generate internal wave beams inclined at the angle

$$\theta = \arccos(\omega/N) \tag{1.13}$$

to the vertical, which is the direction of energy propagation at the group velocity. Accordingly, two-dimensional internal waves have a St. Andrew's cross shape, first

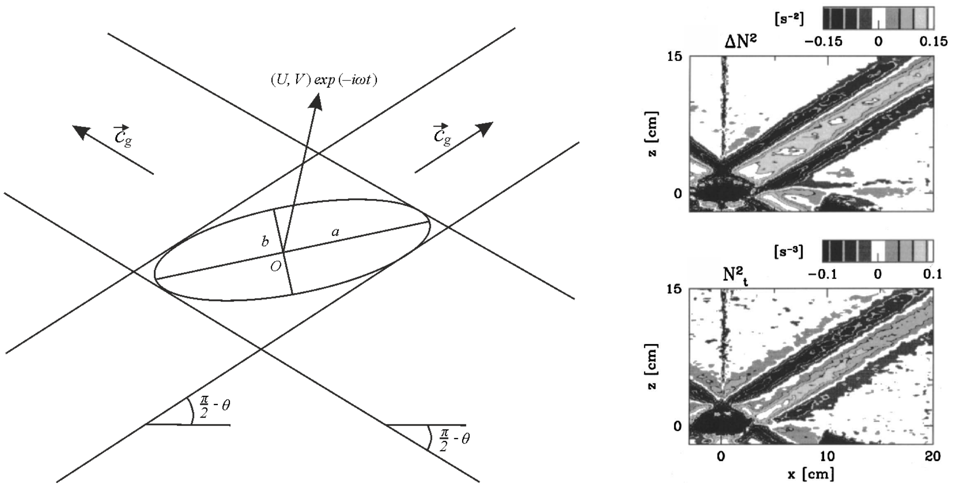

(*a*) (*b*)

Figure 1.4: Internal waves generated by an elliptic cylinder: (*a*) theoretical predictions by Hurley (1997) of inviscid wave beams forming a St. Andrew's Cross delimited by the vertical rays tangent to the cylinder above and below; (*b*) experimental visualisations by Sutherland & Linden (2002) of the vertical density gradient (top) and it's temporal derivative (bottom).

observed experimentally by Görtler (1943) and later Mowbray & Rarity (1967) for a circular cylinder. Quantitative progress, however, had to wait for three decades. A linear theory describing the structure of the waves generated by the small rectilinear vibrations of an elliptical cylinder has been developed for inviscid (Hurley, 1997) and viscous (Hurley & Keady, 1997) fluids (Figure 1.4*a*). Experiments on internal waves were performed by Sutherland *et al.* (1999, 2000) and Sutherland & Linden (2002) for a vertically oscillating elliptical cylinder and by Zhang *et al.* (2007) for a horizontally oscillating circular cylinder to examine the characteristics of both, the strong and weak forcing regimes. These experiments were similar to the pioneering investigations of Mowbray & Rarity (1967) but allowed to measure the amplitude of internal waves everywhere in space and time and thus compare results with the linear viscous theory (Hurley & Keady, 1997) (Figure 1.4*b*). The theoretical predictions were shown in good agreement with the experimental results but overpredicted the wave amplitude and underpredicted the width of the wave beams. The reason for this was identified as the viscous boundary layer generated around the cylinder in the experiments, which is not taken into account by the linear theory.

Internal tidal beams forming a St. Andrew's Cross have been observed experimentally for a wide range of topographies, either fixed in an oscillating barotropic flow or oscillating in a fluid otherwise at rest, in a variety of studies listed earlier in section 1.3.2. Figure 1.5 illustrates the results of two studies, for a continental slope (Gostiaux *et al.*, 2007) and an isolated ridge (Dossmann *et al.*, 2011), both supercritical. Two arms of the Cross are generated for the slope, and four arms for the ridge. In the ocean, the first observations of internal tidal beams were done over

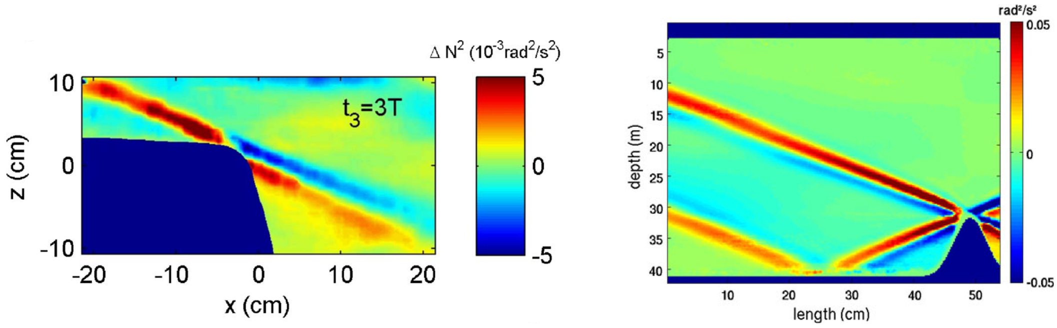

(*a*) (*b*)

Figure 1.5: Experimental internal tide generated by (*a*) barotropic flow over a model continental slope (Gostiaux *et al.*, 2007) and (*b*) oscillation of a Gaussian ridge in a fluid at rest (Dossmann *et al.*, 2011). The plotted quantity is the filtered first harmonic of the vertical density gradient.

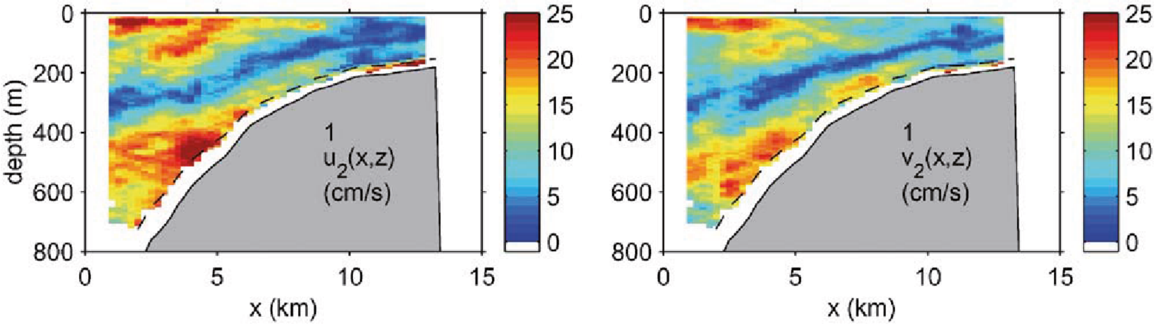

Figure 1.6: Cross-slope (left) and along-slope (right) horizontal velocity amplitude measured by ADCP (Acoustic Doppler Current Profiler) over the continental slope in the Bay of Biscay (Lam *et al.*, 2004).

the continental slope in the Bay of Biscay by Pingree & New (1989) and Pingree & New (1991), using contact measurements; they were complemented later by remote acoustic measurements by Lam *et al.* (2004) and Gerkema *et al.* (2004). These are illustrated in Figure 1.6 and exhibit the same structure reproduced later in the laboratory by Gostiaux *et al.* (2007).

The origin of internal waves as well as their propagation, interaction and breaking cannot be well understood by linear theory. With slight increase of the oscillation amplitude we turn to a weakly nonlinear regime where the wave fields exhibit not only the original oscillation frequency but also higher harmonics. The experiments of Mowbray & Rarity (1967) have shown that the dispersion relation (1.13) admits the generation of a propagative n-th harmonic component with frequency $n\omega$ if $n\omega < N$. Two mechanisms have been considered theoretically for the generation of higher harmonics. The first mechanism, appropriate for subcritical topography, is advection by the nonlinear boundary conditions, investigated by Bell (1975*a*) for the large–amplitude oscillations of flat topography of infinitesimal slope (Figure 1.7*a*).

The n-th harmonic wave amplitude is found proportional to the n-th derivative of the topographic slope, so that the fundamental wave is proportional to the topographic slope, the second harmonic wave is proportional to the topographic curvature, etc. Also, for weak nonlinearity, the n-th harmonic amplitude is found proportional to the n-th power of the oscillation amplitude. The second mechanism, appropriate for supercritical topography, is the nonlinear interaction of colliding and reflecting wave beams, investigated by Tabaei *et al.* (2005) using a small amplitude expansion. With this mechanism, the n-th harmonic amplitude is also proportional to the n-th power of the amplitude of the oscillation amplitude. These nonlinear effects are especially visible in the numerical simulations by Lamb (2004) and Korobov & Lamb (2008) of the barotropic horizontal oscillations over supercritical topography. Figure 1.8 shows a variety of nonlinear interactions among internal waves. In the regions of wave interaction, such as the intersections between waves and boundary layers, between two primary wave beams (tangent to the topography) and between one such beam and its reflection at a boundary, secondary nonlinear beams appear with different inclination to the vertical.

Reflection on the slope has been studied experimentally by Rodenborn *et al.* (2011) to examine the dependence of the second harmonic on the bottom slope and thus verify the theoretical predictions. For the particular case when two primary wave beams have the same vertical direction of propagation (as shown in Figure 1.7*b*) and intersect, the theory of Tabaei *et al.* (2005) predicts the generation of four secondary wave beams. Jiang & Marcus (2009) have predicted theoretically and verified numerically that only two of these secondary wave beams are compatible with the radiation condition (see Figure 1.7*b*).

For a vertically oscillating elliptical cylinder, Sutherland & Linden (2002) obtained, for large oscillation amplitudes, secondary waves at the zone of superposition of propagating upward and downward primary waves. The origin of these second harmonic waves is hypothetically either the fundamental wave–wave interaction, or the interaction of waves with boundary layers. Similar nonlinear effects have been observed in experiments by Zhang *et al.* (2007) for a horizontally oscillating circular cylinder, but for small oscillation amplitudes. These second harmonic waves were generated by the interaction of fundamental waves as predicted by Tabaei *et al.* (2005). However, the second harmonic observed by Zhang *et al.* (2007) at the boundary of the cylinder has not been discussed and is supposed to be generated at the viscous boundary layer of the cylinder (see the discussion in chapter 3 of this thesis).

1.5.2 Three-dimensional waves

Three-dimensional internal waves have a more complex structure. The internal wave generation process in three dimensions has been studied experimentally by Flynn *et al.* (2003) for a vertically oscillating sphere, experimentally and numerically by King *et al.* (2009) for the horizontal oscillations of a hemisphere lying on a flat plane, and numerically by King *et al.* (2010) for the horizontal oscillations of a

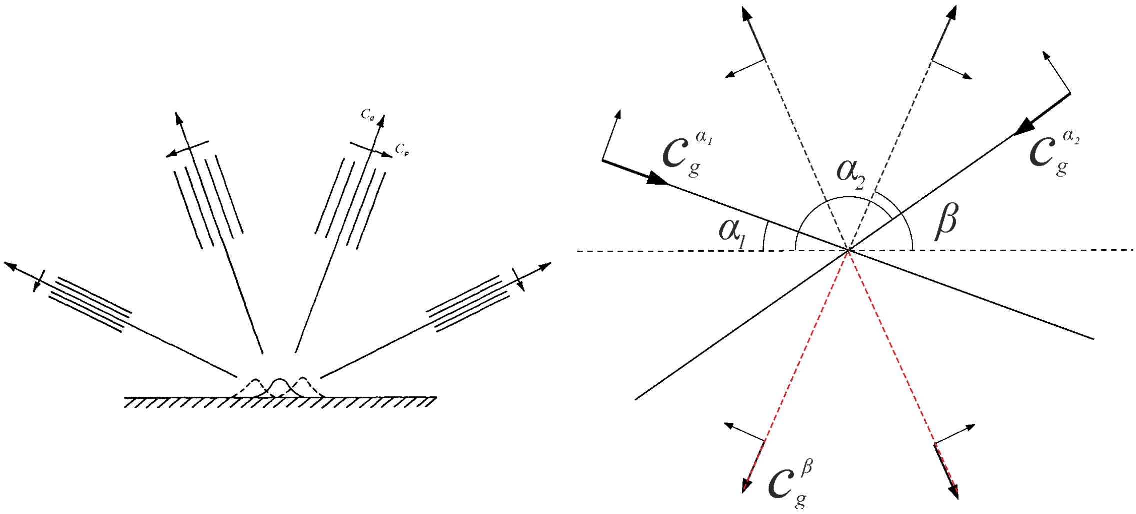

(*a*) (*b*)

Figure 1.7: Generation of higher harmonics according to: (*a*) analytical predictions of Bell (1975*a*) and (*b*) theoretical predictions of Tabaei *et al.* (2005) for colliding waves. The latter image illustrates the scenario when the two internal wave beams have the same vertical direction of propagation; the solid lines show the incident beams, the dashed lines the four secondary beams predicted by Tabaei *et al.* (2005), and the red dashed lines show the only two secondary beams allowed by the radiation conditions according to Jiang & Marcus (2009).

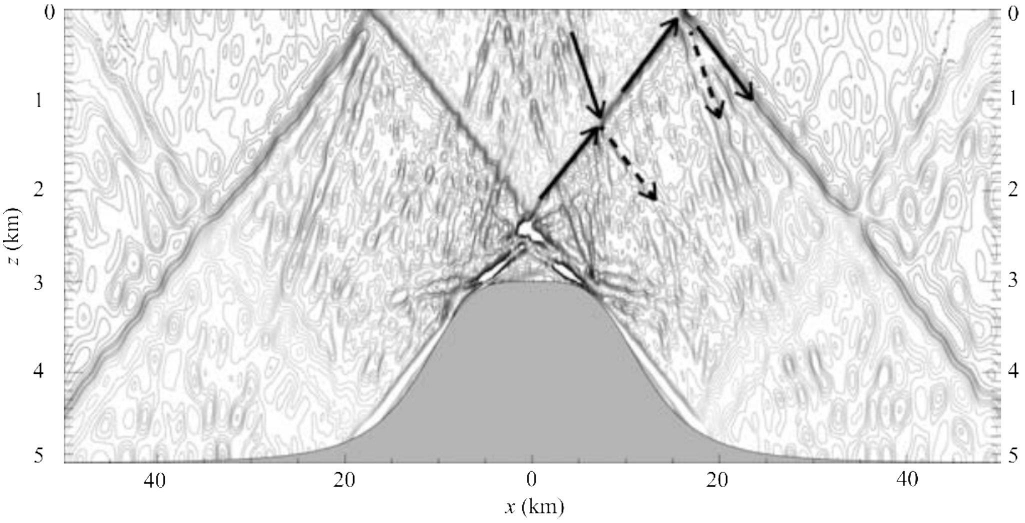

Figure 1.8: Reflection and intersection of internal waves and generation of higher harmonics, numerical simulation of Lamb (2004).

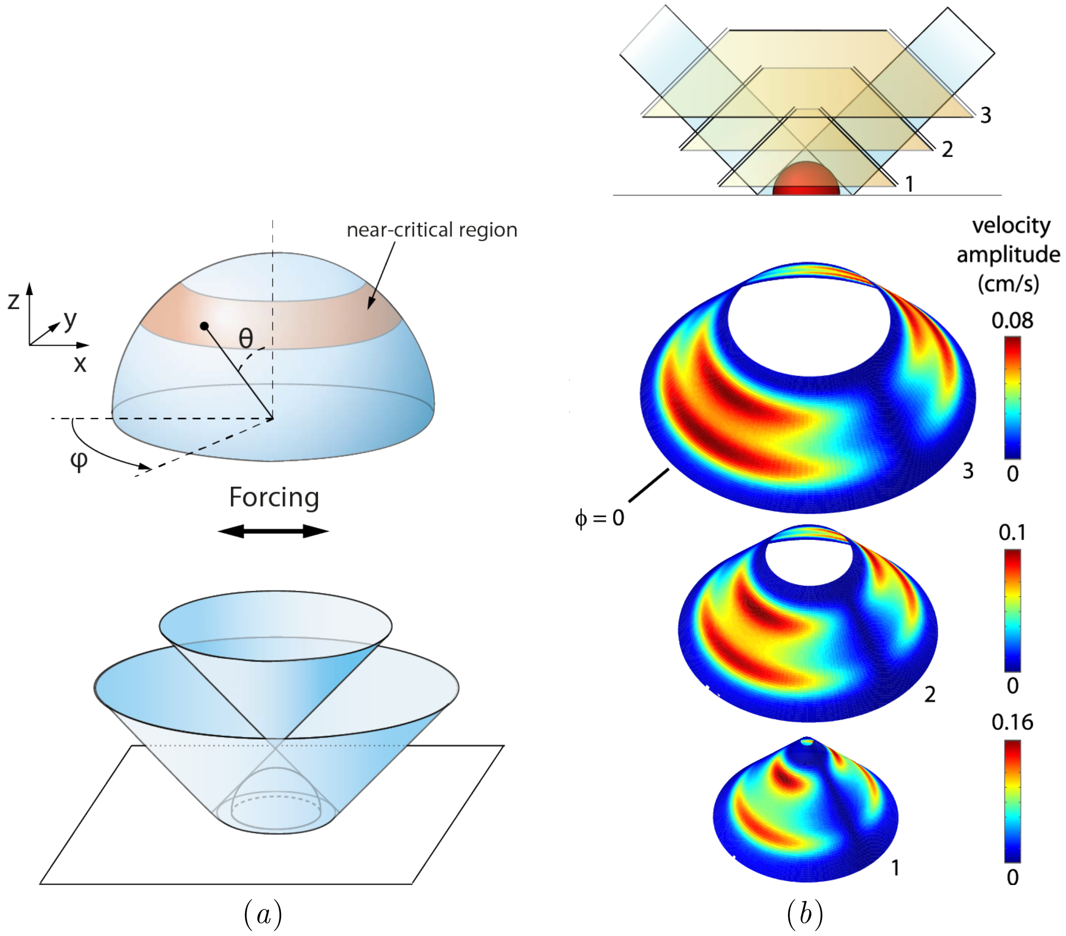

Figure 1.9: Internal waves in three dimensions: (*a*) internal wave cone generated by the horizontal oscillations of a hemisphere, (*b*) velocity amplitude at different conical cross sections showing a maximum in the forcing plane $\phi = 0$ (image from King *et al.*, 2009).

Gaussian seamount. It has been shown that three-dimensional internal wave fields are qualitatively similar to two-dimensional internal wave fields. This is in agreement with Munroe & Lamb (2005), who found for internal tides that despite the three-dimensionality of the topography, most of the total wave energy is radiated in the tidal forcing direction. However King *et al.* (2009) showed that this directivity is superposed on a conical wave structure, which is the three-dimensional analogue of the two-dimensional St. Andrew's Cross (see Figure 1.9*a*, *b*). They also discovered that three-dimensional topography produces a strong mean flow perpendicular to the oscillations of the tidal flow, leading to a large-scale horizontal circulation. In the out-of-forcing plane a second harmonic has been observed.

Theoretically the internal wave generation by a horizontally oscillating sphere has been considered by Voisin *et al.* (2011) and compared with experiments at low oscillation amplitude, measuring the vertical velocity component. The theory included viscous effects and showed good agreement with experimental results. Experiments

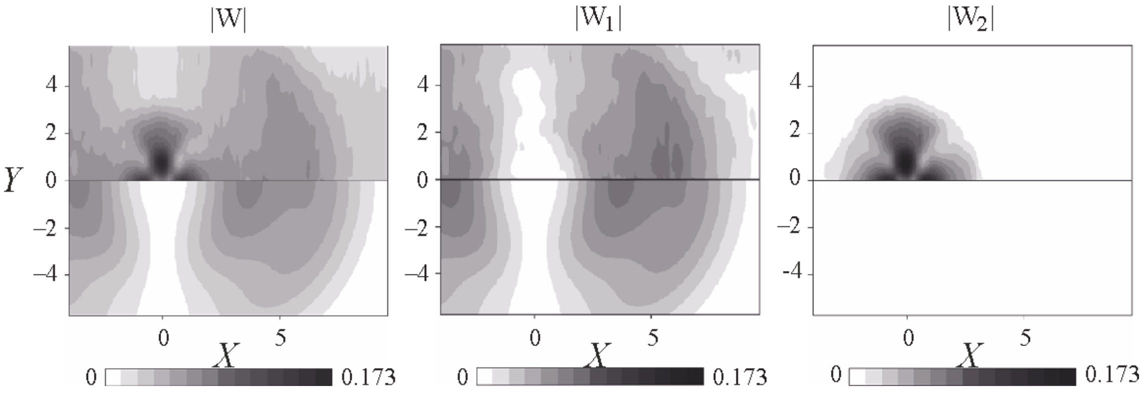

(*a*) (*b*) (*c*)

Figure 1.10: Horizontal structure of the vertical wave amplitude of internal waves generated by a horizontally oscillating sphere: (*a*) total vertical amplitude (first and second harmonic), and Fourier-filtered (*b*) first and (*c*) second harmonic components (image from Ermanyuk *et al.*, 2011). The design of the axis (x, y, z) is the same as in Figure 1.9.

at moderate oscillation amplitude have been performed to show the transition to nonlinearity (Ermanyuk *et al.*, 2011). The radiation patterns of the propagative first and second harmonics have been studied in some detail. They are presented in Figure 1.10 showing the dipolar and quadrupolar structures of the first and second harmonics, respectively. For these harmonics, the two-dimensional theories of Bell (1975*a*) and Tabaei *et al.* (2005) remain valid in three dimensions, with slight modifications (Bell, 1975*b*; Akylas & Karimi, 2012). Their common prediction that the variation of the wave amplitude with the oscillation amplitude is linear for the first harmonic, quadratic for the second, and cubic for the third, has been verified and approved. The first three-dimensional quantitative measurements of all three velocity components for the internal waves generated by an oscillating sphere has been performed by Ghaemsaidi & Peacock (2013). The results show good agreement with the linear three-dimensional viscous theory of Voisin *et al.* (2011).

1.5.3 Generalization

The generation of internal waves by oscillating objects remains a topic of active interest worldwide, with new avenues of research opened every few years. One such avenue is numerical simulation, pioneered by King *et al.* (2009, 2010) for a sphere and recently applied to a cylinder by Winters & Armi (2013) and again to a sphere by Bigot *et al.* (2014). Waves in rotating fluids have been less studied, but have the structure similar to waves in stratified nonrotating fluids. For inertial waves in a rotating nonstratified fluid, the St. Andrew's Cross has been observed for a cylinder by Cortet *et al.* (2010) and a wave cone for a disk by Oser (1958) and Messio *et al.* (2008). For inertia–gravity waves in a rotating stratified fluid, the wave cone has similarly been observed by Peacock & Weidman (2005).

Finally, all these oscillating objects produce separate wave beams without offering any control either on the relative intensity of the beams, or the wave profiles through them. To overcome that limitation, a new wave generator has been developed by Gostiaux *et al.* (2007), composed of oscillating plates and allowing the generation of a single wave beam with a well-defined sinusoidal profile. The generator design has later been modified and refined by Mercier *et al.* (2010). The generator has since been used, customized and improved by several research groups worldwide, and applied to a variety of problems, to mention but a few: the propagation of wave beams (Grisouard *et al.*, 2013; Ghaemsaidi *et al.*, 2016; Allshouse *et al.*, 2016), their interaction (Smith & Crockett, 2014), their instability (Bourget *et al.*, 2013, 2014; Maurer *et al.*, 2016) and the formation of attractors (Scolan *et al.*, 2013; Brouzet *et al.*, 2016*a*,*b*).

1.6 Internal wave focusing

A main interest in internal wave dynamics is the conversion of wave energy into mixing and small-scale dissipation due to a rich variety of mechanisms including wave–wave and wave–current interactions, and overturning motions. Several scenarios have been considered for the energy concentration of internal waves in localised zones. Dauxois & Young (1999) investigated the theory of near-critical reflection of internal gravity waves on a slope. Reflected waves are focused: the width of the wave beam decreases after reflection so that the energy density increases owing to energy conservation. The critical case of internal wave generation when the topographic slope equals the wave propagation angle has been considered numerically by Gayen & Sarkar (2010). The kinetic energy density of internal waves generated at the slope is 15 times larger than that of the incident barotropic tide.

In closed basins multiple reflections can lead to the formation of wave attractors along which energy is concentrated (see e.g Maas *et al.*, 1997; Lam & Maas, 2008). As a first approach, the problem has been considered linearly, giving an idea of the generation mechanisms of geometric focusing. The transition to nonlinear effects has been studied experimentally (Scolan *et al.*, 2013; Brouzet *et al.*, 2016*a*) showing higher harmonic generation and mixing of the stratification.

Another scenario for energy concentration is the two-dimensional intersection and interaction of wave beams, that can be either separate (see for example Teoh *et al.* 1997 and Smith & Crockett 2014) or arising from double-ridge (Echeverri *et al.*, 2011; Xing & Davies, 2011; Klymak *et al.*, 2013) or multiple-ridge (Zhang & Swinney, 2014) configurations. Luzon Strait in the South China Sea is such a double-ridge system (see Figure 1.13*a*), where interference-induced dissipation has been observed in the field by Alford *et al.* (2011), predicted numerically by Buijsman *et al.* (2012) and reproduced in the laboratory by Mercier *et al.* (2013).

A last two-dimensional scenario is internal wave refraction at horizons of high density gradient, investigated by Mathur & Peacock (2009). Variations in the stratification affect the properties of the wave beam, such as width and direction of propagation, leading also to wave reflection at the zones of high density gradients.

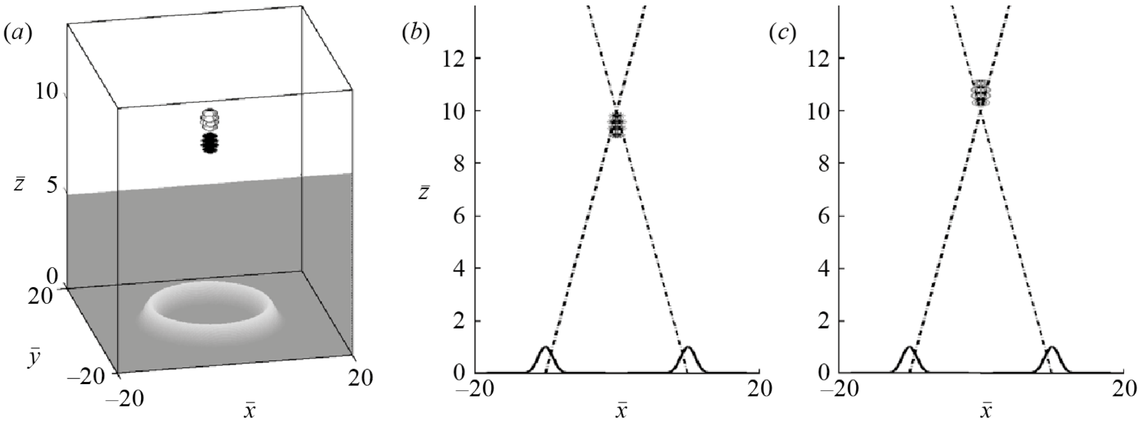

(a) (b) (c)

Figure 1.11: Zones of high wave amplitude from circular Gaussian topography, for (b) the in-phase component and (c) out-of-phase component (from Bühler & Muller, 2007)).

Three-dimensionality offers the possibility of a new type of geometric focusing, by the convergence of azimuthal wave rays. This phenomenon was first noticed for an oscillating sphere by Appleby & Crighton (1987), who introduced the term "focusing singularity". It has hardly been investigated experimentally, though: wave focusing may occur near an oscillating hemisphere (see Figure 3 in King *et al.*, 2009), and a Gaussian mountain (see Figure 3(*e*) in King *et al.* 2010), but it was not discussed. This is because the focusing effect increases with the radius and size of the oscillating object since more energy is transported to the focal zone, but in general its effect is negligible in small scale laboratory experiments with small oscillating spherical objects. First experiments with a 60 cm diameter vertically oscillating torus revealed a strong vortical motion with wave overturning and local mixing in the focal zone (unpublished results, Flór 1997). Theoretically internal wave focusing has been studied by Bühler & Muller (2007) for an inviscid fluid with an oscillating ring having subcritical Gaussian generatrix. The study considered for the first time the effect of geometric focusing into localised regions of high wave amplitude (see Figure 1.11). For a circular Gaussian hill and also for horse-shoe topography the mean flow localised in regions of wave dissipation was considered by Grisouard & Bühler (2012). In a similar experiment in a rotating fluid conducted at LEGI, inertial waves were shown to generate turbulence in the focal zone (Duran-Matute *et al.*, 2013). The breaking of these waves played an important role for the transport of momentum, and the generation of columnar vortices that are typical for two-dimensional turbulence (see Figure 1.12).

Such three-dimensional focusing is suspected in Luzon Strait, where three-dimensional simulations accounting for the horizontal curvature of the double-ridge system exhibited much larger energy dissipation compared with earlier two-dimensional mechanisms (Buijsman *et al.*, 2014). Internal wave focusing has been recently observed in submarine canyons by Vlasenko *et al.* (2016) (Figure 1.13*b*). In addition to ob-

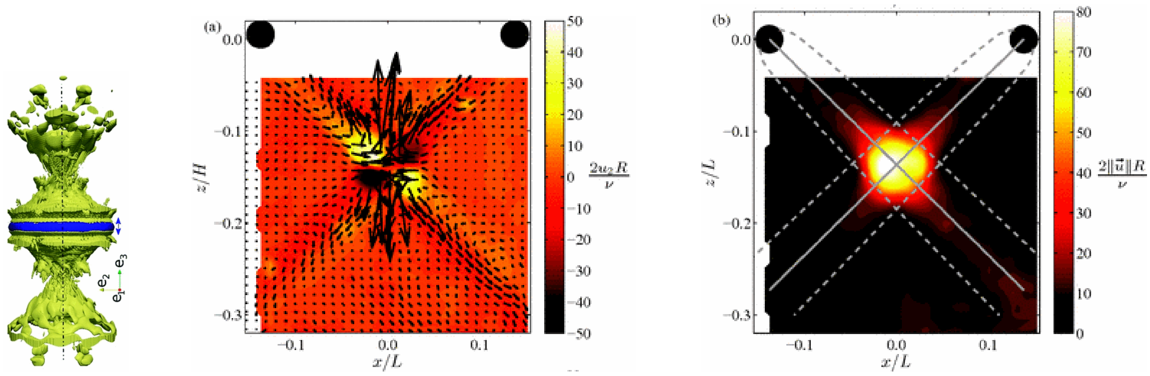

(*a*) (*b*) (*c*)

Figure 1.12: Inertial wave focusing by a vertically oscillating torus: (*a*) numerical calculations; (*b*) and (*c*) experimental results in terms of instantaneous velocity and velocity amplitude, respectively (from Duran-Matute *et al.*, 2013).

servations of trapped waves the problem was considered numerically for an idealized canyon in two- and three-dimensional cases. This study showed the importance of three-dimensional focusing, giving much higher energy concentration. The scenario described by Vlasenko *et al.* (2016) could be similar to mechanisms at the so-called Tore seamount close to Portugal (see Figure 1.13*c*). This crater is thought to result from meteoritic impact and has a torus shape (Ribeiro, 2002, chapter 5). It isolates a water column of 1.2 km height, which is homogenous (Peliz *et al.*, 2009) and could be mixed due to breaking of focusing internal waves.

Apart from the above mentioned studies, the geometric focusing of internal waves deserves further attention in the context of ocean mixing and momentum transport in the Earth's oceans. In this context, a horizontal oscillation is more appropriate. The horizontal oscillation direction also gives a direction to the overturning motions in the focal region, and therefore generates a mean flow that may be relevant to ocean applications (see Bühler, 2009).

1.7 This thesis

The present manuscript develops the three-dimensional experimental study in five chapters. Chapter 2 describes the measurement methods usually used for the laboratory study of internal waves, and the present experimental setup. The two methods used for the present research are Particle Image Velocimetry (PIV) and Laser Induced Fluorescence (LIF). The tools used for data analysis, namely Fourier decomposition, complex demodulation and time frequency representation are also discussed.

In chapter 3 we continue the experimental study of the spatial structure of internal waves generated by a sphere (Ermanyuk *et al.*, 2011) by considering different spheroids. Three major questions are

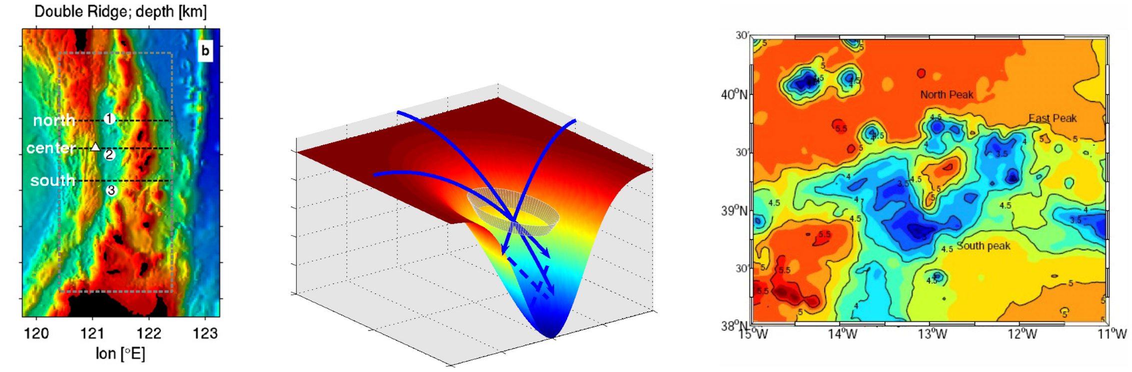

(a) (b) (c)

Figure 1.13: Bathymetry in (a) the Luzon Strait (from Buijsman *et al.*, 2014) and (c) the Tore Seamount (from Peliz *et al.*, 2009); (b) three-dimensional numerical simulation of wave focusing in submarine canyon (from Vlasenko *et al.*, 2016); .

- What is the spatial structure of the n-th harmonic internal wave?
- How does the spatial structure of the waves depend on the features of the wave generator (such as orientation and slope)?
- What is the mechanism of higher harmonic generation (nonlinear boundary layer, interaction or intersection of the fundamental wave beams)?

In the case of a vertically axisymmetric spheroid, the experimental results are compared to the predictions of an adaptation of the three-dimensional theory of Voisin *et al.* (2011).

Chapters 4 and 5 are dedicated to the focusing of internal gravity waves by horizontally oscillating tori of small scale, so that Stokes numbers $St = a^2\omega/\nu = O(100)$, with a the minor radius of the torus, ω the oscillation amplitude and ν the fluid viscosity. The linear regime is considered in chapter 4 and compared with the linear two-dimensional approach based on theory of Hurley & Keady (1997) and with the three-dimensional theory of Voisin (2016). The internal wave energy is investigated as a function of the Keulegan–Carpenter number $Ke = A/a$, with A the oscillation amplitude. We look at the mechanisms of wave focusing in general in order to understand

- How does the wave amplitude and slope amplify?
- What is the contribution of each part of the torus?
- How good are the two- and three-dimensional theoretical predictions?

Chapter 5 focuses on the nonlinear effects due to internal wave focusing. We consider high oscillation amplitudes and introduce a new focusing number, which is a Ke-number corrected for the convergence/divergence of waves. We obtain wave breaking in the focal region and further generation of new waves from the focal zone.

Both evanescent and propagative higher harmonics are observed in the focal region. Their structure and generation mechanism are of interest. The vertical mean flow generated in the focal zone appears to affect the structure of the wave beams, which is also shown.

The last chapter 6 is a separate study of internal wave focusing in a stratified and/or rotating fluid at the large-scale Coriolis platform, with $St = O(1000)$. The problem is fully nonlinear even for low oscillation amplitude. We compare internal gravity waves with the predictions of linear theory. Assuming a turbulent boundary layer, the linear theory is also calculated taking into account an eddy viscosity. We look at the difference between internal gravity, inertia–gravity and inertial waves and discuss the effect of rotation on the structure of the focal zone.

In the conclusion, the results are summarised and the perspectives discussed.

Chapter 2

Experimental setup and procedure

2.1 Measurements of internal waves

In laboratory experiments the reference frame of the barotropic tidal current is generally used, hence the fluid is at rest while the obstacle is oscillating at a given frequency ω. The experiments are conducted in a transparent tank filled with linearly salt-stratified fluid (so the buoyancy frequency N is constant, see Figure 2.1*a*).

There are different techniques to measure internal wave motions in such a fluid. Two-dimensional internal wave fields have first been visualised via non-intrusive techniques, including Schlieren (Görtler, 1943; Mowbray & Rarity, 1967), shown in Figure 2.1*b*, interferometry Peters 1985; Makarov *et al.* 1990) and Moire fringes (Ivanov, 1989; Sakai, 1990). These techniques, though yielding high-resolution visualisations of the phase patterns, require high-quality optical windows in the test tank walls, with fairly limited field of view. Another disadvantage is related to the difficulty of performing quantitative measurements of the wave field parameters.

The advent of digital image processing has allowed an effective access to the quantitative measurement of density-gradient or velocity fields. The synthetic Schlieren technique, still non-intrusive, has been proposed by Sutherland *et al.* (1999) and

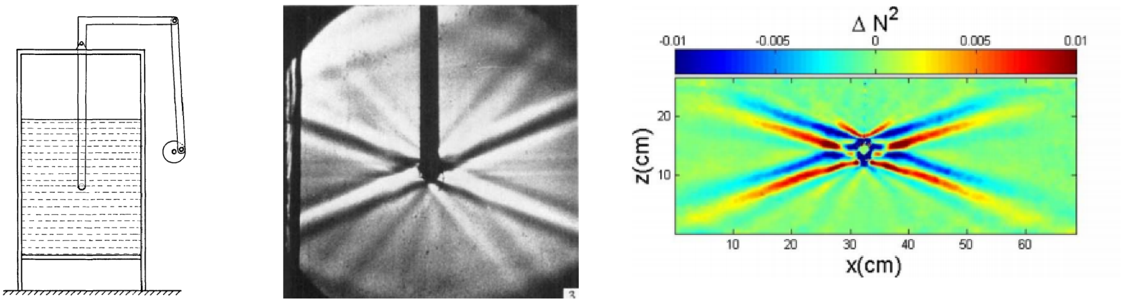

(*a*) (*b*) (*c*)

Figure 2.1: (*a*) Typical experimental setup (Mowbray & Rarity, 1967) and visualisation of the St. Andrew's Cross by (*b*) the Toepler–Schlieren technique (Mowbray & Rarity, 1967) and (*c*) synthetic Schlieren technicue (Mercier *et al.*, 2008).

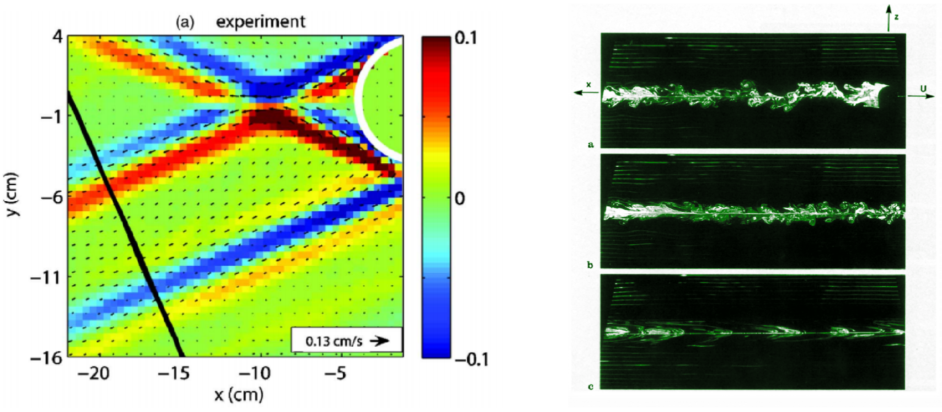

(*a*) (*b*)

Figure 2.2: (*a*) Internal waves generated by a horizontally oscillating cylinder measured with the PIV technique (Zhang *et al.*, 2007); (*b*) wake generated by a horizontally translating sphere visualised with the LIF technique (Hopfinger *et al.*, 1991).

Dalziel *et al.* (2000), and applied to a number of two-dimensional problems by Sutherland & Linden (2002), Ermanyuk & Gavrilov (2005, 2008), Mercier *et al.* (2008) as shown in Figure 2.1*c*, Thomas *et al.* (2009) and Clark & Sutherland (2009). It is based on the fact that a salt concentration in water modifies its refractive index. For a linearly stratified fluid the refractive index is also a linear function of the depth. A light ray passing through the media with such refractive index is bent with an angle, which is directly related to the density gradient. However, in nonlinear experiments when vertical mixing occurs, the average density profile is changed and the wave measurements are distorted. In three-dimensional problems the sinthetic Schlieren technique can be used directly for the measurement of optical distortions integrated along the light ray path (Peacock & Weidman, 2005). A quantitative measurement of axisymmetric internal wave fields, such as for instance those emitted by a vertically oscillating sphere, has been made possible by combining synthetic Schlieren with tomographic inversion (Flynn *et al.*, 2003; Onu *et al.*, 2003). An application to a vertically translating sphere in a uniformly stratified fluid is described in Yick *et al.* (2007). The theoretical possibility of a tomographic inversion for an arbitrary nonaxisymmetric disturbance has been discussed in Décamp *et al.* (2008) but remains to be implemented. An alternative technique of optical tomography is described in Hazewinkel *et al.* (2011) with application to internal-wave attractors.

Alternatively, internal waves can be measured from particle motions using Particle Image Velocimetry (PIV), which is intrusive. Accurate PIV measurements in a continuously stratified fluid require a dense and uniform distribution of particles. However, the preparation of particles matching a given density distribution is often a very elaborate process. Particles are selected such that they are advected by the flow without having inertia. Of course, once this problem is resolved, two- and three-dimensional internal wave fields can be easily measured with the PIV method, as shown in Figure 2.2(*a*) borrowed from Zhang *et al.* (2007).

A technique for the observation of isopycnal displacements, based on the deformation of fluorescent dye lines and shown in Figure 2.2(*b*) has been introduced in Hopfinger *et al.* (1991) and first used for quantitative measurement in Flór *et al.* (2002). An algorithm to process the experimental dye lines and determine their displacement with sub-pixel accuracy has made the automation of this density measurement possible (Ermanyuk *et al.*, 2011; Voisin *et al.*, 2011). The advantage of this technique compared to PIV measurements is the higher resolution. The method is Lagrangian, thus it allows to study effects more precisely. However, the fluorescent dye line method, hereinafter called LIF for Laser-Induced Fluorescence, can provide only with information about the vertical velocity field. In the case when horizontal effects are dominant, the PIV technique is more appropriate. In the present research, several of these experimental techniques have been used, their implementation is described in the next section.

2.2 Experiments in the small tank

2.2.1 General setup

Experiments were carried out in a plexiglas square tank with working depth of 97 *cm* and horizontal dimensions 97 × 97 cm^2. The experimental setup is shown in Figure 2.3.

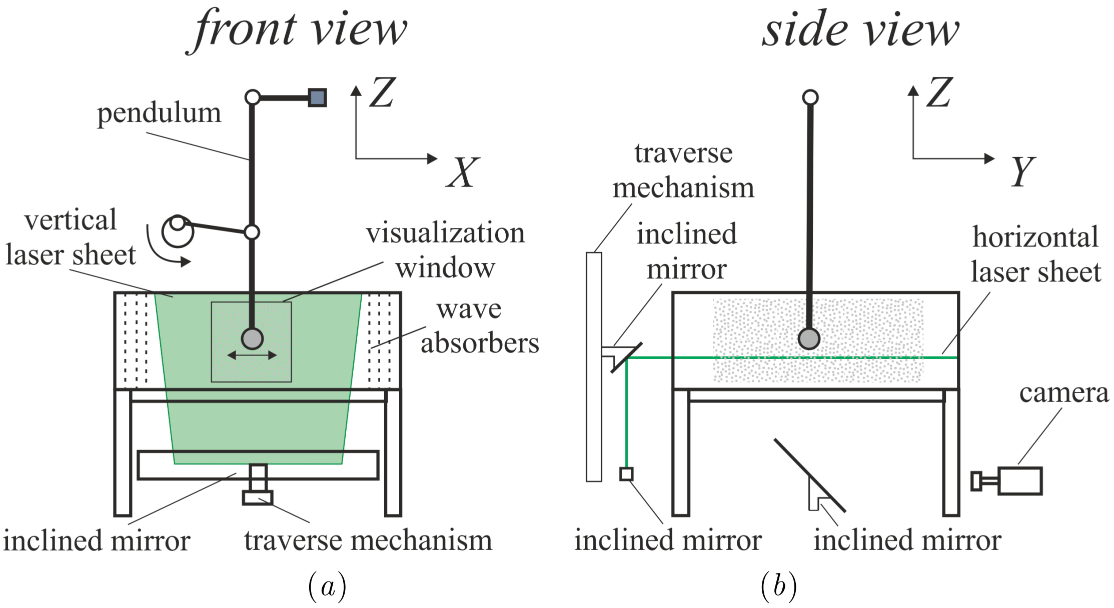

Figure 2.3: Sketch of the experimental setup: (*a*) front view and (*b*) side view, with the seeded particles as light grey dots and the laser plane shown in green. The mobility of the laser plane in the y-direction allows for the measurement of successive planes, and the reconstitution of the horizontal wave field.

The tank was filled to the depth 85 ± 3 cm with a linearly salt-stratified fluid using the conventional double-bucket technique (Fortuin, 1960; Oster & Yamamoto, 1963). The double-bucket system consists of two communicating vessels having a total volume of 1 m^3, that is comparable to the volume of the experimental tank (Figure 2.4*a*). One vessel is filled with salt water, and the other with fresh water, the salt water being obtained by mixing brine, stored in a lower vessel, with fresh water in order to achieve the desired density for a particular stratification.

Generally, the mechanism of the double-bucket system is as follows. Part of the salt water is pumped through the bottom of the salt water vessel to the experimental tank, while another part recirculates back to the vessel through the top. At the same time the fresh water flows into the salt water vessel and reduces the salinity of the fluid. Therefore, during this process the pumped salt water is replaced with fresh water and is mixed in the salt water vessel. The experimental tank is filled via the hosepipe with the salt fluid, of continuously decreasing density, until both vessels of the double-bucket system are nearly empty and the density is approaching that of fresh water. We denote by ρ_1, V_1 and ρ_2, V_2 the density and fluid volume in the vessels with fresh and salt water, respectively (Figure 2.4*a*), taking into account that the density of the salt water and the volumes are functions of time, in the form $\rho_2(t), V_1(t)$ and $V_2(t)$. The constant flow rates Q_1 and Q_2 are respectively between the two vessels and in the hosepipe connecting the system with the experimental tank. If we consider volume conservation

$$\frac{dV_2(t)}{dt} = Q_1 - Q_2, \tag{2.1}$$

we can derive the volume of salt water, $V_2(t) = V_2(0) - (Q_2 - Q_1)t$, and substitute it inside the mass conservation equation

$$\frac{d[\rho_2(t)V_2(t)]}{dt} = \rho_1 Q_1 - \rho_2(t) Q_2, \tag{2.2}$$

to derive the differential equation for the salt water density $\rho_2(t)$;

$$\frac{d\rho_2(t)}{dt} - Q_1 \frac{\rho_1 - \rho_2(t)}{V_2(0) - (Q_2 - Q_1)t} = 0. \tag{2.3}$$

Thus the evolution of $\rho_2(t)$ is

$$\rho_2(t) = \rho_1 - [\rho_1 - \rho_2(0)] \left[1 - \frac{Q_2 - Q_1}{V_2(0)} t \right]^{Q_2/(Q_2 - Q_1)}. \tag{2.4}$$

Now, the experimental tank is filled from above, though a special device consisting of sponged attached tho thin foam sheets, the size of $A3$ paper sheets, floating at the surface of the fluid (Figure 2.4*b*). This device avoid mixing in the tank during filling, with the sponges controlling the flow and the foam sheets minimizing the disturbances in the fluid. With this setup, the vertical position a at which the incoming fluid of density $\rho(t)$ is deposited is

$$z(t) = \frac{Q_2}{D} t,$$

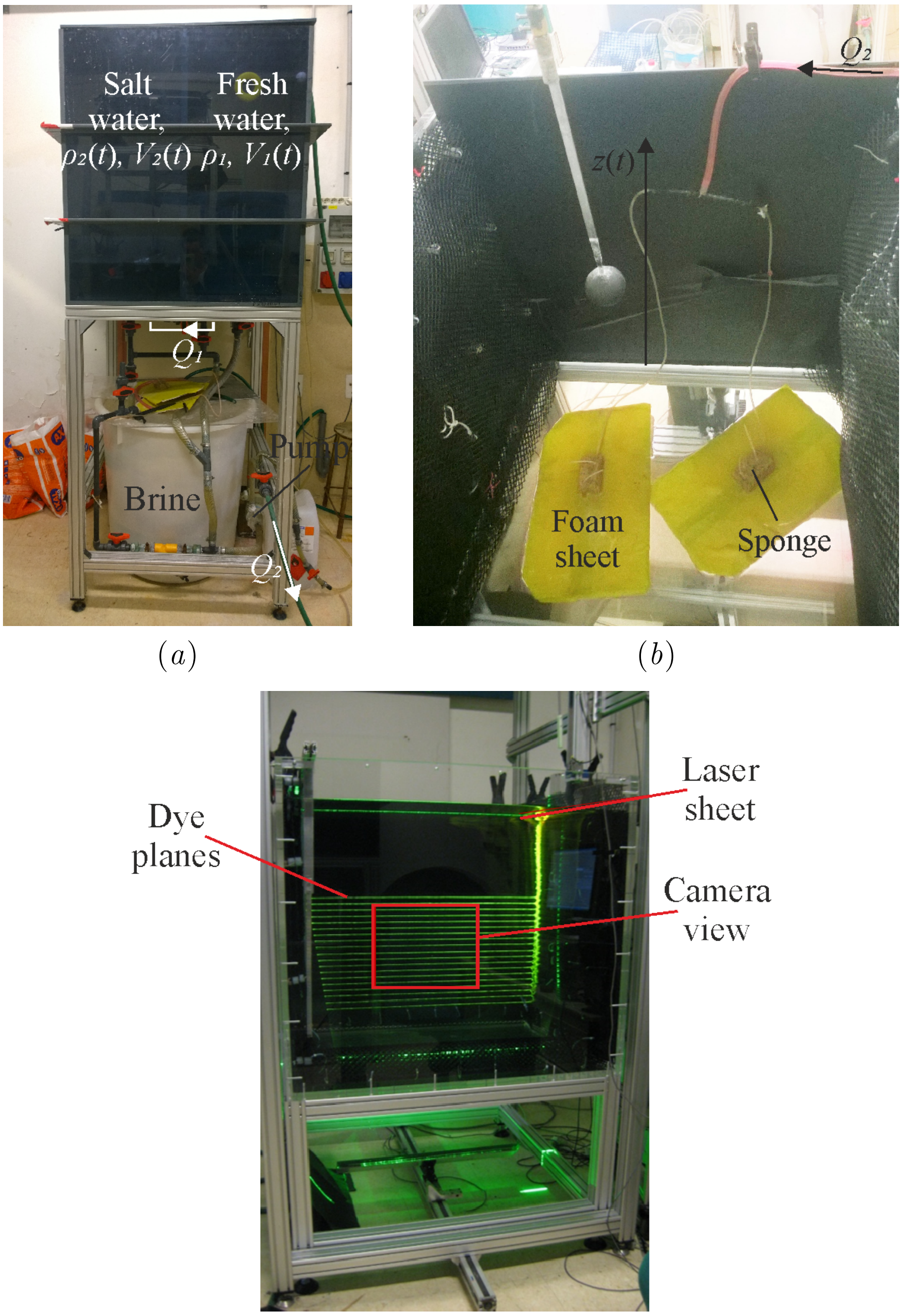

(*a*) (*b*)

(*c*)

Figure 2.4: Small-tank experiments: (*a*) double-bucket system; (*b*) filling device including two foam sheets with sponges in the experimental tank; (*c*) LIF visualisations with dye lines illuminated by a vertical laser sheet.

with D the horizontal cross-section of the experimental tank. Substituting this expression into equation (2.4), we obtain the fluid density in the experimental tank as a function of z,

$$\rho_2(z) = \rho_1 - [\rho_1 - \rho_2(0)] \left[1 - \frac{Q_2 - Q_1}{V_2(0)} \frac{D}{V_2(0)} \right]^{Q_2/(Q_2 - Q_1)}, \tag{2.5}$$

which is linear only if $Q_1/(Q_2 - Q_1) = 1$ and thus $Q_1 = Q_2/2$. To obtain this relation between the flow rates, we used two vessels of equal size connected from below and controlled the flow rate Q_2 with a pump. Properly done, this procedure gives a linear density profile in the experimental tank over the entire depth if $\rho_1 < \rho_2(0)$, except for two boundary layers at the surface of the fluid and at the bottom of the tank. For our experimental tank the process of filling takes approximately 11 hours excluding the preparation of water in the salt water vessel.

The stratification profile was calculated from the density of fluid samples taken at different heights in the fluid and measured with an Anton Paar Density meter. The buoyancy frequency was defined as $N = [(-g/\rho)\, \mathrm{d}\rho/\mathrm{d}z]^{1/2}$ with g the gravitational acceleration and $\rho(z)$ the density distribution over the vertical coordinate z.

A remark should be made about stratification by salinity and temperature gradients. The oceans are stratified due to the presence of gradients in temperature and salinity. In a small scale laboratory experiment the stratification by salinity is more preferable than by temperature. The salt concentration can be controlled more easily than temperature, which changes due to surrounding conditions, and the salt diffusivity is smaller (by two orders of magnitude) than that of temperature. In all cases, evaporation at the surface has a perturbing effect on the stratification. Working with a salinity of about 5-8% allows to neglect this influence of the temperature difference. Experience shows, nevertheless, that winter experiments are always better; hence, it is of use to keep the temperature in the experimental room low, so as to reduce the evaporation and the temperature gradient within the fluid.

2.2.2 Wave generation

Internal waves were generated by the horizontal oscillations of a plexiglas object. As objects we have used a sphere of radius a, an oblate and a prolate spheroid of equatorial radius a and polar radius b, with $a = 3.125$ cm the same as for the sphere, and tori of minor radius $a = 1, 1.5$ and 2 cm and major radius b (Figure 2.5). The aspect ratio, defined as $\epsilon = b/a$, is 1/2 for the oblate spheroid, 1 for the sphere, 2 for the prolate spheroid, 5, 9 and 34 for three tori. These parameters are also presented in Table 2.1. Objects were attached to a pendulum of length $l = 180$ cm, and the oscillations of the pendulum at frequency ω were driven by a crank mechanism. The oscillation amplitude, A, was small compared to the length of the pendulum, and the motion was therefore in good approximation horizontal and sinusoidal. The two side walls of the tank perpendicular to the direction of oscillation were covered with a mesh of 5 cm thickness to avoid wave reflections.

Wave visualisation required illumination with a laser sheet. A continuous 2 W laser with wavelength $\lambda = 512$ μm was used, the laser beam passed through a semicylindrical lens and the resulting laser sheet reflected at an inclined mirror below or

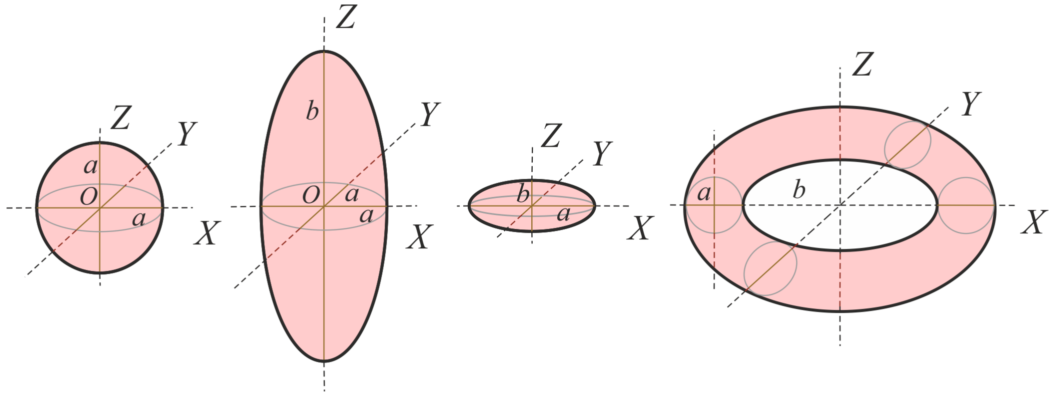

(a) (b) (c) (d)

Figure 2.5: Oscillating objects: (a) sphere; (b) prolate and (c) oblate spheroids; (d) torus.

Object	Axis of revolution	a (cm)	b (cm)	ϵ
Sphere ($\mathcal{S}$)		3.125	3.125	1
Prolate spheroid ($\mathcal{V}$)	vertical (Z)	3.125	6.25	2
Prolate spheroid ($\mathcal{H}$)	horizontal (X)	3.125	6.25	2
Oblate spheroid ($\mathcal{V}$)	vertical (Z)	1.56	3.125	1/2
Oblate spheroid ($\mathcal{H}$)	horizontal (X)	1.56	3.125	1/2
Oblate spheroid (45°)	horizontal, 45°	1.56	3.125	1/2
"Thin" torus	vertical	1.5	13.5	9
"Thick" torus	vertical	2	10	5
"Big" torus	vertical	1	34	34

Table 2.1: Definitions and dimensions of oscillating objects. In the cases of the sphere and spheroids a and b define the equatorial and polar radii, respectively, and in the case of the tori a and b correspond to the minor and major radii, respectively, $\epsilon = b/a$ is the aspect ratio.

behind the tank as shown in Figure 2.3. This mirror was attached to a computer–controlled step motor, of which the use is explained in the next section. Images were recorded by a 10-bit JAI digital camera with CCD of 1380 x 1030 pixels and a 12-bit Dalsa camera with CCD of 1024 x 1024 pixels. The positions of the cameras and the laser sheets will be described more precisely for each series of experiments in the next sections.

Throughout all experiments a Cartesian coordinate system has been used, with origin at the centre of the object, z-axis pointing vertically upwards, and horizontal axes x and y along and perpendicular to the direction of oscillation, respectively (Figure 2.5). Non-dimensional coordinates X, Y and Z have been introduced, defined as

$$(X, Y, Z) = \frac{(x, y, z)}{a},$$

and the velocity components (u, v, w) have similarly been normalized as

$$(U, V, W) = \frac{(u, v, w)}{A\omega}.$$

Each set of experiments, presented in Table 2.2, is characterized by four nondimensional parameters,

$$\epsilon = \frac{b}{a}, \qquad \frac{\omega}{N}, \qquad St = \frac{\omega a^2}{\nu}, \qquad Ke = \frac{A}{a},$$

respectively the aspect ratio defining the geometry of the object, the frequency ratio defining the angle of propagation of the waves, the Stokes number defining the intensity of viscous effects and the Keulegan-Carpenter number defining the intensity of nonlinear effects, where ν is the viscosity of the fluid and N its buoyancy frequency. Through all the rest of this thesis the small-tank experiments will be named according to the nomenclature defined in Table 2.2, such as A_1, A_2, and so forth.

2.2.3 Wave visualisation and data processing for PIV measurements

The waves were visualised using two different methods. The first method was two-dimensional Particle Image Velocimetry (PIV) which allows to measure the velocity field of the flow. Practical recommendations on optimum particle size and seeding are presented in Westerweel (1997). The fluid was seeded with Orgasol® $30\mu m$ particles of density $\rho = 1.2 kg/m^3$. To illuminate particles two positions of laser sheet were performed.

In experiments A_2, B_1 and B_2 the waves were visualised with a vertical laser sheet parallel to the direction of oscillation (Figure 2.3*a*). The position of the sheet was driven by a computer-controlled step motor and allowed for the recording of sequences of vertical planes. To measure period-averaged quantities and determine the amplitudes of the Fourier components of the signal in a vertical plane, the sheet was kept fixed during one oscillation period, and then moved with a prescribed increment $\Delta y = 0.5$ cm to the next position, until enough vertical planes were obtained to reconstruct the three-dimensional wave field by spline interpolation. These measurements were taken after 20 oscillation periods, which is the typical duration required to exclude the effects of internal-wave transients (Voisin, 2003; Ermanyuk & Gavrilov, 2005; Voisin *et al.*, 2011). For experiments D, E, G_3, H_3 and K the vertical laser sheet was kept fixed in the central plane ($Y = 0$) and passed through the transparent bottom of the tank. Long time series (up to 60 oscillation periods) were taken starting from the beginning of the oscillations.

For all experiments with a vertical laser sheet, a camera was set in front of the tank as shown in Figure 2.3(*b*). Images of the illuminated particles were taken

	Method	Object	ϵ	ω/N	St	Ke	Fo	Y	Z
Exp A_1	LIF	Sphere ($\mathcal{S}$)	1	0.76, 0.41	503, 271	0.27		0 to 6.1	-5.09
Exp A_2	LIF	Sphere ($\mathcal{S}$)	1	0.26	101	0.69, 1.37		0 to 5.5	-1.11,-1.37
Exp A_3	PIV	Sphere ($\mathcal{S}$)	1	0.27	290	0.22, 0.37, 0.52, 0.84		0 to 3.2	-1.5
Exp B_1	PIV	Prolate ($\mathcal{V}$)	2	0.29, 0.39	311, 418	0.22, 0.39, 0.58, 0.83		0 to 3	-2.75
Exp B_2	PIV	Prolate ($\mathcal{H}$)	2	0.29	311	0.16, 0.33, 0.6, 0.76		0 to 3	-1.25
Exp C_1	PIV	Prolate ($\mathcal{H}$)	2	0.36	417	0.75		0 to 7	0 to -2.5
Exp C_2	PIV	Prolate ($\mathcal{H}$)	2	0.45	430	0.5		0	-10 to 2
Exp D	PIV	Prolate ($\mathcal{V}$)	2	0.45	430	0.5		0	-6.3 to 4.5
Exp E	PIV	Oblate ($\mathcal{V}$)	1/2	0.34	541	0.56		-8 to 8	-2
Exp F_1	LIF	Oblate ($\mathcal{V}$)	1/2	0.4, 0.8	300, 601	0.617		0 to 5	-6.5 to -1.28
Exp F_2	LIF	Oblate ($\mathcal{H}$)	1/2	0.4, 0.8	300, 601	0.617		0 to 5	-1.74
Exp F_3	LIF	Oblate (45°)	1/2	0.4, 0.8	300, 601	0.617		0 to 5	-1.69
Exp G_1	LIF	Torus	9	0.80	142	0.19, 0.41, 0.65, 0.84, 1.1	0.039, 0.08, 0.13, 0.17, 0.23	0	-1.84 to -21.8
Exp G_2	LIF	Torus	9	0.81	144	0.17, 0.43, 0.62	0.04, 0.08, 0.14	0 to 10	-3.6
Exp G_3	PIV	Torus	9	0.80	164	0.21, 0.57, 0.78, 1.06, 1.26	0.043, 0.12, 0.16, 0.22, 0.26	0	-1 to -16.75
Exp H_1	LIF	Torus	5	0.81	256	0.15, 0.3, 0.52, 0.72	0.036, 0.08, 0.14, 0.20	0	-1.88 to -16.88
Exp H_2	LIF	Torus	5	0.81	256	0.13, 0.29	0.036, 0.08	0 to 5.5	-3
Exp H_3	PIV	Torus	5	0.80	292	0.19, 0.41, 0.6, 0.95, 1.2	0.053, 0.11, 0.16, 0.26, 0.33	0	-1 to -10.88
Exp I	LIF	Torus	5	0.41	129	0.33, 0.58	0.058, 0.10	0 to 10	-1.87 to -14.87
Exp J	PIV	Torus	5	0.60	285	0.3, 1.25	0.072, 0.30	-10 to 10	-6.7
Exp K	LIF & PIV	Torus	34	0.79	65	0.35, 0.75, 1.0, 1.3, 1.6	0.036, 0.076, 0.10, 0.13, 0.16	0	0 to -70
Exp L	PIV	Torus	9	0.39	72	0.6	0.075	-11 to 11	-3

Table 2.2: Experimental parameters for the small-tank experiments in terms of the objects, nondimensional numbers and nondimensional coordinates introduced in section 2.2.2. The focusing wave number *Fo* is introduced in chapter 5.1.

with a time interval such that the maximum in-plane displacement of the particles was smaller than one fourth of the interrogation window size, and the out-of-plane displacement smaller than one fourth of the laser sheet thickness. For the imaging area used in this setup, 1 pixel corresponded to approximately 0.37 mm.

In experiments C, J and L the particles were illuminated with the horizontal laser sheet passed through the side of the tank (Figure 2.3*b*). Different horizontal planes were recorded at different depths by shifting the inclined mirror to a certain vertical position for illumination. For these measurements the thickness of the laser sheet was increased in order to determine the displacement of the particles. Increasing the laser sheet thickness allowed to follow the illuminated particles for a sufficiently long time to use PIV images taken through the bottom of the tank (see Figure 2*b*).

The particle displacement was obtained by cross-correlating two successive images using standard PIV techniques (Fincham & Delerce, 2000). For the PIV calculations, the UVMAT/CIVx software packages developed at LEGI were used[1]. Each image was divided in boxes of a preselected size. The size of one box was large enough to observe a recognizable pattern, and small enough to present little perturbations of the pattern shape between two successive images. The pattern was generated with seeded particles, so that the algorithm could determine its position by calculating the correlation coefficients and selecting their maximum. The velocity was estimated by dividing the obtained displacement pattern by the time interval Δt defined by the acquisition frequency. Each PIV calculation provides two components of the velocity field: the longitudinal horizontal velocity, $\hat{u}$, and the vertical velocity, $\hat{w}$, when the laser sheet was positioned vertically, and the longitudinal, $\hat{u}$, and transverse, $\hat{v}$, horizontal velocities, when the laser sheet was positioned horizontally. Hereinafter a hat $\hat{}$ will denote a velocity component measured by PIV.

The signal obtained by the experimental procedure is periodic in time since the main motion is due to waves. Thus, it is possible to separate it into different components that oscillate at different frequencies (harmonics of the fundamental oscillation frequency). The most convinient way of performing the separation is to use Fourier filtering based on Fourier transformation. The analytical form of Fourier transform of a signal $f(t)$ is

$$F(\omega) = \int_{-\infty}^{+\infty} f(t) \exp^{i\omega t} dt, \tag{2.6}$$

with t the time and ω the frequency. This transform allows to interpret the signal $f(t)$ as a sum of an infinite number of harmonic functions with specific amplitudes and phases. Thus, for any continuous function it is possible to define a discrete function (spectrum) represented by an infinite series of harmonics. For digital processing the discrete form of the Fourier transform (DFT) is used, defined on the time interval $[0, T]$ as

$$f_n = f\left(\frac{nT}{N}\right), \qquad F_k = \frac{N}{T} F\left(\frac{2\pi k}{T}\right) = \sum_{n=0}^{N-1} f_n e^{2\pi i k \frac{n}{N}}, \tag{2.7}$$

---

[1] `http://www.legi.cnrs.fr/web/spip.php?article763`

with N the length of the signal, $n = 1, \ldots N-1$ and $k = 0, \ldots, N-1$ (Van Loan, 1992). For faster computation the Fast Fourier Transform (FFT) algorithm included in the Matlab package is used. An FFT computes the discrete Fourier transform of a sequence by factorizing the DFT matrix into a product of sparse (mostly zero) factors. This algorithm reduces the complexity of the computation from $O(N^2)$ for a DFT to $O(N \log N)$ for the FFT.

In some experiments data were recorded at sequences of vertical planes: one period per plane. The Fourier filtering was applied for these experimental data to decompose fundamental and higher harmonics. More detailed description is presented below in this section.

Another possible algorithm for filtering the waves of a particular frequency is temporal filtering, which is the part of the complex demodulation approach based on Hilbert transformation and first applied to internal waves by Mercier *et al.* (2008). The following steps are involved:

- Fourier transform of the signal in time. This leads to a frequency spectrum having maximum peaks associated with waves of different frequencies. Here we determine the working frequency ω_n, with $n = 0$ for the mean flow, $n = 1$ for the fundamental frequency, $n = 2$ for the second harmonic and so forth, around which we perform the filtering.

- Multiplication of the spectrum by a Hamming window $h(n) = \alpha - \beta cos\left(\frac{n}{N-1}\right)$, with $\alpha = 0.54$ and $\beta = 1 - \alpha = 0.46$. In signal processing, a window function is a mathematical function that is zero-valued outside some chosen interval. The cosine window proposed by Richard W. Hamming is optimized to minimize the maximum side lobe. The constants are approximations of $\alpha = 25/46$ and $\beta = 21/46$, respectively. In our case the Hamming window is centered around the working frequency and has a small frequency width, and therefore it isolates one specific frequency.

- Generation of the complex signal by the inverse temporal Fourier transform.

A similar technique can be applied in order to filter in space by performing the spatial Fourier transform and choosing a working wave vector. Together, spatial and temporal filtering allow to identify a wave with particular (ω, k, m). This is practical for the identification of plane internal waves in space and time.

The complex demodulation in time has been applied to the long time series of experimental data (since long enough series are required for the calculation of Hilbert transforms with sufficient accuracy). The real part of the resulting complex signal is the filtered n-th harmonic, and its modulus is the amplitude of this harmonic. The velocity amplitude is averaged over 8-15 oscillation periods recorded after reaching the steady regime. In the following a filtered n-th harmonic, either by Fourier or complex demodulation, will be denoted with a subscript n, for example $\hat{U}_n$.

2.2.4 Wave visualisation and data processing for LIF measurements

The second visualisation method was the method of fluorescent dye planes introduced by Hopfinger *et al.* (1991) for the qualitative measurements of vertical fluid displacement and Flór *et al.* (2002) for quantitative measurements (Figure 2.4*c*). A set of equidistant dye planes was generated by slowly displacing a rake of horizontally spanned cotton wires through the fluid. These cotton wires were soaked in a fluorescent dye solution and dried before the experiment. The dye planes were illuminated with a moving vertical laser sheet parallel to the direction of oscillation. Data processing was performed with a cross-correlation technique (Voisin *et al.*, 2011; Ermanyuk *et al.*, 2011). The light intensity $I(z)$ along a vertical line across the laser-illuminated fluorescein planes varies as a sequence of Gaussian peaks superposed with a weak random noise. To determine the position of each maximum we calculate the cross-correlation of the experimental signal with a Gaussian

$$G(z, z', s_0) = \exp^{-\frac{(z-z')^2}{2s_0}} / (\sqrt{2\pi} s_0),$$

defined as

$$C(z') = \int I(z) G(z, z', s_0) dz.$$

In practice, the correlation is calculated for discrete values with an increment of 1 pixel, i.e.

$$C_k = \sum_{n=0}^{N-1} G_n I_{n+k}.$$

To reduce the computation time, the Gaussian function $G(z, z', s_0)$ is calculated once for N points, with $N = 4s_0$ to ensure that the tails of the function are sufficiently close to zero, and with centre at $z' = 2s_0$ so that

$$G_n = G(n, 2s_0, s_0).$$

Subpixel interpolation is performed: three upper points at each local maximum of C_k are used to calculate the coefficients of a parabolic fit, allowing the position of the maxima to be determined analytically, with an accuracy of approximately 0.05 pixel.

Prior to the onset of the oscillation, the dye planes were scanned by a laser sheet in the otherwise quiescent fluid to obtain the reference state $\zeta(0)$ for each dye plane. The vertical displacement of this dye line, ζ^t, was measured at a certain position in time t either from two successive images

$$\zeta^t(t) = \zeta(t + \delta t) - \zeta(t),$$

or with respect to the reference state $\zeta^t(0)$, yielding

$$\zeta^t(t) = \zeta(t) - \zeta(0).$$

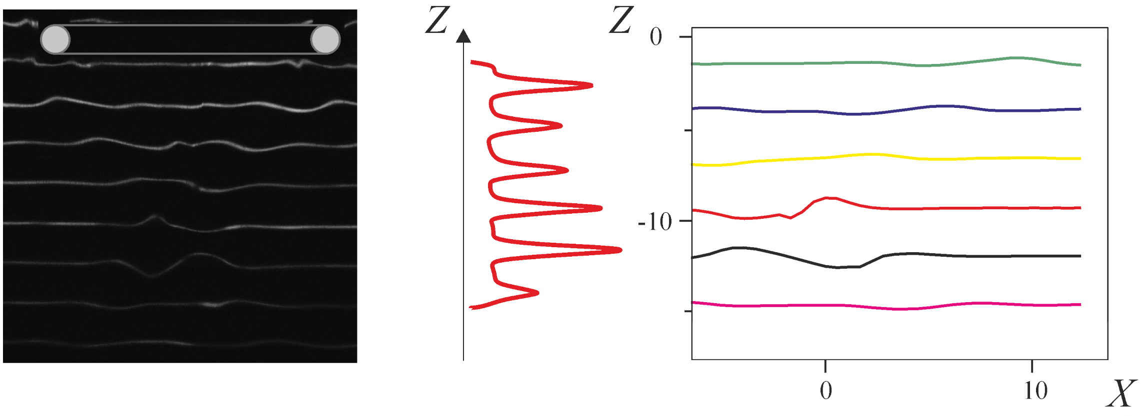

(*a*) (*b*) (*c*)

Figure 2.6: Cross-correlation algorithm for LIF processing; (*a*) original image, (*b*) light intensity profile $I(z)$, (*c*) resulting image.

The local slopes of the dye lines in the plane XZ are defined as

$$S(t) = \arctan\left(\frac{\partial \zeta^t}{\partial x}\right).$$

In practice they were evaluated as

$$S(t) = \arctan\left(\frac{\Delta \zeta^t}{\Delta x}\right), \tag{2.8}$$

where Δx should be sufficiently large compared to the accuracy of measurement of the vertical displacement ζ^t and sufficiently small compared to the radius of the object, a, to resolve the details of the wave profile. The vertical displacements were evaluated as average values over vertical stripes of the width of several pixels (as described in Ermanyuk *et al.*, 2011; Voisin *et al.*, 2011), which defines the horizontal spatial resolution of the data. This gave, for example, $\Delta x = 5$ (≈ 0.253 cm) and 8 pixels (≈ 0.339 cm) for the thick torus in experiment H_1 and thin torus in experiment G_1, respectively.

To reconstruct the three-dimensional distribution of the vertical displacement, a series of images was acquired for different positions in the y-direction. Therefore, the mirror reflecting the laser light (see Figure 2.3*a*) was moved by a computer-controlled step motor with a prescribed increment $\Delta y = 0.8$ cm. At each position the mirror remained fixed during one period of oscillation. This allowed to acquire time-series suitable for subsequent Fourier analysis and evaluation of amplitudes of n-th harmonic components of the signal.

Time-series of vertical displacements $\zeta^t(t_i)$ were analyzed using three different methods. With the first method, the amplitudes of the n-th harmonic components ζ_n and S_n of the signals were determined via Fourier filtering of time-series. Similar analysis has been used in Voisin *et al.* (2011) and Ermanyuk *et al.* (2011). This type of data processing is particularly useful for linear or weakly non-linear processes when the first few harmonics are dominant and can be clearly identified. With the second method, the amplitudes ζ_{rms} and S_{rms} were evaluated as the period-averaged r.m.s. of the corresponding time-series multiplied by $2^{1/2}$ (Sutherland & Linden, 2002). In principle, this quantity takes into account the contribution of all harmonics in the signal. However, owing to the period-averaging procedure the r.m.s. value cannot precisely capture the extreme values of wave amplitude and wave slope, which may instantly occur at a particular phase of oscillation. Of special interest are the extreme slopes which can trigger incipient overturning in the case when the wave crests become steep. Therefore, a third method of data processing was introduced. The time-series $\zeta(t_i)$ and $s(t_i)$ measured at each point were sorted to find the maximum values $\zeta_{max} = \max|\zeta^t(t_i)|$ and $S_{max} = \max|s(t_i)|$.

Thus with these three methods, next to the values ζ_n, ζ_{rms} and ζ_{max}, the slopes S_n, S_{rms} and S_{max} were measured in degrees (after taking the arctangent) allowing to explicitly study the transition of the wave system to overturning. The displacement amplitudes were normalized generally with the oscillation amplitude A, or for the torus in the case when only the focal region was of interest, with the minor radius of the torus a.

PIV and LIF measurements have their advantages and limits, that we discuss in the next section.

2.3 Choice of the visualisation technique for high wave slopes

2.3.1 A note on Eulerian and Lagrangian approaches

Fluid motion can be described with two approaches. Using the Euler approach, one considers a fixed set of points in space, $\vec{x} = (x_1, x_2, x_3)$. At different times t different fluid particles travel through each point, each particle with a specific velocity $\vec{u}$ depending on the time t and position $\vec{x}$, yielding a velocity field $\vec{u}(\vec{x}, t)$. In the Lagrangian approach one considers a fixed set of fluid particles, of position $\vec{\xi_0} = (\xi_{0,1}, \xi_{0,2}, \xi_{0,3})$ at an initial time t_0. For a complete description of the fluid motion it is necessary to know the trajectory of all particles, i.e., the position of each particle at any ulterior point in time $t > t_0$. This means that for each particle we need to know the equation of its trajectory $\vec{\xi} = \vec{\xi}(t)$, and the velocity follows then as $\vec{u} = d\vec{\xi}/dt$. Each particle differs from another in its initial position, $\vec{\xi_0}$, and therefore this value is included in the equation of the trajectory of the particle as a parameter, $\vec{\xi} = \vec{\xi}(t, \vec{\xi_0})$. Lagrangian coordinates are parameters that characterize each point of the medium and do not change during the process. Thus, the Lagrange approach is based on the description of the history of motion of each fluid particle separately. In practice such a description is more complex than the Euler approach in terms of fluid motion equations, but is also more detailed when applied to wave visualisation.

2.3.2 PIV and LIF measurements of wave focusing

In this section we investigate the difference between PIV and LIF measurements, in the particular case of wave focusing by the big torus in K (aspect ratio $\epsilon = 34$) applying both techniques of visualisation at the same time. The oscillation amplitude A is large comparing to the minor radius of the torus a, i.e. the Keulegan-Carpenter number is $Ke = 1.3$. Two cameras are used, one to recognise particles and the other the fluorescein, both illuminated by a vertical laser sheet. Schematically, the propagation of wave beams generated by the big torus in a fluid of finite depth $H = 89$ cm is shown in Figure 2.7(a) with a red square defining the camera view. Wave focusing is obtained, with divergent wave beams absorbed by grids at each side wall and convergent wave beams focusing on the axis $X = Y = 0$. In addition to the focal zone of the direct waves radiated by the torus at $Z = -45$, a second focal zone of waves reflected at the surface is observed close to the torus at $Z = -15$, together with two zones of beam intersection on the sides at $Z = -30$.

Figures 2.7(b,c) show the distributions of vertical, $\hat{W}_1$, and horizontal, $\hat{U}_1$, velocity amplitudes, respectively, obtained with PIV measurements in the vertical plane $Y = 0$ parallel to the direction of oscillation. The amplitude is amplified in both focal zones, forming two symmetric structures of roughly elliptic shape for the vertical velocity, and one structure also of roughly elliptic shape for the horizontal velocity. In the two regions of beam intersection the amplification is not symmetric, but inclined downwards toward the axis. Patterns of vertical displacement amplitude, ζ_1/A, and wave slope, S_1, obtained with LIF measurements are presented in Figures 2.7(d) and (e), respectively. The structure of the vertical displacement is similar to that for the vertical velocity amplitude (Figure 2.7c), consistent with the linear theory according to which, for tune dependence as $\exp^{-i\omega t}$, we have $w = \partial\zeta/\partial t = -i\omega\zeta$. Wave slopes are maximized in both focal zones and zones of beam intersection. In Figure 2.8 distribution of vertical velocity and displacement amplitudes along the direction of oscillation X are presented for different vertical distances from the torus. It can be seen that there is no particular energy loss due to reflection at the surface, as the magnitudes of the velocity and displacement amplitude in the focal zone (Figure 2.8b, $0 < X < 10$) and in zones of wave beam intersection (Figure 2.8c, $15 < X < 20$) remain the same. The effects of wave focusing will be discussed in detail in chapters 4 and 5. Here we only consider the differences in the wave measurement techniques.

The comparison of the results of LIF (a Lagrangian approach) and PIV (an Eulerian approach) is presented in Figure 2.8 for the vertical displacement and vertical velocity amplitude, respectively. The PIV technique provides with qualitative results of two velocity components $\hat{U}$ and $\hat{W}$ while quantitatively profiles of the amplitude in the focal zone. They are systematically lower than the LIF results in the high gradient zones (around, $X = 5$ in Figure 2.8b and $X = 20$ in Figure 2.8c). With increasing oscillation amplitude, the slopes become steeper and the difference between results of LIF and PIV techniques increases. Since we may expect that for steep slopes LIF measurements are more precise than the PIV results, this graph indicates the error made with PIV measurements. The choice of the wave mea-

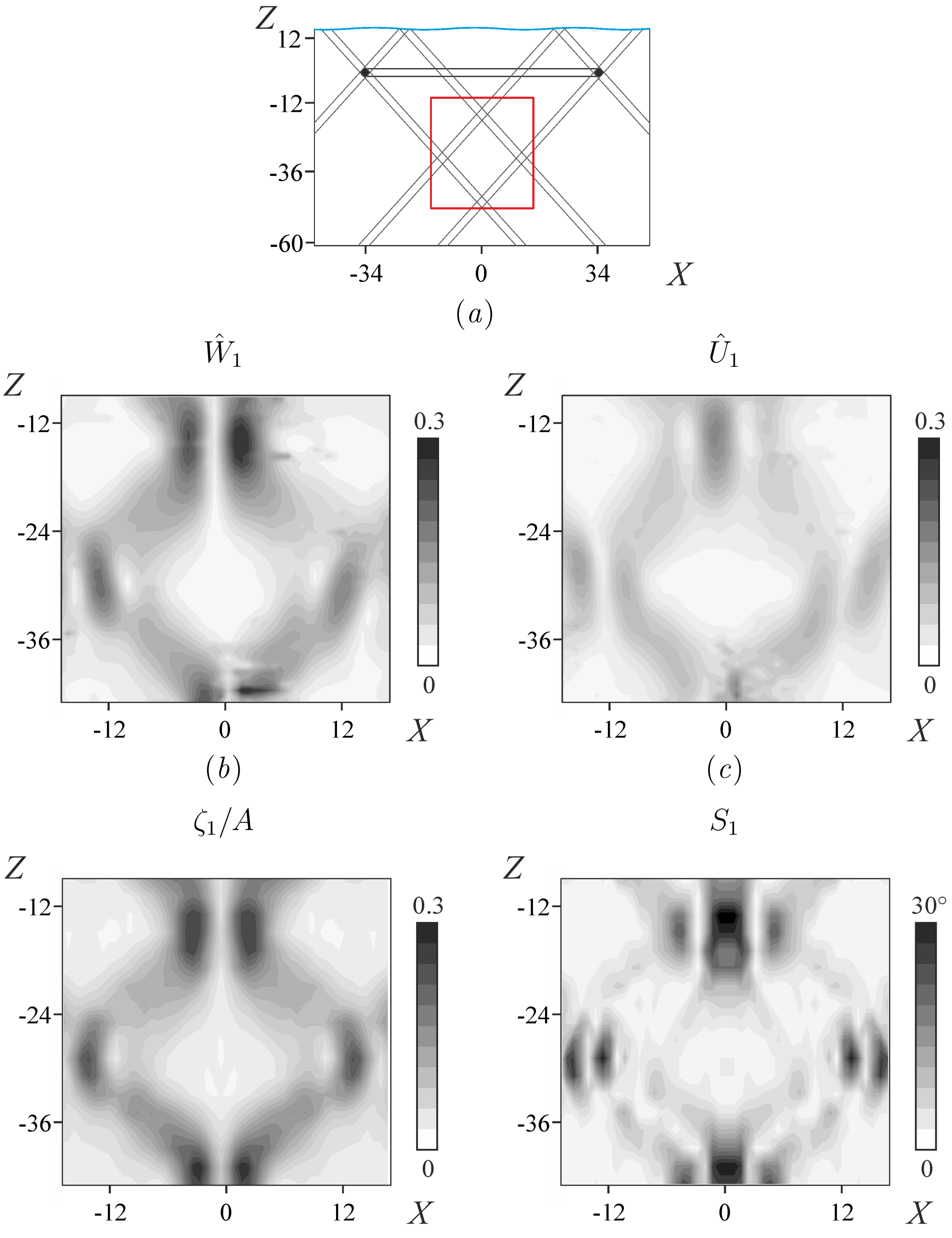

(*a*)

(*b*)

(*c*)

(*d*)

(*e*)

Figure 2.7: (*a*) Schematic illustration of the wave beams generated by the oscillation of the torus ($\epsilon = 34$). Red rectangle shows the experimental field of view. Patterns in the vertical plane $Y = 0$ of (*b*) the vertical velocity, $\hat{W}_1$, and (*d*) the vertical displacement amplitude, ζ_1/A; (*c*) the horizontal velocity amplitude, $\hat{U}_1$, and (*e*) the wave slope, S_1. The patterns (*b*,*c*) were obtained by PIV and the patterns (*d*,*e*) by LIF. [Exp *K* from Table 2.2]

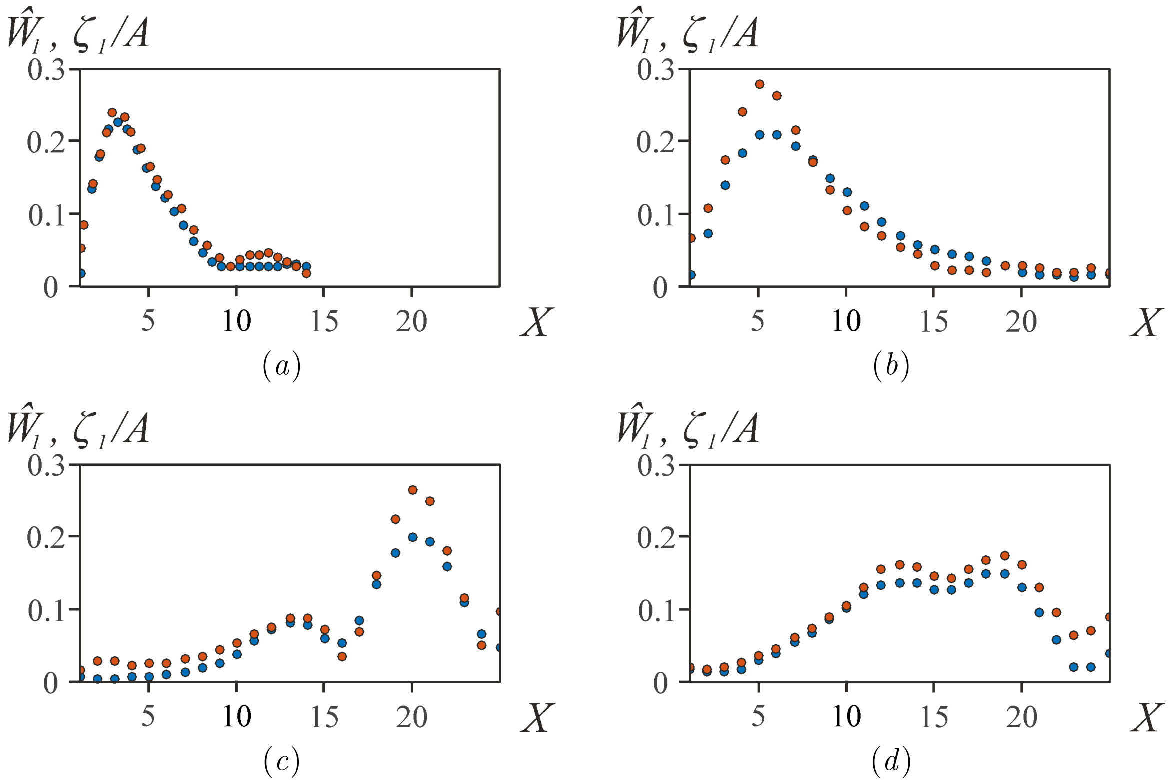

(*a*) (*b*) (*c*) (*d*)

Figure 2.8: Distribution of the vertical velocity $\hat{W}_1$ and vertical displacement ζ_1/A amplitudes at (*a*) $Z = -7$, (*b*) $Z = -15$, (*c*) $Z = -27$ and (*d*) $Z = -33$. Blue and red dots correspond to PIV and LIF measurements, respectively. [Exp K from Table 2.2]

surement method plays therefore an important role for the investigation of wave focusing.

2.4 Experiments at the Coriolis platform

A set of experiments were conducted at the Coriolis rotating platform at LEGI, which is the largest rotating platform in the world. The total platform diameter is 16 m, the tank diameter 13 m and the maximum fluid height 1 m (Figure 2.9). The platform is designed for the experimental modelling of geophysical processes in the presence of background rotation and/or density stratification. Specially designed topographies can be also installed. The large scale of the platform allows to study ocean dynamics with weak viscous effects, hence at high Stokes number St, which is not the case in the small tank described in the previous section. The maximum rotation speed of the filled platform is 2 rotations per minute.

For experiments on wave focusing, a torus consisting of four plexiglas sectors was cut in half horizontally and fitted upside down on a plexiglas plate kept at the surface of the fluid (Figure 2.10*a*). To investigate partial focusing two of these sectors were

(*a*)

(*b*)

Figure 2.9: The Coriolis platform: (*a*) generic view, illustrating the large tank diameter of 13 m (photothèque CNRS M. Fresillon); (*b*) side view of the present setup with the torus at the centre and the laser on the right.

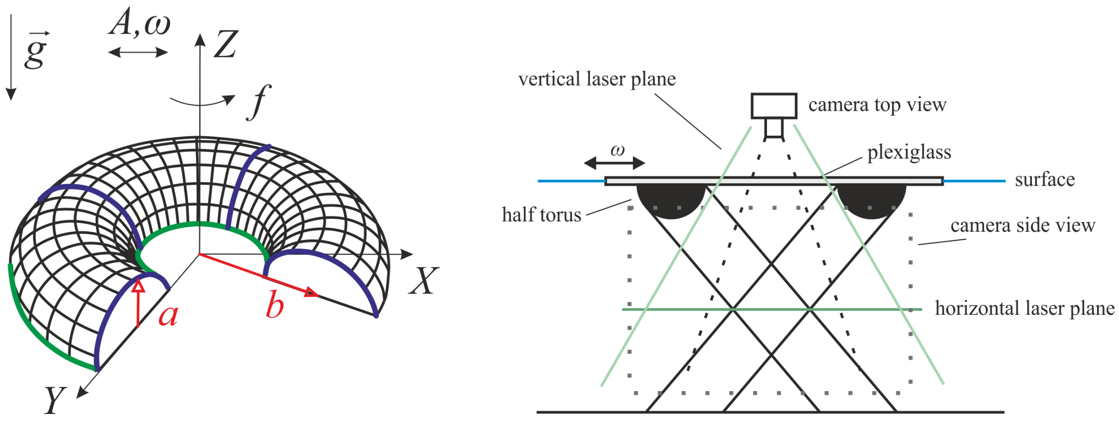

(a) (b)

Figure 2.10: (a) Parameters of the torus used as a wave generator at the Coriolis platform: $a = 15$ cm, $b = 75$ cm; (b) schematic view of internal waves generated by the torus.

removed from the plate to obtain a half–torus. The torus or half–torus, which is of major radius $b = 75$ cm and minor radius $a = 15$ cm, was located at the centre of the platform and oscillated horizontally with various amplitudes $A = 2.5, 5, 10$ and 15 cm, which were either small or comparable with the minor radius. For this large torus, depending on the oscillation frequency, the Stokes number is estimated to be $3800 < St < 6800$. For such large Stokes numbers, we expect the internal wave beams to be bimodal (namely with two maxima across each beam), implying a complex structure of the focal region.

The Cartesian coordinate system was the same as for the small tank, with origin at the centre of the torus at the free surface. The coordinates X, Y and Z are normalized similarly with the minor radius a.

Three types of waves were considered: internal gravity, inertia-gravity and inertial waves. Depending on the wave type the platform, which either stood still or rotated, was filled with a linearly stratified fluid or a homogeneous fluid, and filled to a depth of $H = 90$ cm. Special attention was paid to the fluid level in the rotating case. With the rotation the free surface of the fluid is parabolic ensuring equilibrium between the centrifugal and pressure forces. The vertical position of the torus was adapted when the rotation speed was modified. Stratification was measured with two conductivity probes providing with temperature and salinity profiles as shown on Figure 2.11.

For the wave visualisation standard two-dimensional PIV measurements or volume PIV measurements were performed. For the stratified fluid 5 liters of 200 μm polystyrene particles were used. In the stratified rotating case, smaller 60 μm Orgasol® particles were chosen. Depending on the choice of PIV technique, the laser sheet was positioned either horizontally or vertically. The vertical laser sheet was fixed parallel to the direction of oscillation and illuminated particles in the centre plane of the torus. Images were taken with a 12-bit Dalsa camera with CCD

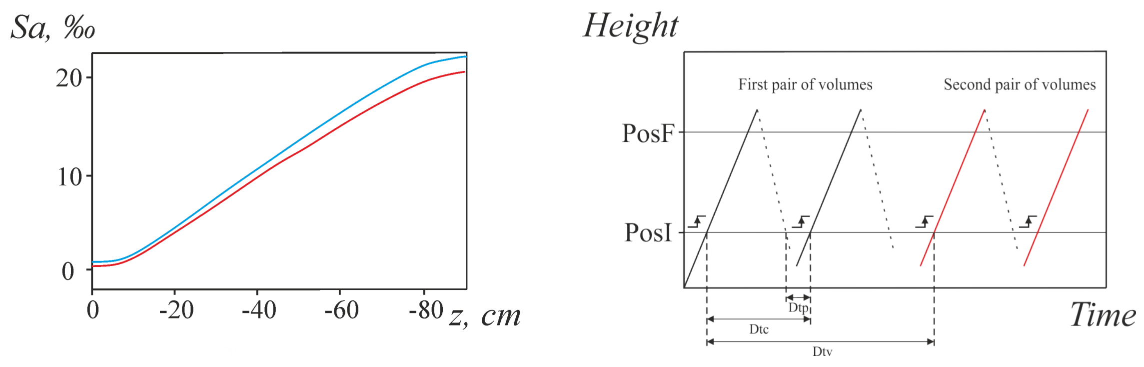

(*a*) (*b*)

Figure 2.11: (*a*) Salinity profile versus depth, z, obtained with two conductivity probes; (*b*) choice of parameters for volume PIV measurements, where $PosI$ and $PosF$ correspond to the initial and final vertical positions of the laser sheet, Dtp is the delay between two volume scans of the same pair, needed for return of the laser sheet to $PosI$, Dtv is the period between two pairs of scans, Dtc is the period of correlation between two scans of the same pair.

of 1024 × 1024 pixels located on the side of the platform (see Figure 2.10*b* and Figure 2.12*b*).

Volume PIV measurements required specific setup and specific settings of the laser and camera. The laser sheet was positioned horizontally and was driven vertically by a computer-controlled motor. The high-speed Falcon camera with CCD of 2432 × 1728 pixels was located at the top and took images of illuminated particles inside the torus. The camera settings and the motor were controlled by special software designed with LabView. The parameters for the camera and the laser motion, introduced in the software are shown schematically in Figure 2.11(*b*). The laser sheet was moved between defined initial position $PosI$ and final position $PosF$. The distance between these positions was 35 ± 3 cm depending on the experiment. Volume measurements were performed around the zone of wave focusing. The time interval between images in one volume was about 20 μs and the parameters (distance and time intervals) were chosen so that the period of correlation (Dtc) between two volumes was maximum 1 s. Each volume scan was performed in pairs, so as to allow this correlation. The time interval between two volume pairs was defined to be 3 s, so as to ensure the return of the laser sheet at its initial position.

The data were analyzed with the home made UVMAT/CIVx program[2]. The correlation was calculated between two images taken at the same level, i.e. two images from volumes in the same pair. The horizontal velocity components $\hat{u}$ and $\hat{v}$ were obtained directly from the data and the vertical velocity was calculated from the continuity equation

$$\frac{\partial w}{\partial z} = -\left(\frac{\partial u}{\partial x} + \frac{\partial u}{\partial y}\right).$$

---

[2] `http://www.legi.cnrs.fr/web/spip.php?article763`

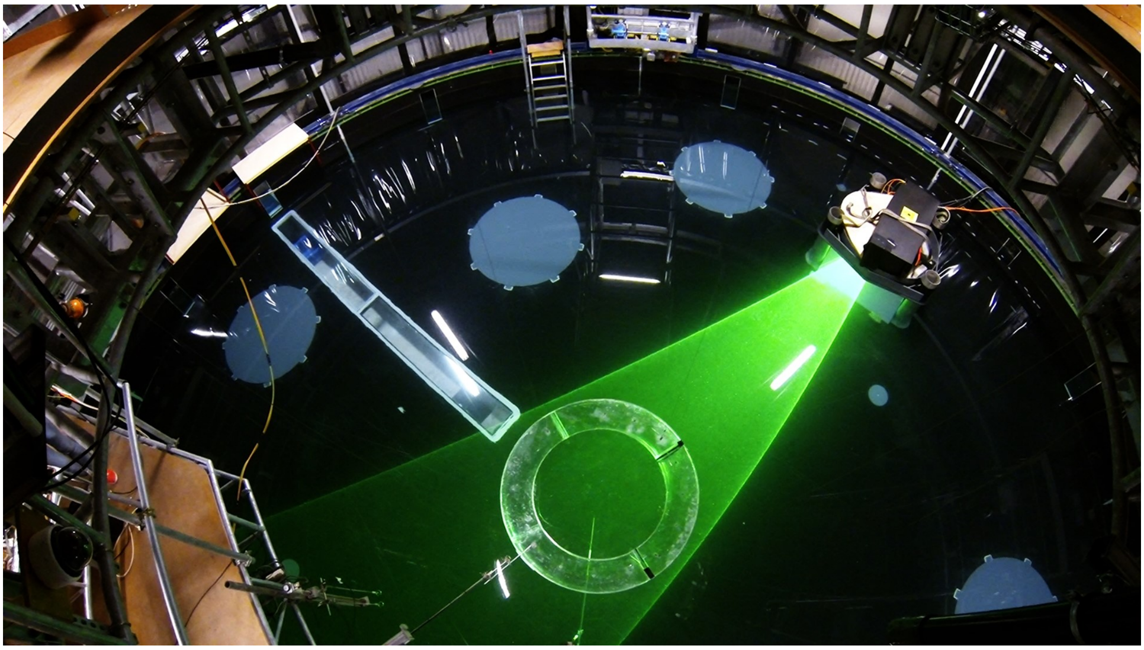

(*a*)

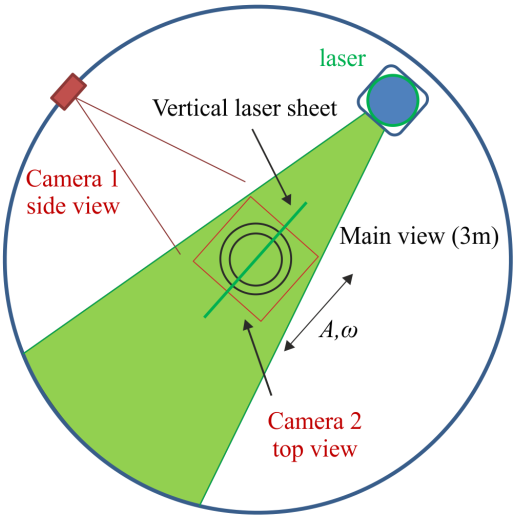

(*b*)

Figure 2.12: Experimental setup: (*a*) top view of the platform during an experiment with horizontal laser sheet, (*b*) schematic setup.

Further treatment included frequency filtering and spectrum analysis described in the previous section.

The experimental parameters are shown in Table 2.3. Experiments 1.1-4 were conducted in a linearly stratified fluid of buoyancy frequency N and experiments 2.1-2 in a linearly stratified and rotating fluid of buoyancy frequency N and inertial frequency f. Experiment 3 was conducted in a rotating fluid of inertial frequency f. Experiments 4.1-3 were performed in the linearly stratified nonrotating fluid with the half–torus oriented either perpendicular (symmetric half–torus in Table 2.3) or parallel (asymmetric half–torus in Table 2.3) to its direction of oscillation. The definitions of the parameters are the same as in the previous section.

	Object	Method	ω/C	$N\ s^{-1}$	$f\ s^{-1}$	Ke	X	Y	Z
Exp 1.1	Torus	PIV	0.6	0.47	0	0.17; 0.33; 0.66; 1	-8 to 8	0	-6 to 0
Exp 1.2	Torus	PIV	0.51	0.5	0	0.17; 0.33; 0.66; 1	-8 to 8	0	-6 to 0
Exp 1.3	Torus	PIV	0.4	0.5	0	0.17; 0.33; 0.66; 1	-8 to 8	0	-6 to 0
Exp 1.4	Torus	Volume PIV	0.51	0.5	0	0.17	-6 to 6	-6 to 6	-5 to -2
Exp 2.1	Torus	PIV	0.51	0.5	0.2	0.17; 0.33; 0.66; 1	-8 to 8	0	-6 to 0
Exp 2.2	Torus	Volume PIV	0.51	0.5	0.2	0.17	-6 to 6	-6 to 6	-5 to -2
Exp 3	Torus	PIV	0.73	0	0.2	0.17; 0.33; 0.66; 1	-8 to 8	0	-6 to -0
Exp 4.1	Half-torus (symmetric)	PIV	0.51	0.5	0	0.17; 0.66	-8 to 8	0	-6 to 0
Exp 4.2	Half-torus (symmetric)	Volume PIV	0.51	0.5	0	0.17; 0.66	-6 to 6	-6 to 6	-5 to -2
Exp 4.3	Half-torus (symmetric)	PIV	0.4	0.5	0	0.33	-8 to 8	0	-6 to 0
Exp 5.1	Half-torus (asymmetric)	PIV	0.51	0.5	0	0.17; 0.66	-8 to 8	0	-6 to 0
Exp 5.2	Half-torus (asymmetric)	Volume PIV	0.51	0.5	0	0.17; 0.66	-6 to 6	-6 to 6	-5 to -2

Table 2.3: Experimental parameters at the Coriolis platform, for the torus with $\epsilon = 5$. ω/C is the nondimensional oscillation frequency with $C = N$ for internal and inertia–gravity waves and $C = f$ for inertial waves.

Chapter 3

Generation of higher harmonic waves by spheroids

Oscillating bodies in stratified fluids may emit higher harmonics in addition to the fundamental waves. The three-dimensional structure of these harmonics is not yet well known. In this chapter we consider the generation of higher harmonic waves by bodies of different curvatures, represented by an oscillating sphere and oblate and prolate spheroids oriented horizontally or vertically. Experimental observations are compared with the linear theory of Voisin *et al.* (2011) in the axisymmetric case of an oblate spheroid of vertical axis, and with the nonlinear theoretical predictions according to Bell (1975*a*) for wave generation by boundary advection, and Tabaei *et al.* (2005) and Jiang & Marcus (2009) for wave generation at wave beam intersection. Measurements of the horizontal flow field allow us to make hypotheses about the horizontal structure of the n-th harmonic radiation patterns. These measurements are performed using LIF and PIV techniques. An additional set of experiments, visualising horizontal planes close to the oscillating objects, was performed for a better understanding of mechanisms that are responsible for the generation of higher harmonics.

3.1 Structure of first and higher harmonics generated by a sphere

In a uniformly stratified fluid, the oscillation of a body with a vertical axis of revolution generates internal waves that propagate along double cones, tangent to the body above and below, with apices on the axis and generatrices inclined at the angle θ to the vertical, defined from the dispersion relation (1.13). This relation admits the generation of a propagative n-th harmonic component of the wave field if $n\omega/N < 1$ (Figure 3.1). The effective generation of the n-th harmonic requires an appropriate choice of the non dimensional oscillation amplitude $Ke = A/a$ and frequency ω/N. Obviously, Ke should be large enough for the amplitude of the n-th harmonic, proportional to Ke^n, to be observable. Based on the knowledge of the

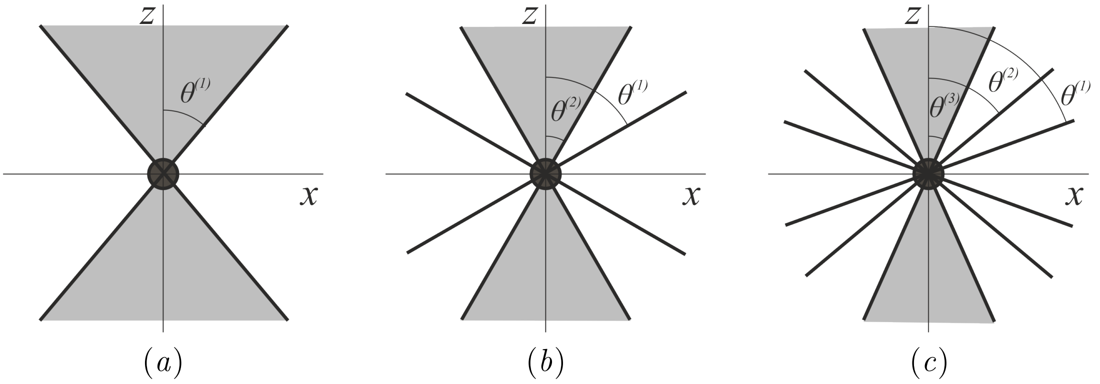

Figure 3.1: Schematic structure of fundamental and higher harmonic waves for (a) $1/2 < \omega/N < 1$, (b) $1/3 < \omega/N < 1/2$ and (c) $1/4 < \omega/N < 1/3$. The domain of interest corresponding to the innermost wave cone is shown in light grey.

behavior of the first harmonic (also called fundamental wave in the text below), a plausible conjecture for the frequency tuning can be formulated. It is known that for oscillating circular cylinders and spheres the maximum power radiated by the first-harmonic waves is found in the range of ω/N between 0.7 and 0.8, regardless of the oscillation direction (Voisin *et al.*, 2011). We make the conjecture that this prediction remains true for the n-th harmonic, irrespective of its actual generation mechanism, so that generation is most effective when $0.7 < n\omega/N < 0.8$, and that the particular geometry of the wave field has little influence on it. This condition was used for the frequency tuning in the present experiments.

The spatial structure of the first and second harmonics emitted by an oscillating sphere has been studied in Ermanyuk *et al.* (2011), who showed the first harmonic to be dipolar, with a radiation pattern as $\cos\phi$ with ϕ the azimuthal angle measured from the X-direction of oscillation, and the second harmonic to be quadrupolar, with radiation pattern as $\cos 2\phi$. Here we restrict ourselves to a demonstration of the dipolar (Figure 3.2a) and quadrupolar (Figure 3.2b) radiation patterns for the cases when the oscillation amplitude is low. Wave visualisation is performed with the LIF technique, and the low signal level leads to a maximum vertical displacement of the dye lines between two successive images well below 1 pixel (Voisin *et al.*, 2011; Ermanyuk *et al.*, 2011). These examples demonstrate the robustness of the experimental technique.

Figure 3.3(a) shows the distribution of the first harmonic component of the vertical displacement amplitude ζ_1/A (see the definition of ζ_n and the nondimensional coordinates X, Y, Z in section 2.2.3), for a horizontal cross section of the wave cone for the case corresponding to Figure 3.1(a). The wave cone in this experiment has its generatrices inclined at $\theta^{(1)} = 41°$ to the vertical. The characteristic two bean-like shape of the cross section represents a dipolar wave pattern which agrees well with the theoretical variation of the velocity amplitude as $\cos\phi$ (Voisin *et al.*, 2011). This implies maximum radiation along the longitudinal x-direction and no radiation along the transverse Y-direction.

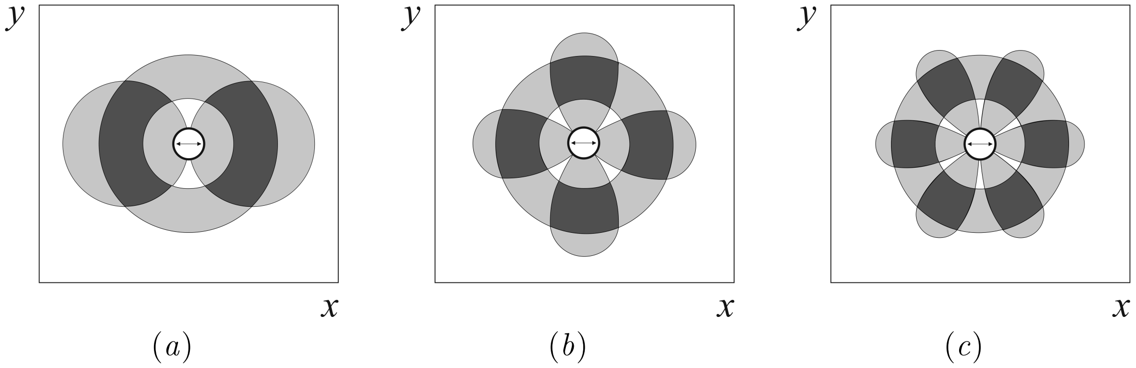

(a) (b) (c)

Figure 3.2: Horizontal structure of dipolar, quadrupolar and octupolar internal waves. The annular propagation of the waves from the conical geometry in Figure 3.1 and the 2^n-polar radiation pattern as $\cos(n\phi)$ are represented in light grey and their combination in dark grey.

Figure 3.3(*b*)shows the distribution of the second harmonic component of the vertical displacement amplitude ζ_2/A for the same conditions as in Figure 3.3(*a*) but after changing the frequency ratio from $\omega/N = 0.76$ to $\omega/N = 0.41$. The frequency $2\omega/N \approx 0.8$ corresponds to effective generation of the second harmonic and yields a wave cone with generatrices inclined at $\theta^{(2)} = 35°$ to the vertical, while the generatrices for the first harmonic are inclined at $\theta^{(1)} = 66°$ (see Figure 3.1*b*). The three-dimensional structure of the corresponding wave pattern is quadrupolar (see Figure 3.3*b*), with maximum radiation along the X- and Y-directions and $\cos(2\phi)$ shaped azimuthal variation.

The amplitude of higher harmonics is lower than that of the fundamental wave, as has been shown in Ghaemsaidi & Peacock (2013) in terms of the total velocity field, including the three velocity components. In order to increase the wave amplitude of the third harmonic we increase the oscillation amplitude Ke from 0.27 to 1.56 (see Figure 12*a* in Ermanyuk *et al.*, 2011). The distribution of the third harmonic amplitude ζ_3/A is shown in Figure 3.4. The characteristic angles of the wave cones for these experimental conditions are $\theta^{(1)} = 75°$, $\theta^{(2)} = 59°$ and $\theta^{(3)} = 39°$ (see Figure 3.1*c*). To obtain the third harmonic wave the frequency was tuned at $3\omega/N \approx 0.8$. The camera sampling frequency was set at one frame per second yielding 36 frames per period, which is a sufficient number to resolve the third harmonic. An octupolar structure is clearly visible, with 6 azimuthal poles implying an amplitude variation as $\cos(3\phi)$. More detailed investigation on the structure of the third harmonic wave will be presented in section 3.3.

The present observations show that the spatial structure of the first three harmonics of the wave field are respectively dipolar, quadrupolar and octupolar. According to this trend we expect that for the n-th harmonic wave a radiation pattern of multipolar order 2^n, varying as $\cos(n\phi)$ and having $2n$ azimuthal lobes in the horizontal plane. Because of the complexity of this structure and narrowness of the wave cone it is less obvious to visualize the radiation patterns for higher wave

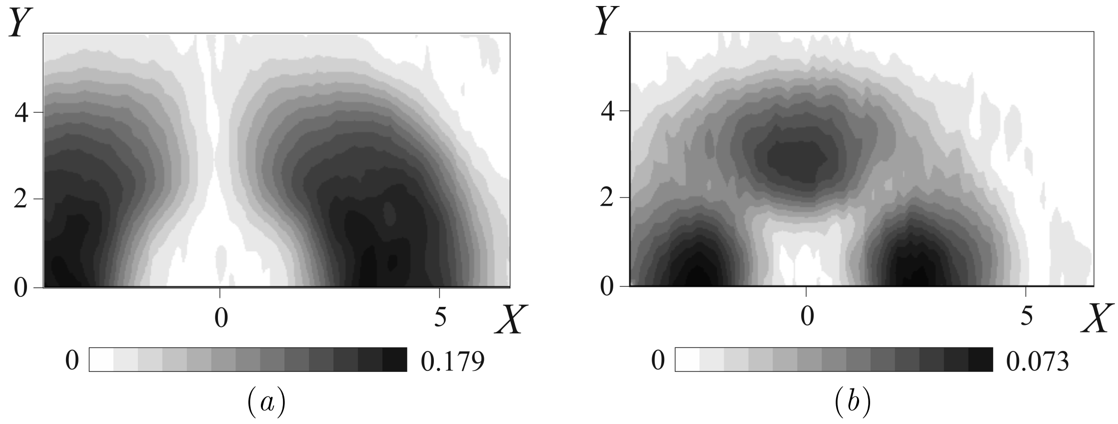

Figure 3.3: Radiation patterns of the vertical displacement amplitude for an oscillating sphere at $Ke = 0.27$: (a) dipolar pattern ζ_1/A for the first harmonic wave, corresponding to the upper half of Figure 3.2(a); (b) quadrupolar pattern ζ_2/A for the second harmonic wave, corresponding to the upper half of Figure 3.2(b). The horizontal cross section of the wave field is taken at $Z = -5.09$, with the X-axis oriented along the direction of oscillation and the Y-axis toward the camera. [Exp A_1 from Table 2.2]

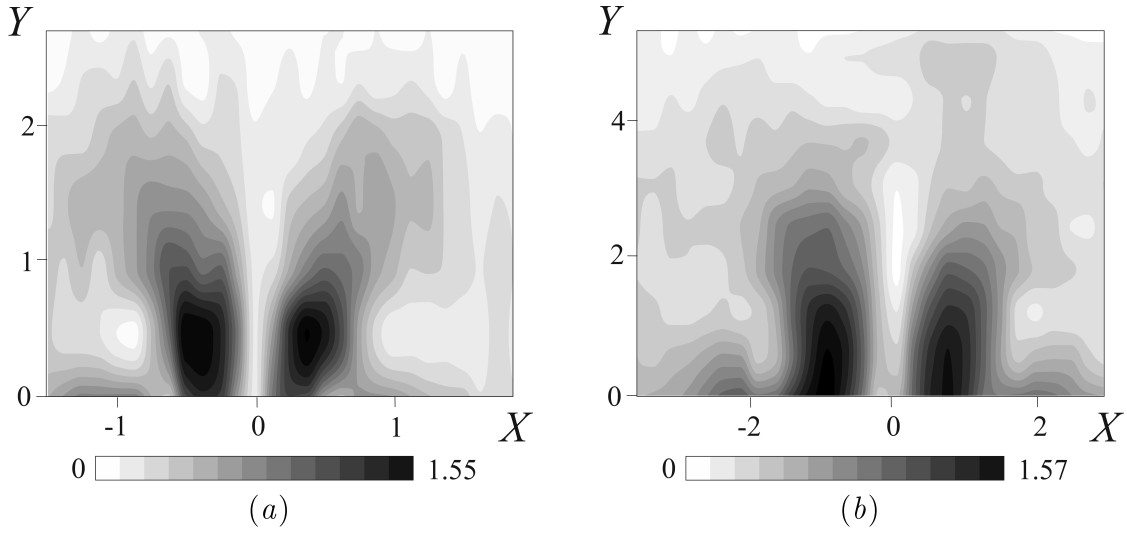

Figure 3.4: Octupolar radiation pattern of the vertical displacement amplitude ζ_3/A of the third harmonic wave corresponding to the upper half of Figure 3.2c for an oscillating sphere with (a) $Ke = 1.35$ at $Z = -1.37$ and (b) $Ke = 0.69$ at $Z = -1.11$. [Exp A_2 from Table 2.2]

modes.

The numerical results described in Lamb (2004) and Korobov & Lamb (2008), illustrated in Figure 1.8 show that the internal wave structure is due to the interplay of first and higher harmonics in the vertical plane. The here-presented results show that, in addition, the complexity of the wave structure in the horizontal plane increases with the harmonic wave number. The interaction of multipolar radiation patterns may lead to complex interference patterns above realistic bottom topographies.

3.2 Wave generation by a spheroid

3.2.1 Comparison with the linear theory

Three dimensional theoretical predictions for a sphere by Voisin *et al.* (2011) can be extended to a spheroid of vertical axis, equatorial radius a, polar radius b and aspect ration $\epsilon = b/a$, oscillating horizontally at the frequency $\omega < N$, with position $(A, 0, 0)\sin(\omega t + \Theta)$.

In nondimensional Cartesian coordinates $(X, Y, Z) = (x, y, z)/a$ the normalised velocity components $(U, V, W) = (u, v, w)/(A\omega)$ are given by:

$$\begin{aligned} U = {} & \frac{2\mathrm{i}\epsilon\cos^2\theta\sin\theta}{\sqrt{\cos^2\theta+\epsilon^2\sin^2\theta}} \frac{\mathrm{e}^{-\mathrm{i}(\omega t+\Theta)}}{1+D(\Upsilon)} \int_0^\infty \mathrm{d}K, K j_1\left(K\sqrt{\cos^2\theta+\epsilon^2\sin^2\theta}\right) \\ & \times \left[\frac{X^2}{X^2+Y^2} J_2\left(K\sqrt{X^2+Y^2}\cos\theta\right) - \frac{J_1\left(K\sqrt{X^2+Y^2}\cos\theta\right)}{K\sqrt{X^2+X^2}\cos\theta}\right] \\ & \times \exp\left(-\frac{K^3|Z|}{2St\sin\theta}\right)\exp(-\mathrm{i}K|Z|\sin\theta), \end{aligned} \tag{3.1}$$

$$\begin{aligned} V = {} & \frac{2\mathrm{i}\epsilon\cos^2\theta\sin\theta}{\sqrt{\cos^2\theta+\epsilon^2\sin^2\theta}} \frac{\mathrm{e}^{-\mathrm{i}(\omega t+\Theta)}}{1+D(\Upsilon)} \int_0^\infty \mathrm{d}K\, K j_1\left(K\sqrt{\cos^2\theta+\epsilon^2\sin^2\theta}\right) \\ & \times \frac{XY}{X^2+Y^2} J_2\left(K\sqrt{X^2+Y^2}\cos\theta\right) \\ & \times \exp\left(-\frac{K^3|Z|}{2St\sin\theta}\right)\exp(-\mathrm{i}\kappa|z|\sin\theta), \end{aligned} \tag{3.2}$$

$$\begin{aligned} W = {} & \frac{2\epsilon\cos^3\theta}{\sqrt{\cos^2\theta+\epsilon^2\sin^2\theta}} \frac{\mathrm{e}^{-\mathrm{i}(\omega t+\Theta)}}{1+D(\Upsilon)} \int_0^\infty \mathrm{d}K\, K j_1\left(K\sqrt{\cos^2\theta+\epsilon^2\sin^2\theta}\right) \\ & \times \frac{X}{\sqrt{X^2+Y^2}} J_1\left(K\sqrt{X^2+Y^2}\cos\theta\right) \\ & \times \exp\left(-\frac{K^3|Z|}{2St\sin\theta}\right)\exp(-\mathrm{i}K|Z|\sin\theta)\,\mathrm{sign}\,Z, \end{aligned} \tag{3.3}$$

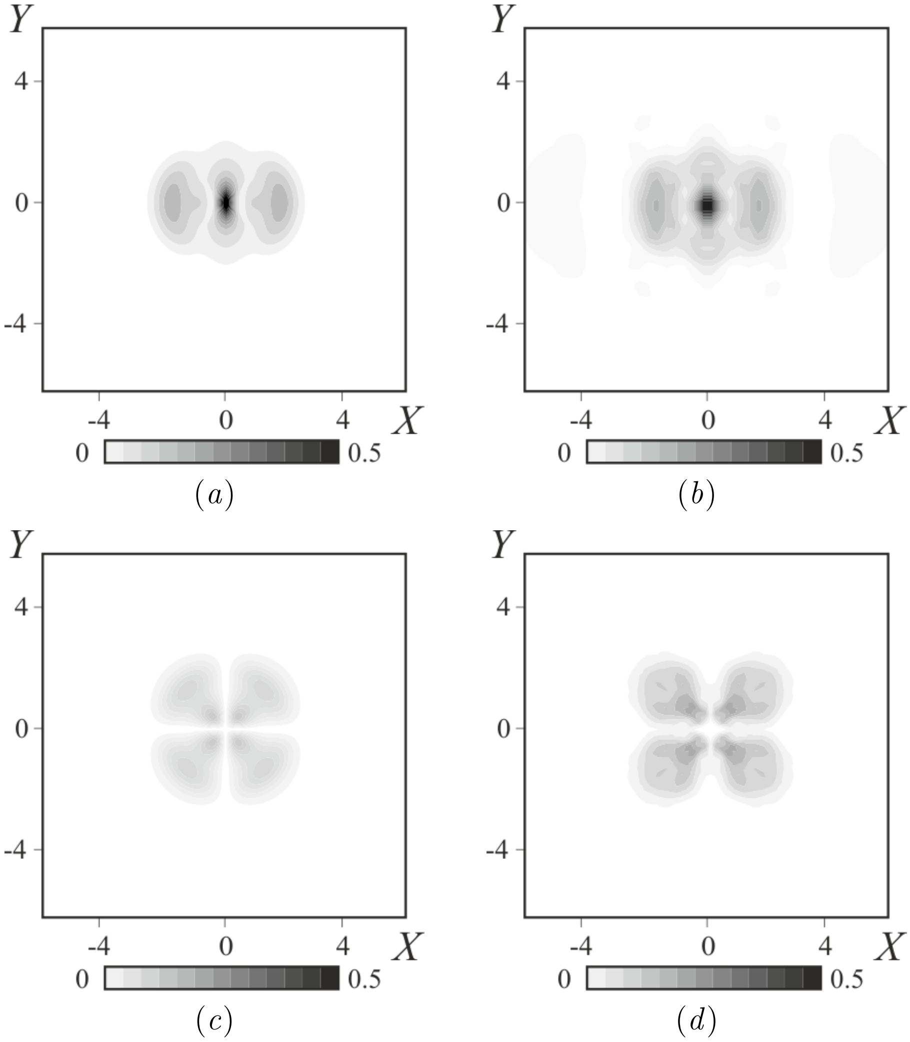

Figure 3.5: Theoretical calculations from equations (3.1), (3.2) (left column) and experimental results (right column) for (*a*,*b*) the longitudinal, $\hat{U}_1$, and (*c*,*d*) the transversal, $\hat{V}_1$ horizontal velocity amplitudes for an oblate spheroid ($\mathcal{V}$) of $\epsilon = 1/2$ at $Z = -2$. [Exp *E* from Table 2.2]

where $j_1(x) = (\sin x)/x^2 - (\cos x)/x$ a spherical Bessel function, $J_2(x)$ a cylindrical Bessel function, and

$$D(\Upsilon) = \frac{1}{1+\Upsilon^2}\left[1 - \frac{\Upsilon}{\sqrt{1+\Upsilon^2}}\left(\mathrm{i}\frac{\pi}{2} + \operatorname{arcsinh}\Upsilon\right)\right],$$

with

$$\Upsilon = \epsilon \tan\theta.$$

Figure 3.5 represents the patterns of longitudinal, $\hat{U}_1$, and transversal, $\hat{V}_1$, horizontal velocity components for an oblate spheroid ($\mathcal{V}$) of aspect ratio $\epsilon = 1/2$ as measured with the PIV technique and calculated from the theory (equations 3.1 and

3.2) in the horizontal plane $Z = -1$. The longitudinal velocity amplitude is maximal at the centre. The transverse component has a "clover-like" structure and is zero at the centre. Figure 3.5 shows good agreement between theoretical and experimental results.

The patterns of vertical displacement amplitude obtained from equation (3.3) and LIF measurements are shown in Figures 3.6(a) and (b), respectively for an oblate spheroid ($\mathcal{V}$). Again, good agreement is obtained between the theory and the experiment close to the object (Figure 3.7a,b) even for high oscillation amplitude ($Ke = 0.617$). However, experiments show that the waves are bimodal even far away from the object while the linear theory predicts the transition to a unimodal structure (Figure 3.7c,d). From these results we conclude that increasing of oscillation amplitudes decreases viscous effects.

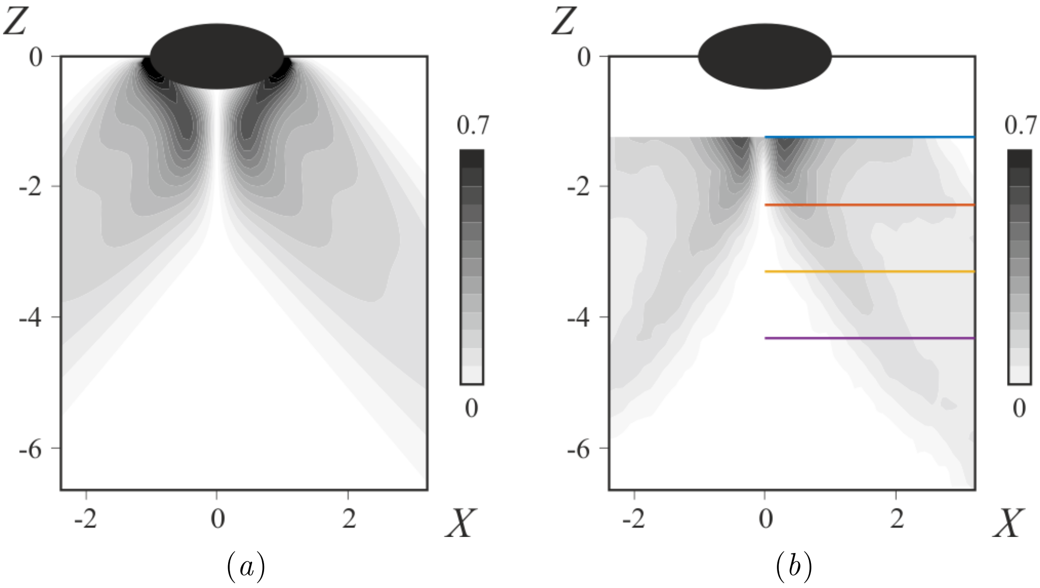

(a) (b)

Figure 3.6: Patterns of the vertical displacement amplitude ζ_1/A in XZ-plane obtained from (a) the theoretical calculations (equation 3.3) and (b) LIF measurements for the oblate spheroid ($\mathcal{V}$). [Exp F_1 from Table 2.2]

3.2.2 First and second harmonics

Experiments F_{1-3} involve an oblate spheroid oscillating horizontally at the amplitude $Ke = 0.617$, with it's axis in three different orientations. Figure 3.8 shows horizontal cross-sections of the vertical displacement amplitudes of the first harmonic (right column, $\omega/N = 0.8$) and second harmonic (left column, $\omega/N = 0.4$) for the three configurations. For $\omega/N > 0.5$ and high oscillation amplitudes Ke, the higher harmonics, if present due to onset of nonlinear effects, are evanescent. This regime allows us to study the fundamental wave separately. As has been shown previously for a Gaussian seamount (Holloway & Merrifield, 1999; Munroe & Lamb, 2005) and for a sphere (Ermanyuk *et al.*, 2011; Voisin *et al.*, 2011), the horizontal

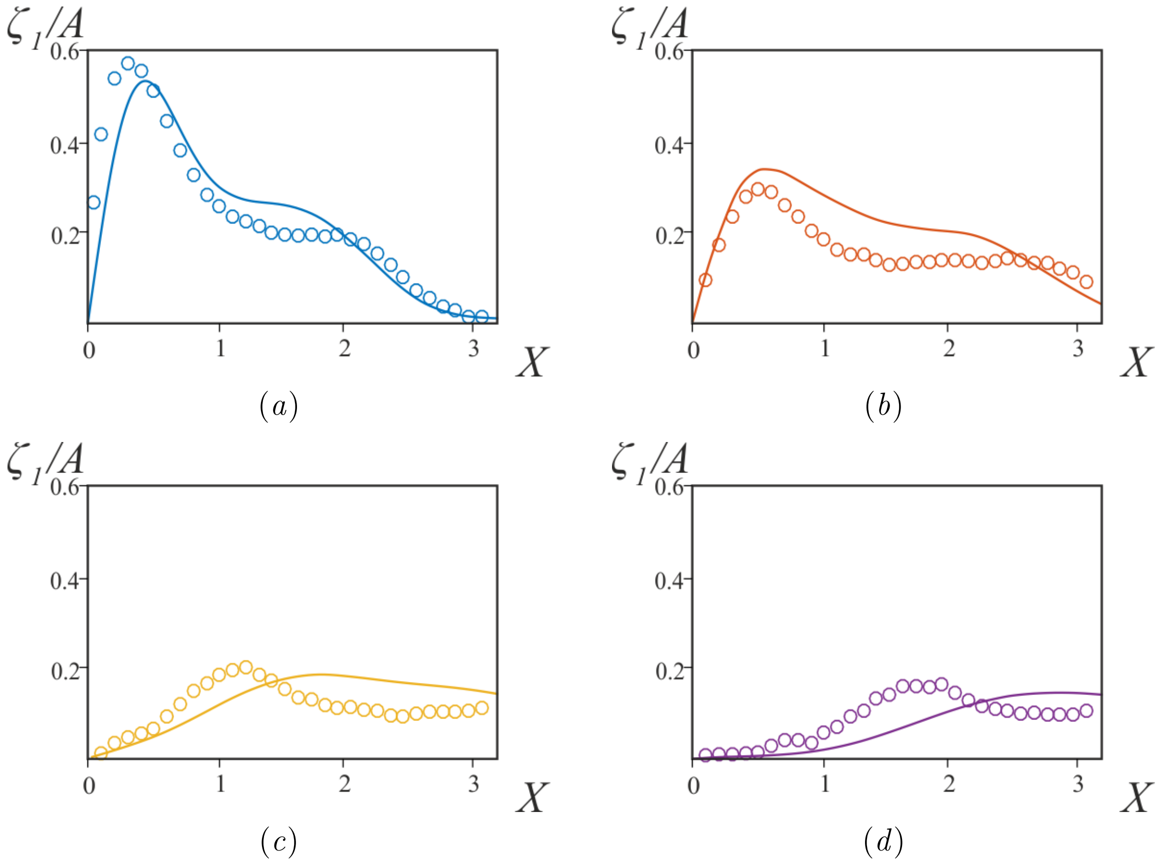

(*a*) (*b*) (*c*) (*d*)

Figure 3.7: Distributions of the vertical displacement amplitude ζ_1/A along the direction of oscillation X, obtained at (a) $Z = -1.28$, (b) $Z = -2.30$, (c) $Z = -3.32$ and (d) $Z = -4.35$ for the oblate spheroid $(\mathcal{V})$. The solid lines represent the theoretical calculations (equation 3.3), and the dots the experimental measurements. [Exp F_1 from Table 2.2]

distribution exhibits a dipolar radiation pattern in all three cases. The dependence of the vertical displacement distribution on the geometry of the body can clearly be seen in Figure 3.8 (right column) as well as in Figure 3.9(a), where a comparison of the profiles at $Y = 0$ is presented. Here the symmetry of the body plays a role: in experiments F_1 and F_2 the bodies are symmetric with respect to the YZ-plane, while in case F_3 the body is rotated by 45° hence loses this symmetry. We can observe that the distribution of vertical velocity is symmetric in experiments F_1 and F_2 while the plane of symmetry has been rotated by the same angle for experiment F_3.

Oscillations at the frequency $\omega/N = 0.4$ (< 0.5) admit the propagation of a second harmonic along with the fundamental wave. Figure 3.9(b) presents the experimental amplitude profiles of the second harmonic for experiments F_{1-3}. The second harmonic depends on the object's shape in the same way as described previously for the first harmonic. More detailed analysis of higher harmonics generation will be presented in section 3.3.

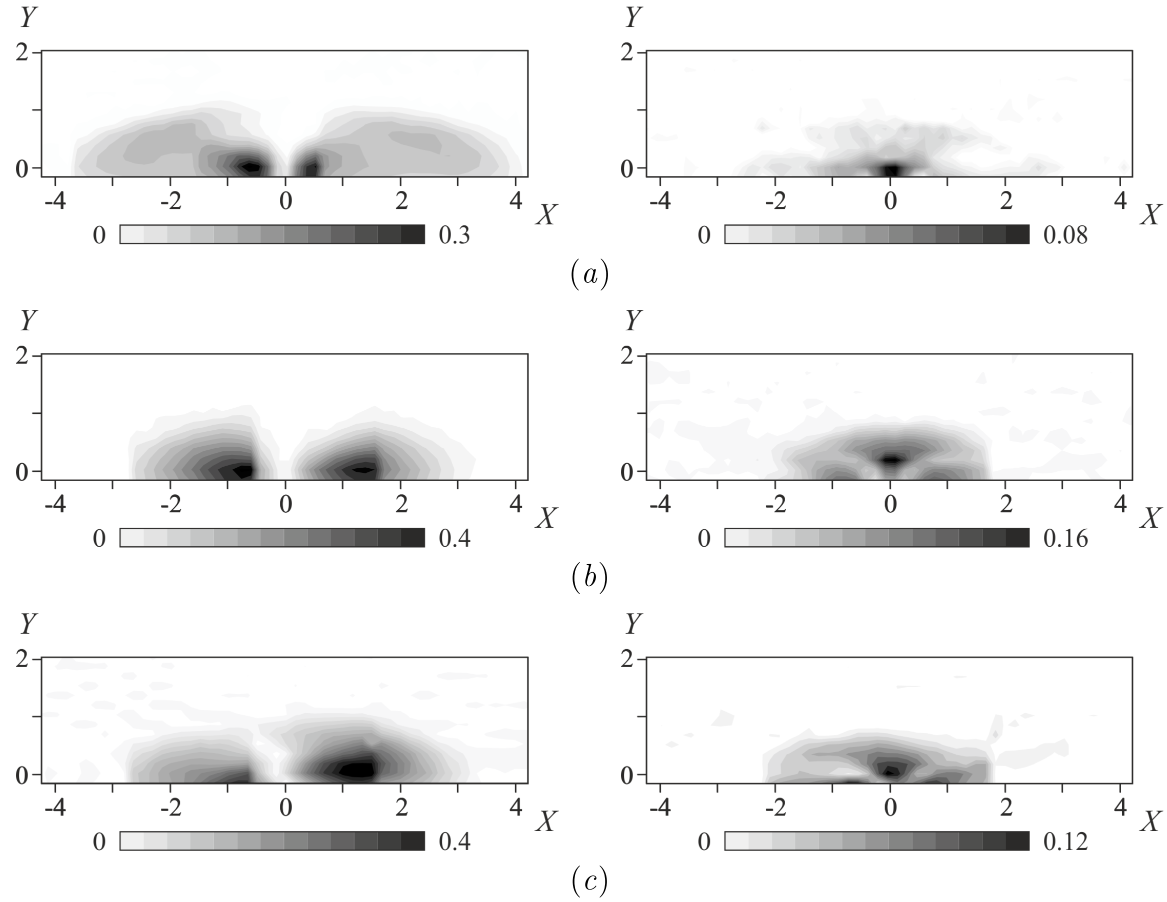

Figure 3.8: Horizontal cross-sections of the vertical displacement amplitude for the oblate spheroid oscillating at $Ke = 0.617$ (a) at $Z = -1.28$ for the configuration ($\mathcal{V}$) namely with the spheroid axis oriented along the direction Z, (b) at $Z = -1.74$ for the configuration ($\mathcal{H}$) namely with the spheroid axis oriented along the direction X, (c) at $Z = -1.69$ for the configuration (45°), namely with the spheroid axis in the XY-plane at 45° to the direction X. The left and right columns represent the first ζ_1/A and the second ζ_2/A harmonic amplitudes, respectively. [Exp $F_1 - F_3$ from Table 2.2]

The profiles on Figure 3.9 show also that the vertical displacement amplitude in experiment F_2 is smaller than in experiment F_1. Since the experimental parameters were kept constant, the geometry of the body (size and slope with respect to the X- and Y- directions) is seen to affect the amplitude.

Together with the results obtained by Ermanyuk *et al.* (2011) and Voisin *et al.* (2011) this investigation provides more detailed information about the horizontal structure of internal waves in the ocean. The amplitude of the first and higher harmonics depends on the slope of the underwater mountain, the horizontal distribution depends on its shape and on the direction of the barotropic tide oscillation.

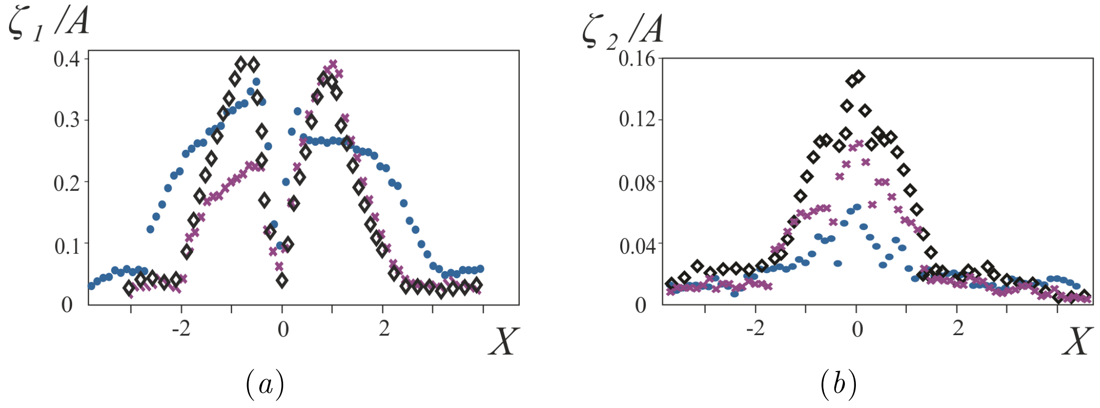

(*a*) (*b*)

Figure 3.9: Experimental profiles of the vertical displacement amplitudes of (*a*) the first harmonic (fundamental wave) and (*b*) the second harmonic for the oblate spheroid. Blue, black and purple symbols represent the results for the configurations ($\mathcal{H}$), ($\mathcal{V}$) and (45°), respectively, as defined for Figure 3.8. [Exp $F_1 - F_3$ from Table 2.2]

3.3 Mechanisms of higher harmonic generation[*]

3.3.1 Vertical structure

The wave patterns emitted by a horizontally oscillating prolate spheroid of aspect ratio $\epsilon = 2$ are shown in Figure 3.10 for the cases when the spheroid axis is either horizontal and along the direction of oscillation (prolate spheroid ($\mathcal{H}$)), or vertical (prolate spheroid ($\mathcal{V}$)). The change in the orientation of the spheroid allows for the study of different curvatures of the oscillating object, so as to discriminate between the different possible mechanisms of higher harmonic generation, illustrated in Figure 3.11. Either the higher harmonic waves result from the nonlinear interaction of the fundamental waves in the zones where their beams intersect, as modelled theoretically by Tabaei *et al.* (2005) and Jiang & Marcus (2009), or the higher harmonic waves are produced by nonlinear boundary advection at the surface of the object, as modelled by Bell (1975*a*) for subcritical object of infinitisimal slope. For this second mechanism, when the object is supercritical, second harmonic generation will take place at the critical points $\varepsilon_2 = 1$ where the slope s of the object is equal to the slope of the second harmonic wave, i.e.

$$\varepsilon_i = \frac{s}{\sqrt{\omega_i^2/(\omega_i^2 - N^2)}} = 1,$$

with $i = 1, 2$ for the first and the second harmonics, respectively ($\omega_2 = 2\omega_1$).

For the prolate spheroid ($\mathcal{H}$) in the left column of Figure 3.10, one notices the generation of second harmonic waves on the sides at $Z = 0$, at the intersections of

---

[*] This section is a modified version of the article "Generation of higher harmonic waves on spheroids", in preparation for submission, and reproduced in Appendix A.

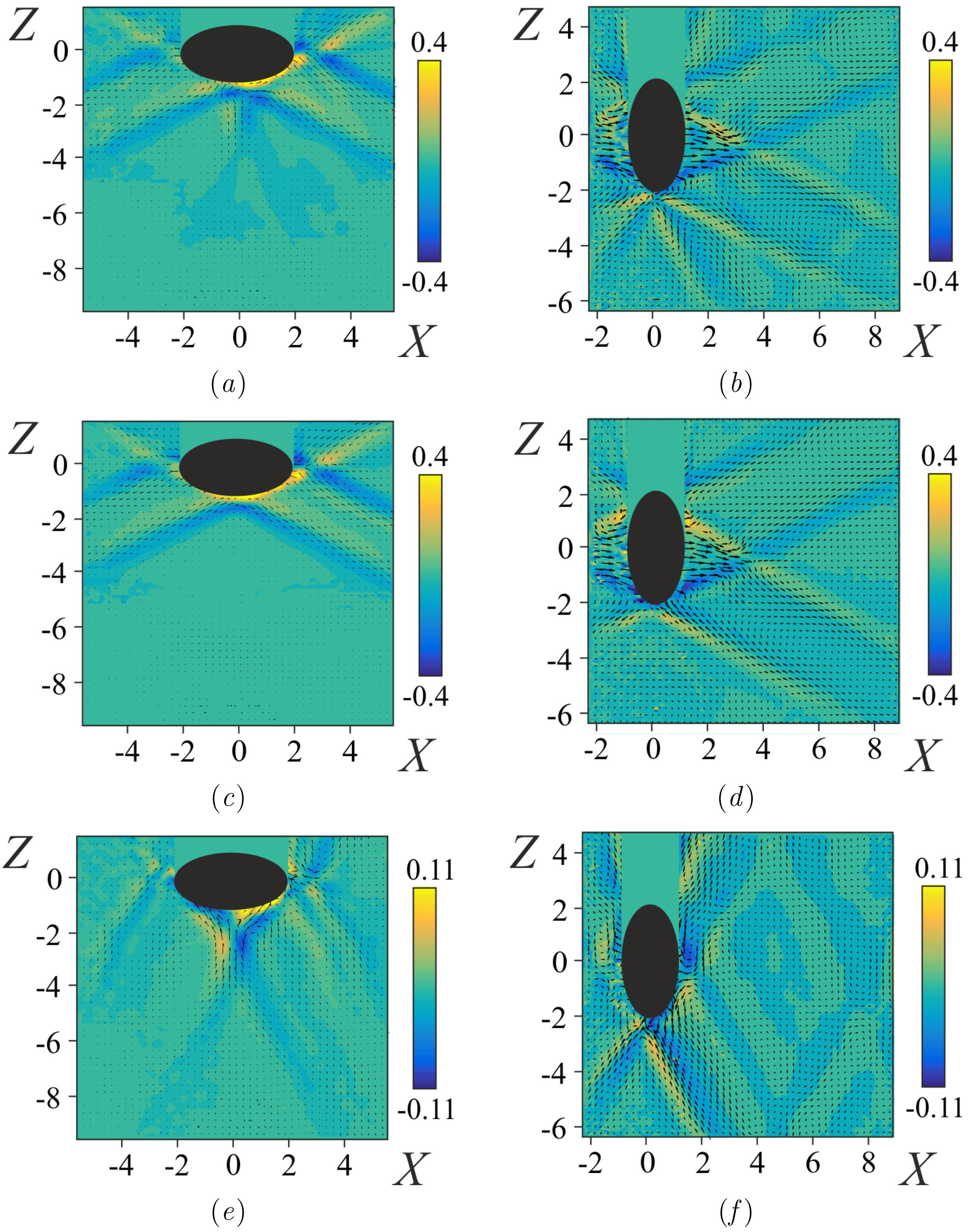

Figure 3.10: Snapshot patterns of vorticity (color) and velocity (vector field) in the vertical plane of symmetry $Y = 0$ for the wave field generated by a prolate spheroid ($\mathcal{H}$) (left column) and a prolate spheroid ($\mathcal{V}$) (right column); (a,b) total wave field, (c,d) first harmonic and (e,f) second harmonic. [Exp C_2 and D from Table 2.2]

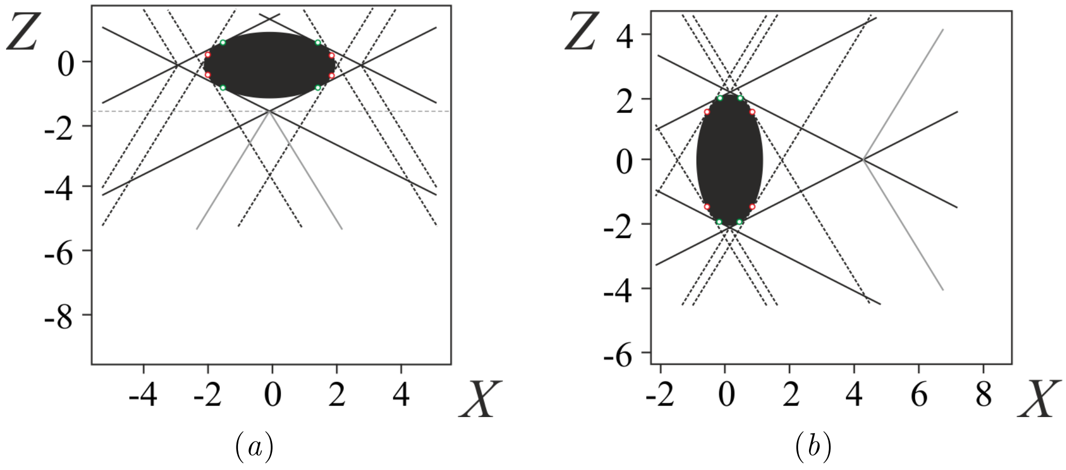

Figure 3.11: Schematic distribution of the first and second harmonic waves generated by a prolate spheroid of (*a*) horizontal axis ($\mathcal{H}$) and (*b*) vertical axis ($\mathcal{V}$). The solid lines represent the fundamental wave rays and the dashed lines the second harmonic rays; the dots correspond to the critical points $\varepsilon_i = s/\sqrt{\frac{\omega_i^2}{\omega_i^2 - N^2}} = 1$ at which the wave rays are tangent to the spheroid, with $i = 1, 2$ for the first harmonic (green dots) and second harmonic (red dots), respectively. Fundamental and second harmonic generation is shown from the critical points ε_i and from the points of fundamental beam intersection; of the latter the harmonic waves that are not observed in the experiment are represented by grey lines. The horizontal grey line determine the vertical position of the fundamental beam intersection Z^*.

the fundamental waves. In agreement with the theory of Tabaei *et al.* (2005) and Jiang & Marcus (2009), only second harmonic waves are generated that propagate away from the obstacle. The waves below (and above) the spheroid, by contrast, are generated at the boundary and appear to have their origin at the critical points $\varepsilon_2 = 1$, then intersect below the spheroid. In this zone the waves focus and therefore amplify in wave energy (Figure 3.10*e*). However, this zone is closer to the object than one may expect from the dispersion relation (1.13) for a second harmonic wave (see the sketch in Figure 3.11). The responsible mechanism for the shift of the focal zone seems to be a strong overturning motion near the boundary layer close to the area $(-1 < X < 1, Z = -1)$. This motion deflects the second harmonic waves emanating from the critical points, and is clearly visible in Figure 3.10(*e*) and in the horizontal plane views in Figure 3.12, obtained for slightly different parameters and discussed in greater detail in section 3.3.2.

Near the focal point $(X, Z) \approx (0, -3)$ its effect vanishes and the second harmonic waves propagate again with the inclination predicted by the dispersion relation. Since our oscillating object is not axisymmetric, the focal zone gets a complex shape and the focal point turns into a curve (see Figure 9 in Bühler & Muller, 2007). In order to verify the possibility of overturning, one can base the Richardson number on the boundary layer thickness at the surface of the object, δz, i.e.

$$Ri = \frac{N^2}{(A\omega/\delta z)^2},$$

with $Ri < 1/4$ for shear instability according to theory of Miles (1961). For the velocity and stratification in this experiment, this corresponds to a threshold boundary layer thickness of $\delta z < 0.35$ cm. In view of the here much thinner boundary layer, the overturning below the spheroid is likely to occur. However we observe similar effects for very high Stokes numbers as described in chapter 6.

For the prolate spheroid ($\mathcal{V}$) in the right column of Figure 3.10, the results, obtained for the same stratification, amplitude and oscillation frequency, show again the generation of fundamental and second harmonics at critical points. However, the intersection of the fundamental waves at $Z = 0$ does not result in the generation of a second harmonic wave. Since this intersection is at a larger distance from the spheroid, the wave amplitude may have decreased significantly along its path. Zhang *et al.* (2007) also notice that the second harmonics disappear for weaker wave amplitudes. The sketches of the wave patterns in Figure 3.11(a) and (b) resume the observations.

3.3.2 Horizontal structure

Complementary experiments were conducted to determine the position of higher harmonic generation using a horizontal laser sheet at the lower boundary of the spheroid at $Z = -1$ and in the zone of primary beam intersection Z^* (see the horizontal line in Figure 3.11a) calculated from formulas (3.14) in Hurley (1997) as

$$Z^* = \sqrt{\cot^2\theta + \epsilon^2}.$$

The associated value $\Delta Z = |Z - Z^*|$ appears to be too small for the sphere ($\epsilon = 1$, $\omega/N = 0.41$, $\Delta Z = 0.1$) but for the prolate spheroid ($\mathcal{H}$) of $\epsilon = 2$ oscillating with frequency $\omega/N = 0.4$ this distance is large enough for measurements ($\Delta Z = 0.33$).

The distributions of amplitudes of the first and the second harmonics of the horizontal velocity $\hat{U}$ in the horizontal plane at $Z = -1$ are presented in Figure 3.12. The second harmonic close to the object has a quadrupolar structure ($-2 < X < 2$). The second harmonics at $|X| = 4$ and $|X| = 6$ are in agreement with the vertical structure shown in Figure 3.10(e) and correspond respectively to the outgoing wave beam generated at the critical point $\varepsilon_2 = 1$ and the wave beam generated in the zone of fundamental wave intersection at $Z = 0$. Figure 3.13 (a) shows that the amplitude of the second harmonic wave has its maximum close to the surface of the spheroid and decreases with the distance from the object.

To determine the wave spectrum generated by the prolate spheroid ($\mathcal{H}$) and its evolution with time (Bourget *et al.*, 2013), a time–frequency representation described in Flandrin (1998) is used, namely, for the velocity u,

$$Q_u(t,\omega) = \left\langle \left| \int_{-\infty}^{+\infty} d\tau \; u \exp^{-i\omega\tau} h(t-\tau) \right|^2 \right\rangle_{xy \text{ or } xz}, \tag{3.4}$$

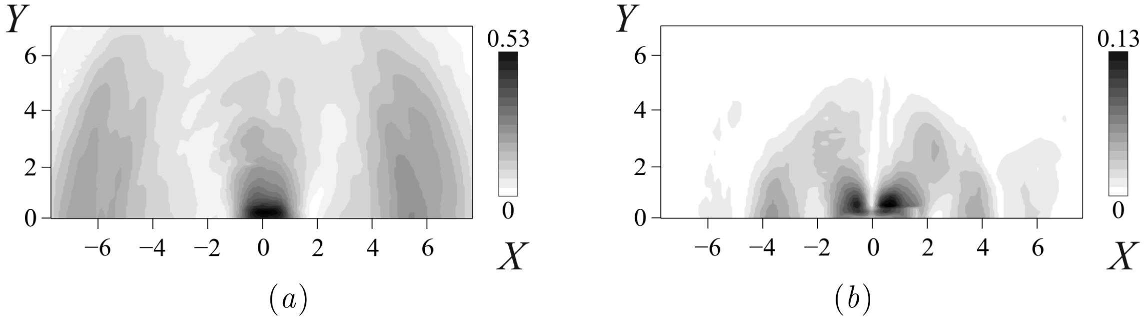

Figure 3.12: Radiation patterns for (a) the first and (b) the second harmonic wave of the horizontal longitudinal velocity $\hat{U}$ at the boundary ($Z = -1$) of the oscillating prolate spheroid ($\mathcal{H}$). [Exp C_1 from Table 2.2]

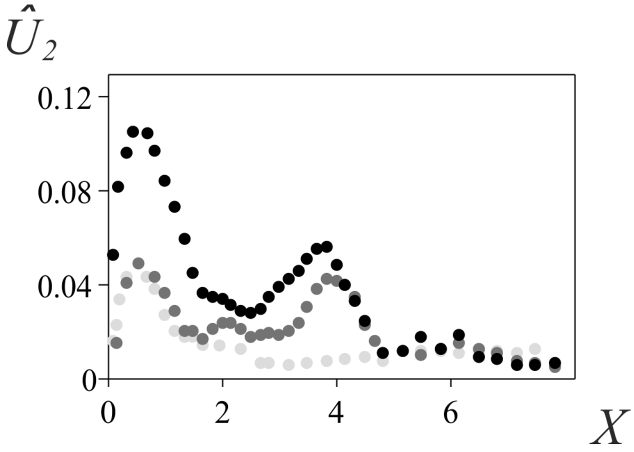

Figure 3.13: Profiles of the second harmonic of horizontal velocity amplitude $\hat{U}_2$ along the X-axis, at $Z = -1$ (black dots), $Z = -1.47$ (dark grey dots) and $Z = -1.91$ (light gray dots) for the prolate spheroid ($\mathcal{H}$). [Exp C from Table 2.2]

where $h(t) = 0.54 - 0.46 \cos\left(2\pi \frac{t}{T}\right)$ is a smoothing Hamming window and the average is taken over an interrogation area in either the xy-plane or the xz-plane.

Figure 3.14 shows the time–frequency spectrum of the horizontal velocity $\hat{u}$ averaged in space inside a small horizontal rectangle ($-2 < X < 2, -1 < Y < 1$) at $Z = -1$. The first two harmonics are propagative ($\omega/N < 1$), with their generation starting at $t = 0$, and their frequency remaining constant for all 40 oscillation periods; all higher harmonics are evanescent ($\omega/N > 1$). The development of these evanescent waves is visible in Figure 3.14 over $0 < T < 10$.

Figure 3.15 shows that in addition to the second harmonic frequency ($\omega_2 = 0.9$ rad/s) waves are generated at a slightly lower frequency around $\omega_{2^-} \approx 0.8$ rad/s. We notice that the frequency interval between these waves increases with time. The presence of an additional frequency in the time–frequency diagram confirms the deviation of the second harmonic observed in Figure 3.10(e) below the prolate spheroid ($\mathcal{H}$).

The normalized kinetic energy E was calculated from the vertical and horizontal

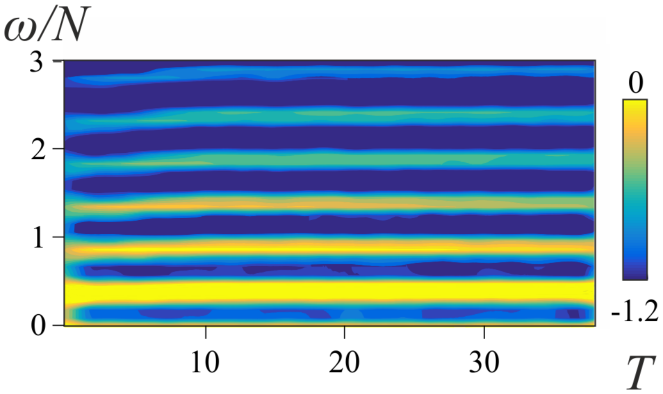

Figure 3.14: Time–frequency spectrum $\log_{10}(Q_u(t,\omega)/Q_0)$ for the horizontal longitudinal velocity $\hat{u}$ generated by the prolate spheroid $(\mathcal{H})$ in the horizontal plane $Z = -1$. The spectrum is averaged over the area $-2 < X < 2$, $-1 < Y < 1$, $T = (\omega t)/2\pi$ and $Q_0 = \max[Q_u(t,\omega_1)]$. [Exp C_1 from Table 2.2].

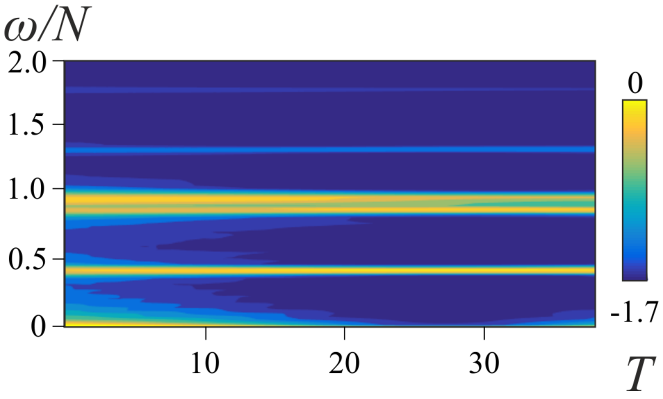

Figure 3.15: Time–frequency spectrum $\log_{10}(Q_w(t,\omega)/Q_0)$ for the vertical velocity $\hat{w}$ generated by the prolate spheroid $(\mathcal{H})$ in the vertical plane $Y = 0$. The spectrum is averaged over the area $-2.5 < X < 2.5$, $-4 < Z < -1$, $T = (\omega t)/2\pi$ and $Q_0 = \max[Q_w(t,\omega_1)]$. [Exp C_2 from Table 2.2]

longitudinal velocity components for waves generated by prolate spheroid $(\mathcal{H})$ in the vertical plane $Y = 0$, where the transverse velocity component is 0 (see Figure 3.5) and averaged over the $-b < X < b$ for all $-6 < Z < -1$:

$$E = \frac{\left\langle \frac{1}{2}\left[(\hat{u}_a^{(i)})^2 + (\hat{w}_a^{(i)})^2\right]\right\rangle_x}{\frac{1}{2}(A\omega)^2}. \tag{3.5}$$

The distribution of averaged kinetic energy along the vertical axis Z is shown in Figure 3.16 for the first and second harmonics. The fundamental wave energy has its maximum close to the object boundary and linearly dissipates with distance Z. The energy of the second harmonic wave has two maxima: one close to the object $(Z = -1)$ and in the zone of secondary beam intersection $(Z = -2.3$, see Figure 3.10e). Due to focusing the second harmonic is dominant for $-6 < Z < -3$.

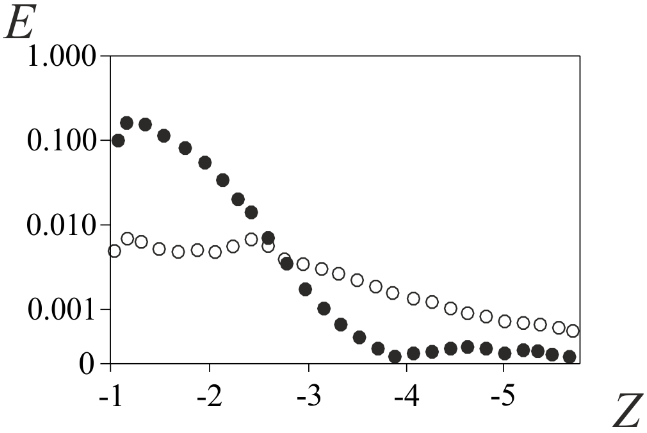

Figure 3.16: Distribution of the kinetic energy E defined by eq. (3.5) of the first harmonic (dots) and second harmonic (circles) along Z in the plane $Y = 0$ for the prolate spheroid ($\mathcal{H}$). [Exp C_2 from Table 2.2]

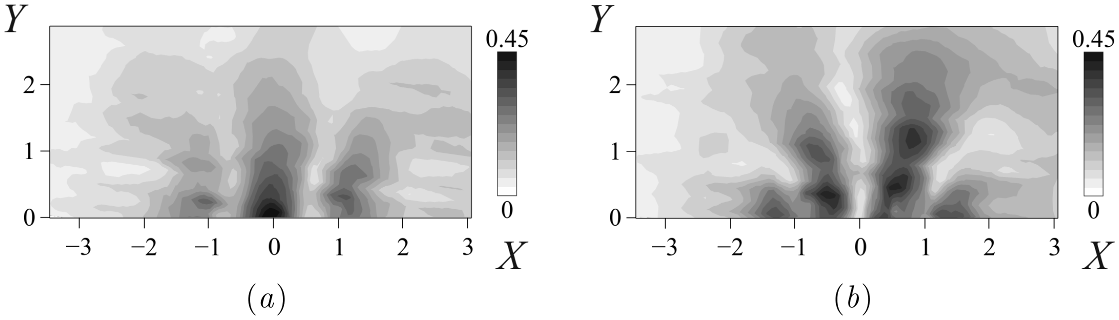

Figure 3.17: Octupolar radiation pattern corresponding to the upper half of Figure 3.2(c), for (a) the horizontal velocity amplitude of the third harmonic wave, $\hat{U}_3$, and (b) the vertical velocity amplitude of the third harmonic wave, $\hat{W}_3$ at $Ke = 0.52$ and $Z = -1.66$. [Exp A_3 from Table 2.2]

Distributions of the third harmonic component emitted by the sphere ($\mathcal{S}$) are shown in Figure 3.17 for the horizontal velocity $\hat{U}_3$ and the vertical velocity $\hat{W}_3$, complimenting the LIF measurements presented earlier in Figure 3.4. The third harmonics frequency is estimated as $3\omega/N \approx 0.8$. An octupolar structure is clearly visible, with 6 azimuthal lobes implying on amplitude variation as $\sin(3\phi)$ for the horizontal velocity amplitude and $\cos(3\phi)$ for the vertical velocity amplitude.

The distribution of the amplitudes of the third harmonic along the X-axis is presented in Figure 3.18 for objects of different curvature: sphere ($\mathcal{S}$), prolate spheroid ($\mathcal{V}$) and prolate spheroid ($\mathcal{H}$). The horizontal axis is normalized as $X = x/L$, where L is the length scale in the direction of oscillation, i.e. $L = a$ in the case of the sphere ($\mathcal{S}$) and prolate spheroid ($\mathcal{V}$), and $L = b$ in the case of the prolate spheroid ($\mathcal{H}$). All six azimuthal lobes of the third harmonic generated by the sphere have the same form, size and amplitude distribution but in the case of the prolate spheroid ($\mathcal{V}$), the amplitude of the azimuthal lobes along the X-axis is smaller compared to the

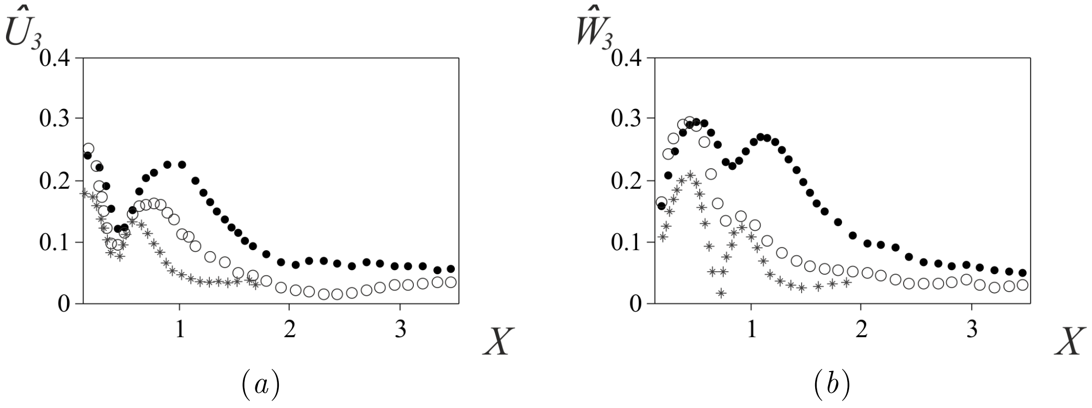

Figure 3.18: Profiles of the third harmonic of the (a) horizontal, $\hat{U}_3$, and (b) vertical, $\hat{W}_3$, velocity fields at $Y = 0$. Dots, circles and stars correspond to results for the oscillating sphere $(\mathcal{S})$ measured at $Z = -1.66$, for the prolate spheroid $(\mathcal{V})$ at $Z = -2.4$ and for the prolate spheroid $(\mathcal{H})$ at $Z = -1.66$, respectively, for $Ke = 0.56 \pm 0.04$. Note, the vertical distance to the boundary of the object is the same in all cases, but Z values vary because of the scaling. [Exp A_3 and $B_{1,2}$ from Table 2.2]

amplitude of the same lobes for the sphere ($0.4 < X < 1$ for $\hat{U}_3$ and $0.9 < X < 1.2$ for $\hat{W}_3$). We notice that the structure of the wave pattern approximately scales with the slope of the object. The amplitude of the higher harmonic waves changes significantly with the shape of the object, and is higher for "steeper" objects.

The dependance of the extreme values of the amplitudes of the first three harmonics on the oscillation amplitude is presented in Figure 3.19. The logarithmic representation shows that the amplitudes of the horizontal velocity $\hat{U}$ and vertical velocity $\hat{W}$ are independent of the oscillation amplitude for the normalized fundamental wave, and vary as Ke and Ke^2 for the normalized second and third harmonics, respectively, implying variations as Ke, Ke^2 and Ke^3 for the original dimensional velocities, respectively. This trend is in agreement with the two-dimensional theories of Bell (1975*a*), Tabaei *et al.* (2005) and Jiang & Marcus (2009), and with previous experimental studies on fundamental and second harmonic waves generated by an oscillating sphere (Ermanyuk *et al.*, 2011).

3.4 Conclusions

In view of former observations on the relevance of the fundamental wave and higher harmonics (Ermanyuk *et al.*, 2011; Ghaemsaidi & Peacock, 2013), a note should be made on higher harmonics in three-dimensional flows. In the two-dimensional case the energy content of the higher harmonics is usually relatively low, as demonstrated for the second harmonic in Zhang *et al.* (2007). However, in the three-dimensional case, the amplitude of the second harmonic can be higher than the amplitude of the first for a sphere (Ermanyuk *et al.*, 2011) or comparable to it for Gaussian topogra-

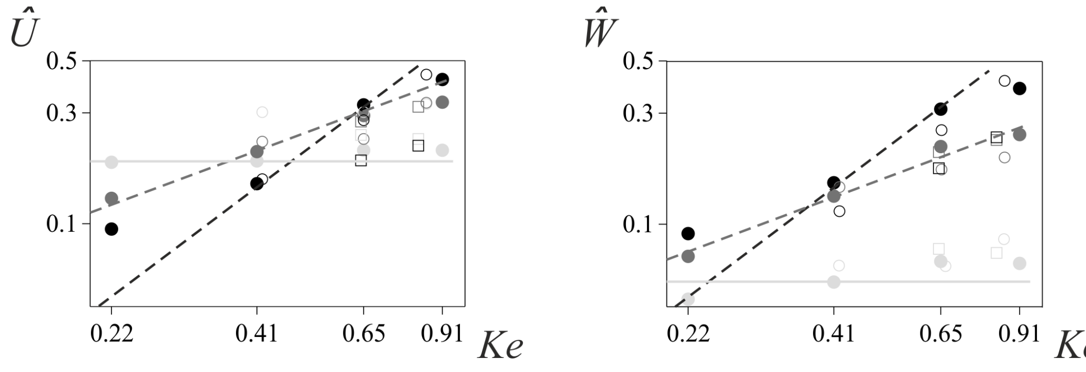

(*a*) (*b*)

Figure 3.19: Variations of the peak magnitudes of the first three harmonics with oscillation amplitude Ke for the (a) horizontal, $\hat{U}$, and (b) vertical, $\hat{W}$, velocity fields. First, second and third harmonics are represented with light gray, dark gray and black color, respectively, and compared with the theoretical predictions for the sphere (solid light gray line), and with the linear regressions for $\hat{U}_2$ and $\hat{W}_2$ (dashed dark grey lines) and $\hat{U}_3$ and $\hat{W}_3$ (dashed black lines). The dots, circles and squares correspond to results for the oscillating sphere ($\mathcal{S}$), prolate spheroid ($\mathcal{V}$) and prolate spheroid ($\mathcal{H}$), respectively. [Exp A_3 and $B_{1,2}$ from Table 2.2]

phy over a flat bottom (King *et al.*, 2010). The reason for this difference is related to the fact that, at low oscillation frequencies ω/N and fixed amplitude Ke, the power P of internal waves that are generated by horizontally oscillating bodies varies as $(\omega/N)^2$ for a circular cylinder and $(\omega/N)^5$ for a sphere (Voisin *et al.*, 2011), and similar asymptotic behavior is valid for elliptic cylinders and spheroids (Ermanyuk, 2002). Accordingly, at low frequency ω/N and fixed Ke the amplitude of the first, linear harmonic is much smaller in three dimensions than in two and can more easily be overtaken by the amplitude of the higher, nonlinear harmonics. Therefore, for low oscillation frequencies ω/N, that are relevant to geophysical applications, we may have a situation where the fundamental wave generated by barotropic flow over three-dimensional topography is weak while a higher n-th harmonic is strong. Reciprocally, higher harmonics are of interest for three-dimensional topography because of their high energy content under appropriate conditions. The azimuthal harmonic wave structure may have an influence on the energy and mass fluxes in the vicinity of underwater mountains.

In this study we have shown that fundamental and second harmonic waves are generated at critical points at the boundaries in agreement with former observations (Zhang *et al.*, 2007). Intersections of the fundamental wave beams lead to the generation of second harmonic waves, when their wave amplitude exceeds a certain threshold (Tabaei *et al.*, 2005; Jiang & Marcus, 2009). When the amplitude of oscillation exceeds this threshold, the consequent nonlinear overturning motion also leads to the generation of higher harmonics that appear weakly trapped near the region of generation. Further research is needed to show the threshold amplitude for which these nonlinear motions emit higher harmonic wave beams. It is also shown that in agreement with previous observations (Ermanyuk *et al.*, 2011) and theoretical predictions (Bell, 1975*a*) the amplitude of the first three harmonics grows linearly, quadratically and cubically, respectively, with increasing oscillation amplitude.

Chapter 4

Internal wave focusing by a horizontally oscillating torus: linear aspects*

In the ocean, mountain ridges occur more frequently than isolated mountains. Oscillations of the barotropic tide over a curved mountain ridge can cause not only diverging waves which gradually decrease with distance due to viscosity, but also converging waves which increase in amplitude with distance from the ridge toward a focal region. To generate focusing internal waves, a torus (ring) having a vertical axis of revolution oscillated horizontally in a linearly stratified fluid. Such a configuration produces both diverging and converging internal waves. As in a classical situation considered in previous studies of three-dimensional flows (Flynn *et al.*, 2003; King *et al.*, 2009; Voisin *et al.*, 2011; Ermanyuk *et al.*, 2011) for spherical geometry, diverging waves decrease with distance owing to viscosity and the cross-section of the wave cone increases. In contrast the converging waves increase in amplitude with distance from the ring toward the focal region, where high wave amplification and breaking may be expected. At moderate Reynolds numbers typical for laboratory experiments this trend is opposed by viscous dissipation. Turbulence has been observed in the focal region of inertial waves generated by a vertically oscillating torus in a rotating fluid conducted at LEGI (Duran-Matute *et al.*, 2013). The breaking of these waves played an important role for the transport of momentum, and the generation of columnar vortices that are typical for two-dimensional turbulence. Apart from the above mentioned studies, the geometric focusing of internal waves deserves further attention in the context of ocean mixing and momentum transport in the Earth's oceans.

In this chapter an experimental study on internal waves emitted by a horizontally oscillating torus in a linearly stratified fluid is presented. Two internal wave cones are generated with the kinetic energy focused at the apices of the cones above and below the torus where the wave amplitude is maximal. Internal waves are measured

---

*This chapter is a modified version of the article "Internal wave focusing by a horizontally oscillating torus", accepted for publication in *J. Fluid Mech.* and reproduced in Appendix B

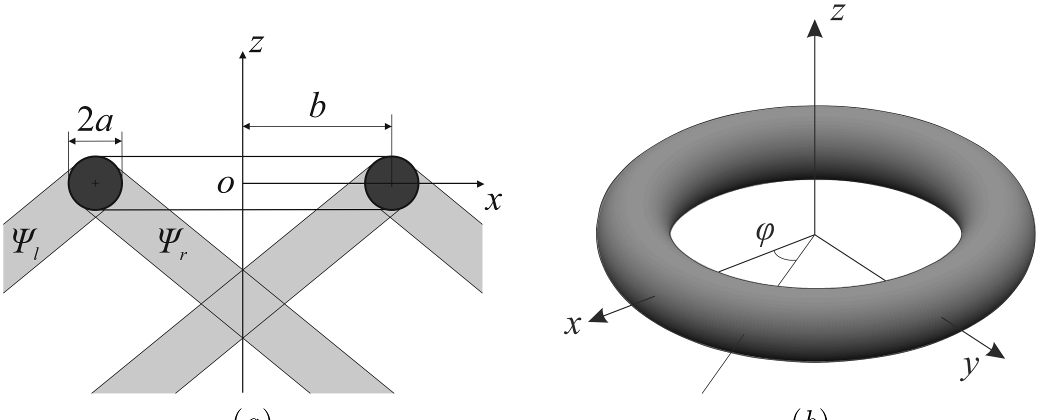

(a) (b)

Figure 4.1: Geometry of the torus: (a) view in a vertical plane and (b) three-dimensional view defining the coordinate system.

via precise tracking of the distortion of horizontal fluorescein-dye planes created in the tank prior to the experiments and illuminated by a vertical laser sheet. The distortion of the dye planes gives direct access to the Lagrangian measurement of local wave amplitudes and wave slopes. Complementary measurements have been taken with the PIV technique.

4.1 Theoretical considerations

In this section we first consider the two-dimensional theory of Hurley & Keady (1997) adapted to the three-dimensional case of the torus as a simple approach of the features of converging wave beams. The next step is to consider the fully three-dimensional theory.

4.1.1 Two-dimensional theory

We consider a torus of which the geometrical parameters are defined in Figure 4.1. The torus is submerged into a uniformly stratified fluid of buoyancy frequency N. The shape of the generatrix is circular with diameter $2a$, and b is the radius of the circle of the centres cross-sections. A Cartesian coordinate system (see Figure 4.1b) is introduced, with the z-axis pointing upwards. The origin of the coordinate system O is taken at the mean position of the center of the torus which undergoes rectilinear harmonic oscillations with frequency ω. The non-dimensional geometry can be characterized by the aspect ratio $\epsilon = b/a$. We assume that the torus is slender, i.e. ϵ is large. The non-dimensional coordinates X, Y and Z are introduced after normalization of x, y and z with the radius of the generatrix, a.

Let us consider first the vertical oscillations of the torus with amplitude A, which is assumed to be small compared to a so that the Keulegan–Carpenter number $Ke = A/a \ll 1$ and the waves are linear. The Stokes number $St = \omega a^2/\nu$, with

ν the kinematic viscosity, is assumed to be sufficiently large, i.e. $St \gg 1$. In the experiments described below, $St = O(100)$ which guarantees a sufficiently small non-dimensional boundary layer thickness δ/a. This allows the boundary layer to be neglected, so the forcing at the torus is of inviscid free-slip type and viscosity affects only the propagation of the waves. To construct an approximate solution we use an approach similar to the strip theory in marine hydrodynamics (Newman, 1977*a*,*b*).

Suppose that each radial cross-section of the torus oscillates vertically and generates internal wave beams described by equation (3.7) in Hurley & Keady (1997) for a cylinder. For brevity this equation is not reproduced here. Indeed, the assumptions $Ke \ll 1$ and $St \gg 1$ are in agreement with Hurley & Keady (1997). This linear solution plays a role of an "inner" solution, which is approximately valid at each radial cross-section $\phi = const$, where ϕ is the azimuthal angle in the cylindrical coordinate system (r, z, ϕ), with $r = (x^2 + y^2)^{1/2}$. For vertical oscillations the problem is axisymmetric and all cross-sections $\phi = const$ are equivalent. Without loss of generality we consider oscillations in the plane xOz (see Figure 4.1). The stream function for a single cylinder,

$$\psi^1_{HK}(x, z, t) = \Psi^1_{HK}(x, z) \exp(-\mathrm{i}\omega t),$$

is constructed as a sum of four stream functions describing the four beams of the St. Andrew's Cross wave pattern (see Sutherland *et al.*, 1999)

$$\Psi^1_{HK}(x, z) = \Psi^+_l + \Psi^+_r + \Psi^-_l + \Psi^-_r, \tag{4.1}$$

where the superscripts + and − refer, respectively, to the upper and lower half-plane, whereas the subscripts l and r refer, respectively, to the beams propagating to the left and the right.

For the second cylinder the solution $\Psi^2_{HK}(x, z)$ is analogous. Assuming that b/a is sufficiently large, the solution for the system of two cylinders can be written as

$$\Psi_{HK}(x, z) = \Psi^1_{HK}(x, z) + \Psi^2_{HK}(x, z), \tag{4.2}$$

where the appropriate choice of signs and phases in eq. (4.1) assure that both cylinders oscillate vertically and in phase. The instantaneous vertical displacement of fluid particles due to the oscillation of the two cylinders is then evaluated as

$$\zeta^t_{HK}(x, z, t) = (\mathrm{i}/\omega) \exp(-\mathrm{i}\omega t) \frac{d}{dx} \Psi_{HK}(x, z). \tag{4.3}$$

The corresponding distribution of wave amplitudes is denoted as $\zeta_{HK}(x, z)$.

Further, we introduce the geometric correction factor for convergence (divergence) of the wave field. Let us consider a point C with coordinates (x_C, z_C) in the two-dimensional wave field generated by a system of two cylinders. The density of the energy flux at point C is proportional to the wave amplitude squared $(\zeta_{HK}(x_C, z_C))^2$. Since the torus is slender, we can equate the energy fluxes due to internal waves emitted by vertical oscillations of a torus of major radius b and minor radius a, and due to a system of two cylinders (see Figure 4.1) of radius a and length πb. We obtain then

$$(\zeta(r_C, z_C))^2 \pi r_C = (\zeta_{HK}(x_C, z_C))^2 \pi b,$$

where $r_C = x_C$ at $\phi = 0$. Finally, we obtain in non-dimensional cylindrical coordinates

$$\zeta(R, Z) = (R/\epsilon)^{-1/2} \zeta_{HK}(R, Z), \tag{4.4}$$

where $R = r/a$. The term $(R/\epsilon)^{-1/2}$ assures a proper decay of the wave amplitude at infinity.

Let us note that in the case of vertical oscillations of two cylinders the wave amplitude $\zeta_{HK}(x, z)$ is symmetric with the respect to the vertical axis $x = 0$ and non-zero at $x = 0$. Therefore the approximate solution predicts a divergence of wave amplitudes of the form of $X^{-1/2}$ in the focal region at $X \to 0$. This result shows that near-field interactions should be taken into account in this zone in order to develop a more advanced linear theory. Also, in realistic situations, one can expect strong spatially localized non-linear effects in forms of vertical jets. Such effects have been indeed observed for inertial waves in Duran-Matute *et al.* (2013) and have been shown to create a localized turbulence zone due to a cascade of instability events.

Now, let us adapt the same approach in the spirit of strip theory (Newman, 1977*a*,*b*) to a slender torus undergoing horizontal oscillations with amplitude A along the x-axis. The local forcing is then taken as a projection of horizontal oscillations on the radial coordinate in the form $A \cos \phi$. Obviously, equations (4.1)–(4.3) remain valid in the case of horizontal oscillations of a system of two cylinders, with the important difference that the signs and phases of motions in wave beams should now be chosen such that the wave amplitude $\zeta_{HK}(x, z) = 0$ at $x = 0$ and the instantaneous wave profiles are anti-symmetric with respect to the vertical axis $x = 0$. The geometric conversion introduced in (4.4) remains valid but now, owing to azimuthal modulation of the wave field, eq. (4.4) for wave amplitudes transforms into

$$\zeta(R, Z, \phi) = (R/\epsilon)^{-1/2} \zeta_{HK}(R, Z) |\cos \phi|.$$

For horizontal oscillations, $\zeta_{HK}(R, Z)$ is proportional to R at a fixed Z in a small vicinity of $R = 0$, and therefore $\zeta(R, Z, \phi)$ is proportional to $R^{1/2}$ as R tends to 0. Thus, the wave amplitude remains limited but the wave slope tends to the vertical. This qualitatively indicates a possibility of overturning in the focal region, which is a qualitatively different behaviour compared to the case of vertical oscillations.

To characterize the forcing of internal waves, the Keulegan-Carpenter number $Ke = A/a$ is often used (see e.g. Voisin *et al.*, 2011; Ermanyuk *et al.*, 2011). Though this number characterizes the non-linearity close to the torus, it does not take into account the geometric effect of focusing at larger distances from the torus. Supposing that in the focal zone the wave motion can be confined to a zone with radius a, the amplitude may increase to

$$\zeta_{corr} = \zeta_{HK} (b/a)^{1/2} = \zeta_{HK} \epsilon^{1/2}$$

i.e. with a factor $\epsilon^{1/2}$ due to focusing. The same correction factor has been introduced earlier in Bühler & Muller (2007). Note that the above-described theory neglects the near-field wave interactions in the focal region. Also, the viscous damping in the above solution is adapted from Hurley & Keady (1997), and therefore neglects additional shear close to the focal region. Therefore it is expected to provide a quantitative estimate with a reasonable accuracy only in the vicinity of the torus. The effects of finite values of Ke, St and ϵ in experiments are discussed below.

4.1.2 Three-dimensional theory

In this section we present the three-dimensional theory for the horizontally oscillating torus developed by Voisin (2016). This theory considers a ring torus of centre O, vertical axis Oz, minor radius a, major radius b and aspect ratio $\epsilon = b/a$, oscillating at the frequency $\omega < N$ along the x-axis with position $(A, 0, 0)\sin(\omega t + \Theta)$, and takes into account the kinematic viscosity ν. The regime is linear, such that $Ke \ll 1$, the torus thin, such that $\epsilon \gg 1$, and the fluid weakly viscous, such that $St \gg 1$.

In nondimensional coordinates $(X, Y, Z) = (x, y, z)/a$, the velocity field (u, v, w) has nondimensional components $(U, V, W) = (u, v, w)/(\omega A)$ given by

$$\begin{aligned} U = {} & \mathrm{i}\pi\epsilon\cos\theta\sin\theta \mathrm{e}^{-\mathrm{i}(\omega t+\Theta-\theta)} \int_0^\infty \mathrm{d}K\, K J_1(K) J_0(K\epsilon\cos\theta) \exp\left(-\frac{K^3|Z|}{2St\sin\theta}\right) \\ & \times \left[J_2\left(K\sqrt{X^2+Y^2}\cos\theta\right) \frac{X^2}{X^2+Y^2} - \frac{J_1\left(K\sqrt{X^2+Y^2}\cos\theta\right)}{K\sqrt{X^2+Y^2}\cos\theta} \right] \\ & \times \exp(-\mathrm{i}K|Z|\sin\theta), \end{aligned} \tag{4.5}$$

$$\begin{aligned} V = {} & \mathrm{i}\pi\epsilon\cos\theta\sin\theta \mathrm{e}^{-\mathrm{i}(\omega t+\Theta-\theta)} \int_0^\infty \mathrm{d}K\, K J_1(K) J_0(K\epsilon\cos\theta) \exp\left(-\frac{K^3|Z|}{2St\sin\theta}\right) \\ & \times J_2\left(K\sqrt{X^2+Y^2}\cos\theta\right) \frac{XY}{X^2+Y^2} \exp(-\mathrm{i}K|Z|\sin\theta), \end{aligned} \tag{4.6}$$

$$\begin{aligned} W = {} & \pi\epsilon\cos^2\theta \mathrm{e}^{-\mathrm{i}(\omega t+\Theta-\theta)} \operatorname{sign} Z \int_0^\infty \mathrm{d}K\, K J_1(K) J_0(K\epsilon\cos\theta) \exp\left(-\frac{K^3|Z|}{2St\sin\theta}\right) \\ & \times J_1\left(K\sqrt{X^2+Y^2}\cos\theta\right) \frac{X}{\sqrt{X^2+Y^2}} \exp(-\mathrm{i}K|Z|\sin\theta), \end{aligned} \tag{4.7}$$

where J_0 and J_1 denote Bessel functions. The associated distributions of vertical and horizontal velocity amplitudes in XZ-plane for a torus with $b/a = 5$ is shown in Figures 4.2(*a,c*).

With $\zeta = \mathrm{i}w/\omega$ the vertical displacement of fluid particles, the isopycnal planes have slopes

$$S_x = \frac{\partial\zeta}{\partial x} = \mathrm{i}Ke\frac{\partial W}{\partial X}, \tag{4.8}$$

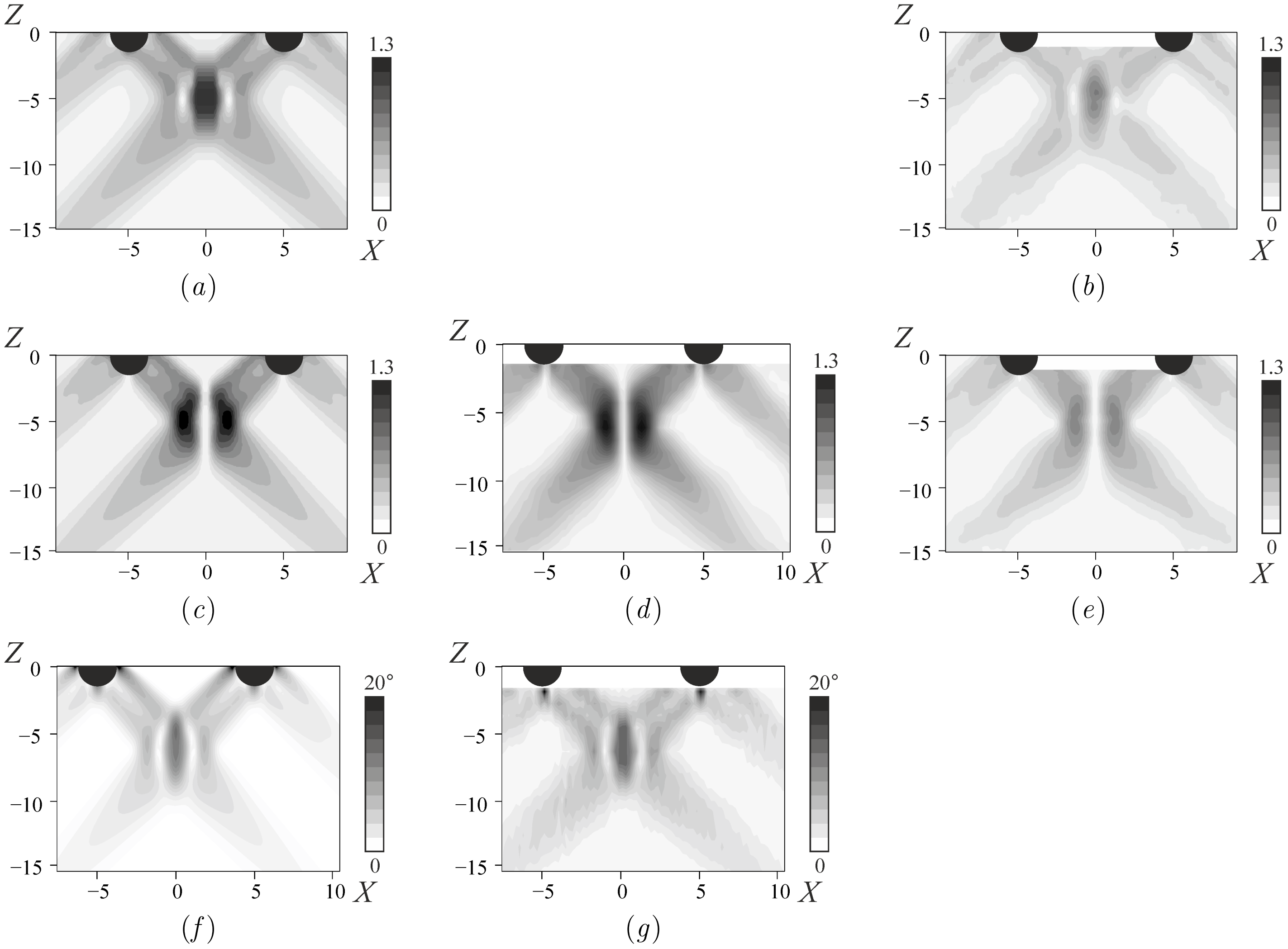

(a) (b) (c) (d) (e) (f) (g)

Figure 4.2: Theoretical (first column) and experimental (second and third columns) amplitude patterns of the (*a*,*b*) the horizontal velocity, (*c*-*e*) vertical velocity and (*f*,*g*) the isopycnal slope in the centre plane $Y = 0$ for the thick torus of $\epsilon = 5$ oscillating at $Ke = 0.15$ and 0.19. Theory is calculated from equations (4.5), (4.7) and (4.8) and the measurements are obtained with LIF (second column) and PIV (third column). [Exp $H_{1,3}$ from Table 2.2]

$$S_y = \frac{\partial \zeta}{\partial y} = \mathrm{i}Ke\frac{\partial W}{\partial Y} \tag{4.9}$$

along the x- and y-axes, respectively, where

$$\begin{aligned}\frac{\partial W}{\partial X} = {} & -\pi\epsilon\cos^3\theta \mathrm{e}^{-\mathrm{i}(\omega t+\Theta-\theta)}\operatorname{sign} Z\int_0^\infty \mathrm{d}K\, K^2 J_1(K)J_0(K\epsilon\cos\theta)\exp\left(-\frac{K^3|Z|}{2St\sin\theta}\right)\\ & \times\left[J_2\left(K\sqrt{X^2+Y^2}\cos\theta\right)\frac{X^2}{X^2+Y^2} - \frac{J_1\left(K\sqrt{X^2+Y^2}\cos\theta\right)}{K\sqrt{X^2+Y^2}\cos\theta}\right]\\ & \times\exp(-\mathrm{i}K|Z|\sin\theta), \qquad (4.10)\\ \frac{\partial W}{\partial Y} = {} & -\pi\epsilon\cos^3\theta \mathrm{e}^{-\mathrm{i}(\omega t+\Theta-\theta)}\operatorname{sign} Z\int_0^\infty \mathrm{d}K\, K^2 J_1(K)J_0(K\epsilon\cos\theta)\exp\left(-\frac{K^3|Z|}{2St\sin\theta}\right)\\ & \times J_2\left(K\sqrt{X^2+Y^2}\cos\theta\right)\frac{XY}{X^2+Y^2}\exp(-\mathrm{i}K|Z|\sin\theta). \qquad (4.11)\end{aligned}$$

The distribution of wave slope amplitude in the XZ-plane for the same torus is shown in Figure 4.2(*f*).

4.2 Linear regime: comparison with linear theory

The predictions of the linear theory are now compared with experimental results in the linear regime, i.e. for low oscillation amplitude, represented by Keulegan–Carpenter number $Ke \approx 0.15$. Three tori are used, of aspect ratios $\epsilon = 5, 9$ and 34, called thick, thin and big tori, respectively, in the following; the actual dimensions of these tori are presented in Table 2.1. Figure 4.2 shows theoretical calculations for the thick torus obtained with equations (4.5), (4.7) and (4.8) (first column) and experimental results available from LIF (second column) and PIV (third column) in the central plane parallel to the direction of oscillation, $Y = 0$. Experimental data are filtered via Fourier (LIF) and frequency (PIV) filtering and the first harmonic is presented, denoted by a subscript 1 in the following. Focusing of internal waves is obtained. The oscillation of the torus generates diverging beams outside the torus ($|X| > 5$) and converging beams which increase in amplitude toward the focal zone. At low Ke the amplified vertical displacement, ζ_1/A (corresponding to the LIF measurements in Figure 4.2*d*), and velocity, $\hat{W}_1$ (corresponding to the PIV measurements in Figure 4.2*e*), amplitudes forming two symmetrical elliptic-shaped structures in the focal region due to the symmetry of the problem. The amplified horizontal velocity amplitude $\hat{U}_1$ (Figure 4.2*b*) forms an elliptic-shaped structure in the centre of the focal region. Patterns in Figure 4.2 quantitatively demonstrate that experimental results are well compared with three-dimensional theoretical predictions.

Experimental results are also presented in Figure 4.3(*a*) for the thin torus with $\epsilon = 9$ in terms of the vertical amplitude displacement ζ_1 and wave slope S. Note also that the waves in the focal zone have a unimodal structure, i.e. there is a single wave beam due to the dominant effect of viscosity, in contrast to the bimodal structure often observed very near to oscillating objects, while viscosity is secondary (for a discussion see e.g. Voisin *et al.*, 2011). Though the general flow evolution was very similar to that of the thick torus (Figure 4.2, third column), its larger radius a implied a larger Stokes number (260 instead of 150) causing a rather bimodal wave structure near the torus which turned into a single beam near the focal region. In the case of very large tori, however, one may expect a multi focal region because of the bimodal wave structure. In view of the range of accessible Stokes numbers, this was not observed in the present experiments.

Figures 4.4(a) and (b) show the distribution of the amplitudes of horizontal velocity $\hat{U}_1$ and vertical velocity $\hat{W}_1$, obtained with PIV, along the direction of oscillation X close to the torus ($Z = -1.88$, red symbols) and in the focal zone ($Z = -7.88$, blue symbols) for the thick torus oscillating with low amplitude $Ke = 0.19$. LIF results are presented with crosses for the vertical displacement amplitude and solid lines show the predictions of the linear theory of section 4.1.2. The vertical velocity amplitude in the focal zone obtained with PIV is significantly lower than theoretical predictions while the LIF results are in very good comparison with the theory. The same behavior is obtained for the horizontal velocity amplitude in the focal zone. The horizontal velocity profile has a high slope close to the torus for the converging beam ($X = 3$); there, a difference between the PIV results and the theory are also noticeable. For the diverging beam ($5 < X < 10$) the experimental results are in very good comparison with the linear theory. Difference between PIV and LIF measurements has also been discussed in section 2.3.

Figure 4.5 shows the wave amplitude profile across the wave beam in the plane XZ for a range of distances $|Z|$ from the centre of the thin torus up to the middle of the focal zone. Good agreement of the experiment with the theory of section 4.1.1 is observed at low values of Ke, and close to the torus. Thus, a simple geometric correction is fully sufficient for quantitative description of the main effects due to convergence (divergence) of the waves in the vicinity of a curved elongated body. Thereby it provides a consistent framework for the quantitative interpretation of the experimental results almost everywhere in the wave field, except in the focal region.

For the focal region, the theory shows that focusing amplifies the wave amplitude to a factor 3, in qualitative agreement with the correction factor $\epsilon^{1/2}$ introduced in Bühler & Muller (2007). This can be observed in Figure 4.5(f) ($|Z| = 12.51$) from the comparison of the calculated wave amplitudes for the torus (solid line) and the reference case of the two parallel cylinders of infinite length (dashed line). The experimental wave amplitudes in the focal zone are significantly lower (roughly by 30%) than the theoretical estimate. Indeed the theory of section 4.1.1 neglects the near-field interference between the wave components from the different azimuthal planes in the focal zone, leading to unrealistic infinite wave slopes at the vertical Z-axis.

The linear theory of section 4.1.2 considers these three-dimensional effects and describes the wave behavior well compared with experimental results even in the focal region.

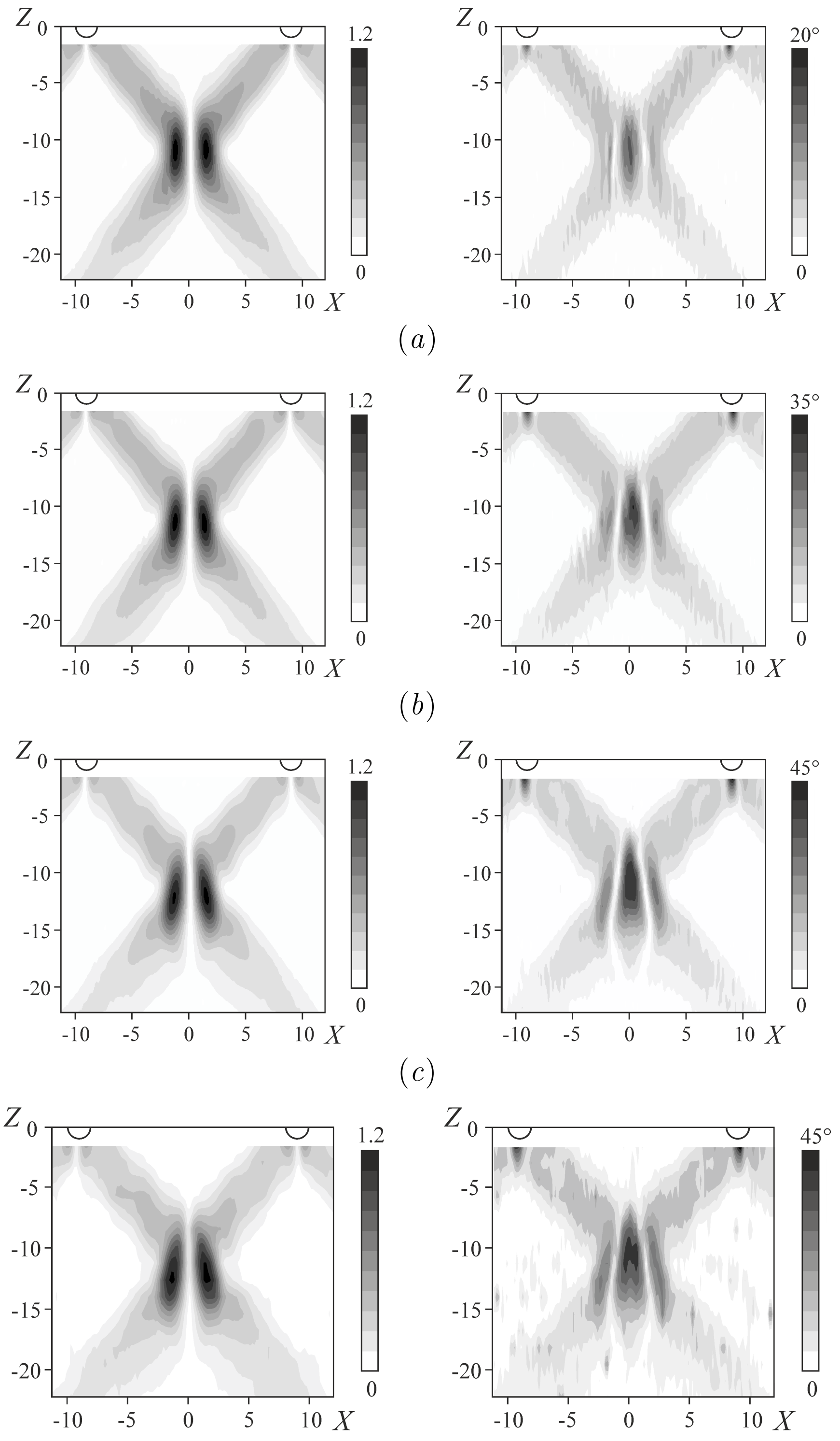

(*a*)

(*b*)

(*c*)

(*d*)

Figure 4.3: Contour plots of the displacement amplitude ζ_1/A (left column) and wave slope amplitude S_1 (right column) in the XZ-plane, for the thin torus of $\epsilon = 9$ oscillating at (a) $Ke = 0.19$; (b) 0.41 and (c) 0.65; (d) contour plots of ζ_{max}/A and S_{max} for $Ke = 0.65$. [Exp H_1 from Table 2.2]

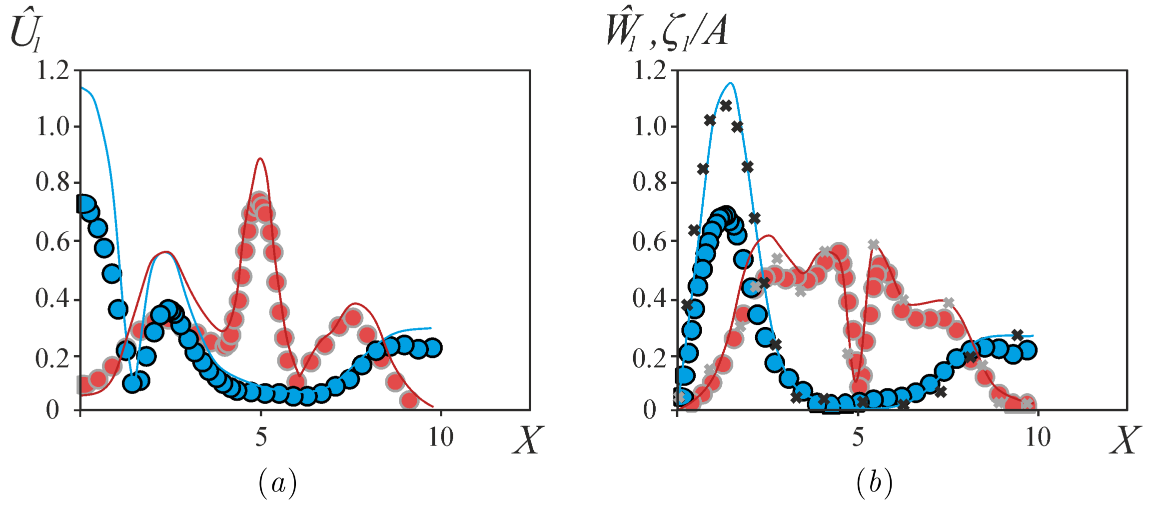

Figure 4.4: Distribution of (a) horizontal and (b) vertical velocity amplitude along the direction of oscillation X, close to the torus at $Z = -1.88$, (red symbols) and in the focal zone at $Z = -7.88$, (blue symbols and black crosses, corresponding to PIV and LIF data, respectively). The theoretical predictions of section 4.1.2 are shown with solid lines. [Exp $H_{1,3}$ from Table 2.2]

4.3 Weakly nonlinear effects

4.3.1 Wave pattern in the XZ-plane

Figure 4.3(a–c) shows the typical evolution of the first harmonic wave patterns for different oscillation amplitude, represented by the Keulegan-Carpenter number Ke, in terms of contours of the vertical displacement amplitude ζ_1/A, and wave slope S_1. For comparison Figure 4.3(d) represents the unfiltered wave fields in terms of ζ_{max}/A and S_{max}. A higher level of noise is observed for these non filtered max-type quantities. Figures 4.3(c) and (d) show a high resemblance indicating that at moderate oscillation amplitude, the dominant contribution to the wave field is represented by the first harmonic wave obtained after Fourier filtering, as can be expected since higher harmonics are evanescent for this forcing.

The wave amplitudes close to the torus are roughly two times smaller than the wave amplitudes in the focal region, but the wave slopes close to the torus and in the focal region are comparable. The onset of overturning occurs therefore not only in the focal region but also near to the torus. It should be noted that this latter overturning is rather due to the steep slope of the circular cross-section, an effect that would most likely be absent for a Gaussian shaped torus. At low Ke the amplified wave amplitude in the focal region forms then two symmetric structures having an elliptical shape due to the anti-symmetry of the instantaneous wave profiles with respect to the YZ-plane, where the wave amplitude is zero. As Ke increases, these regions of maximum amplitude slightly shift into the Z-direction away from the torus. The nonlinear evolution of the wave field is well visible in terms of wave

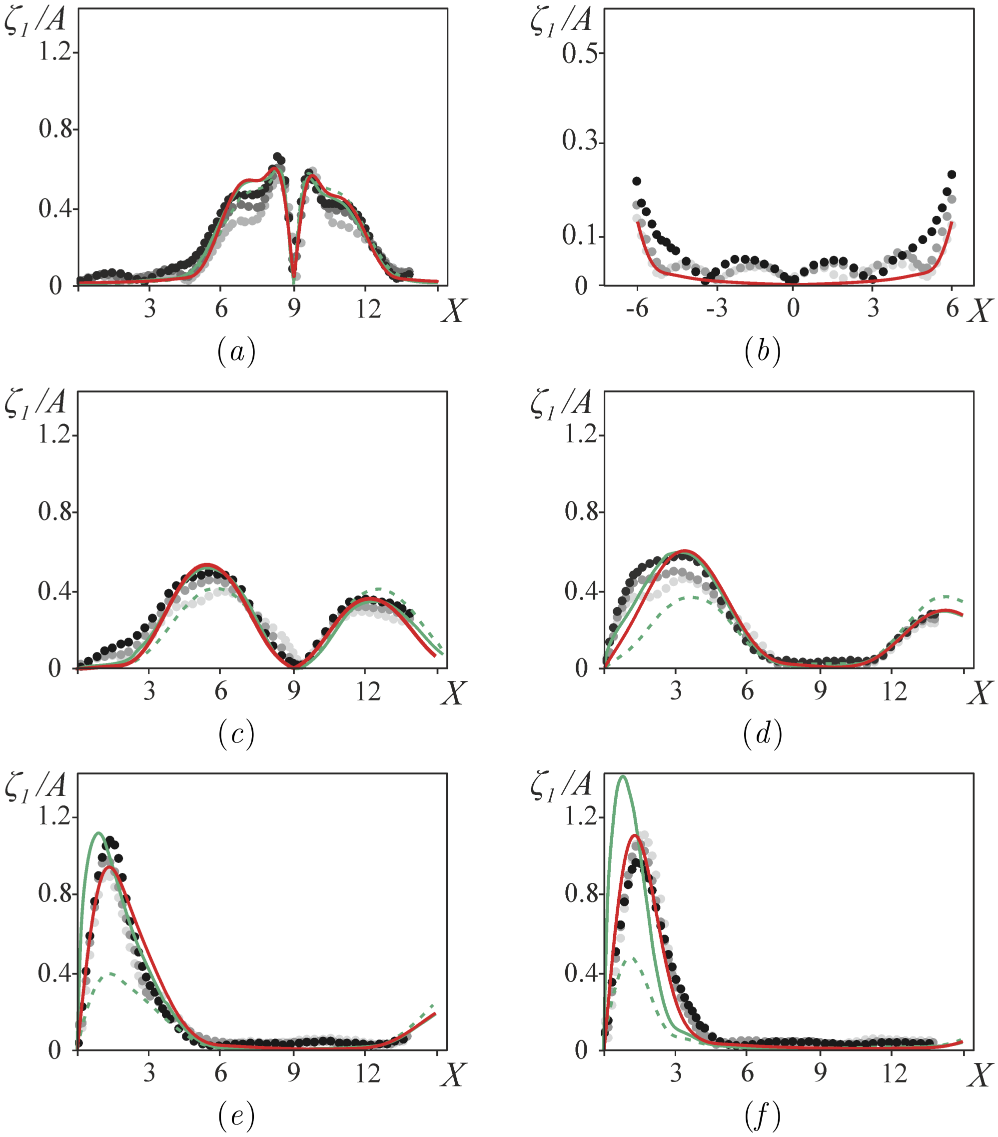

Figure 4.5: Vertical displacement amplitude ζ_1/A as a function of X in the plane $Y = 0$, at different heights Z below the centre of the torus, namely (a) $Z = -1.84$, (b) $Z = -1.84$ zoomed in including negative values of X (the centreline of the torus is at $X = 0$); (c) $Z = -4.48$, (d) $Z = -7.17$, (e) $Z = -9.84$, and (f) $Z = -12.51$. The focal zone is located at $Z = -11.2$. The dashed and solid green lines represent, respectively, the theoretical prediction (eq. 4.3) for two oscillating cylinders and the prediction (eq. 4.4) corrected for convergence; the red lines show the prediction (eq. 4.7) of the three-dimensional theory. The black, grey and light grey dots correspond to the LIF experimental measurements at $Ke = 0.19, 0.41$ and 0.65, respectively. [Exp G_1 from Table 2.2]

slopes. At low Ke the focal region (Figure 4.3*b*) has a nearly elliptic shape. As Ke increases, the focal region takes a spearhead-like shape (Figures 4.3*f, h*), indicating the higher shear in the outer part of the focal region, and incipient overturning. As a consequence, the waves are hindered by nonlinear effects in the focal region.

The experimental data presented in Figure 4.5 provide a qualitative information on the non-linear trends in the wave amplitude as function of the oscillation amplitude Ke. With increasing Ke, the normalized wave amplitude of the first harmonic, ζ_1/A, typically decreases almost everywhere in the wave field except in the focal region: the amplitude profiles marked by light grey and dark grey symbols are consistently lower than the profiles marked by black symbols. This trend is in agreement with the non-linear trends observed for the two- (Zhang *et al.*, 2007) and three-dimensional (Voisin *et al.*, 2011; Ermanyuk *et al.*, 2011) cases. The opposite trend is seen in Figure 4.5(f) in the focal region at $|Z| = 12.51$ where higher normalized wave amplitudes ζ_1/A correspond to higher Ke. Thus, a linear extrapolation of the low-amplitude experimental data to a high-amplitude case should be done with care: it tends to underestimate the wave amplitudes in localized zones of the focal region and to overestimate the wave amplitudes in all other regions of the wave field. Interestingly, in the middle of the focal region, located around $|Z| = 11.2$, the linear scenario applies in a remarkably wide range of A as discussed below.

It is worth to make a special remark concerning the data presented in Figure 4.5(b). The low-amplitude standing-wave pattern seen close to the centre of the torus can hardly be interpreted within a linear approach. The whole inner region delimited by the conical wave beams emitted by the torus seems to undergo a weak resonant motion. Its amplitude is typically an order of magnitude smaller than the amplitude of the main wave beams but at high oscillation amplitude A it is high enough to deform the straight wave beams (compare the form of isolines of wave amplitudes in the first column of Figure 4.3 at low and high amplitudes). The mechanism providing the energy flux to this motion is unclear and will be considered elsewhere.

The typical cross-sections of the total velocity amplitude at $Y = 0$ are shown in Figure 4.6 (left column) for the thick torus obtained with the PIV technique. Results are shown in terms of the total velocity

$$|\boldsymbol{U_1}| = \sqrt{(\hat{U}_1)^2 + (\hat{W}_1)^2}.$$

A note should be made on the calculations of this velocity. The standard PIV technique gives two velocity components: the vertical velocity $\hat{W}$ and the longitudinal horizontal velocity $\hat{U}$. Results are presented in the vertical plane through the centre of the torus parallel to the direction of oscillation. As shown in Figure 5.8(c) in section 5.2, the transverse horizontal velocity $\hat{V}$ is zero in this plane in the case of a non-rotating stratified fluid.

The total velocity amplitude is strongly amplified in the focal region. There is a standing wave in the horizontal direction and a propagating wave in the vertical direction. In the linear case two regions of highest amplitude are located symmetrically on either side of the Z-axis in the focal zone and have an elliptic shape.

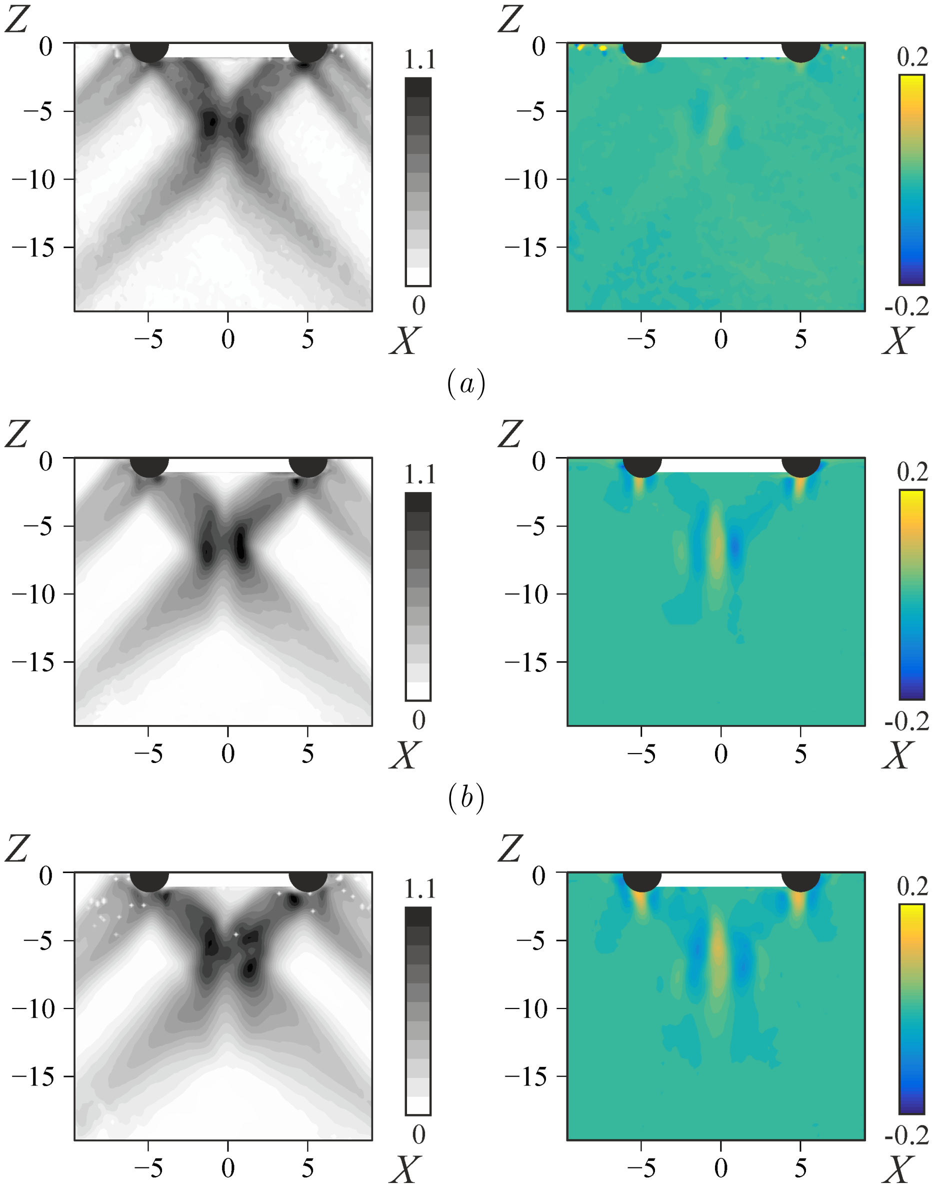

(*a*)

(*b*)

(*c*)

Figure 4.6: Experimental wave patterns in the XZ-plane for the thick torus with $\epsilon = 5$ in terms of the total velocity amplitudes, $|\boldsymbol{U_1}| = \sqrt{\hat{U}_1^2 + \hat{W}_1^2}$, (left column) and the vertical velocity $\hat{W}_0$ of the zero frequency component, phase averaged over 10 oscillation periods (right column). Images (a), (b) and (c) correspond to $Ke = 0.19$, 0.41 and 0.6, respectively. [Exp H_3 from Table 2.2]

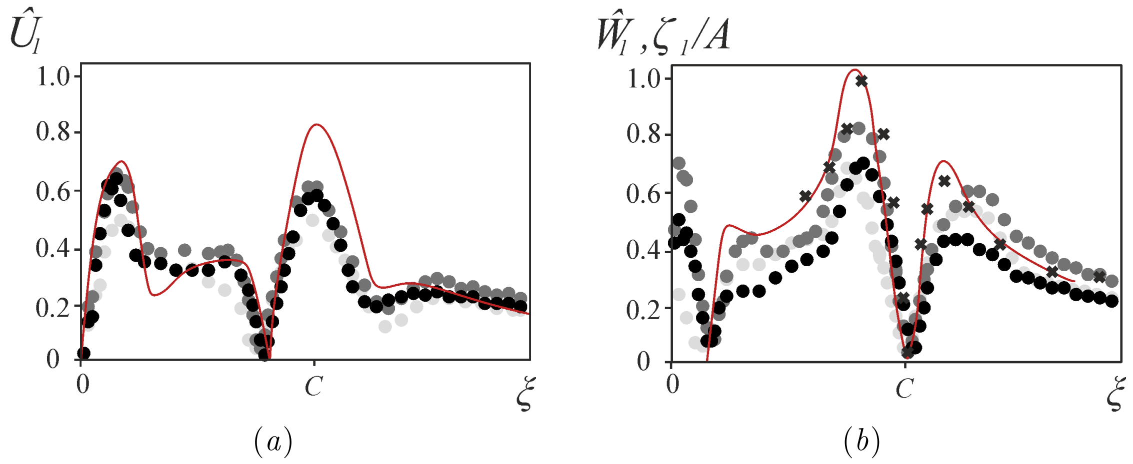

Figure 4.7: Distribution of (a) horizontal velocity amplitude $\hat{U}_1$ and (b) vertical velocity amplitude $\hat{W}_1$ along the direction of the wave beam ξ, with C the focal zone centre $(X = 0, Y = 0, Z = -6.5)$; light grey, dark grey and black dots represent PIV data for $Ke = 0.19, 0.6$ and 1.2, respectively $(\epsilon = 5, \omega/N = 0.8$, Exp H_3 in Table 2.2), black crosses show LIF data for $Ke = 0.3$ $(\epsilon = 5, \omega/N = 0.81$, Exp H_1 in Table 2.2). Theoretical predictions are shown with solid lines.

Hence, the contribution of the vertical velocity is larger than that of horizontal velocity. At moderate oscillation amplitude the regions of high velocity amplitude shift along the Z-axis away from the torus, increasing the cross-section of the wave cones which continue to propagate after focusing. This effect is most likely caused by the generation of a vertical mean flow in the focal zone for moderate oscillation amplitude, due to symmetry of the object and horizontal direction of oscillation. Filtered zero-frequency flow $\hat{W}_0$, averaged over 10 oscillation periods after reaching the stable regime 20 oscillation periods after the beginning of oscillations, is shown in Figure 4.6 (right column). This flow can represent either standing waves in the focal region or a mean flow propagating vertically away from the torus. For low oscillation amplitude the zero-frequency flow is negligibly small (Figure 4.6a, right column). With increasing oscillation amplitude this flow is generated in the focal zone and close to the torus, its maxima is $\hat{W}_0^* = \hat{W}_1^*/6$ (see Figure 4.6c). The mean flow in the focal zone can be responsible for local changes in the stratification and therefore, shift the focal zone vertically away from the torus.

The distributions of vertical and horizontal velocity amplitude along the direction ξ of the converging wave beam are shown in Figure 4.7(a) and (b), respectively, for the thick torus. Three different oscillation amplitudes are considered $Ke = 0.19$, 0.6 and 1.2. The results show a high velocity amplitude close to the torus, which slightly decreases due to viscous effects and subsequently increase due to focusing near the focal region. Due to the symmetry of the problem and the horizontal oscillations of the torus the vertical velocity amplitude is zero at the centre C of the focal zone and has two peaks on either sides. The horizontal velocity amplitude has its maximum in the centre C (note that for the vertically oscillating torus the structure of the horizontal and vertical velocity is converse). With increasing oscillation amplitude the nondimentional velocity amplitude in the focal zone grows (as in Figure 4.5*f*), but decreases beyond a certain value of Ke larger than 1. The possible explanations could be breaking of waves and loss of energy close to the torus or PIV calculations error for high velocity.

4.3.2 Wave pattern in the XY-plane

To study the azimuthal distribution of the wave amplitude, the wave fields in the XY-plane were reconstructed from series of images taken particularly in experiments G_2 and H_2 of Table 2.2. Figures 4.8 and 4.9 show the contours of wave amplitude ζ_1/A and associated radial distributions $\zeta_1(R)/(A\cos\phi)$ for the first harmonic wave close to the torus, with ϕ the angle with respect to the plane of symmetry. With this scaling, the data are found to collapse reasonably well on a more or less common curve, for both tori (see Figures 4.8*a* and 4.9*b*). We also note that the agreement with the linear theory presented in section 4.1.1 is within an error of about 10% for both cases. For the thick torus (see Figure 4.9*a*) the shape of the wave is slightly different due to its bimodal character. Also here the theoretical prediction remains quite reasonable (note that the original theory of Hurley & Keady (1997), used in section 4.1.1, takes this and related viscous effects into account). For larger oscillation amplitudes, the theoretical prediction is systematically higher than the measured values due to nonlinear effects that are shown to deform the straight wave rays (see Figures 4.3*c*). With increasing azimuthal angle ϕ the wave amplitude decreases and therefore also the energy radiated by the torus. The departure of the observed profiles for ϕ tending to 90° arises partially due to higher noise-to-signal ratio for these waves, and partially due to the fully three-dimensional nature of the flow. For azimuthal angles close to 90 degrees the cosine variation of the wave amplitude with the azimuthal angle is therefore no longer valid, especially for a thick torus.

4.4 Conclusions

In this chapter we presented an experimental study of linear and weakly nonlinear internal wave focusing by an oscillating torus. Experiments were performed for Stokes numbers between 150 and 260 implying weakly viscous regime. To characterise the focusing wave energy the Keulegan–Carpenter number Ke was used. Experimental profiles in the vertical plane of oscillation show that the horizontal and vertical velocities form one elliptic-shaped structure and two symmetric elliptic-shaped structures in the focal zone, respectively. The results show amplification of the wave amplitude toward the focal zone. The wave slopes close to the torus and in the focal zone are comparable. The experimental results were compared with the predictions of two linear theories. The first two-dimensional theory is based on the viscous theory of Hurley & Keady (1997) corrected for the convergence and divergence of the wave beams. Experiments and theory are in good comparison for the diverging

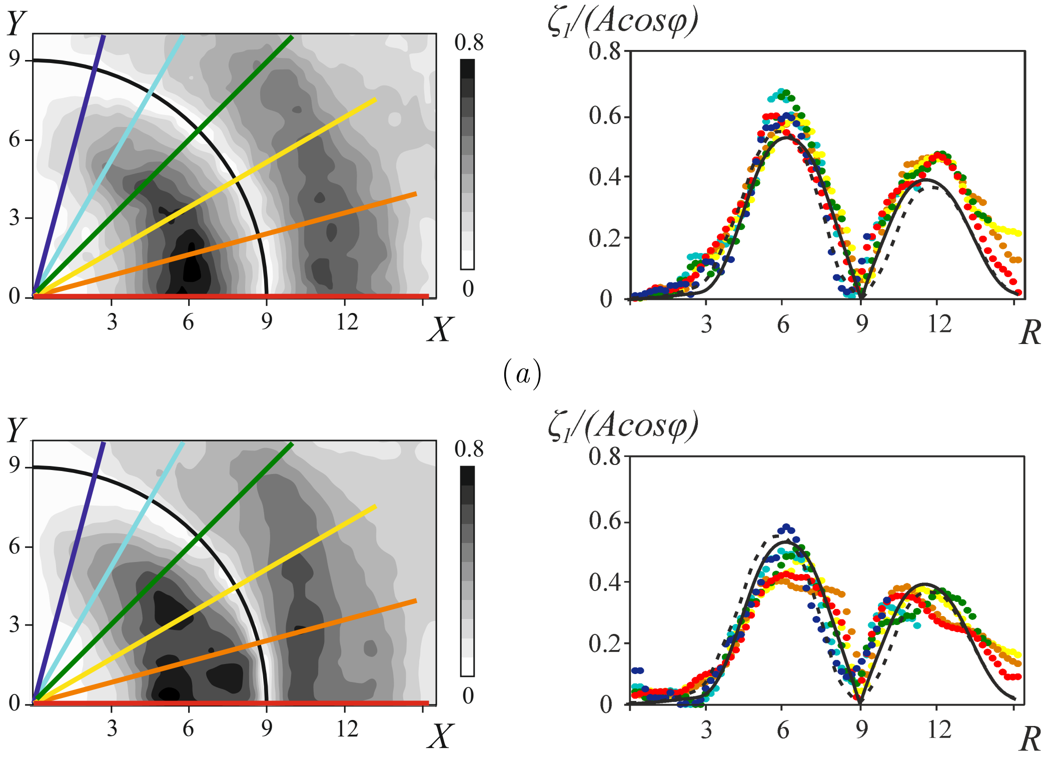

(*a*)

(*b*)

Figure 4.8: Contours of the normalized wave amplitude ζ_1/A (left panel) and the corresponding radial distributions $\zeta_1(R)/(A\cos\phi)$ (right panel) close to the thin torus ($\epsilon = 9$) at $Z = -3.6$ for (a) $Ke = 0.17$ and (b) $Ke = 0.63$, where $R = r/a$ is the non dimensional radial coordinate. The black solid line corresponds to eq. (4.7) and the dashed line corresponds to eq. (4.4). [Exp G_2 from Table 2.2]

wave beams and close to the torus, though the theory overestimates the amplitude in the focal zone. The second three-dimensional theory was inspired by the theory for an oscillating sphere (Voisin *et al.*, 2011). These calculations compare well with the experimental results. Azimuthal distributions of wave profiles have also been measured. It is found that the wave amplitude varies as the cosine of the azimuthal angle with good accuracy at low amplitude of oscillations in the case of the torus of aspect ratio 9, which can be considered as a sufficiently "thin" one. At lower aspect ratio, for the torus with $\epsilon = 5$, a fully three-dimensional theory is required.

The studies on internal wave generation by underwater ridges usually assume that the effect of curvature is small, and that the wave field can be evaluated from a two-dimensional theory applied locally to a selected cross-section of the bottom topography. Our case represents a model of a curved ridge which shows the importance of the focusing effect.

Further, as we increased the oscillation amplitude we observed that the focal zone shifted down away from the torus, possibly due to the generation of a mean flow in the focal region. Nonlinear wave amplitude amplification close to the torus

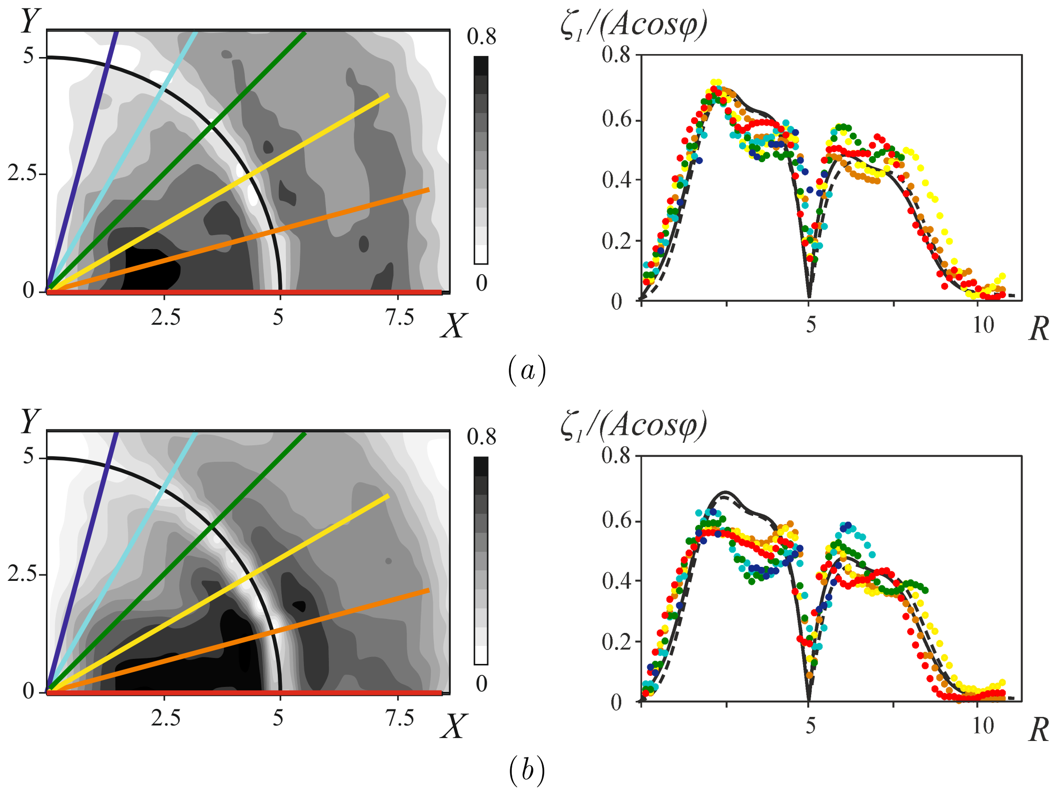

Figure 4.9: As in Figure 4.8 for the thick torus ($\epsilon = 5$), with (a) $Ke = 0.13$ and (b) $Ke = 0.29$ at $Z = -3.0$, where $R = r/a$ is the non dimensional radial coordinate. The solid black line corresponds to predictions of three-dimensional theory and the dashed line corresponds to eq. (4.4). [Exp H_2 from Table 2.2]

and in the focal zone, that is observed at moderate oscillation amplitude might cause local overturning and mixing. These strongly nonlinear aspects of wave focusing are considered in chapter 5.

Chapter 5

Internal wave focusing by a horizontally oscillating torus: nonlinear effects

In the previous chapter we have considered mainly linear aspects of wave focusing. For small oscillation amplitudes and limited variation in aspect ratio $\epsilon = b/a$, the Keulegan–Carpenter number Ke represented the variation in wave amplitude and slope well. Beyond a certain amplitude of oscillation ($Ke = 0.5$), nonlinear effects are expected which are considered in this chapter. In view of the different focusing effects with torus size we introduce a focusing wave number Fo, instead of the Keulegan–Carpenter number Ke, that takes into account the convergence of the waves. Wave amplitudes and isopycnal slopes are investigated as functions of Fo and show wave breaking at a critical value $Fo = 0.09$. The Richardson number Ri is defined in two ways, with the first based on the horizontal shear from PIV measurements and the second based on the baroclinic vorticity calculated from LIF results. The latter Richardson number appears to be proportional to the cotangent of the isopycnal slope S. The effect of wave breaking in the focal zone is considered together with the generation and structure of higher harmonics in the focal zone and close to the torus.

5.1 Wave breaking and mean flow

5.1.1 Maximum wave amplitude and overturning

We define the extreme values of the vertical displacement amplitudes ζ^*_{max}/a and ζ^*_1/a and isopycnal slopes S^*_{max} and S^*_1 in Figure 5.1 (see the definitions of ζ_{max}, ζ_1, S_{max} and S_1 in section 2.2.4). The variation of the maximum displacement and maximum slope with the Keulegan–Carpenter number Ke are presented in Figures 5.2(a) and (b), respectively, for both tori. The overall good agreement between ζ^*_{max}/a and ζ^*_1/a confirms, as mentioned in chapter 4, the dominance of the first harmonic wave. For larger Ke the increasing wave steepness and the increasing

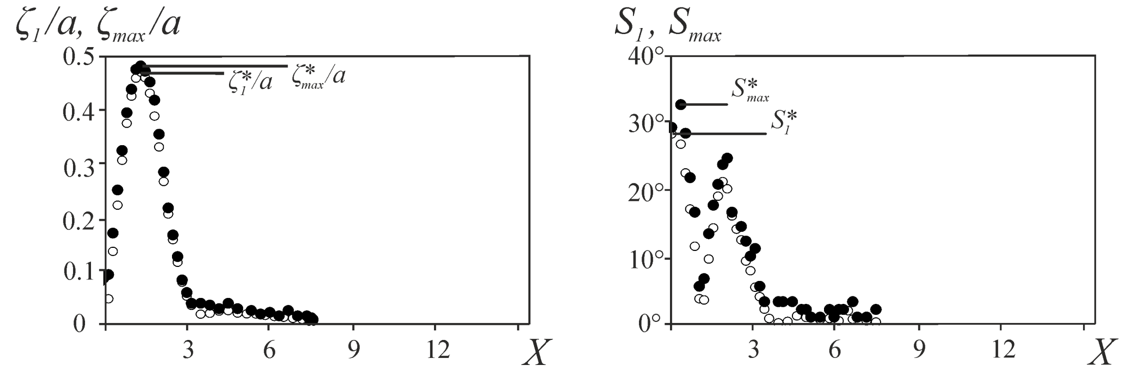

(a) (b)

Figure 5.1: LIF measurements of the amplitudes of (a) the vertical displacement and (b) the isopycnal slope in the central plane according to the definitions given in section 2.2.4 for the thin torus at $Ke = 0.41$. Open circles indicate the first harmonic filtered values (ζ_1/a, S_1) and filled circles the unfiltered max-type estimates (ζ_{max}/a, S_{max}). The represented level is the focal zone at $Z = -11.2$ for $0 < X < 6$ (open and filled circles). The symbol $*$ refers to the extrema plotted in Figure 5.2. [Exp G_1 from Table 2.2]

difference between S^*_{max} and S^*_1 (see Figure 5.2b) suggest the presence of nonlinear effects. From the experimental images incipient overturning is observed at $Ke = 0.81$ and $Ke = 1.1$ for the thick and thin tori with $\epsilon = 5$ and $\epsilon = 9$, respectively (see Figure 5.3).

To characterize the forcing of internal waves we used the Keulegan–Carpenter number. Although this number remains relevant close to the torus, it does not take into account the geometric effect of focusing at larger distances from the torus since the torus radius b introduces an extra dimension that is relevant for the wave amplitude. Supposing that the oscillation region can reduce to a minimal radius a, the amplitude may increase to $\zeta_{corr} = \zeta_{HK}(b/a)^{1/2} = \zeta_{HK}\epsilon^{1/2}$ i.e. with a factor $\epsilon^{1/2}$ due to focusing (see the theoretical considerations in section 4.1.1). As mentioned in chapter 4, for a Gaussian-shaped torus, Bühler & Muller (2007) obtained the same increase of the amplitude with $\epsilon^{1/2}$. Conversely, to generate a wave with this amplitude in the focal zone with an object that is simply connected in space, the object should oscillate with amplitude $\zeta_{corr}\epsilon^{-1/2}$. Taking further into account the variation of the displacement amplitude with the propagation angle as $\sin^{1/2}\theta\cos\theta$ for the generation at each cylindrical cross-section (see Voisin *et al.*, 2011), we obtain instead of the Keulegan–Carpenter number a number Fo for an imaginary object in the focal zone,

$$Fo = \frac{A}{a}\left(\frac{b}{a}\right)^{-1/2}\sin^{1/2}\theta\cos\theta = \frac{A}{a}\epsilon^{-1/2}\sin^{1/2}\theta\cos\theta.$$

For $\omega = 0$ and $\omega = N$, the focusing effect tends to zero and it is maximal for $\theta = 45^o$. We will call this number the focusing wave number.

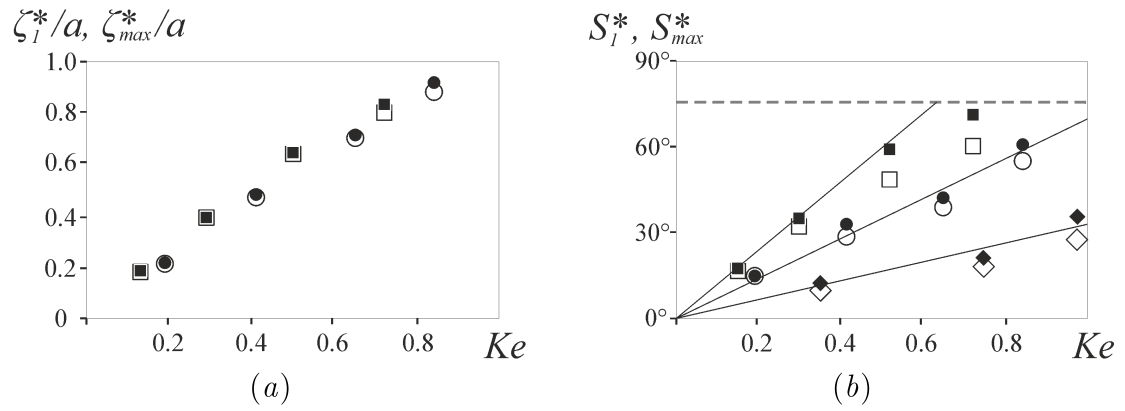

Figure 5.2: Maximum (*a*) vertical displacement and (*b*) maximum isopycnal slope against *Ke*. Filled and open symbols are as in Figure 5.1 with circles for the thin torus at $Z = -11.2$, squares for the thick torus at $Z = -7$, and diamonds for the big torus at $Z = -45$.

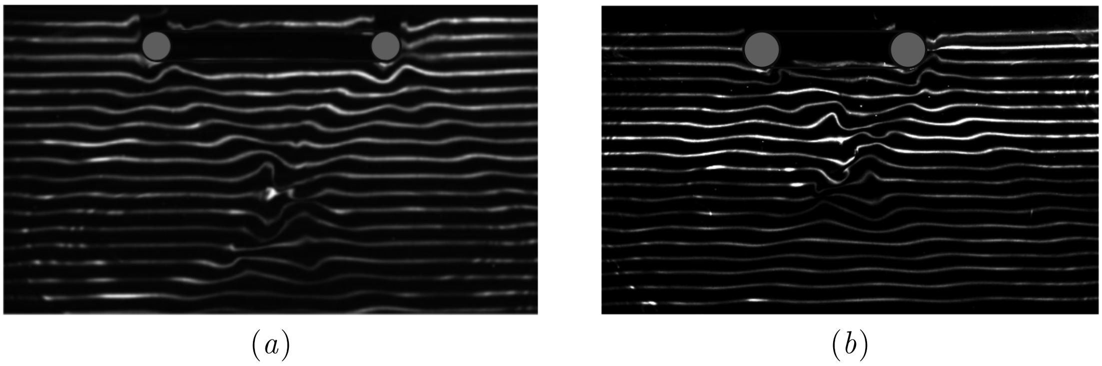

Figure 5.3: Dye visualisation (before data processing) of the overturning of the isopycnal lines in the plane of symmetry for experiments with large-amplitude oscillations, for (*a*) the thin torus at $Ke = 0.818$ and (*b*) the thick torus at $Ke = 1.1$; in both cases $Fo \approx 0.09$.

The evolution of the maximum isopycnal slope against *Fo* is presented in Figure 5.4(*a*). The focusing number includes corrections for the focusing of wave energy and the direction of propagation. It depend on the major radius of the torus *b*, and therefore the isopycnal slopes obtained for all three tori with $\epsilon = 5$, 9 and 34 collapse on one line. This result suggests the focusing number as an appropriate nondimensional parameter for converging waves when the oscillation amplitude is large. The trend in the data in Figure 5.4(*a*) clearly shows that wave breaking can be expected for $Fo = 0.22$. Indeed, from the dye images shown in Figure 5.3, we recognise well-developed overturning regions in the wave pattern. As expected, these regions are located close to the surface of the torus and in the focal region, corresponding to the zones of high local slopes which can be identified in Figure 4.3.

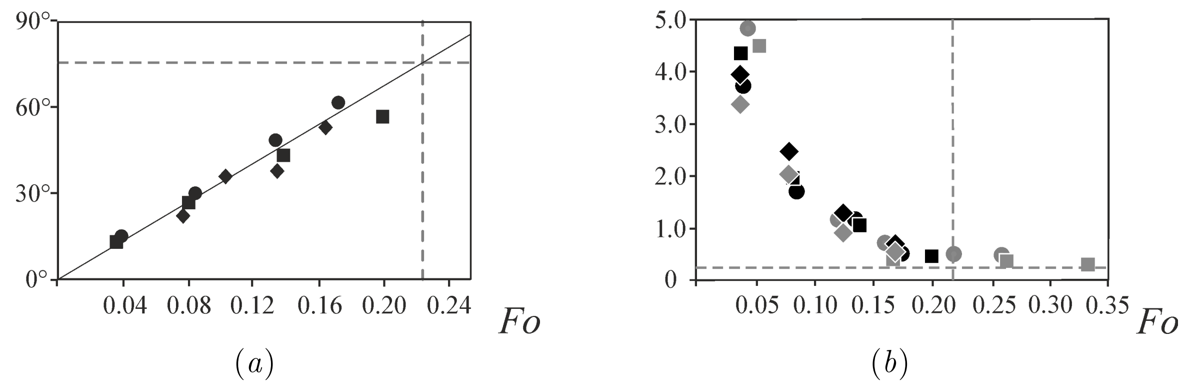

Figure 5.4: (*a*) Same as Figure 5.2(*b*), but against *Fo*. (*b*) Richardson numbers *Ri* from PIV data (grey symbols) for experiments G_3 (circles), H_3 (squares) and K (diamonds), and Ri_{wave} from LIF data (black symbols) for experiments G_1 (circles), H_1 (squares) and K (diamonds) with parameters given in Table 2.2. The vertical gray lines denote the value of *Fo* corresponding to the onset of overturning.

5.1.2 Richardson number

With the PIV data in the focal region, the horizontal shear and thus the local Richardson number in the wave can be calculated as

$$Ri = \frac{N^2}{(\partial \hat{u}_1/\partial z)^2},$$

where the stratification N is measured at the start of the experiment; the vertical gradient in velocity is measured from the PIV velocity data over a typical grid distance of $\Delta z = 4$ pixels (≈ 0.3 cm). The values of this number are displayed in grey in Figure 5.4(*b*). Asymptotic limit of $Ri \approx 0.25$, corresponding to overturning in stratified shear flows (see Miles, 1961), is reached when the focusing wave number *Fo* approaches a value between 0.20 and 0.25 for tori of different aspect ratios.

Miles criterion was developed for a flow with vorticity due to the presence of a shear flow, and no baroclinic vorticity in its basic state. For the critical value of $Ri = 0.25$, vorticity of the shear flow is accumulated by the Kelvin–Helmholtz instability until breaking occurs. In the present experiments there is no shear flow, and the instability is not of the Kelvin Helmholtz type. However, the amplitude of the waves is represented by baroclinic vorticity. This amplitude (or baroclinic vorticity) is continuously increased due to the focusing of wave energy, until the critical value is reached and breaking occurs. Though the sources of vorticity and mechanism for overturning are essentially different, the present results suggest that the criterion and, as shown below, the critical value are the same.

The LIF method allowed to precisely measure the isopycnal slope S expressed in degrees after taking arctan, for the tori of different aspect ratios. Observations of visualizations showed a nearly linear dependence for $Fo < 0.15$ with the waves remaining linear and passing almost without modification through the focal region.

Small changes with respect to the linear regime were found to occur for *Fo* around 0.15, whereas for approximately $Fo > 0.22$ the onset of wave breaking was observed and the waves were hindered to pass through the focal region. From this isopycnal slopes one can derive directly the local wave-Richardson number which can be defined as the ratio between the buoyancy frequency, N^2, and the y-component of the baroclinic vorticity of the wave, yielding in the Boussinesq approximation

$$Ri_{wave} = N^2 \left(\frac{\nabla p \times \nabla \rho}{\rho^2} \right)_y^{-1} \approx \frac{N^2}{-g\rho \frac{\partial \rho}{\partial x}} = \frac{\Delta x}{\Delta z}\Big|_{\rho=\mathrm{const}} = \frac{1}{S}$$

where the index y indicates the y component of the baroclinic vorticity vector. In Figure 5.4(b) the wave Richardson number is displayed as a function of the focusing wave number *Fo*. Even though it is derived in a different manner, it shows also that wave breaking is reached when $Ri_{wave} \approx 0.25$ at $Fo \approx 0.22$ in coherence with the observations from the PIV measurements and shear instability. This local Richardson number indicates the maximum slope which an isopycnal plane may have before it becomes unstable and overturns. This overturning is found to occur for an isopycnal slope of $S \approx 75°$ (see Figure 5.4b), where the slope is measured over a horizontal lengthscale δx (see section 2.2.4) near $X = 0$.

5.1.3 Effects of wave breaking in the focal zone

In order to investigate the wave pattern in the focal zone of the first harmonic wave, the spatio–temporal evolution was recorded for a line across this zone, and represented in so-called Hövmöller (space–time) diagrams in Figures 5.5(a,b). For small oscillation amplitudes (see Figure 5.5a, $Fo = 0.3$) the wave pattern can still be considered linear and this region represents a standing wave. The corresponding energy spectrum shows that all the energy is in the first harmonic wave (see Figure 5.5c). For large oscillation amplitudes corresponding to $Fo = 0.3$, however, the wave breaking in the focal region is found to emit a specific wave spectrum with most energy again in the first harmonic wave, and a non negligible signal of higher harmonics (see Figure 5.5b and d). Note that since $\omega/N = 0.6$, these higher harmonics are evanescent in contrast to the propagating waves shown in Figure 5.7. The energy in the second harmonic evanescent wave is about 1/5th of the first harmonic wave, corresponding to the ratio in the velocity amplitudes represented in Figure 5.5. The energy of the higher harmonics appears to decrease almost exponentially with the harmonic order. Further details of this spectrum and the turbulence in the focal region will be considered in chapter 6.

5.2 Higher harmonics

When oscillations take place at the frequency ω, in addition to the fundamental first harmonic wave at frequency ω, the dispersion relation admits the radiation or higher harmonic waves with frequencies $n\omega$, where $n = 2, 3 \ldots$ and $n\omega < N$ (see Mowbray

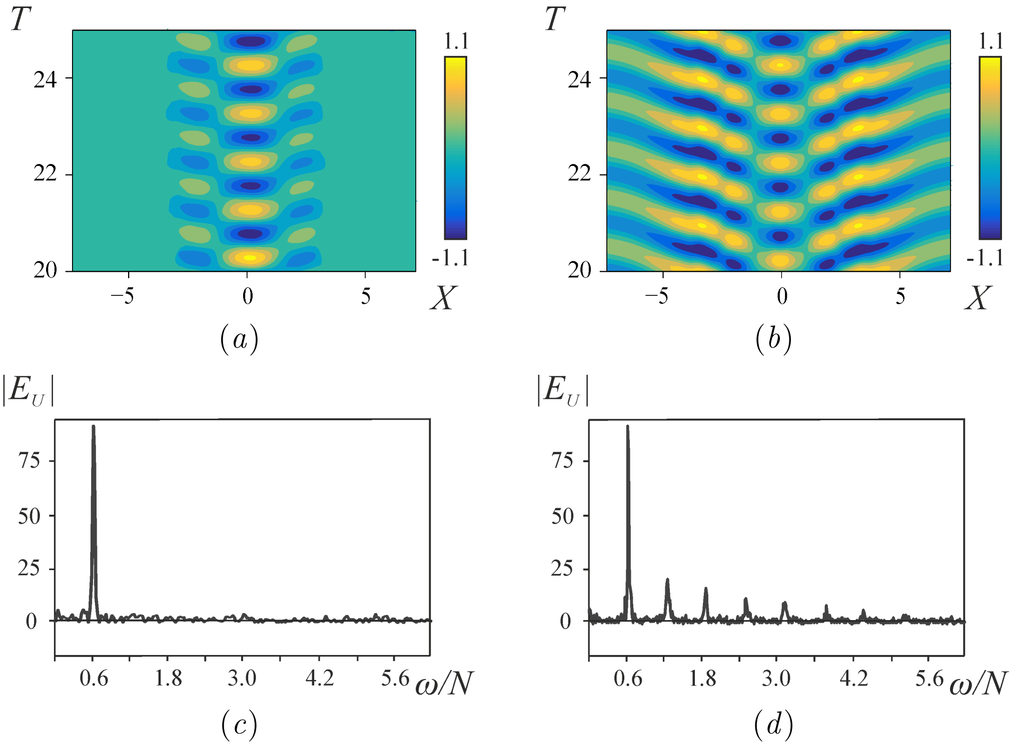

Figure 5.5: Spatio–temporal (Hövmöller) diagram of the horizontal velocity in the focal zone ($Z = -6.7$, $Y = 0$) for the thick torus with (*a*) $Fo = 0.072$, and (*b*) $Fo = 0.3$, for $\omega/N = 0.6$. Five periods of the first harmonic wave are presented starting from the 20^{th} period, when the steady regime has been reached. Images (*c*) and (*d*) represent the variations of the energy spectrum $|E_U|$ normalized with the velocity of oscillation with the nondimensional frequency ω/N. [Exp *J* from Table 2.2]

& Rarity, 1967). For $\omega > N/2$ all higher harmonics are evanescent but for $\omega < N/2$ some of them are able to propagate. Here, experiments with $\omega/N < 0.5$ allows us to study the focusing of both first and second harmonic waves.

5.2.1 Vertical structure

Unlike the case of an isolated wave beam, nonlinear effects can turn out to be particularly important in the case of beam intersection. Filtering the frequency 2ω reveals an evanescent second harmonic localized in the focal region for moderate amplitude of oscillation, $Ke = 0.78$, as shown in Figure 5.6. Tabaei *et al.* (2005) and Jiang & Marcus (2009) have studied in detail the different structures of colliding waves and secondary beams resulting from their quadratic interactions. The angle between the fundamental wave and the second harmonic wave has to be

$$\theta_2 = (\theta_1^1 - \theta_1^2)/2$$

(Tabaei *et al.*, 2005), where θ_1^1 and θ_1^2 are the angles between the group velocity vectors of the fundamental waves and the horizontal plane. In the present configuration, the focal region consists of four interactions described in Tabaei *et al.* (2005), each causing the appearance of secondary beams. In the present experimental conditions the angle θ_1^1 between the fundamental waves and the horizontal is close to 45°, so that the angle θ_2 between the second harmonic wave and the horizontal plane is 90° (see the schematic picture in Figure 5.6c). The observations of the second harmonic wave in the focal zone is in agreement with those theoretical predictions.

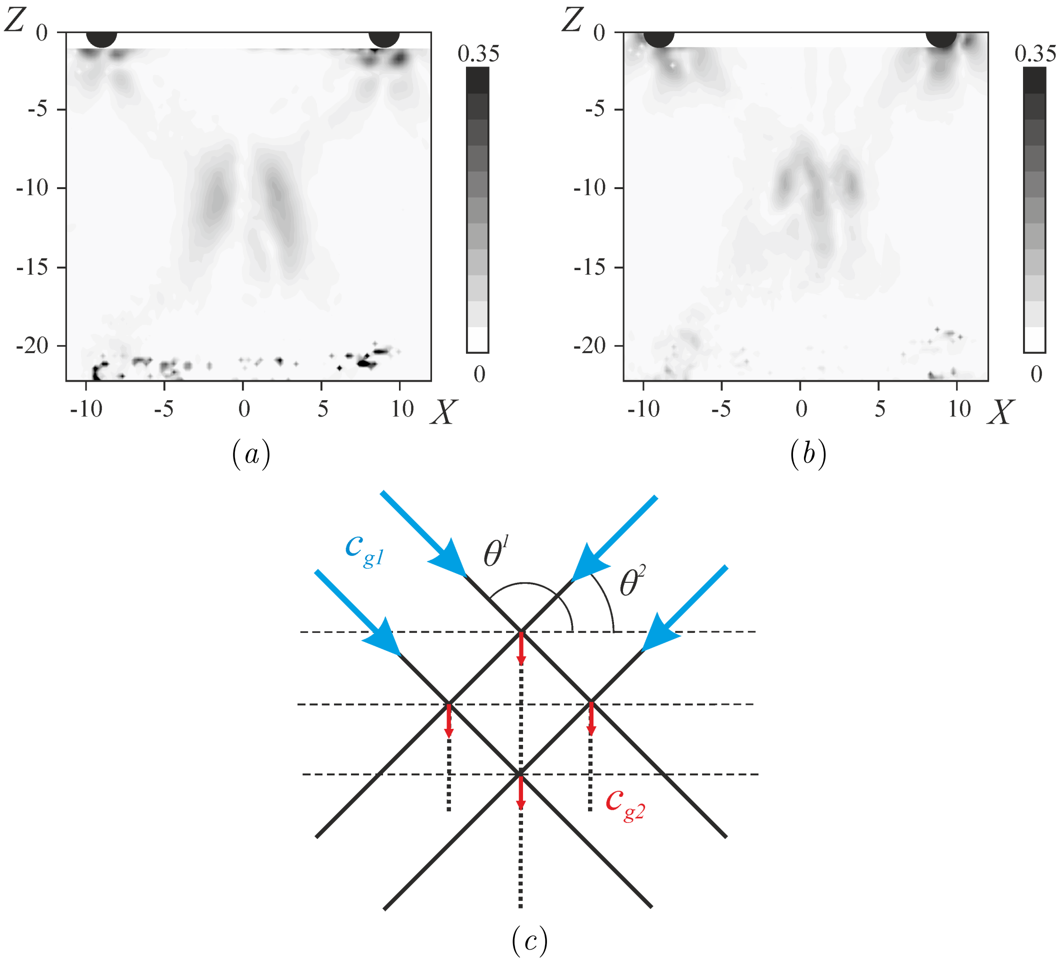

(a) (b)

(c)

Figure 5.6: Distributions of the second harmonic of (a) the horizontal velocity amplitude $\hat{U}_2$ and (b) the vertical velocity amplitude $\hat{W}_2$. (c) Schematic predictions of higher harmonic generation in the zones of primary beam intersections according to theory of Tabaei *et al.* (2005) and corrections of Jiang & Marcus (2009); blue and red arrows correspond to the group velocity vectors c_g1 of the first and c_g2 of the second harmonic wave. [Exp G_3 from Table 2.2]

For effective generation of a propagative second harmonic the oscillation frequency was tuned to $\omega/N = 0.42$. Figure 5.7(a) shows the wave pattern that we may expect for the first harmonic together with the observed filtered first harmonic displacement amplitude from the LIF measurements for the thick torus, with a neat amplification of the amplitude in the focal zone. The second harmonic component produces a significant contribution to the total wave field (see Figure 5.7*b*). The lines indicate the expected second harmonic wave pattern and the waves expected from wave intersections (see Tabaei *et al.*, 2005). Only the wave rays with negative vertical group velocity which allow for the generation of secondary beams are represented (Jiang & Marcus, 2009). The second harmonic wave has a maximum amplitude that is 2.3 times smaller than that for the first harmonic, and is present over a much larger area; it is therefore not less important. From the vertical and horizontal structure of this second harmonic, displayed in Figures 5.7(*b*) and (*c*), respectively, we notice that the second harmonic wave maxima has a complicated structure. It appears difficult to explain the observed second harmonic waves with the intersections of the first harmonic waves. The details of these intersections will be investigated in more detail in the next section. Well below this region (at $Z = -7$ to -10) the second harmonic wave has a quadrupolar structure.

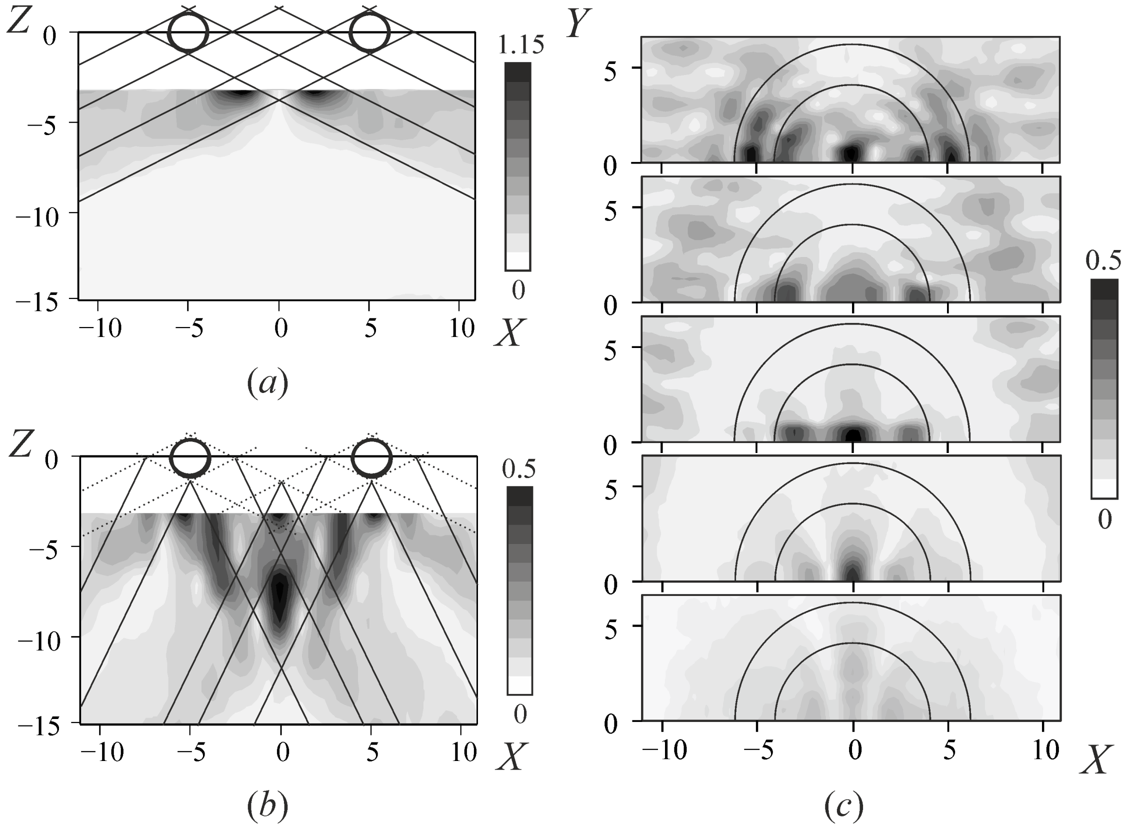

Figure 5.7: Side views of the experimental ray pattern (grey contours) and expected ray pattern (lines) for (a) the first harmonic amplitude ζ_1/A and (b) the second harmonic amplitude ζ_2/A emerging respectively from the oscillating torus and ray intersections, for the thick torus at $\omega/N = 0.41$ and $Ke = 0.58$; (c) Top views of the second harmonic amplitude ζ_2/A at the levels $Z = -3$, -5, -7, -9 and -11 from top to bottom. [Exp I from Table 2.2]

5.2.2 Horizontal structure

For detailed investigations of the second harmonic generated close to the torus (as in the upper image of Figure 5.7*c*) complementary PIV experiments with a horizontal laser sheet have been performed for the thin torus oscillating with frequency $\omega/N = 0.39$. Figure 5.8 shows their results at the zone of first harmonic beam intersection ($Z = -3$) in terms of the amplitudes of the longitudinal horizontal velocity $\hat{U}$ (upper row), and the transverse horizontal velocity $\hat{V}$ (lower row). The first harmonic is presented in the left column. The zone of amplification of the longitudinal velocity is clearly seen at the centre of the focal region (Figure 5.8*a*) and has an elliptic shape. The transverse component has a clover-like structure in the focal zone with zero velocity amplitude in central planes parallel and perpendicular to the direction of oscillation (Figure 5.8*c*, $Y = 0$, $X = 0$). These features of the transverse velocity component have been used in section 4.3 for the calculations of the total velocity in the central plane parallel to the direction of oscillation ($Y = 0$).

The time-frequency spectrum (see section 3.3.2, equation 3.4) for two horizontal components of the velocity shows higher harmonic generation in the focal zone of the fundamental wave (see Figure 5.9). The first and second harmonics are propagative, whereas all higher harmonics are evanescent. Starting from the second harmonic, a small variation of the frequency with time can be noticed; first and second harmonics start to be generated at $t = 0$, while the third and higher harmonics appear later after 4 to 10 oscillation periods. One can notice a temporary generation of waves of frequencies $\omega_{i^*} = 0.22, 0.44, 0.66\ldots$. The contribution of these waves to the flow field is negligible comparing to the first and second harmonic. Their generation mechanism is not clear.

Figure 5.10 shows the Hövmöller diagrams for the horizontal velocity component $\hat{U}$. For the first harmonic, standing waves are obtained in the focal zone as described in sections 4.3 and 5.1. The time-space diagram for the second harmonic is presented as a key to understand its structure in the focal zone of the fundamental waves. The phase velocity vectors in Figure 5.10(*b*) show that the second harmonic waves are generated below the torus and in the focal zone, which is in agreement with the structure obtained in Figures 5.7(*b,c*). In the horizontal plane $Z = -3$ the amplitude of these second harmonics is as in the right column of Figure 5.8.

5.3 Conclusions

In this chapter we have considered the nonlinear aspects of internal wave focusing. To characterise the wave field in relation to the forcing, the focusing wave number Fo has been introduced. For different levels in the fluid and for tori of different sizes, the isopycnal slope measurements have been found to collapse as a function of this number. A linear wave regime has been discerned for $Fo < 0.04$, whereas non-linear effects start to occur at values close to $Fo \approx 0.04$. Wave breaking occurs for $Fo \approx 0.09$, corresponding to a local (shear) Richardson number $Ri = 0.25$, in accordance with the classical theory of shear instability. This value coincides with

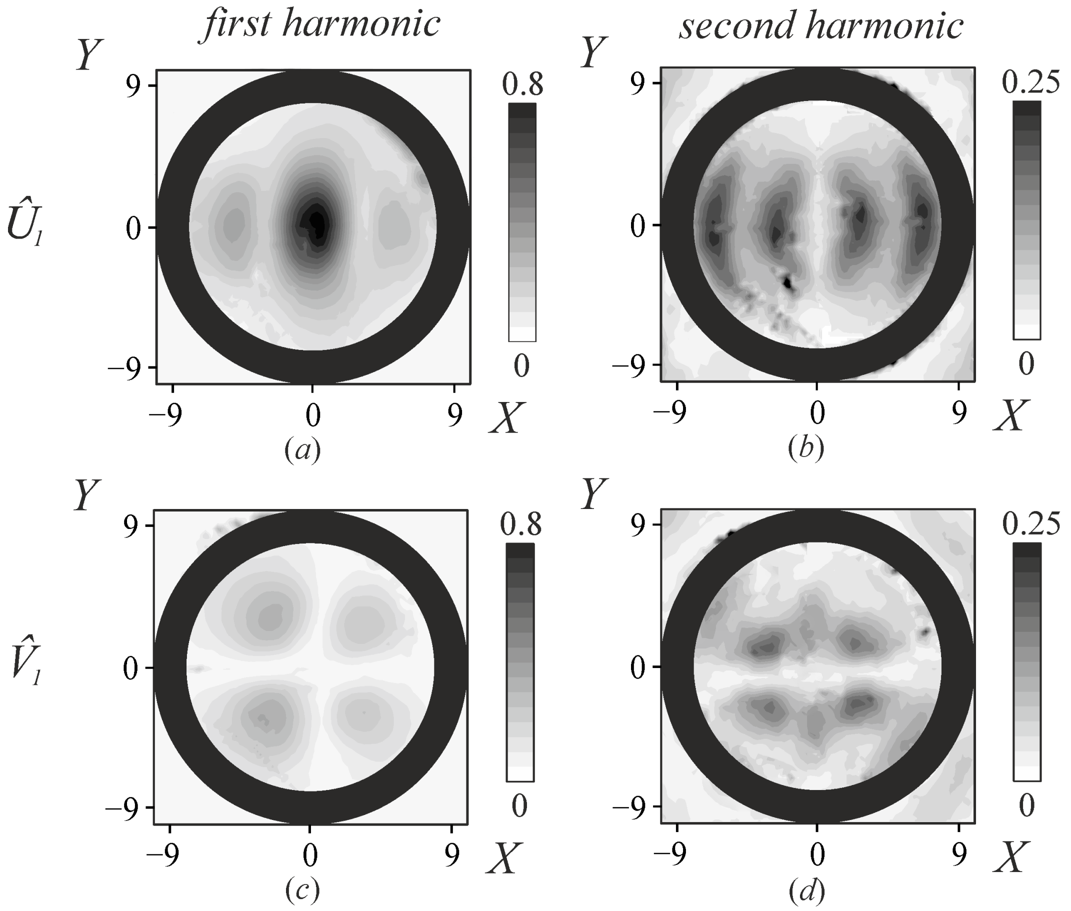

(*a*) (*b*) (*c*) (*d*)

Figure 5.8: Amplitude patterns for the first harmonic (left column) and the second harmonic (right column); (*a*,*b*) the longitudinal horizontal velocity $\hat{U}$ and (*c*,*d*) the transverce horizontal velocity $\hat{V}$. Black circles indicate the position of the thin torus. Measurements are taken in the zone of first harmonic intersection at $Z = -3$. [Exp *L* from Table 2.2]

the Richardson number calculated from the wave steepness. Wave breaking occurs for an isopycnal slope of $\theta = 75°$.

When the waves break in the focal region, radiation of waves has been observed away from the focal zone. In addition, higher harmonics are generated in the focal region. The evanescent and propagative second harmonics generated at the intersections of the fundamental (first harmonic) waves have been studied in some details. Their generation is in agreement with the theory of Tabaei *et al.* (2005) corrected by Jiang & Marcus (2009). The propagating second harmonic waves focus as well, resulting in a complex vertical and horizontal structure. The amplitude amplifies in the focal zone. The maximum amplitude of the second harmonic waves in the focal region is found to be about 2.3 times weaker than that of the first harmonic wave.

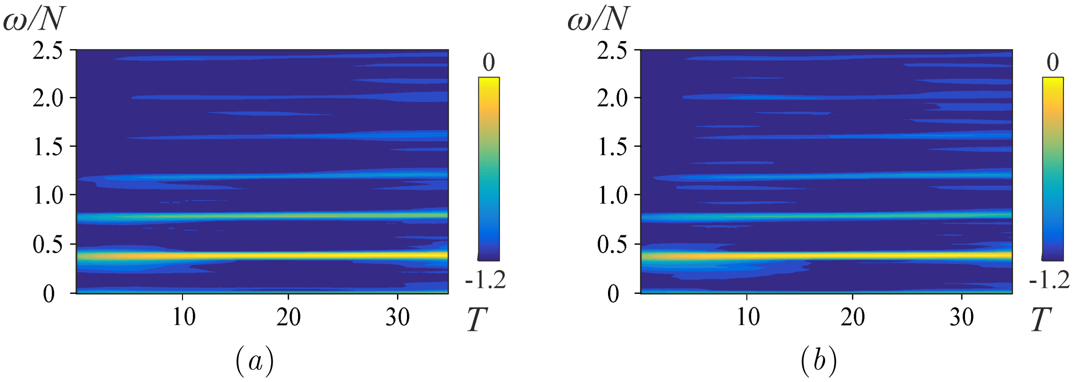

(*a*) (*b*)

Figure 5.9: Time–frequency spectra $\log_{10}(Q_{u,v}(t,\omega)/Q_0)$ for the (a) longitudinal velocity component $\hat{u}$ and (b) transverse velocity component $\hat{v}$ in the focal zone $Z = -3$ for the thin torus, with Q defined by equation (3.4) and $Q_0 = \max[Q_{u,v}(t,\omega_1)]$. [Exp L from Table 2.2]

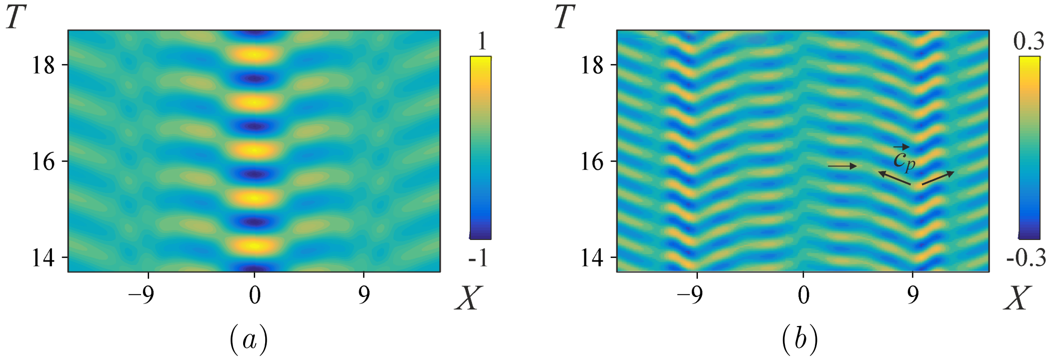

(*a*) (*b*)

Figure 5.10: Spatio-temporal (Hövmöller) diagram for (a) the first and (b) the second harmonic of the longitudinal horizontal velocity $\hat{U}$ in the focal zone ($Z = -3$, $Y = 0$) for the thin torus. The data are presented for five periods of oscillation starting from the 14^{th} when the steady regime has been reached. Black arrows show the phase velocity vectors. [Exp L from Table 2.2]

Chapter 6

High Stokes number wave focusing by a circular ridge: Internal, inertial and inertia–gravity waves[*]

Wave focusing by a horizontally oscillating torus is considered as a possible scenario for energy concentration in localized zones representing hot spots for incipient overturning in the oceans. Important mixing of stratification due to internal wave focusing has been observed by Buijsman *et al.* (2014) in Luzon Strait in the South China Sea, and may be a cause for the mixing observed by Peliz *et al.* (2009) at Tore Seamount in the West Iberia Margin.

First experiments on geometric focusing have been conducted by Duran-Matute *et al.* (2013) who obtained wave turbulence in the focal region for a vertically oscillating torus in a rotating fluid. In chapter 4 we showed with a horizontally oscillating torus in a linearly stratified fluid that at low Stokes numbers $St \approx 200$ the wave amplitude increases toward the focal region, forming one zone of amplitude amplification. In this zone one expects overturning and mixing of waves.

The present experimental results were obtained for a much larger torus of minor radius $a = 15$ cm and major radius $b = 75$ cm mounted at the Coriolis platform, of 13 m diameter, giving access to large Stokes numbers $3800 < St < 6800$. They report some new aspects of the dynamics of internal focusing waves in rotating and stratified fluids, and the possibility of wave breaking in the focal region.

Internal waves are generated according to the dispersion relation

$$\omega = \sqrt{f^2 \sin^2 \theta + N^2 \cos^2 \theta}, \tag{6.1}$$

with θ the angle between the wave beam and the vertical. Depending on whether the fluid is stratified and still ($N \neq 0, f = 0$), or stratified and rotating ($N \neq 0, f \neq 0$), or homogeneous and rotating ($N = 0, f \neq 0$), we shall refer to the waves as internal gravity, inertia–gravity or inertial, respectively. In the present

---

[*] This chapter is a complemented version of the communication "High Stokes number wave focusing by a circular ridge: Internal, inertial and inertia–gravity waves" presented at the 8th (San Diego, *Int. Symp. Strat. Flows*, August 29–September 1, 2016) and reproduced in Appendix C

experiments we consider the angle θ to be fixed ($\approx 60°$) for all types of waves for better comparison. In the case of internal gravity waves this angle corresponds to $\omega/N = \arccos\theta = 0.51$, so that all harmonics but the first are evanescent (Mowbray & Rarity, 1967).

6.1 Internal gravity waves

6.1.1 Comparison with the linear theory

The linear theory described in Voisin (2016) and recalling in section 4.1.2 allows us to calculate the amplitude of internal gravity waves which may be expected for high Stokes number $St = (\omega a^2)/\nu = 4500$, with $\nu = 0.01$ cm^2/s the molecular viscosity. These results are presented in Figure 6.1 (a) for the horizontal $\hat{U}_1$ and vertical $\hat{W}_1$ velocity components in the vertical plane $Y = 0$, and show the bimodal structure of the wave beams. Comparing the theory in Figure 6.1(a) with the experimental results in Figure 6.1(c), one notices a difference in structure. This difference can be caused by mixing in the turbulent boundary layer at the surface of the torus. The theoretical formulas can be therefore recalculated with an eddy viscosity $\nu_{eddy} = 0.4$ cm^2/s $\gg \nu$. The eddy viscosity was selected manually in accordance with two criteria: the maximum velocity value and thickness of the focal zone (see Figure 6.2). The results are presented in Figure 6.1(b) and show slightly better agreement with the experiment in Figure 6.1(c): in both, the focal zone is formed of two zones of amplitude amplification at the centre for the horizontal velocity and four zones of amplitude amplification for the vertical velocity. But the beams in the experiments remain narrower than predicted with the theory, and the focal region is confined to an area two times smaller.

Another specificity of the experimental wave beams is the origin of generation. The upper critical ray delimiting the wave beam is vertically shifted downwards compared with the theoretical calculations, and with the experimental and numerical observations for a hemisphere (King *et al.*, 2009). As a consequence, the upper part of the focal zone is lower than predicted. This shift is caused by the turbulent motion close to the surface of the fluid and to the mounting plate (as also observed for the prolate spheroid in chapter 3). However the lower part of the focal region is well predicted by the linear theory calculated with the eddy viscosity ν_{eddy} (see Figure 6.1b and c at $Z = -3$ for the horizontal velocity and $Z = -2.5$ for the vertical velocity).

6.1.2 Effects of increasing oscillation amplitude

The evolution of the first harmonic velocity patterns for different oscillation amplitudes Ke is presented in Figure 6.3 in terms of the velocity amplitude for the oscillation frequency $\omega/N = 0.51$. For the low oscillation amplitude, $Ke = 0.16$, the velocity amplitude is strongly amplified in the focal zone. Surprisingly, in contrast to the observations for low Stokes numbers in chapter 4, the normalised velocity

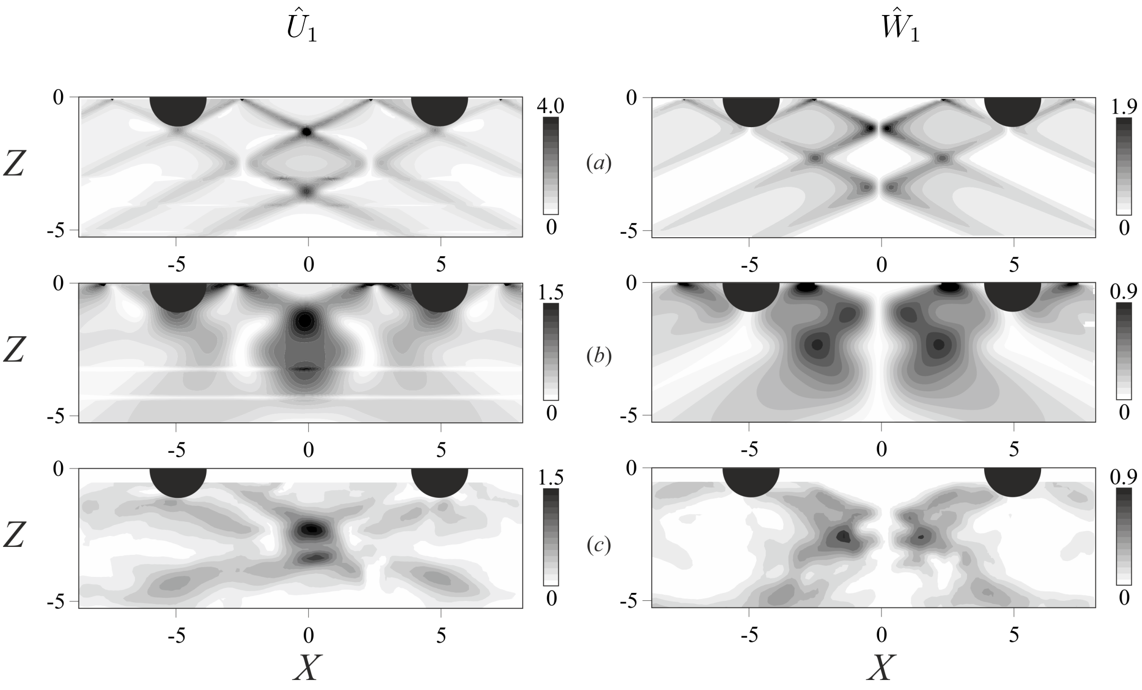

Figure 6.1: Horizontal velocity amplitude $\hat{U}_1$ (left column) and vertical velocity amplitude $\hat{W}_1$ (right column) for internal gravity waves in the vertical plane of symmetry $Y = 0$ at $Ke = 0.17$: (a) theoretical predictions based on molecular viscosity; (b) theoretical predictions based on an eddy viscosity $\nu = 0.4$ cm^2/s; (c) experimental results after filtering the first harmonic. The occurrence of spurious maxima at $Z = 0$ in the theory is discussed in Voisin (2016). [Exp 1.3 from Table 2.3]

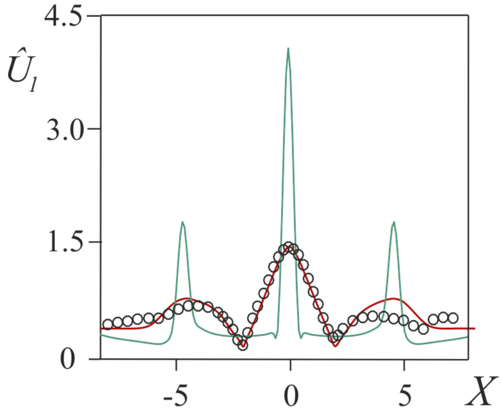

Figure 6.2: Comparison of the horizontal velocity amplitude $\hat{U}_1$ obtained experimentally (black circles) with predictions of the linear theory calculated with the molecular viscosity $\nu = 0.01$ cm^2/s (green line) and with an eddy viscosity $\nu = 0.4$ cm^2/s (red line). The data are presented at Z corresponding to the highest value of the velocity amplitude, i.e $Z = -1.5$ for the theory and $Z = -2.2$ for the experiment.

amplitude in the focal region decreases as the normalised oscillation amplitude Ke increases. Most likely energy loss is caused by wave breaking in the focal region and close to the object. Also the structure of the focal region is different: the two zones of amplitude amplification of the horizontal velocity amplitude merge into one, and the four zones of amplitude amplification of the vertical velocity shift along the wave beams away from the centre (see Figure 6.3). Mean flow is generated in the focal zone, its structure being similar to that obtained in chapter 4 for the vertical velocity. In the present experiments also the horizontal mean flow is nonzero (Figure 6.4). From this point onwards only experimental results obtained at low oscillation amplitude $Ke = 0.17$ will be presented in the rest of this chapter.

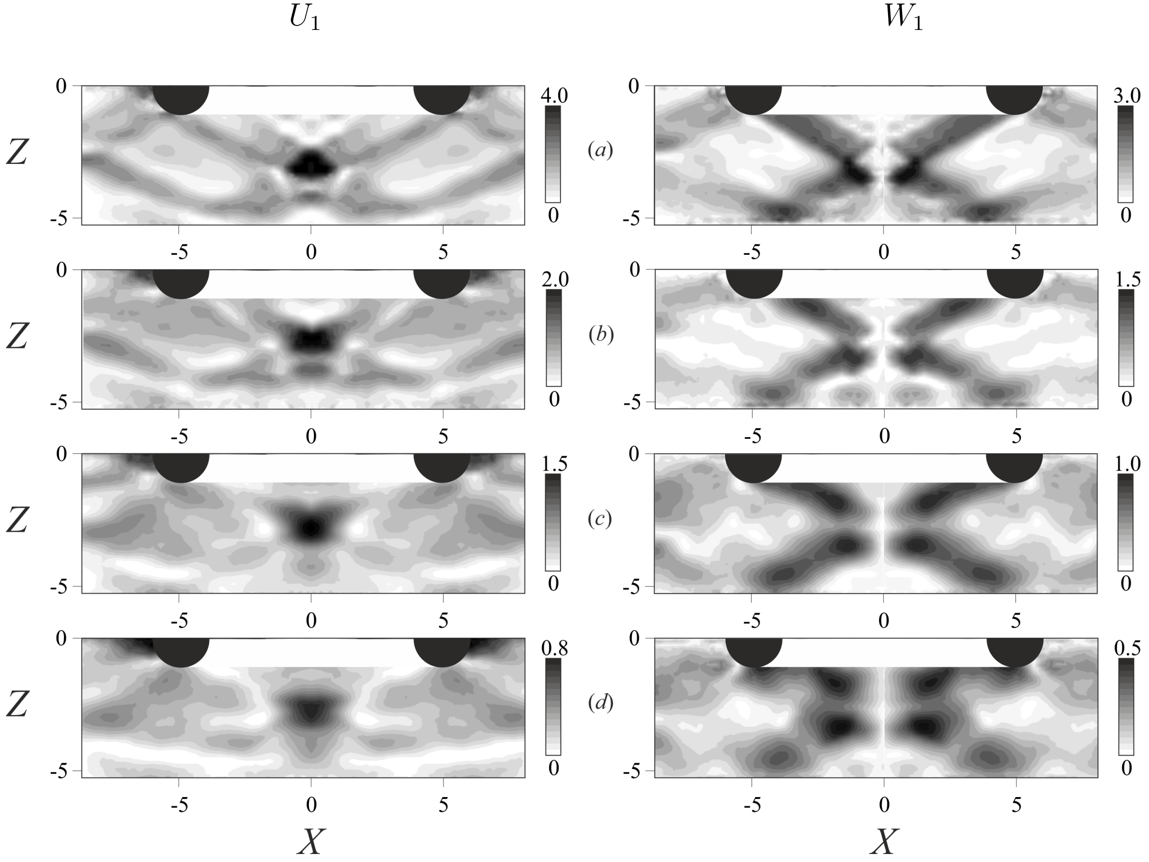

Figure 6.3: Amplitude patterns of the horizontal velocity $\hat{U}_1$ (left column) and the vertical velocity $\hat{W}_1$ (right column) in the vertical plane of symmetry $Y = 0$ with $Ke = 0.17$, 0.33, 0.66 and 1 From top to bottom. [Exp 1.2 from Table 2.3]

6.2 Vorticity field

The difference between the internal waves generated in stratified and/or rotating fluid is studied by considering the horizontal and vertical vorticity fields. In the

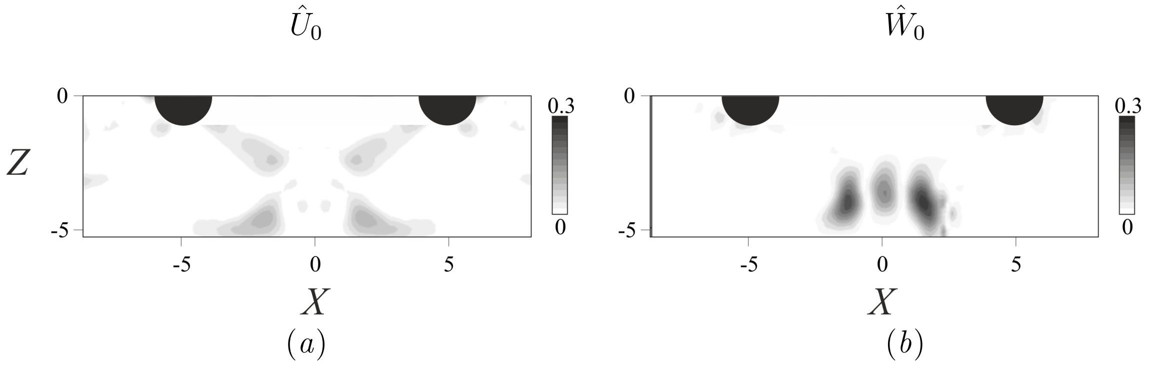

(a)

(b)

Figure 6.4: Amplitude patterns of the (a) horizontal velocity $\hat{U}_0$ and (b) vertical velocity $\hat{W}_0$ of the mean flow in the vertical plane of symmetry $Y = 0$, for $Ke = 0.66$. [Exp 1.2 from Table 2.3]

presence of rotation (Figure 6.5*b*), inertia–gravity wave motion is found over a bigger region than for internal gravity waves. This is because the waves propagate in beams, with edges at the critical rays tangent to the torus and to its image at the surface. For inertia–gravity waves, these rays turn out to be further apart than for internal gravity waves. The reason for this is unclear, but seems connected with the boundary layer at the mounting plate supporting the torus, since this is where reflection takes place. As a consequence, there are four clearly identifiable separate zones of critical ray intersection in Figure 6.5(*b*), compared with one single diamond-shaped zone of intersection of wave beams in Figure 6.5(*a*). The vertical vorticity field of internal gravity waves exhibits a dipolar structure in the focal zone, which transforms for inertia–gravity waves into a "Yin–Yang-shaped" structure (Figure 6.5*d,e*). The overall structure of the inertial wave beams (Figure 6.5*c*) resembles that for internal gravity waves. The overturning motion in the focal region is intense, and results there in a vertically standing inertial wave motion with alternating red-blue vorticity (McEwan, 1973).

The three-dimensional view of the vertical vorticity field was reconstructed from the Volume PIV measurements, and its iso-surfaces are presented in Figures 6.6 (*a*) and (*b*) for internal gravity and inertia–gravity waves, respectively. The presence of a dipolar vortex for the nonrotating stratified fluid demonstrates nonlinear effects in the focal zone of internal gravity waves (Figure 6.6*a*). The vorticity structure for inertia–gravity waves reveals that the positive and negative vortices are twisted around each other (Figure 6.6*b*) due to the presence of background motion. This motion takes place through 2/3 of the depth. The Rossby radius of deformation was calculated as $R_o = (Nh)/f$, with $h = 2H/3$ and $H = 90$ cm, and predicts the size of the vortex to be 150 cm, close to what has been observed.

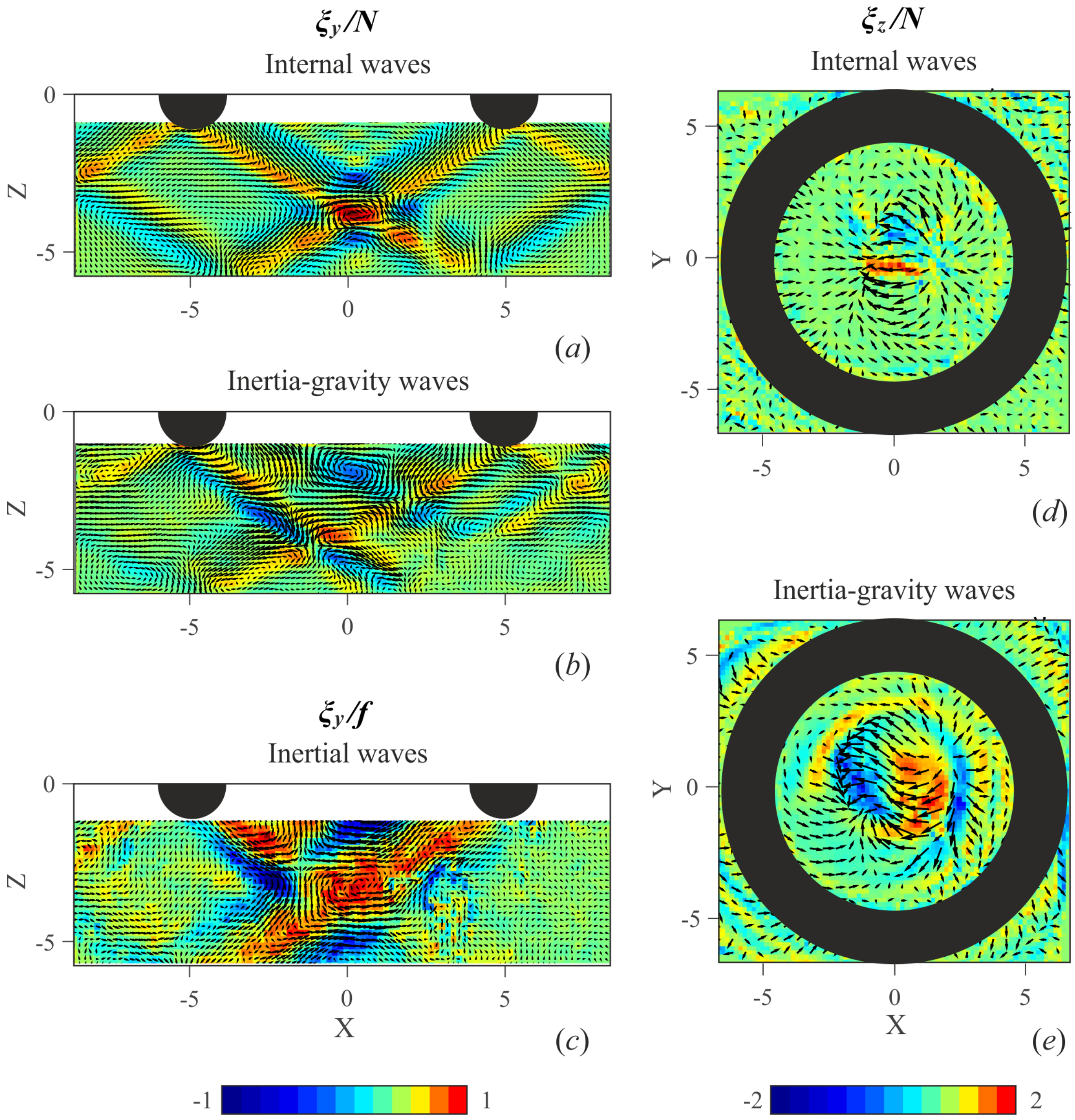

Figure 6.5: Instantaneous velocity vectors together with (a-c) instantaneous horizontal transverse vorticity ξ_y/N or ξ_y/f in the vertical plane of oscillation $Y = 0$ at $Ke = 0.17$ (the color scale is the same in all three images), and (d,e) vertical vorticity ξ_z/N in the horizontal plane through the centre $Z = -4$ of the focal zone for internal gravity waves (the color scale is the same in both images) [Exp 1.2 and 1.4 from Table 2.3]

6.3 Kinetic energy

Patterns of the normalized total kinetic energy

$$E = \frac{1}{2}\frac{\hat{U}_1^2 + \hat{V}_1^2 + \hat{W}_1^2}{(A\omega)^2}$$

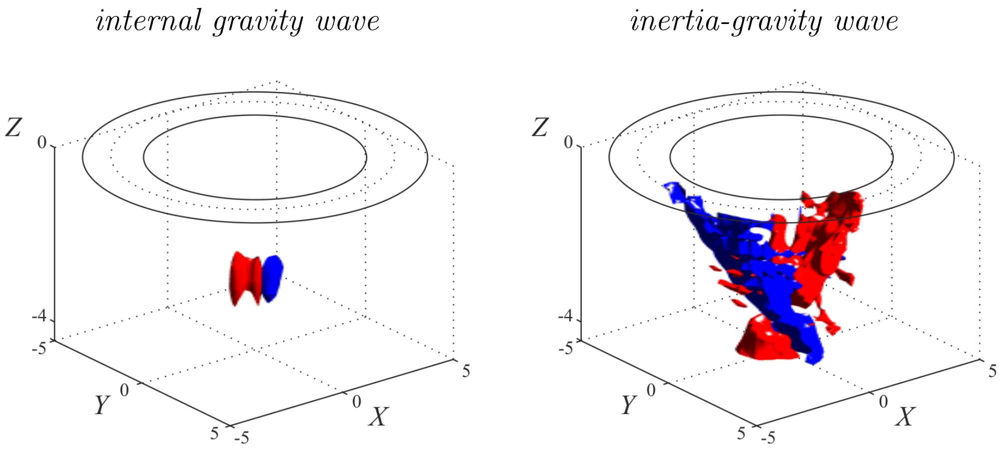

(*a*) (*b*)

Figure 6.6: Isosurface of the instantaneous vertical vorticity field $\xi_z/N = \pm 0.6$, reconstructed from the volume PIV measurements for (*a*) internal gravity waves and (*b*) inertia–gravity waves. Red and blue colors indicate positive and negative vorticities, respectively. The horizontal section of the torus at $Z = 0$ is shown with black curves. [Exp 1.4 from Table 2.3]

in the vertical plane of symmetry $Y = 0$, obtained with Volume PIV technique are presented in Figures 6.7(*a*) and (*b*) for internal gravity and inertia-gravity waves, respectively. As expected, the energy of the internal gravity waves is amplified in the diamond-shaped focal region. In the presence of rotation the focal region changes its structure. In addition to the one zone of amplitude amplification in the centre observed for internal gravity waves, the energy is focused above this zone closer to the torus and at both sides of the initial zone (see Figure 6.7*b*).

The distribution of horizontally averaged total kinetic energy is shown in Figure 6.8. The energy of internal gravity waves increases toward the focal zone, having its maxima at $Z = -3$. For inertia–gravity waves an amplification is observed close to the torus ($Z = -1.5$) and in the focal zone ($Z = -3$), where the wave energy is nearly equal to that for internal gravity waves.

6.4 Time–frequency representation

Figures 6.9(*a*) and (*b*) show the time–frequency representation of the horizontal velocity $\hat{u}$ (see chapter 3, eq. (3.4) for details) averaged over a small area close to the torus and in the focal zone, respectively. Close to the torus the first two harmonics of internal gravity waves appear. In the focal zone the nonlinear interactions result even for low oscillation amplitude $Ke = 0.17$ in the generation of evanescent higher harmonics after four oscillation periods. From the experimental results we notice that with the present sizes of the object and experimental tank nonlinear effects

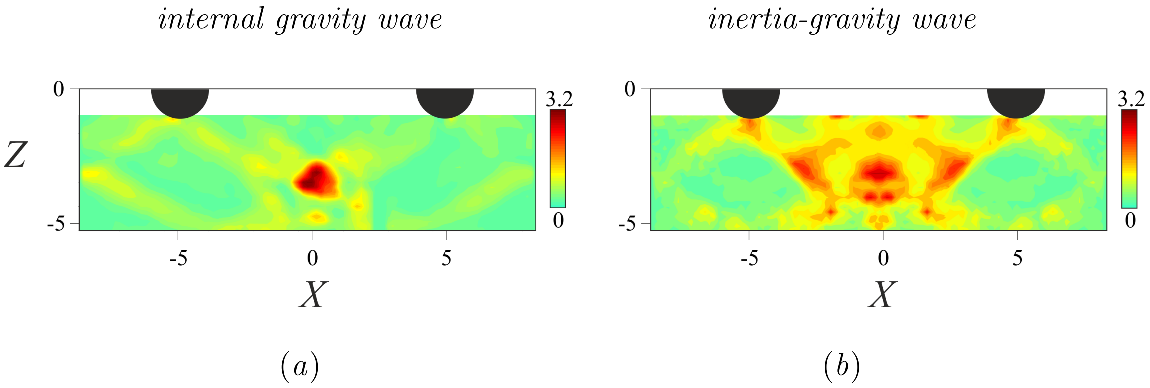

Figure 6.7: Total kinetic energy of (a) internal gravity waves and (b) inertia–gravity waves in the vertical plane of symmetry, $Y = 0$, obtained with volume PIV technique. [Exp 1.4 and 2.2 from Table 2.3]

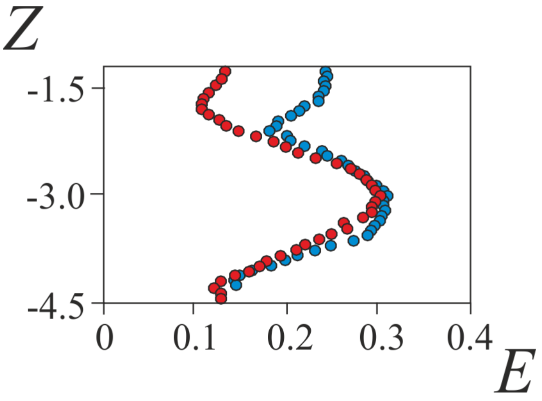

Figure 6.8: Vertical distribution of total kinetic energy averaged along the horizontal in the area $(-5 < X < 5, -5 < Y < 5)$ that is inside the vertical projection of the torus, for experiments 1.4 (blue dots) and 2.2 (red dots) from Table 2.3.

always take place in the focal region, by contrast with the observations at lower sizes in chapter 4.

The time–frequency diagram calculated for the density signal from a conductivity probe in the focal zone is in agreement with the same representation for the velocity (Figure 6.10a). It can be seen that higher harmonics vary in time but in average remain at their frequency $n\omega/N$. Fourier filtering of the density signal (Figure 6.10b) shows that the density amplitude normalised with the buoyancy frequency, ρ^*/N, has a maximum at the fundamental frequency and decreases nearly exponentially with increasing harmonic frequency $n\omega/N$ for internal gravity as well as for inertia–gravity waves. This result is in agreement with that obtained from the velocity field (Figure 6.9b) which also shows qualitatively a decrease in energy with increasing frequency $n\omega/N$. Therefore, the energy distribution is similar for internal gravity and inertia–gravity waves.

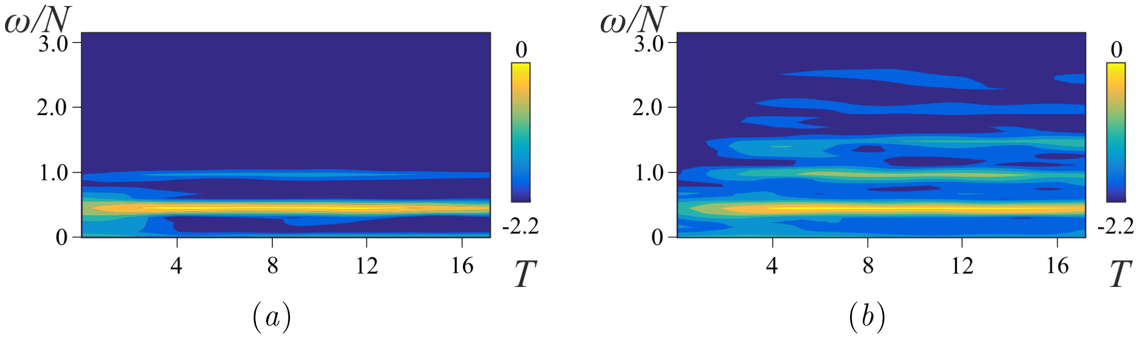

Figure 6.9: Time–frequency spectrum $\log_{10}(Q_u(t,\omega)/Q_0)$ for internal gravity waves in the plane $Y = 0$ at $Ke = 0.17$, with $Q_0 = \max[Q_u(t,\omega_1)]$ and $T = (\omega t)/2\pi$. The horizontal velocity $\hat{u}$ is averaged over (a) the near-field area $-5 < X < -4$, $-1.7 < Z < -1$ and (b) the focal area$-1 < X < 1$, $-4 < Z < -2.6$. [Exp 1.2 from Table 2.3]

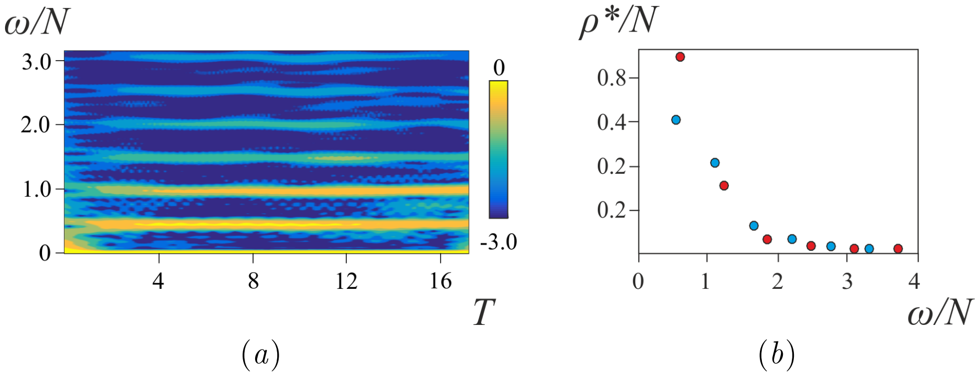

Figure 6.10: Data obtained with the conductivity probe in the focal zone of internal gravity waves at $Ke = 0.17$: (a) Time–frequency representation for internal gravity waves, obtained as in Figure 6.9(b); (b) Fourier-filtered density amplitude ρ^* against normalized oscillation frequency, ω/N. Blue and red dots represent results for internal gravity and inertia–gravity waves, respectively. [Exp 1.2 from Table 2.3].

6.5 Conclusions

In this chapter we have investigated the focusing of internal waves by an oscillating torus in the presence of both rotation and stratification, for high Stokes numbers $St = O(1000)$. The experiments were performed at the large Coriolis platform, 13 m in diameter, using a big torus ($a = 15$ cm, $b = 75$ cm). The results showed that the wave generation and propagation regime is nonlinear even for the smallest oscillation amplitude. The wave beams were seem to have a bimodal structure and the focal region to consist of several zones of velocity amplitude amplification. The internal gravity waves generated for small oscillations of the torus were compared with the linear theory, considering the eddy viscosity at the boundary layer of the torus. Though a slight difference in the focal zone structure has been obtained, the theory and experiments matched well. We expected the same growth of the velocity amplitude with the oscillation amplitude as in previous observations described in chapter 5. Surprisingly, with the present experimental conditions, the velocity amplitude of internal waves decreased with increasing oscillation amplitude and changed its structure in the focal region.

Comparing the vorticity fields obtained for internal gravity, inertia–gravity and inertial waves, we notice changes in the wave and focal zone structures. For internal gravity waves the overturning motion is localized in the focal zone, while for the inertial waves it is spread over the entire depth. Inertia-gravity waves overturning motion localized in four zones of wave beam intersection. The vertical vorticity field showed dipolar motion in the focal zone that transformed in the presence of rotation into a “Yin–Yang-shaped” structure.

The total kinetic energy was investigated for internal gravity and inertia–gravity waves. Without rotation the energy was concentrated in the focal zone, while in the presence of rotation high energy was also observed close to the torus and in both sides of the focal region.

With the time–frequency analysis we obtained the generation of higher harmonics in the focal zone. Their energy decreased exponentially with the harmonic order n.

General conclusions

An experimental study of the generation of internal waves has been performed for different three-dimensional bodies.

In this thesis I have continued the earlier study of an oscillating sphere (Ermanyuk *et al.*, 2011; Voisin *et al.*, 2011) by investigating the horizontal oscillations of spheroidal objects. Based on an extension of the theoretical calculations of Voisin *et al.* (2011) to the axisymmetric case of an oblate spheroid of vertical axis, good agreement was found with experimental results obtained with Laser Induced Fluorescence (LIF) in the vertical plane and Particle Image Velocimetry (PIV) in the horizontal plane. Several more elaborate configurations have been considered to understand the dependence of the velocity amplitude distribution of the waves on the shape and orientation of the object. It has been shown that the horizontal amplitude distribution for oblate spheroids of horizontal and vertical axes is similar to that for a sphere. The distribution is wider when axis is vertical compared to when it is horizontal, and the normalized amplitude is lower. Turning the axis at an angle to the direction of oscillation in the horizontal plane turns by the same angle the horizontal amplitude distribution.

Several aspects on higher harmonic wave generation near oscillating boundaries of various slope have been considered. In particular, fundamental and second harmonic waves are generated at the critical points of the boundaries, in agreement with former observations (Zhang *et al.*, 2007). In addition, a separate set of second harmonic waves is generated at the intersections of the fundamental wave beams, when their wave amplitude exceeds a certain threshold (Tabaei *et al.*, 2005; Jiang & Marcus, 2009). As the amplitude increases, the nonlinear overturning motion close to the boundary also leads to the generation of higher harmonics that appear weakly trapped near the region of generation. Further research is needed to show the threshold amplitude for which this nonlinear motions emit higher harmonic wave beams.

The highest amplitudes were obtained for the object with the strongest slope (a prolate spheroid of vertical axis). Thus, in the ocean, the propagation of internal tides and their amplitude depend not only on the direction of oscillation and frequency of the barotropic tide but also on the slope and curvature of the bottom topography as well. According to the theory of Bell (1975*a*), which is two-dimensional and applies to topographies of infinitesimal slope, the first three harmonics depend on the oscillation amplitude linearly, quadratically and cubically, respectively and are proportional to the first, second and third derivatives of the topographic profile, hence to the slope, curvature and derivative of the curvature, respectively. The same dependence on the oscillation amplitude was observed in three dimensions for a sphere and for a prolate spheroid in our experiments, but a third harmonic was also observed for the sphere despite its constant curvature.

The horizontal structure of the higher harmonics has been studied for a sphere and for a prolate spheroid. It has been shown that the radiation patterns of the first three harmonics are dipolar, quadrupolar and octupolar, respectively. According to this trend we expect for the n-th harmonic wave a radiation pattern of multipolar order 2^n having $2n$ azimuthal poles in the horizontal plane. Because of the complexity of this structure and narrowness of the wave, as well as their weakness in amplitude compared to the fundamental, it is less obvious to visualize the radiation patterns for higher wave modes.

The geometric focusing of internal waves generated by a horizontally oscillating torus has then been investigated. Experiments were conducted in the weakly viscous regime, i.e. for Stokes numbers between 150 and 260. In a first approach we used the Keulegan-Carpenter number Ke to characterise the amplitude of focusing, thus neglecting the amplification of the waves due to the effect of focusing. Though these results are satisfactory, the focusing leads actually to a strong amplification of the wave amplitude along its ray path, with a maximum wave amplitude at the focal point where wave breaking can be expected for certain oscillation amplitudes. To characterise the focused wave field, a focusing number Fo has been introduced, and for different levels in the fluid and different size tori, the wave amplitude has been found to collapse as a function of this number. A linear wave regime is discerned for $Fo < 0.15$, whereas non-linear effects start to occur at values close to $Fo \approx 0.15$. Wave breaking occurs for $Fo \approx 0.22$, corresponding to a local (shear) Richardson number $Ri = 0.25$, in accordance with classical theory for shear instability. This value coincides with the Richardson number calculated from the wave steepness. Wave breaking occurs for an isopycnal slope of $\theta = 75°$.

As a first approximation, the field of focusing waves has been approached by making use of the two-dimensional theory of Hurley & Keady (1997) that was adapted by including a term for the wave convergence. This theory shows qualitative agreement with the observed wave field, and gives reasonable quantitative results up to a vertical distance from the torus of 5 times its radius. However, there is an increasing discrepancy between the data and the theory when approaching the focal zone, for the entire range of wave amplitudes. This difference is about 30% and indicates that the present theory is not satisfactory for the study of the focal region.

After Fourier filtering the wave amplitude, the three-dimensional structure of the second harmonic waves has been identified. This structure is quadrupolar in the focal zone. Some of the observed maxima in the wave field of the second harmonic wave suggest that intersections of wave rays also emit waves, in agreement with the theory of Tabaei *et al.* (2005). The maximum amplitude of the second harmonic waves in the focal region is found to be about 2.3 times weaker than that of the first harmonic wave.

Focusing of internal wave energy is a rather recent subject, and opens perspectives to new ways of generating waves and turbulence in the ocean. The overturning in the present experiments has been observed at moderate Reynolds numbers when internal waves are strongly damped by viscous effects. Similarly, internal-wave breaking over other shapes of curved topography (see Bühler & Muller, 2007) may serve as an effective mechanism for the generation of "hot spots" responsible for abyssal mixing. The use of the number Fo and the measurements based on wave steepness allow us to make more precise estimations of the relevance of wave breaking due to wave focusing.

For a realistic bottom topography the effects of viscosity are small (see the discussion in Voisin *et al.*, 2011). We may consider whether wave breaking is likely to occur or not, using the above focusing number. For a M_2 tidal oscillation frequency of approximately 12 hours and a typical ocean stratification one obtains $\omega/N \approx 0.3$ corresponding to an angle of wave propagation of 17°. Considering a large mountain 1 km height, 1 km minor radius and 60 km major radius, so that $a = 1$ km and $b = 60$ km, we obtain for the critical oscillation amplitude $A_c \approx 0.22\ \sqrt{ab}/(\sin^{1/2}\theta\cos\theta) = 874$ m, which is of the same order as the tidal excursions which are typically of 100 m. Note that this critical value might be overestimated since viscous effects in the present laboratory flow (Stokes number $\mathrm{O}(10^2)$) are much stronger than in the ocean (Stokes number $\mathrm{O}(10^8)$). Smaller mountains with smaller values of a and b require also smaller critical amplitudes. Thin large ridges as well as thick small ridges of realistic sizes can thus be expected to cause overturning waves due to focusing. The recent observation of intense mixing in the Mid-Atlantic Ridge (see Dale & Inall, 2015) near a spur-shaped mountain not known as a "hot spot" for mixing, seems to correspond well with this category of wave breaking due to focusing.

In order to consider high Stokes number waves, experiments have been performed at the Coriolis platform. We have measured the three-dimensional wave structure for internal gravity, inertial and inertia–gravity waves. In contrast to our expectations, for these high Stokes numbers the amplitudes of the vertical and horizontal velocities decrease with increasing oscillation amplitude, possibly due to wave breaking close to the oscillating torus. Wave amplification occurs in the focal zone rather at low oscillation amplitudes. For high oscillation amplitudes an energy spreading along the wave beam is observed. The horizontal vorticity field has a similar structure for internal gravity and inertial waves, though the intensity of the motion is higher for inertial waves and the vorticity spreads through the entire depth due to energy loss by diapycnal mixing. In the presence of both rotation and stratification, four vortices have been observed in the focal region. The vorticity field demonstrates the presence of nonlinear effects in the focal zone which cause the dipolar motion to be deformed by the background rotation into a "Yin–Yang-shaped" structure. For inertia–gravity waves this motion is twisted and spreads through 2/3 of the fluid depth. The size of the vortex corresponds to the Rossby radius of deformation.

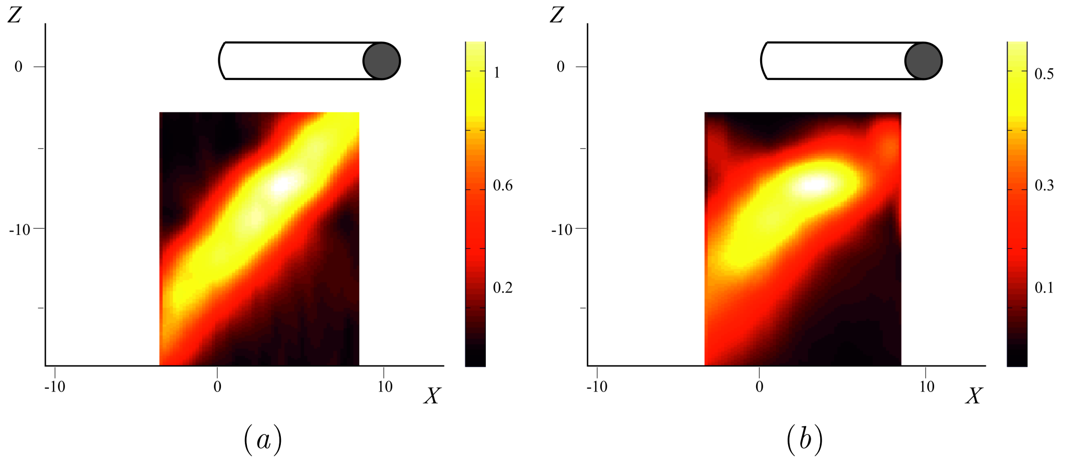

(a) (b)

Figure 6.11: Non-axisymmetric wave focusing by a horizontally oscillating half-torus, oriented perpendicular to the X-direction, at $\omega/N = 0.8$, $\epsilon = 9$ and $St = 148$: patterns of the vertical displacement amplitude in the vertical plane $Y = 0$ for (a) $Ke = 0.19$ and (b) $Ke = 0.84$.

Spectral analysis of the velocity and density in the focal zone shows the generation of higher harmonics in zones of intersection of the fundamental wave beams. Most of the energy is in the fundamental wave, whereas the higher harmonics are evanescent and their energy decreases exponentially. Our large scale experiment, providing Stokes number of 4500, generates turbulence in the focal region, a source of mean flow generation and mixing. The effect of this turbulence on the wave beam can be taken into account by means of an eddy viscosity.

Perspectives

The experiments at the Coriolis platform have revealed new aspects of nonlinear internal wave focusing at high Stokes number, not observed in smaller-scale experiments at lower Stokes number. For example, the wave turbulence obtained in small-scale experiments for inertial waves (Duran-Matute *et al.*, 2013) was not observed at the Coriolis platform. Clearly, further investigation of the problem is required.

The importance of the three-dimensionality of wave focusing can be confirmed by looking at the non-axisymmetric case of the oscillations of a half-torus. In the vertical central plane one obtains a wave beam with amplitude increasing toward the focal zone and decreasing afterward, as seen in Figures 6.11(a) and (b) showing the wave amplitude obtained from a LIF experiment in the small tank with a thin half-torus of dimensions $a = 1.5$ cm and $b = 13.5$ cm oscillating with $Ke = 0.19$ and 0.84, respectively. Focusing is clearly observed despite the absence of two opposite interfering beams as in Figure 4.1, thereby showing that focusing is a product of the horizontal curvature of the wave generator, through the interference of beams

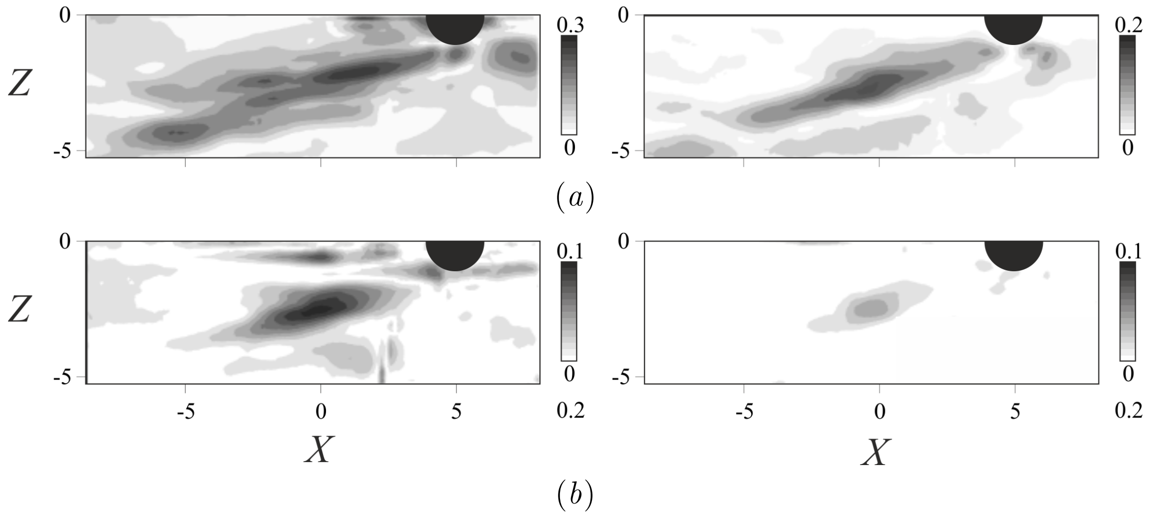

Figure 6.12: Patterns of the horizontal (left column) and vertical (right column) velocity amplitude in the vertical plane $Y = 0$ for the filtered (a) first harmonic and (b) mean flow. Experimental parameters: Exp 4.3 in Table 2.3.

propagating in different azimuthal planes. The waves continue to propagate after focusing, bending at high oscillation amplitudes into an arc shape with a peak in the focal region. A possible explanation is the horizontal net transport of momentum away from the focal zone, which could not be observed in the axisymmetric focusing by a full torus.

Experiments with a half-torus differently oriented with respect to the forcing direction have been performed at the Coriolis platform (experiments 4.1 to 5.2 in Table 2.3). A first set of experiments used a vertical laser plane. The patterns of horizontal and vertical velocity amplitudes are presented in Figure 6.12. Horizontal mean flow generation is observed in the focal zone (Figure 6.12 b) and divide the first harmonic wave beam in two after focusing, one propagating at the angle according to the dispersion relation and another propagating along the direction of the mean flow (Figure 6.12 a).

Experiments 4.2 and 5.2 with Volume PIV should provide more detailed information about nonlinear effects in the focal zone. It is also of interest to compare waves generated by “symmetric” and “asymmetric” half-tori, oriented perpendicular and parallel to the direction of oscillation, respectively. In the latter case generation of a horizontal mean flow perpendicular to the direction of oscillation away from the half-torus is expected. Clearly, the Coriolis platform setup for wave focusing is promising and deserves more study.

Appendices

Appendix A

Generation of higher harmonic waves on spheroids

Generation of higher harmonic waves on spheroids

Natalia Shmakova,[1,*] Evgeny Ermanyuk,[1,2] and Jan-Bert Flór[1]

[1]*Laboratoire des Écoulements Géophysiques et Industriels (LEGI),*
CNRS–Université Grenoble Alpes, F38000, Grenoble, France
[2]*Lavrentyev Institute of Hydrodynamics,*
Siberian Branch of the Russian Academy of Sciences,
Prospekt Lavrentyev 15, Novosibirsk 630090, Russia

(Dated: October 21, 2016)

Abstract

Oscillating bodies in stratified fluids may emit higher harmonics in addition to the fundamental waves. The three dimensional structure of these higher harmonics is not yet well known. Here we consider higher harmonics of the internal wave field as generated by different horizontally oscillating spheroids in a uniformly stratified fluid. Higher harmonics are observed at the intersections of fundamental wave beams, and at the critical points of the topography where the topographic slope equals the wave slope. The velocity amplitude of the fundamental, second and third harmonic wave grow respectively linearly, quadratically or with the power 3 with the scaled oscillation amplitude A/a, with a the radius of the object. Higher harmonics are generated by nonlinear instability at the boundary layer at the surface of the object, and nonlinear effects in the zone of primary beams intersection. Higher harmonic waves may intersect and focus, therefore increase in energy, and become dominant over the fundamental wave. Also the horizontal structure of the wave amplitude is measured. The results suggest that the n-th harmonic of the internal wave field is associated with a radiation diagram corresponding to a multipole of order 2^n, with $2n$ directions of propagation.

PACS numbers: 92.10.hj,47.55.Hd,47.35.Bb

---

[*] natalia.shmakova@legi.cnrs.fr

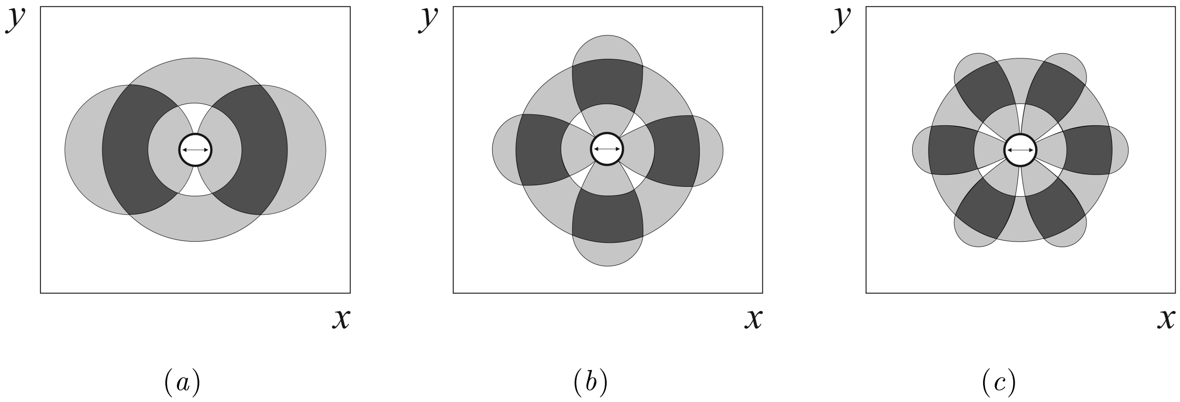

FIG. 1. Horizontal structure of dipolar, quadrupolar and octupolar internal waves. The annular propagation of the waves and the 2^n-polar radiation pattern as $cos(n\phi)$ are represented by light gray and their combination by dark gray.

I. INTRODUCTION

Internal waves are generated by the barotropic tide in the Earth ocean and are known to play an important role for its energy balance [1–4]. Motivated by this application, in a large number of studies, the oscillation of idealized bodies of different shapes in a linear stratified fluid has been investigated. Seen from the reference frame of the fluid, the wave generation by an oscillating body is comparable to that of the interaction of the barotropic tide with bottom topography. Most well known are the classical experiments of Mowbray and Rarity [5], which show that, the dispersion relation for internal waves generated by a cylinder, oscillating with frequency ω in a linearly stratified fluid with buoyancy frequency N, admits for the propagation of n-th harmonic component [5] of the wave field if $n\omega < N$. Though linear wave theory for elliptic cylinders [6, 7] adequately predicts the observed fundamental wave [8], the higher harmonics, as shown by Sutherland and Linden [9] and Zhang et al. [10], seem to be due to fully nonlinear dynamics. Korobov and Lamb [11] showed numerically that the interaction between the fundamental wave and higher harmonics in the vicinity of an underwater mountain ridge creates a complex fine-scale structure over the entire fluid depth.

In three dimensions, such as for the waves generated by an oscillating sphere, higher harmonics have a non-trivial distribution of wave amplitudes in the azimuthal direction in addition to the structure demonstrated by Korobov and Lamb [11]. For this geometry, the linear theory has been described and experimentally verified [12]. A detailed study on the radiation pattern of the propagative first and second harmonics has been performed in Ermanyuk et al. [13]. It was shown that first and second harmonics have respectively dipolar and quadrupolar radiation patterns. The shapes of these patterns are shown in Fig. 1 together with the octupolar radiation pattern. The existence of high harmonics has also been demonstrated for an isolated Gaussian hill by King et al. [14]. It is however not possible to extrapolate the experimental data obtained in King et al. [14] and Ermanyuk et al. [13] to predict the azimuthal structure of the n-th harmonic.

The aim of the present paper is to consider the generation of higher harmonic internal waves near topography of different curvature, here represented by an oscillating sphere, and a prolate spheroid oriented horizontally or vertically. Experimental observations are compared with the theoretical predictions according to Bell [15] for the waves on curved boundaries, and Tabaei et al. [16] and Jiang and Marcus [17] for the wave generation at wave beam intersections. The measurements of the horizontal flow field allow us to make hypothesis about the horizontal structure of the n-th harmonic radiation patterns. Measurements are performed using the PIV technique. An additional set of experiments, visualizing horizontal planes close to the oscillating objects, was performed for a better understanding of mechanisms that are responsible for the generation of higher harmonics.

II. EXPERIMENTAL SETUP AND DATA PROCESSING

Experiments were conducted in a plexiglass square tank with working depth of 97 cm and horizontal dimensions 97 × 97 cm^2 filled to a depth of 90 cm with a linearly stratified fluid [see Fig. 2(a,b)]. Salt was used as stratifying agent and tap water as working fluid. The stratification was measured by taking density samples at different heights in the fluid. A least square fit provided the density gradient and the related value of the buoyancy frequency $N(z) = [-(g/\rho)(d\rho/dz)]^{1/2}$, with g the gravity acceleration and $\rho(z)$ the density distribution with the vertical coordinate z. In the present experiments $N = 1 \pm 0.08$ rad/s. The kinematic viscosity in experiments was constant, $\nu = 1.1$ mm^2/s. Waves were generated by horizontally oscillating a plexiglass spheroid of equatorial radius a and polar radius b, attached to a pendulum of length 1.3 m. The aspect ratio for the spheroids was $b/a = 1$ (sphere) and $b/a = 2$ (prolate spheroid) with $a = 3.125$ cm in both cases [Fig. 2(c–e)]. The surface of

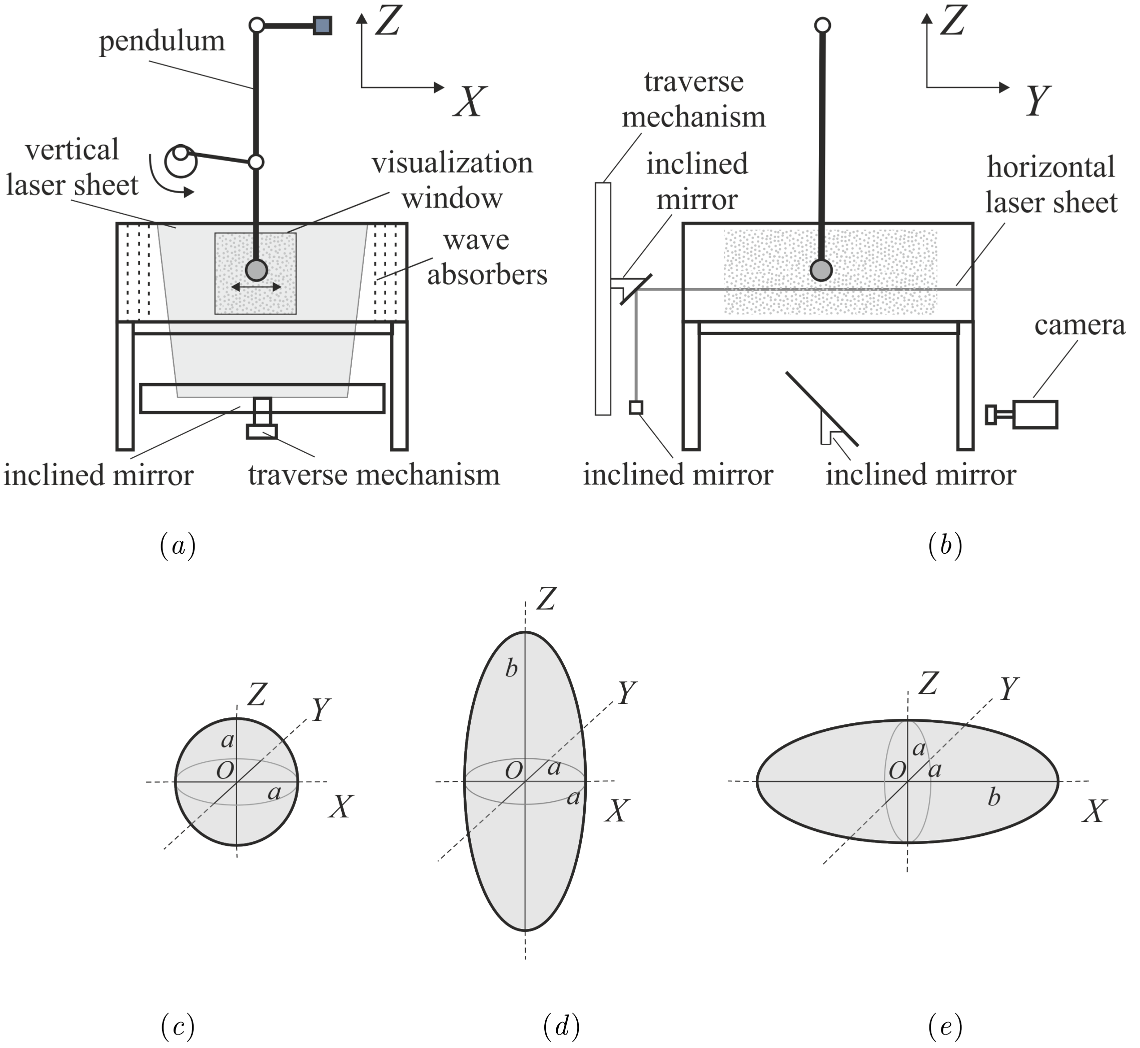

FIG. 2. Schematic views of the experimental setup: (*a*) front view with vertical laser plane; (*b*) side view with horizontal laser plane. Geometry of oscillating objects: (*c*) sphere ($\mathcal{S}$), prolate spheroid with (*d*) vertical axis of revolution, ($\mathcal{V}$), and (*e*) horizontal axis of revolution, ($\mathcal{H}$).

the spheroids was painted black to avoid reflections of the laser light. The oscillations of the pendulum were driven by a crank mechanism. The motion was in good approximation horizontal and sinusoidal, with amplitude A and frequency ω. Wave absorbers were placed along the tank walls perpendicular to the plane of oscillation, effectively suppressing wave reflections. The wave pattern generally became steady after 10 oscillation periods.

To measure the velocity field a two-dimensional particle image velocimetry (PIV) technique was used. The size of visualization window was 36 × 36 cm^2 and 53 × 53 cm^2 for vertical and horizontal plane, respectively. Images were recorded with a 12-bit DALSA digital camera with CCD matrix of 1024 × 1024 pixels. Prior to the experiment, the fluid was seeded with Orgasol® 30 μm particles of density $\rho = 1.2$ kg/m^3. During the experiment, the particles were illuminated with either a vertical, or a horizontal laser sheet. The vertical laser sheet passed through the transparent bottom of the tank and was parallel to the direction of oscillation as shown in Fig. 2(a). Different vertical planes could be illuminated by moving the inclined mirror on the traverse mechanism. The position of the sheet was computer-controlled and allowed for the recording of sequences of planes. To measure period-averaged quantities and determine the amplitudes of the Fourier components of the signal in a vertical plane, the sheet was kept fixed during one oscillation period, and then moved 0.5 cm to the next position, until enough vertical planes were obtained to reconstruct the three-dimensional wave field by spline interpolation. The horizontal laser sheet passed through the side wall and its vertical position was controlled by shifting the inclined mirror shown in Fig. 2(b). In order to process the data with Fourier transform techniques [18, 19] (and in particular with the Hilbert transform) long time series were taken.

In the experiments, successive images of the wave field were taken at time intervals $\Delta t = 0.2$ s. This interval was chosen to be sufficiently small compared to the period of oscillations so that the number of images per period was large, i.e., between 56 and 84. The particle displacement was obtained by cross correlating two successive images using the CIV velocity image correlation algorithm (UVMAT/CIVx [20]). Fourier decompositions of time series of horizontal, $u(t)$, and vertical, $w(t)$, velocity were used to separate the fundamental wave and its higher harmonics. For the vertical plane the amplitude of horizontal, u_a, and vertical, w_a, velocity was defined as root-mean-square of $u(t)$ and $w(t)$, respectively. The absolute value of Hilbert transformation of $u(t)$ and $w(t)$ was taken in the horizontal plane. The non-dimensional coordinates $(X, Y, Z) = (x, y, z)/L$ are used, with the x- and y-axes respectively parallel and perpendicular to the direction of oscillation of the spheroids, as shown in Fig. 2 (c) and $(x, y, z) = (0, 0, 0)$ at the center of the object at rest. L is the lengthscale in the direction of oscillation, i.e. $L = a$ in case of sphere ($\mathcal{S}$) and prolate spheroid with vertical axis of revolution ($\mathcal{V}$), and $L = b$ in case of the prolate spheroid having a horizontal axis of revolution ($\mathcal{H}$). Non dimensional horizontal (longitudinal) and vertical velocity amplitudes, are respectively given by $U_a = u_a/A\omega$ and $W_a = w_a/A\omega$.

III. RESULTS

In a uniformly stratified fluid, the oscillation of a body generates internal waves that propagate along a double cone, with the apex located in the center of the body and the generatrices inclined at the angle

$$\theta = \arccos \Omega \tag{1}$$

to the vertical, were $\Omega = \omega/N$ is the frequency ratio [21]. The dispersion relation (1) admits for the generation of a propagative n-th harmonic component of the wave field if $n\Omega < 1$. The horizontal structure of the first and the second harmonic has been studied in Ermanyuk et al. [13].

The effective generation of the n-th harmonic requires an appropriate choice of the non dimensional oscillation amplitude A/a, and oscillation frequency Ω. Obviously, A/a should be large enough for the amplitude of the n-th harmonic, proportional to $(A/a)^n$, to be observable. Based on the knowledge of the behavior of the first harmonic, a plausible conjecture for the frequency tuning can be formulated. It is known that for oscillating circular cylinders and spheres the maximum power radiated by the first-harmonic waves is found in the range of Ω between 0.7 and 0.8, regardless the oscillation direction [12]. Since the particular geometry of the wave field has little influence on the frequency corresponding to the maximum radiated power, we can make a conjecture that the n-th harmonic, irrespective of its actual generation mechanism, is most effectively generated when $0.7 < n\Omega < 0.8$. This condition was used for the frequency tuning in the present experiments.

A. Vertical structure

The wave patterns emitted by a horizontally oscillating prolate spheroid are shown in Fig. 3 with its long axis horizontal at the left [prolate spheroid $(\mathcal{H})$], and its long axis vertical at the right [prolate spheroid $(\mathcal{V})$]. This change in the position of the spheroid allows for the study of different curvature topography with the stratification. At the left column of Fig. 3, one notices the generation of second harmonic waves at $Z = 0$ at the intersections of the fundamental waves. In agreement with the theory of Tabaei et al. [16] and Jiang and Marcus [17] only fundamental and second harmonic waves are generated that propagate away from the obstacle. The waves below (and above) the spheroid are generated

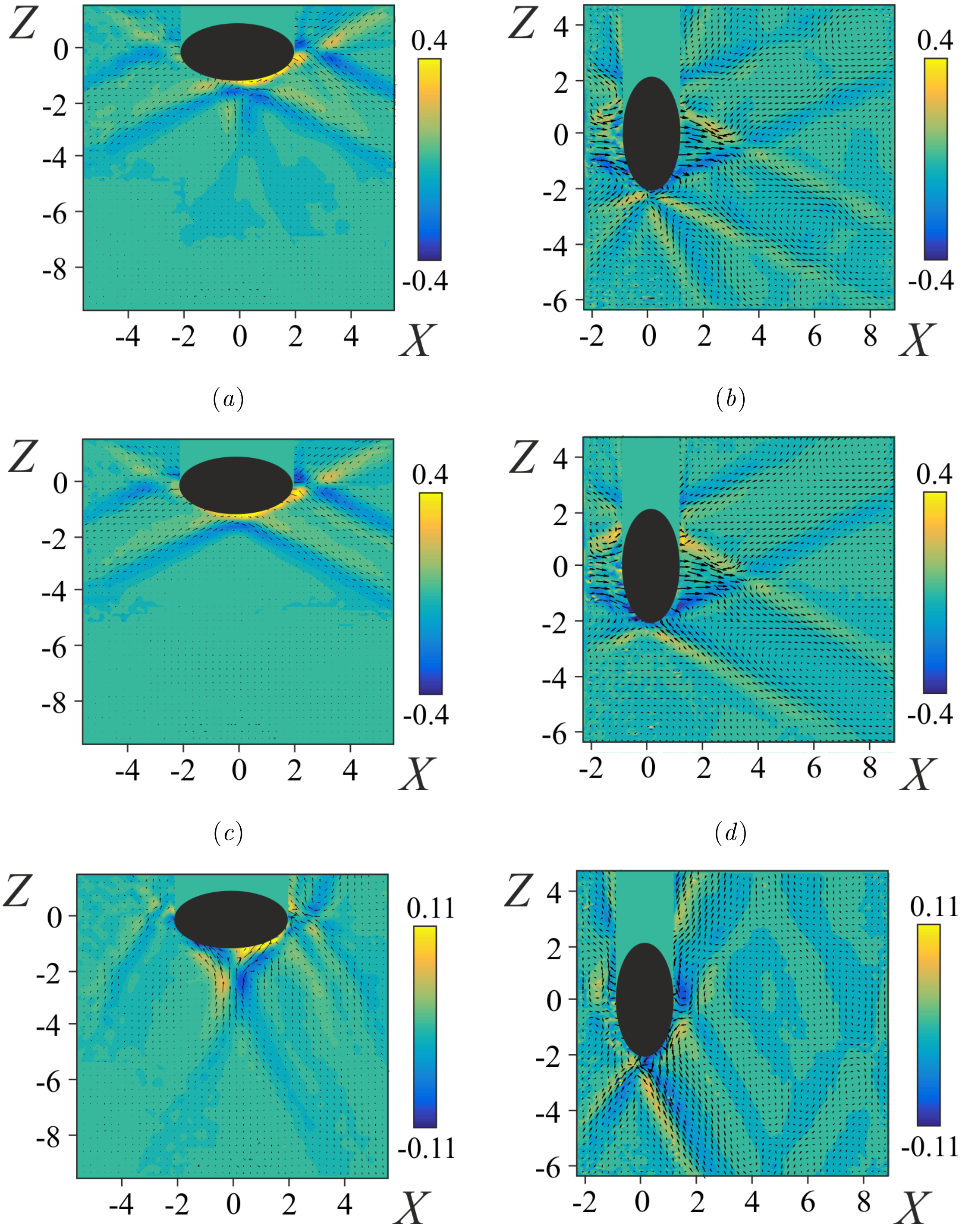

(*a*) (*b*)

(*c*) (*d*)

(*e*) (*f*)

FIG. 3. Snapshot patterns of vorticity (color) and velocity (vector field) of the wave field in the vertical plane of symmetry generated by a prolate spheroid $\mathcal{H}$ (left column) and a prolate spheroid $\mathcal{V}$ (right column); (*a*,*b*) total (fundamental and second harmonic), (*c*,*d*) first harmonic and (*e*,*f*) second harmonic. Experimental parameters: $N = 0.89$ rad/s, $\Omega = 0.44$, $A/a = 0.5$.

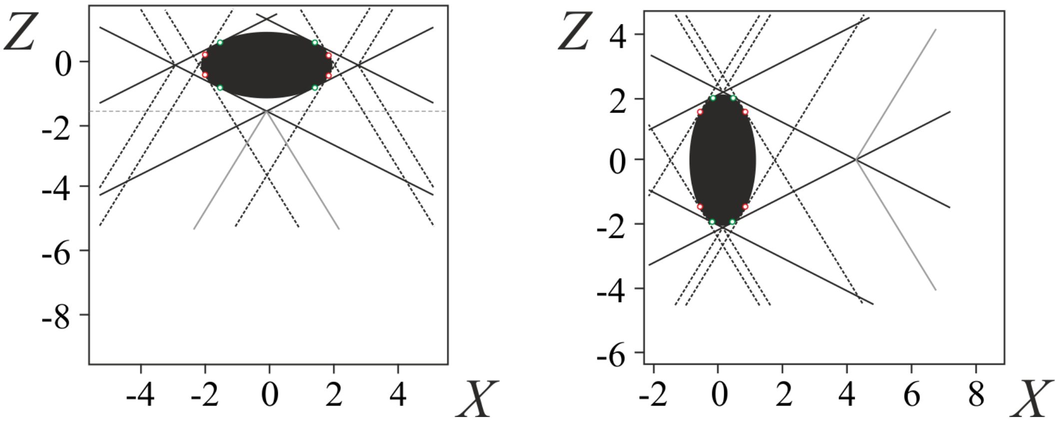

(a) (b)

FIG. 4. (a,b) Schematic distribution of the first and second harmonics of waves generated by prolate spheroid ($\mathcal{H}$) and ($\mathcal{V}$), respectively; dots correspond to critical points $\varepsilon = s/\sqrt{\frac{\omega_i^2}{\omega_i^2-N^2}} = 1$, with $i = 1, 2$ for the first (green dots) and second (red dots) harmonic, respectively. Fundamental and second harmonic generation is shown from the the critical points ε_i, and as predicted by theory [16, 17]; of the latter the harmonic waves that are not observed in the experiment are represented by gray lines. The horizontal gray line determine the vertical position of fundamental wave beams intersection Z^*.

at the boundary, and appear to have their origin at the critical points, where the slope of the topography s equals the slope of the harmonic wave, i.e.

$$\varepsilon_i = \frac{s}{\sqrt{\omega_i^2/(\omega_i^2 - N^2)}} = 1,$$

$i = 1, 2$ for the first and the second harmonics, respectively ($\omega_2 = 2\omega_1$) [Fig. 4 (a)]. Second harmonic wave beams emitted from the critical points $\varepsilon_2 = 1$ intersect below the spheroid. In this zone the waves focus and therefore amplify in wave energy [Fig. 3 (e)]. However, this zone is closer to the object then one may expect from the dispersion relation $\theta = \arccos(2\Omega)$ (see sketch in Fig. 4) for a second harmonic wave. In view of the weak slope of the topography Bell's theory [15] could apply and be responsible for harmonic emission. Both waves are well visible also in horizontal plane views in Fig. 5 (a) and (b), for slightly different parameters. However, the absence at a larger distance of a second harmonic wave beam being emitted from the point $(X, Z) = (0, -1)$ on the spheroid suggests nonlinear effects. There is a nonlinear interaction between the second harmonic wave emitted at the critical point and the overturning motion near the boundary layer. As a consequence this wave is deviated

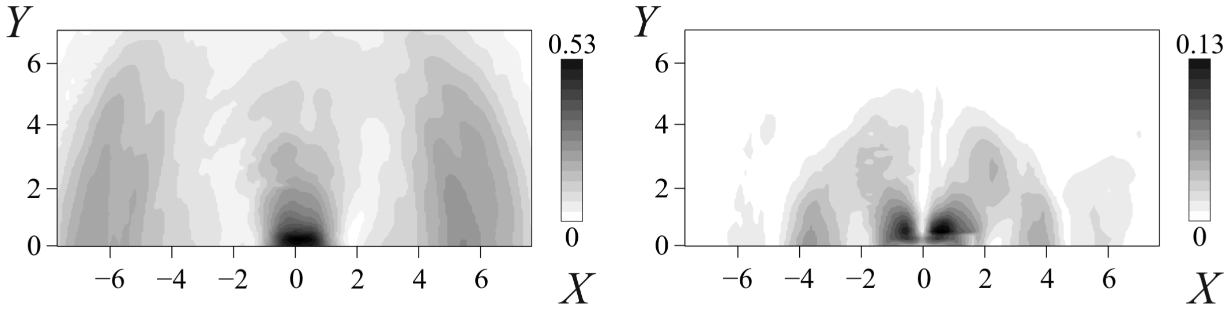

(a) (b)

FIG. 5. Radiation patterns for (a) the first and (b) the second harmonic wave of the horizontal longitudinal velocity field at the boundary ($Z = -1$) of the oscillating prolate spheroid ($\mathcal{H}$). Experimental parameters $A/a = 0.75$, $N = 1.08$ rad/s, $\Omega = 0.4$.

first horizontally. Near the focal point $(X, Z) = (0, -3)$ this wave propagates again in the direction of the second harmonic wave. One can base the Richardson number on the boundary layer thickness at the surface of the object δz, i.e.

$$Ri = \frac{N^2}{[(A\omega)/\delta z]^2},$$

with $Ri < 1/4$ for shear instability according to Miles' [22] theory on shear instability. For the velocity and stratification in this experiment, this corresponds to a threshold boundary layer thickness of $\delta z < 0.35$. In view of the much thinner boundary layer, the overturning below the spheroid is likely to occur.

At the right column of Fig. 3, the results are shown for the vertically positioned prolate spheroid ($\mathcal{V}$), for the same stratification, amplitude and oscillation frequency. Again fundamental and second harmonics are generated at critical points. However, the intersection of the fundamental waves at $Z = 0$ does not result in the generation of a second harmonic wave. Since this intersection is at a larger distance from the spheroid, the wave amplitude may have decreased significantly along its path. Zhang, King and Swinney [10] also notice that the second harmonics disappear for weaker wave amplitudes. The sketches of the wave patterns in Fig. 4(a) and 4(b) resume the observations.

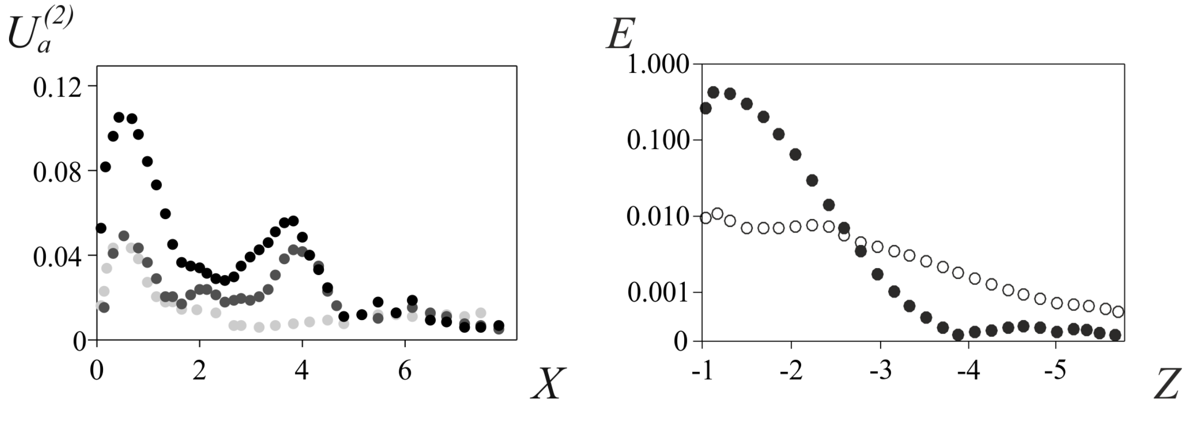

(a) (b)

FIG. 6. (a) Profiles of second harmonic of horizontal velocity field at $Z = -1$ (black dots), $Z = -1.47$ (dark gray dots) and $Z = -1.91$ (light gray dots) for oscillating prolate spheroid ($\mathcal{H}$). Data obtained at $Y = 0$ with $A/a = 0.75$, $N = 1.08$ rad/s, $\Omega = 0.4$. (b) Distribution of the kinetic energy $E = C \cdot \frac{\left\langle 0.5\left[(u_a^{(i)})^2+(w_a^{(i)})^2\right]\right\rangle_x}{0.5(A\omega)^2 l}$ of the first (dots) and second (circles) harmonic along Z. Experimental parameters: $A/a = 0.5$ and $\Omega = 0.45$.

B. Horizontal structure

Complementary experiments were conducted to determine the position of higher harmonic generation using horizontal laser sheet at $Z = -1$ and in the zone of primary beam intersection Z^* [see the horizontal line in Fig. 4 (a)]. Z^* is calculated from formulas (3.14) in Hurley [6]. This value appears to be too small for the sphere ($\Delta Z = 0.1$) but for the prolate spheroid ($\mathcal{H}$) oscillating with frequency $\Omega = 0.4$ and amplitude $A/a = 0.75$ this distance is large enough for measurements ($\Delta Z = 0.33$).

Distributions of amplitudes of the first and the second harmonics of the horizontal velocity $U/(A\omega)$ in the horizontal plane at $Z = -1$ are presented in Fig. 5. The second harmonic close to the object has a quadrupolar structure ($-2 < X < 2$). The second harmonics at $|X| = 4$ and $|X| = 6$ are in agreement with the vertical structure shown in Fig. 3 (e) and correspond respectively to the out-coming wave beams generated at the critical point $\varepsilon_2 = 1$ and the wave beam generated in the zone of fundamental wave intersection at $Z = 0$. Figure 6(a) shows that the amplitude of the second harmonic wave has its maximum close to the surface of the spheroid and decreases with the distance from the object.

To determine the wave–spectrum generated by the prolate spheroid ($\mathcal{H}$) and its evolution

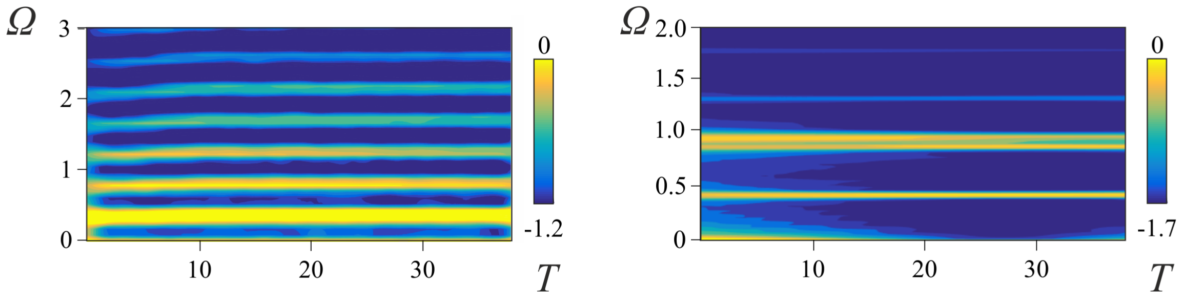

(a) (b)

FIG. 7. Time-frequency diagram for the waves generated by the prolate spheroid $(\mathcal{H})$, color bar shows (a) $\log_{10}(S_U(t,\omega)/S(t,\omega_0))$ averaged over $-2 < X < 2$, $-1 < Y < 1$ in the horizontal plane $Z = -1$ for the horizontal longitudinal velocity u; experimental parameters: $A/a = 0.75$ and $\Omega = 0.4$. (b) $\log_{10}(S_W(t,\omega)/S(t,\omega_0))$ measured in $-2.5 < X < 2.5$, $Y = 0$ and $-4 < Z < -1$ for the vertical velocity w. Experimental parameters: $A/a = 0.5$ and $\Omega = 0.45$.

with time [23] a time-frequency representation described in Flandrin [19] is used:

$$S(t,\omega) = \left\langle \left| \int_{-\infty}^{+\infty} du \; u \exp^{-i\omega u} h(t-u) \right|^2 \right\rangle_{xy}, \tag{2}$$

where $h(t) = 0.54 - 0.46\cos(\omega t)$ is a Hamming window and the average is taken over an interrogation area xy.

Figure 7(a) shows the time–frequency diagram for the logarithm of S averaged in space inside small rectangle $(-2 < X < 2, -1 < Y < 1, Z = -1)$. Under experimental conditions the first two harmonics are propagative, with their generation starting at $t = 0$, and their frequency remaining constant for all 40 oscillation periods; all higher harmonics are evanescent. The development of these evanescent waves is visible in Fig. 7(a) $0 < T < 10$, $\Omega > 1$. Figure 7(b) shows that in addition to the second harmonic frequency ($\omega_2 = 0.9$ rad/s) waves are generated at lower frequency $\omega_{2^-} \approx 0.8$ rad/s. We notice that the frequency interval between these waves increases with time.

The normalized total kinetic energy E was integrated in the horizontal for all Z:

$$E = C \cdot \frac{\left\langle 0.5 \left[(u_a^{(i)})^2 + (w_a^{(i)})^2 \right] \right\rangle_x}{0.5(A\omega)^2 l},$$

where $C = 4\frac{\pi ab + (a-b)^2}{a+b}$ is an approximate solution of integration over an ellipse, and $l = 2b$, for waves generated by prolate spheroid $(\mathcal{H})$. The distribution of averaged kinetic energy along the vertical axis Z is shown in Fig. 7(b) for the first and second harmonics. The

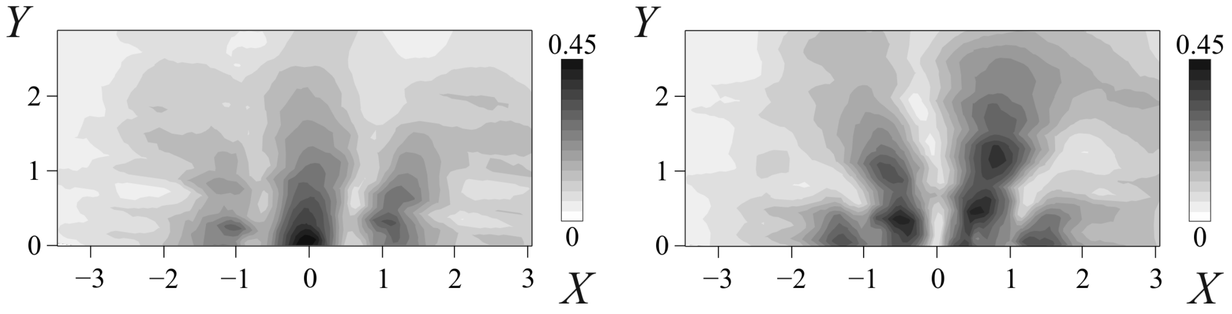

(a) (b)

FIG. 8. Octupolar radiation pattern corresponding to the upper half of Fig. 1(c): gray levels visualize (a) the horizontal velocity amplitude of the third harmonic wave $U_a^{(3)}$, and (b) the vertical velocity amplitude of the third harmonic wave $W_a^{(3)}$. Experimental parameters: oscillating sphere with $a = 3.125$ cm, $A/a = 0.91$ at $Z = -1.66$, $N = 1$ rad/s, $\Omega = 0.27$.

fundamental wave energy has it's maximum close to the object boundary and linearly dissipates with distance Z. The energy of the second harmonic wave has two maxima: one close to the object ($Z = -1$) and in the zone of two secondary beams intersection [$Z = -2.3$, see Fig. 3(e)]. Due to focusing the second harmonic dominates over the first harmonic component for $-6 < Z < -3$.

Distributions of the third harmonic component emitted by the sphere ($\mathcal{S}$) of the horizontal longitudinal velocity $U_a^{(3)}$, and the vertical velocity $W_a^{(3)}$, are shown in Fig. 8. The third harmonics frequency is estimated as $3\Omega \approx 0.8$. An octupolar structure is clearly visible, with 6 azimuthal poles implying the amplitude variation as $\sin(3\phi)$ for the horizontal velocity amplitude and $\cos(3\phi)$ for the vertical velocity amplitude.

The distribution of the amplitudes of the third harmonic along the X-axis is presented in Fig. 9 for objects of different curvature: sphere ($\mathcal{S}$), prolate spheroid with vertical axis of revolution ($\mathcal{V}$) and prolate spheroid with horizontal axis of revolution ($\mathcal{H}$). All six azimuthal poles of the third harmonic generated by the sphere have the same form, size and amplitude distribution but in the case of an oscillating prolate spheroid ($\mathcal{V}$), the amplitude of the azimuthal poles along the X-axis is smaller compared to the amplitude of the same poles for the sphere ($0.4 < X < 1$ for $U_a^{(3)}$ and $0.9 < X < 1.2$ for $W_a^{(3)}$). We notice that the structure of the wave pattern approximately scales with the slope of the object. The amplitude of the higher harmonic waves changes significantly with the shape of the object, and is higher for

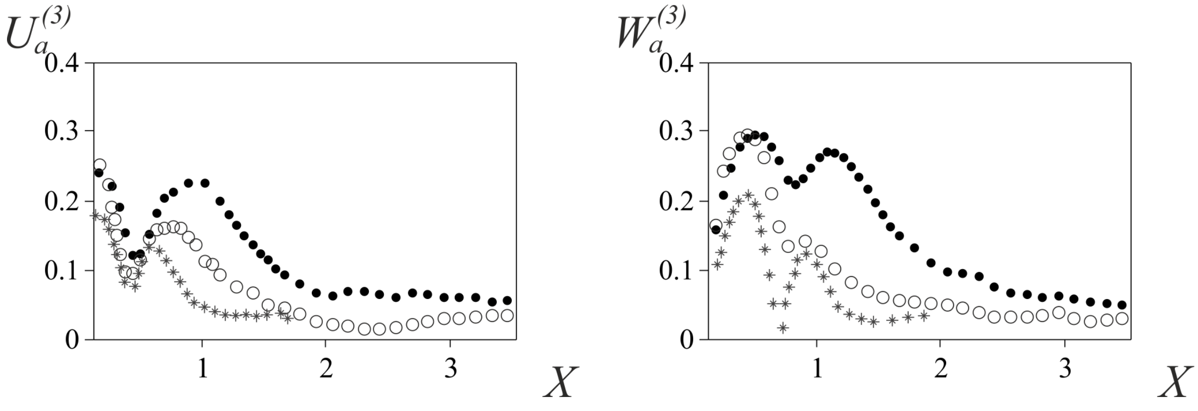

(a) (b)

FIG. 9. Profiles of the third harmonic of (a) horizontal ($U_a^{(3)}$) and (b) vertical ($W_a^{(3)}$) velocity field at $Y = 0$. Dots, circles and stars correspond to results for the oscillating sphere ($\mathcal{S}$) (measured at $Z = -1.66$), prolate spheroid ($\mathcal{V}$) ($Z = -2.4$) and prolate spheroid ($\mathcal{H}$) ($Z = -1.66$), respectively. Experimental parameters: $A/a = 0.65$, $N = 1$ s^{-1}, $\Omega = 0.27$. (The vertical distance to the boundary of the object is the same in all cases, but Z values vary because of the scaling).

’steeper’ objects.

The dependance of extreme values of non dimensional amplitudes of first three harmonics on the non dimensional oscillation amplitude is presented in Fig. 10. The logarithmic representation shows that the amplitude of horizontal (U_a) and vertical (W_a) velocity is independent of the oscillation amplitude for the normalized fundamental wave, and varies as A/a and $(A/a)^2$ for the normalized second and third harmonics, respectively. This trend is in agreement with the two-dimensional theory of Bell [15] and previous experimental studies on fundamental and second harmonic waves generated by an oscillating sphere [13].

In view of former observations on the relevance of the fundamental wave and higher harmonics [13, 24], a note should be made on higher harmonics in three-dimensional flows. In the two-dimensional case the energy content of the higher harmonics is usually relatively low, as demonstrated for the second harmonic in Zhang et al. [10]. However, in the three-dimensional case, the amplitude of the second harmonic can be higher than the amplitude of the first for a sphere [13] or comparable to it for Gaussian topography over a flat bottom [14]. The reason for this difference is related to the fact that, at low oscillation frequencies Ω and fixed amplitude A/a, the power P of internal waves that are generated by horizontally oscillating bodies varies as Ω^2 for a circular cylinder and Ω^5 for a sphere [12], and similar

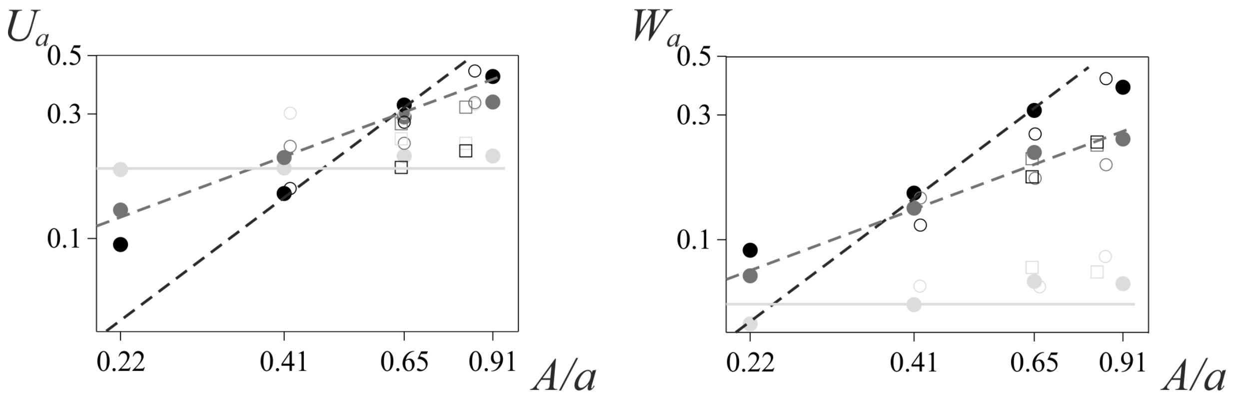

(a) (b)

FIG. 10. Variations of the peak magnitudes of the first three harmonics with oscillation amplitude A/a for (a) horizontal (U_a) and (b) vertical (W_a) velocity field. First, second and third harmonics are represented with light gray, dark gray and black color, respectively, and compared with theoretical predictions for the sphere (solid light gray line), and linear regressions for $U_a^{(2)}$ ($W_a^{(2)}$) and $U_a^{(3)}$ ($W_a^{(3)}$) (dashed dark gray and black lines). Dots, circles and squares correspond to results for oscillating sphere ($\mathcal{S}$), prolate spheroid ($\mathcal{V}$) and prolate spheroid ($\mathcal{H}$), respectively. $N = 1$ rad/s, $\Omega = 0.27$.

asymptotic behavior is valid for elliptic cylinders and spheroids [25]. Accordingly, at low frequency Ω and fixed A/a the amplitude of the first, linear harmonic is much smaller in three dimensions than in two and can more easily be overtaken by the amplitude of the higher, nonlinear harmonics. Therefore, for low oscillation frequencies Ω, that are relevant to geophysical applications, we may have a situation where the fundamental wave generated by barotropic flow over three-dimensional topography is weak while a higher n-th harmonic is strong. Reciprocally, higher harmonics are of interest for three-dimensional topography because of their high energy content under appropriate conditions. The azimuthal harmonic wave structure may have an influence on the energy and mass fluxes in the vicinity of underwater mountains.

IV. CONCLUSIONS

In this study, several aspects on higher harmonic wave generation near oscillating boundaries of varying slope have been considered. In particular, fundamental and second harmonic waves are generated at the critical point at the boundaries in agreement with former observations [10]. Intersections of the fundamental wave beams lead to the generation of second harmonic waves, when their wave amplitude exceeds a threshold [16, 17]. When the amplitude of oscillation exceeds a certain threshold, the nonlinear overturning motion also leads to the generation of higher harmonics that appear weakly trapped near the region of generation. Further research is needed to show the threshold amplitude for which this nonlinear motions emit higher harmonic wave beams. It is also shown that in agreement with previous observations [13] and theoretical predictions [15] the amplitude of the first three harmonics grows linearly, quadratically and cubically, respectively, with increasing of oscillation amplitude.

Further, the present observations show that the spatial structure of the radiation pattern of the first three harmonics of the wave field is respectively dipolar, quadrupolar and octupolar. According to this trend we expect that for the n-th harmonic wave radiation pattern of multipolar order 2^n has $2n$ azimuthal poles in the horizontal plane. Because of the complexity of the structure and narrowness of the wave it is less obvious to visualize the radiation patterns for higher wave modes.

The numerical results described in Korobov and Lamb [11] show the internal wave structure that is due to the interplay of first and higher harmonics in the vertical plane. The here presented results show that, in addition in the horizontal plane, the complexity of the horizontal wave structure increases with the harmonic wave number. The interaction of multipolar radiation patterns may lead to complex interference patterns above realistic bottom topographies.

ACKNOWLEDGMENTS

NS greatly acknowledge the help of Stephan Mercier and Jean-Marc Barnoud for their technical help and assistance with the experimental setup. NS and JBF acknowledge finance of the LabEx OSUG@2020 (Investissements d'avenir ANR10LABX56) for experimental equipment. EE acknowledges his appointments as a visiting professor at University

Joseph Fourier in 2011.

---

[1] E. G. Morozov, Deep-Sea Res I **42**, 135 (1995).

[2] W. Munk and C. Wunsch, Deep-Sea Res. I **45**, 1977 (1998).

[3] V. Vlasenko, N. Stashchuk, and K. Hutter, *Baroclinic Tides: Theoretical Modeling and Observational Evidence* (Cambridge University Press, 2005).

[4] C. Garrett and E. Kunze, Annu. Rev. Fluid Mech. **39**, 57 (2007).

[5] D. E. Mowbray and B. S. H. Rarity, J. Fluid Mech. **28**, 1 (1967).

[6] D. G. Hurley, J. Fluid Mech. **351**, 105 (1997).

[7] D. G. Hurley and G. Keady, J. Fluid Mech. **351**, 119 (1997).

[8] B. R. Sutherland, S. B. Dalziel, G. O. Hughes, and P. F. Linden, J. Fluid Mech. **390**, 93 (1999).

[9] B. R. Sutherland and P. F. Linden, Phys. Fluids **14**, 721 (2002).

[10] H. P. Zhang, B. King, and H. L. Swinney, Phys. Fluids **19**, 096602 (2007).

[11] A. S. Korobov and K. G. Lamb, J. Fluid Mech. **611**, 61 (2008).

[12] B. Voisin, E. V. Ermanyuk, and J.-B. Flór, J. Fluid Mech. **666**, 308 (2011).

[13] E. V. Ermanyuk, J. B. Flór, and B. Voisin, J. Fluid Mech. **671**, 364 (2011).

[14] B. King, H. P. Zhang, and H. L. Swinney, Geophys. Res. Lett. **37**, L14606 (2010).

[15] T. Bell, J. Fluid Mech. **67**, 705 (1975).

[16] A. Tabaei, T. Akylas, and K. Lamb, J. Fluid Mech. **526**, 217 (2005).

[17] C.-H. Jiang and P. S. Marcus, Physical Review Letters **102** (2009).

[18] M. Mercier, N. Garnier, and T. Dauxois, Phys. Fluids **20** (2008).

[19] P. Flandrin, *Time–Frequency/Time–Scale Analysis* (Academic Press, San Diego, 1999).

[20] `http://www.legi.cnrs.fr/web/spip.php?article763`.

[21] T. Peacock and P. Weidman, Exp. Fluids **39**, 32 (2005).

[22] J. W. Miles, Journal of Fluid Mechanics **10**, 496 (1961).

[23] B. Bourget, T. Dauxois, S. Joubaud, and P. Odier, Journal of Fluid Mechanics **723**, 1 (2013).

[24] S. J. Ghaemsaidi and T. Peacock, Experiments in fluids **54**, 1 (2013).

[25] E. V. Ermanyuk, Exp. Fluids **32**, 242 (2002).

Appendix B

Internal wave focusing by a horizontally oscillating torus

Internal wave focusing by a horizontally oscillating torus

E. V. Ermanyuk[1,2] N. D. Shmakova[1] and J.-B. Flór[1] †

[1]Laboratoire des Écoulements Géophysiques et Industriels, CNRS–Université Grenoble Alpes,
BP 53, 38041 Grenoble, France

[2] Lavrentyev Institute of Hydrodynamics, Siberian Branch of the Russian Academy of Science,
Prospekt Lavrentyeva 15, Novosibirsk 630090, Russia

(Received xx; revised xx; accepted xx)

This paper presents an experimental study on internal waves emitted by a horizontally oscillating torus in a linearly stratified fluid. Two internal wave cones are generated with the kinetic energy focused at the apices of the cones above and below the torus where the wave amplitude is maximal. Their motion is measured via tracking of distortions of horizontal fluorescein-dye planes created prior to the experiments, and illuminated by a vertical laser sheet. The distortion of the dye planes gives a direct access to the Lagrangian displacement of local wave amplitudes and slopes, and in particular, allows to calculate a local Richardson number. In addition Particle Image Velocimetry (PIV) measurements are used. Maximum wave slopes are found in the focal region and close to the surface of the torus. As the amplitude of oscillations of the torus increases, wave profiles in the regions of maximum wave slopes evolve non-linearly toward local overturning.

A theoretical approximation based on the theory of Hurley & Keady (1997) is presented and shows, for small amplitudes of oscillation, a very reasonable agreement with the experimental data. For the focal region the internal wave amplitude is found to be overestimated by the theory.

The wave breaking in the focal region is investigated as a function of the Keuligan-Carpenter number, $Ke = A/a$, with A the oscillation amplitude, and, a the short radius of the torus. A linear wave regime is found for $Ke < 0.4$, nonlinear effects start at $Ke \approx 0.6$ and breaking for $Ke > 0.8$. For large forcing, the measured wave amplitude normalized with the oscillation amplitude decreases almost everywhere in the wave field, but increases locally in the focal region due to nonlinear effects. Due to geometric focusing the amplitude of the wave increases with $\sqrt{\epsilon}$, with $\epsilon = b/a$, and b is the mean radius of the torus. The relevance of wave focusing due to ocean topography is discussed.

Key words: Ocean mixing, internal wave focusing, wave breaking, stratified fluids.

1. Introduction

In the oceans, the interaction of the tidal motion with the bottom topography is continuously generating internal waves (Bell 1975; Vlasenko *et al.* 2005; Garrett & Kunze 2007). There is a reasonable agreement about the global rate of energy of 3.7 TW from lunar and solar tides, of which about 1TW is converted into the baroclinic tide (Morozov 1995; Garrett & Kunze 2007). The transfer of this energy into mixing is relevant to the

---

† ermanyuk@hydro.nsc.ru, natalia.shmakova@legi.grenoble-inp.fr, jan-bert.flor@legi.cnrs.fr

general circulation in the oceans, and is therefore also of interest to climate modelling (Wunsch & Ferrari 2004; Ferrari & Wunsch 2008).

Over the past decades, the mechanism of internal wave generation has been studied in some detail for oscillating objects of various idealised geometries. Most well known are the classical flow visualisations of Mowbray & Rarity (1967) of wave rays emitted by an oscillating cylinder in the shape of a St Andrews-cross. Linear theory for two-dimensional internal waves generated by the oscillation of an elliptical cylinder of Hurley (1997) and Hurley & Keady (1997) was shown to be in good agreement with quantitative experimental results (see Sutherland *et al.* 1999, 2000; Sutherland & Linden 2002; Ermanyuk 2000; Ermanyuk & Gavrilov 2002). For ridges of Gaussian, exponential, or witch-of-Agnesi shape Llewellyn Smith & Young (2002) extended analytic estimates of Bell (1975) to compare internal tidal conversion rate, an approach that later has been applied to the waves generated by a vertical barrier (Llewellyn Smith & Young 2003). The ridge- and plateau-type geometries of specific shape are shown to generate no propagating internal waves for certain frequencies and depths (Maas 2011).

Three dimensional effects of internal waves are particularly considered in King *et al.* (2009). For a horizontally oscillating hemisphere they revealed the conical structure of wave beams and asymmetric bi-modal structure. For moderate forcing, a flow perpendicular to the forcing direction was found, leading to a large-scale horizontal circulation. The internal wave pattern generated by a horizontally oscillating sphere was compared with the three dimensional linear theory in Voisin *et al.* (2011). This theory included viscous effects and showed good agreement with experiments at low oscillation amplitude, and also allowed to better investigate the transition from bi-modal to uni-modal waves. At moderate oscillation amplitude, the propagative first and second harmonics were shown to have radically different horizontal patterns and are respectively of dipole and quadrupole type in the horizontal plane (Ermanyuk *et al.* 2011). More complex geometries have also been considered. Bühler & Muller (2007) developed the linear theory for the oscillation of a ring with a subcritical Gaussian generatrix, and consider for the first time the effect of geometric focusing of wave energy into localised regions of high wave amplitude. Some examples on this effect of focusing are given. For a circular Gaussian hill and horse-shoe topography also the mean flow localised in regions of wave dissipation are considered (Grisouard & Bühler 2012).

As mentioned above, a main interest in internal wave dynamics is the conversion of wave energy into mixing and small-scale dissipation due to a rich variety of mechanisms including wave-wave and wave-current interactions, and overturning motions. Several scenarios have been considered for the energy concentration of internal waves in localised zones, of which we recall the most recurrent ones: i) nearly critical reflection at continental slope (e.g. Dauxois & Young 1999; Gayen & Sarkar 2010), ii) energy concentration at attractors (Maas *et al.* 1997; Echeverri *et al.* 2011; Scolan *et al.* 2013; Guo & Holmes-Cerfon 2016), iii) internal wave refraction at horizons of high density gradient (e.g. Mathur & Peacock 2009), iv) interaction of wave beams in two dimensions (Teoh *et al.* 1997; Xing & Davies 2011; Zhang & Swinney 2014), and, as mentioned above, v) geometric focusing by three dimensional topography (Bühler & Muller 2007; Grisouard & Bühler 2012), recently also observed near canyons (Vlasenko *et al.* 2016; Dale & Inall 2015).

These latter studies (v) are novel compared to the various types of two dimensional focusing because of the convergence of the internal wave rays. Similarly as lightwaves passing through a convex lens the wave rays converge to a focal point, adding a fundamentally new aspect to the internal wave dynamics. Conservation of energy flux through

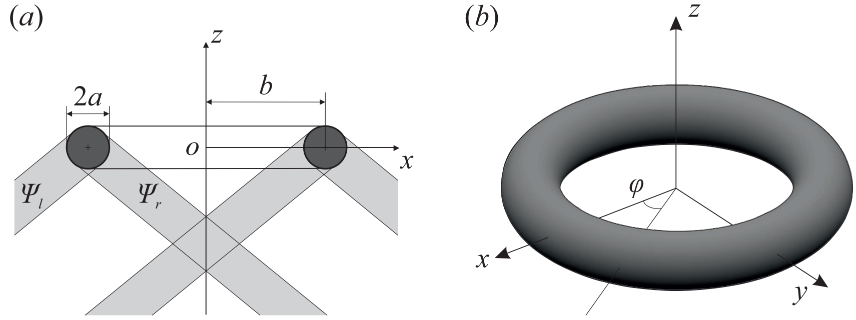

FIGURE 1. Geometry of the torus: in (a) view in vertical plane and (b) three-dimensional view defining the coordinate system.

a surface which reduces with distance, implies a continuous increase of energy density along the rays towards the focal point and a decrease after passing through it.

Geometric focusing of internal wave energy has hardly been investigated experimentally. Wave focusing may occur near an oscillating hemisphere (see figure 3 in King *et al.* 2009), and Gaussian mountain (see figure 3(e) in King *et al.* 2010), but was not discussed. The focusing effect increases with the radius and size of the oscillating object since more energy is transported to the focal zone, but in general its effect is negligible in small scale laboratory experiments with small oscillating spherical objects and has therefore not been reported before. First experiments with a 60 cm diameter vertically oscillating torus revealed a strong vortical motion with wave overturning and local mixing in the focal zone (unpublished results, Flór 1997). In a similar experiment in a rotating fluid, inertial waves showed to generate turbulence in the focal zone (Duran-Matute *et al.* 2013). In the context of the tidal motion in the oceans, a horizontal oscillation is more appropriate. The horizontal oscillation direction also gives a direction to the overturning motions in the focal region, and therefore generates a mean flow that may be relevant to ocean applications (see Bühler 2009).

In the present paper we investigate the wave pattern generated by a horizontally oscillating torus, the criterion for the onset of wave breaking, and observations of the nonlinear aspects of the wave generation in the focal region. We focus on the linear and weakly nonlinear regime, and consider the second harmonic generation and mean flow aspects in a separate contribution. The oscillating torus (or ring) generates "outward" moving diverging waves, and "inward" converging waves. As is known from previous studies on the oscillation of three-dimensional objects of spherical geometry (see Flynn *et al.* 2003; King *et al.* 2009; Voisin *et al.* 2011; Ermanyuk *et al.* 2011), diverging waves gradually decrease in amplitude with distance due to the increasing cross-section of the wave cone and viscous dissipation. For the present flows under consideration, the diverging waves are indeed relatively weak. The converging waves, however, increase in amplitude with distance from the torus toward the focal regions, leading to wave amplification and breaking.

In the next section §2, theoretical considerations are presented on the focusing of internal waves. The description of the experimental installation and techniques is given in §3 of the present paper. The results of experiments with internal waves are described in §4, and the main results and possible oceanic applications are presented in §5.

2. Theoretical considerations

We consider a torus of which the geometrical parameters are defined in figure 1. The torus is submerged into a uniformly stratified fluid with the buoyancy frequency $N = [(-g/\rho)\,\partial\rho/\partial z]^{1/2}$, where $\rho(z)$ is the density distribution in z-direction and g is the gravity acceleration. The shape of the generatrix is circular with diameter $2a$, and b is the radius of the centres of the circular cross-sections. A Cartesian coordinate system (see figure 1*b*) is introduced, with the z-axis pointing upwards. The origin of the coordinate system O is taken at the mean position of the center of the torus which undergoes rectilinear harmonic oscillations with frequency ω. The non-dimensional geometry can be characterized by the aspect ratio $\epsilon = b/a$. We assume that the torus is slender, i.e. ϵ is large. The non-dimensional coordinates X, Y and Z are introduced after normalization of x, y and z with the radius of the generatrix, a.

Let us consider first the vertical oscillations of the torus with amplitude A, which is assumed to be small compared to a so that the Keulegan-Carpenter number $Ke = A/a \ll 1$. The Stokes number defined as $\beta = \omega a^2/\nu$, with ν the kinematic viscosity, is assumed to be sufficiently large, i.e. $\beta \gg 1$. In the experiments described below, $\beta = O(100)$ which guarantees a sufficiently small non-dimensional boundary layer thickness δ/a. To construct an approximate solution we use an approach similar to the strip theory in marine hydrodynamics (Newman 1977*b*,*a*).

Suppose that each radial cross-section of the torus oscillates vertically and generates internal wave beams described by equation (3.7) in Hurley & Keady (1997). For brevity this equation is not reproduced here. Indeed, assumptions $Ke = A/a \ll 1$ and $\beta \gg 1$ are in agreement with Hurley & Keady (1997). This linear solution plays a role of an "inner" solution, which is approximately valid at each radial cross-section $\phi = const$, where ϕ is an azimuthal angle in the cylindrical coordinate system (r, z, ϕ), with $r = (x^2 + y^2)^{1/2}$. For vertical oscillations the problem is axisymmetric and all cross-sections $\phi = const$ are equivalent. Without loss of generality we consider oscillations in the plane xOz (see figure 1). The stream function for a single cylinder,

$$\psi^1_{HK}(x, z, t) = \Psi^1_{HK}(x, z)\exp(i\omega t),$$

is constructed as a sum of four stream functions describing the four beams of the St. Andrew-cross wave pattern (see Sutherland *et al.* 1999)

$$\Psi^1_{HK}(x, z) = \Psi^+_l + \Psi^+_r + \Psi^-_l + \Psi^-_r, \tag{2.1}$$

where the superscripts $+$ and $-$ refer, respectively, to the upper and lower half-plane, whereas the subscripts l and r refer, respectively, to the beams propagating to the left and the right.

For the second cylinder the solution $\Psi^2_{HK}(x, z)$ is analogous. Assuming that b/a is sufficiently large, the solution for the system of two cylinders can be written as

$$\Psi_{HK}(x, z) = \Psi^1_{HK}(x, z) + \Psi^2_{HK}(x, z), \tag{2.2}$$

where the appropriate choice of signs and phases in eq. 2.1 assure that both cylinders oscillate vertically and in-phase. The instantaneous vertical displacement of fluid particles due to the oscillation of two cylinders is then evaluated as

$$\zeta^t_{HK}(x, z, t) = (i/\omega)\exp(i\omega t)\frac{d}{dx}\Psi_{HK}(x, z). \tag{2.3}$$

The corresponding distribution of wave amplitudes is denoted as $\zeta_{HK}(x, z)$.

Further, we introduce the geometric correction factor for convergence (divergence) of the wave field. Let us consider a point C with coordinates (x_C, z_C) in the two-dimensional wave field generated by a system of two cylinders. The density of the energy flux at point C is proportional to the wave amplitude squared $(\zeta_{HK}(x_C, z_C))^2$. Since the torus is slender, we can equate the energy fluxes due to internal waves emitted by vertical oscillations of a torus of mean radius b and small radius a, and due to a system of two cylinders (see figure 1) of radius a and length πb. We obtain then

$$(\zeta(r_C, z_C))^2 \pi r_C = (\zeta_{HK}(x_C, z_C))^2 \pi b,$$

where $r_C = x_C$ at $\phi = 0$. Finally, we obtain in non-dimensional cylindrical coordinates

$$\zeta(R, Z) = (R/\epsilon)^{-1/2} \zeta_{HK}(R, Z), \tag{2.4}$$

where $R = r/a$. The term $(R/\epsilon)^{-1/2}$ assures a proper decay of the wave amplitude at infinity.

Let us note that in the case of vertical oscillations of two cylinders the wave amplitude $\zeta_{HK}(x, z)$ is symmetric with the respect to the vertical axis $x = 0$ and non-zero at $x = 0$. Therefore the approximate solution predicts a divergence of wave amplitudes of the form of $X^{-1/2}$ in the focal region at $X \to 0$. This result shows that near-field interactions should be taken into account in this zone in order to develop a more advanced linear theory. Also, in realistic situations, one can expect strong spatially localized non-linear effects in forms of vertical jets. Such effects have been indeed observed for inertial waves in Duran-Matute *et al.* (2013) and have been shown to create a localized turbulence zone due to a cascade of instability events.

Now, let us adapt the same approach in the spirit of strip theory (Newman 1977*b*,*a*) to a slender torus undergoing horizontal oscillations with amplitude A along the x-axis. The local forcing is then taken as a projection of horizontal oscillations on the radial coordinate in form $A \cos \phi$. Obviously, equations (2.1)–(2.3) remain valid in the case of horizontal oscillations of a system of two cylinders, with the important difference that the signs and phases of motions in wave beams should now be chosen such that the wave amplitude $\zeta_{HK}(x, z) = 0$ at $x = 0$ and the instantaneous wave profiles are anti-symmetric with respect to the vertical axis $x = 0$. The geometric conversion introduced in (2.4) remains valid but now, owing to azimuthal modulation of the wave field, eq. (2.4) for wave amplitudes transforms into

$$\zeta(R, Z, \theta) = (R/\epsilon)^{-1/2} \zeta_{HK}(R, Z) |\cos \theta|.$$

For horizontal oscillations, $\zeta_{HK}(R, Z)$ is proportional to R at a fixed Z in a small vicinity of $R = 0$, and therefore $\zeta(R, Z, \theta)$ is proportional to $R^{1/2}$ as R tends to 0. Thus, the wave amplitude remains limited but the wave slope tends to the vertical. This qualitatively indicates a possibility of overturning in the focal region, which is a qualitatively different behaviour compared to the case of vertical oscillations.

To characterize the forcing of internal waves, the Keulegan-Carpenter number $Ke = A/a$ is often used (see e.g. Voisin *et al.* 2011; Ermanyuk *et al.* 2011). Though this number characterizes the non-linearity close to the torus, it does not take into account the geometric effect of focusing at larger distances from the torus. Supposing that in the focal zone the wave motion can be confined to a zone with radius a, the amplitude may increase to $\zeta_{corr} = \zeta_{HK}(b/a)^{1/2} = \zeta_{HK}\epsilon^{1/2}$ i.e. with a factor $\epsilon^{1/2}$ due to focusing. The same correction factor has been introduced earlier in Bühler & Muller (2007). Note that the above-described theory neglects the near-field wave interactions in the focal region. Also, the viscous damping in the above solution is adapted from Hurley & Keady (1997), and therefore neglects additional shear close to the focal region. Therefore it is expected to provide a quantitative estimate with a reasonable accuracy only in the vicinity of the torus. The effects of finite values of Ke, β and ϵ in experiments are discussed below.

When oscillating an obstacle with frequency ω, in addition to the fundamental first harmonic wave oscillating at frequency ω, the dispersion relation admits wave radiation

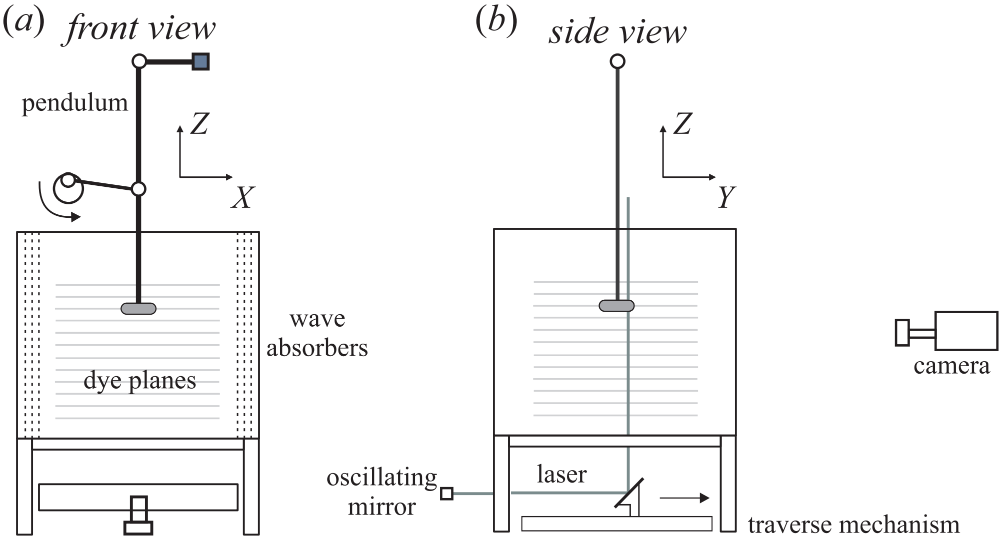

FIGURE 2. Sketch of the experimental set-up: (*a*) front view and (*b*) side view, with the light grey lines the fluorescein dye planes and the laser plane shown in dark grey. $(X, Y, Z) = (x, y, z)/a$ are the nondimensional coordinates. The torus oscillates in the X-direction (plane of view), Z is in the vertical direction. The mobility of the laser plane in the Y-direction allows for the measurement of successive planes, and the reconstitution of the horizontal wave field.

for higher harmonics with frequencies $n\omega$, where $n = 2, 3...$, were $\omega n < N$ (see Mowbray & Rarity (1967)). In contrast, for $\omega > N/2$ all higher harmonics are evanescent. In the experiments described below the value of $\Omega = \omega/N > 0.5$ so that the higher harmonics are evanescent and the effect due to focusing of the first-harmonic waves emitted by the torus can be studied in isolation.

3. Experimental set-up and measurement procedure

3.1. *Experimental set-up*

To measure the evolution of wave amplitudes and slopes with distance from the ring we use the Laser Induced Fluorescein (LIF) techniques (for details see Voisin *et al.* 2011; Ermanyuk *et al.* 2011).

This technique is based on the accurate tracking of distortions of iso-density surfaces (fluorescent dye planes), and allows to measure the amplitude of the vertical velocity with a very high precision. Since dye tracers are followed in time the recording is of Lagrangian type, in contrast with Eulerian-type techniques (PIV or Synthetic Schlieren) usually employed in experimental studies on waves. For waves of small amplitude the two types of measurements yield essentially the same results. As the wave amplitude increases, Lagrangian measurements allow to study the evolution of wave profiles toward overturning via direct measurement of wave slopes. Complementary PIV measurements provided information about profiles of horizontal velocity and its distribution over a horizontal plane.

Two tori have been used in the present experiments, a "thin ring" with $a = 1.5$ cm and $b = 13.5$ cm, and a "thick ring" with $a = 2$ cm and $b = 10$ cm. The aspect ratio $\epsilon = b/a$ is respectively equal to 9 for the "thin", and 5 for the "thick" one. At the experimental value of frequency $\omega = 0.65$ rad/s the Stokes numbers are $\beta = 150$ and 260 respectively for the thin and the thick torus.

	Method	ϵ	Ke	Ω	$N\,\mathrm{s}^{-1}$	Z	Z_{focal}	Y
Exp A	LIF	9	0.19; 0.41; 0.65; 0.84; 1.1	0.80	0.72	-1.84 to -21.8	-11.2	0
Exp B	LIF	5	0.15; 0.3; 0.52; 0.72	0.81	0.72	-1.88 to -16.88	-5.5	0
Exp C	LIF	9	0.17; 0.43; 0.62	0.81	0.72	-3.6	-11.2	0 to 10
Exp D	LIF	5	0.13; 0.29	0.81	0.72	-3	-5.5	0 to 5.5
Exp F	PIV	5	0.19; 0.41; 0.6; 0.95; 1.2	0.80	0.83	-1 to -10.88	-4.7	0
Exp G	PIV	9	0.21; 0.57; 0.78; 1.06; 1.26	0.80	0.83	-1 to -16.75	-7.8	0

TABLE 1. Experimental parameters, with $\epsilon = b/a$ the torus aspect ratio, $Ke = A/a$ the Keulegan-Carpenter number and $\Omega = \omega/N$, where A and ω are respectively the oscillation amplitude and frequency, and Z_{focal} corresponds to the geometrical point of intersection of the wave rays. The buoyancy frequency, N, is represented in dimensional values.

The experiments are conducted in a plexiglas 100 cm cubic tank filled to a working depth of 90 cm with a linearly salt-stratified fluid using the conventional double-bucket technique (see figure 2). The stratification profile is calculated from the density of fluid samples taken at different heights in the fluid and measured with an Anton Paar Density meter. The values of the buoyancy frequency N are listed in Table 1.

Internal waves are generated by a horizontally oscillating plexiglas torus that is painted black to avoid laser light reflections. It is attached to the end of a pendulum of length $l = 180$ cm, and the oscillations of the pendulum at frequency ω are driven by a crank mechanism. The oscillation amplitude, A, of the torus is small compared to the length of the pendulum, and the motion is therefore in good approximation horizontal and sinusoidal. The two side walls perpendicular to the direction of the oscillation of the cylinder are covered with a mesh of 5 cm thickness to avoid wave reflections. In some cases also the bottom and the back wall were covered with wave absorbers, but no difference in results could be noticed. After 10 oscillation periods the wave pattern reaches the steady-state in the region of interest. Measurements are taken after 20 oscillations, which is the typical duration used to exclude the effects of internal-wave transients (see Voisin 2003; Ermanyuk & Gavrilov 2005, 2008; Voisin *et al.* 2011).

For the method of fluorescein dye planes (first employed in Hopfinger *et al.* (1991) and Flór *et al.* (2002)), a set of equidistant dye planes is generated by slowly displacing a rake of horizontally spanned cotton threads through the fluid. These cotton threads are soaked in a concentrated fluorescein solution and dried before the experiment. The dye planes are illuminated with a vertical laser sheet parallel to the direction of oscillations. The data processing is performed with a version of cross-correlation technique described in Voisin *et al.* (2011) and Ermanyuk *et al.* (2011), from which the vertical displacements of the dye lines are determined with the accuracy of approximately 0.05 pixel. The laser sheet is perpendicular to the dyeplanes and shows therefore dyelines on the recordings (see figure 9).

Prior to the onset of the oscillations, the horizontal dye planes are scanned by a laser sheet in the otherwise quiescent fluid to obtain the reference state ζ_0 for each dye plane. The vertical displacement of these dyelines, ζ', is measured at a certain position in time with respect to the reference state ζ_0, i.e. $\zeta'(x,t) = \zeta' - \zeta_0'$ (the prime is to note that this value does not necessarily correspond to a particle displacement). The local slopes of wave profiles in plane XZ are measured as $s(t) = \arctan(d\zeta(t)/dx)$. In practice the slope at position (X, Z) is evaluated as

$$s(t) = \arctan(\Delta\zeta(t)/\Delta x), \tag{3.1}$$

where Δx should be sufficiently large compared to the accuracy of measurement of vertical displacements $\zeta(t)$ and sufficiently small compared to the radius of the generatrix a to resolve the details of wave profiles. The wave slope represents a sensitive and physically important measure of the baroclinic torque of the wave, caused by the shear. This slope is related to the Richardson number and is therefore an indication for overturning, as is discussed further in §4.4. As described in Voisin *et al.* (2011) and Ermanyuk *et al.* (2011), the vertical displacements are evaluated as the average values over vertical stripes of width of several pixels, which defines the horizontal spatial resolution of the experimental data. In the present experiments Δx is taken equal to the horizontal spatial resolution, with $\Delta x = 5$ (≈ 0.253 cm) and 8 pixels (≈ 0.339 cm) for respectively the "thin" and the "thick" torus.

To reconstruct a quasi three-dimensional distribution of the wave amplitudes (note that the velocity in y-direction is not measured), a series of images was acquired for different positions in y-direction. Therefore, the mirror reflecting the laser light (see figure 2) was moved by a computer-controlled step motor with a prescribed increment $\Delta y = 0.8$ cm. At each position the mirror remained fixed during one period of oscillation. This allowed to acquire time-series suitable for subsequent Fourier analysis and evaluation of amplitudes of harmonic components.

For the Particle Image Velocimetry (PIV) measurement the algorithm of Fincham & Delerce (2000) was used, and the optimum particle size and seeding density of Westerweel (1997) were followed. The fluid was seeded with Orgasol® 30 μm particles of density $\rho = 1.2$ kg/m^3, illuminated with a vertical and horizontal laser sheet. The particle displacement was obtained using the UVMAT/CIVx software package developed at LEGI †. Successive images are taken with a time increment of $\Delta t = t_{i+1} - t_i = 0.5$ s, which is kept constant in all experiments.

3.2. *Data analysis and parameters*

Time-series of vertical displacements $\zeta(t_i)$ are analyzed using three different methods. With the first method, the amplitudes of the n-th harmonic components of the signal ζ_n and S_n are determined via Fourier filtering of time-series. Similar analysis has been used in Voisin *et al.* (2011) and Ermanyuk *et al.* (2011). This type of data processing is particularly useful for linear or weakly non-linear processes when the first few harmonics are dominant and can be clearly identified. With the second method, the amplitudes ζ_{rms} and S_{rms} are evaluated as the period-averaged r.m.s. of the corresponding time-series multiplied by $2^{1/2}$ (Sutherland & Linden 2002). In principle, this quantity takes into account the contribution of all harmonics in the signal. However, owing to the period-averaging procedure the r.m.s. value cannot precisely capture the extreme values of wave amplitude and wave slope, which may instantly occur at a particular phase of oscillation. Of special interest are the extreme slopes which can trigger incipient overturning in the case wave crests become steep. Therefore, a third method of data processing was introduced. Time-series $\zeta(t_i)$ and $s(t_i)$ measured at each point were sorted to find the maximum values of $\zeta_{max} = \max|\zeta(t_i)|$ and $S_{max} = \max|s(t_i)|$.

Thus with these three methods, next to the values ζ_n, ζ_{rms} and ζ_{max}, the slopes S_n, S_{rms} and S_{max} were measured in degrees allowing to explicitly study the transition of the wave system to overturning. The wave amplitudes are normalized generally with the oscillation amplitude, A, or in case only the focal region is of interest, the generatrix of the torus, a. The governing parameters of experimental runs performed in this study are presented in Table 1.

---

† `http://www.legi.cnrs.fr/web/spip.php?article763`

4. Results and discussion

4.1. *Wave pattern in XZ-plane*

Figure 3(*a-c*) shows the typical evolution of the first harmonic wave patterns for different oscillation amplitude, represented by the Keulegan-Carpenter number Ke, in terms of contours of wave amplitude ζ_1/A, and contours of wave slope S_1. For comparison figure 3(d) represents the unfiltered wave fields in terms of ζ_{max}/A and S_{max}. A higher level of noise is observed for these non filtered max-type quantities. Figures 3(c) and (d) show a high resemblance indicating that at moderate oscillation amplitude, the dominant contribution to the wave field is represented by the first harmonic wave obtained after Fourier filtering, as can be expected since higher harmonics are evanescent for this forcing.

Wave amplitudes close to the torus are roughly two times smaller than the wave amplitudes in the focal region, but the wave slopes close to the torus and in the focal region are comparable. The onset of overturning occurs therefore not only in the focal region but also near to the torus. It should be noted that this latter overturning is rather due to the steep topography, an effect that would most likely be absent for a Gaussian-shaped torus. At low Ke the amplified wave amplitude in the focal region forms then two symmetric ellipses due to the anti-symmetry of the instantaneous wave profiles with respect to YZ plane, where the wave amplitude is zero. As Ke increases, these regions of maximum amplitude slightly shift into the Z-direction away from the torus. The non-linear evolution of the wave field is well visible in terms of wave slopes. At low Ke the focal region (figure 3*b*) is nearly elliptic. As Ke increases, the focal region takes a spearhead-like shape (figure 3*f, h*), indicating the higher shear in the outer region of the focal region, and incipient overturning. As a consequence, the waves are hindered by nonlinear effects in the focal region.

Note also that the waves in the focal zone have a unimodal structure, i.e. there is a single wave beam due to the presence of viscosity in contrast to the bimodal structure often observed very near to oscillating objects (for a discussion see e.g. Voisin *et al.* (2011)). Though the general flow evolution was very similar to that of the thick torus ($\epsilon = 5$), its larger generatrix a implied a larger Stokes number, (260 instead of 150) causing a rather bimodal wave structure near the torus which turned into a single beam near the focal region. In the case of very large tori, however, one may expect a multi focal region because of the bimodal wave structure. In view of the range of accessible Stokes numbers, this was not observed in the present experiments.

4.2. *Comparison of measurements with linear theory*

Figure 4 shows the wave amplitude across the wave beam measured in plane XZ at different distances Z from the centre of the torus. The experimental distributions of the scaled amplitude, $\zeta_1(X)/A$ for the torus with $\epsilon = 9$ are presented for a range of $|Z|$ values up to the middle of the focal zone. Good agreement with the theory described in §2 is observed at low values of Ke, and close to the torus. Thus, a simple geometric correction is fully sufficient for quantitative description of the main effects due to convergence (divergence) of waves in the vicinity of a curved elongated body. Thereby it provides a consistent framework for quantitative interpretation of the experimental results almost everywhere in the wave field, except the focal region.

For the focal region, the theory shows that focusing amplifies the wave amplitude to a factor 3, in qualitative agreement with the correction factor $\epsilon^{1/2}$ introduced in Bühler & Muller (2007). This can be observed in figure 4(f) ($|Z| = 12.51$) from the comparison of the calculated wave amplitudes for the torus (solid line) and the reference case of the two parallel cylinders of infinite length (dash line). The experimentally measured wave

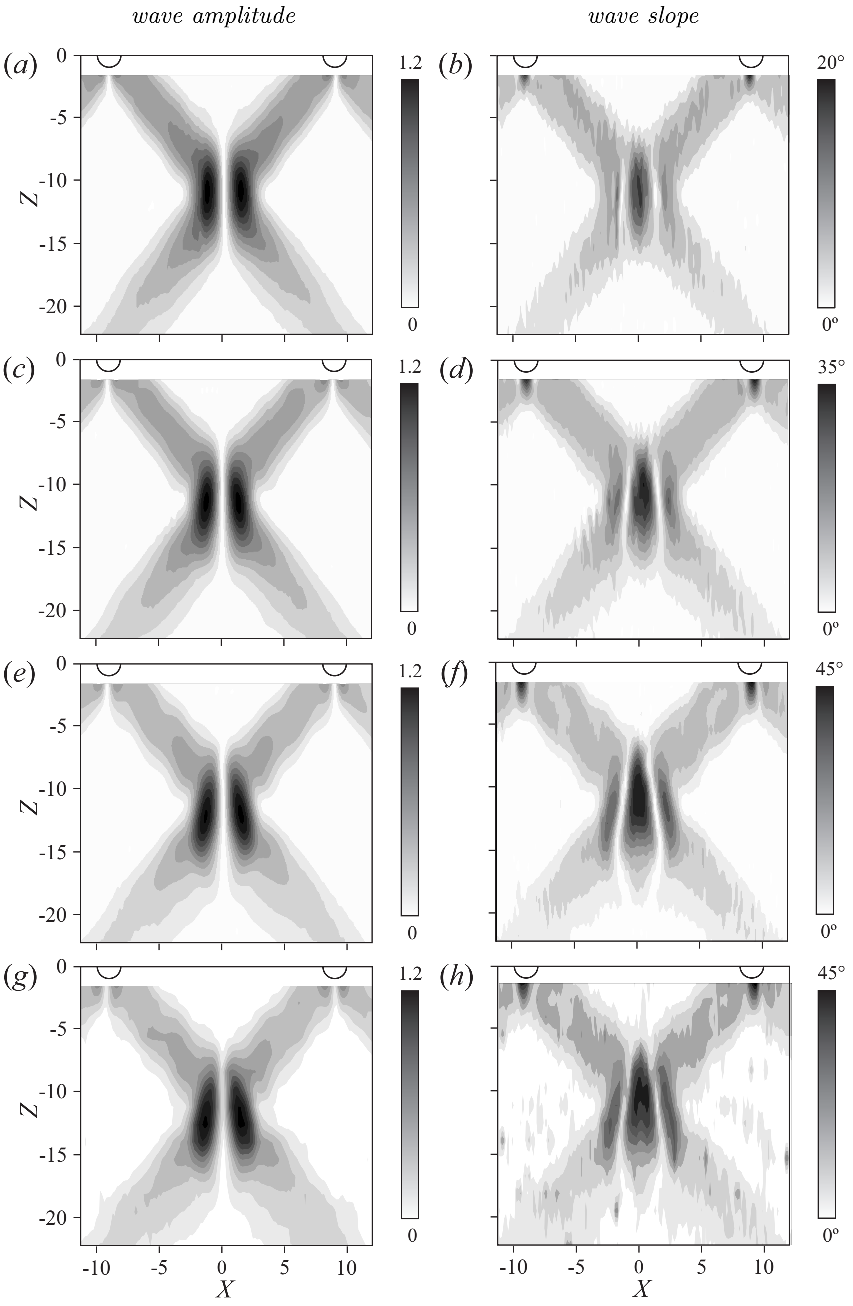

FIGURE 3. Contour plots of the wave amplitude ζ_1/A (left column) and wave slope S_1 (right column) in the XZ-plane, with (a,b) $Ke = 0.19$; (c,d) 0.41 and (e,f) 0.65. (g,h) contour plots for ζ_{max}/A and S_{max} for $Ke = 0.65$. Exp A, with torus aspect ratio $\epsilon = 9$. Data is obtained from LIF measurements.

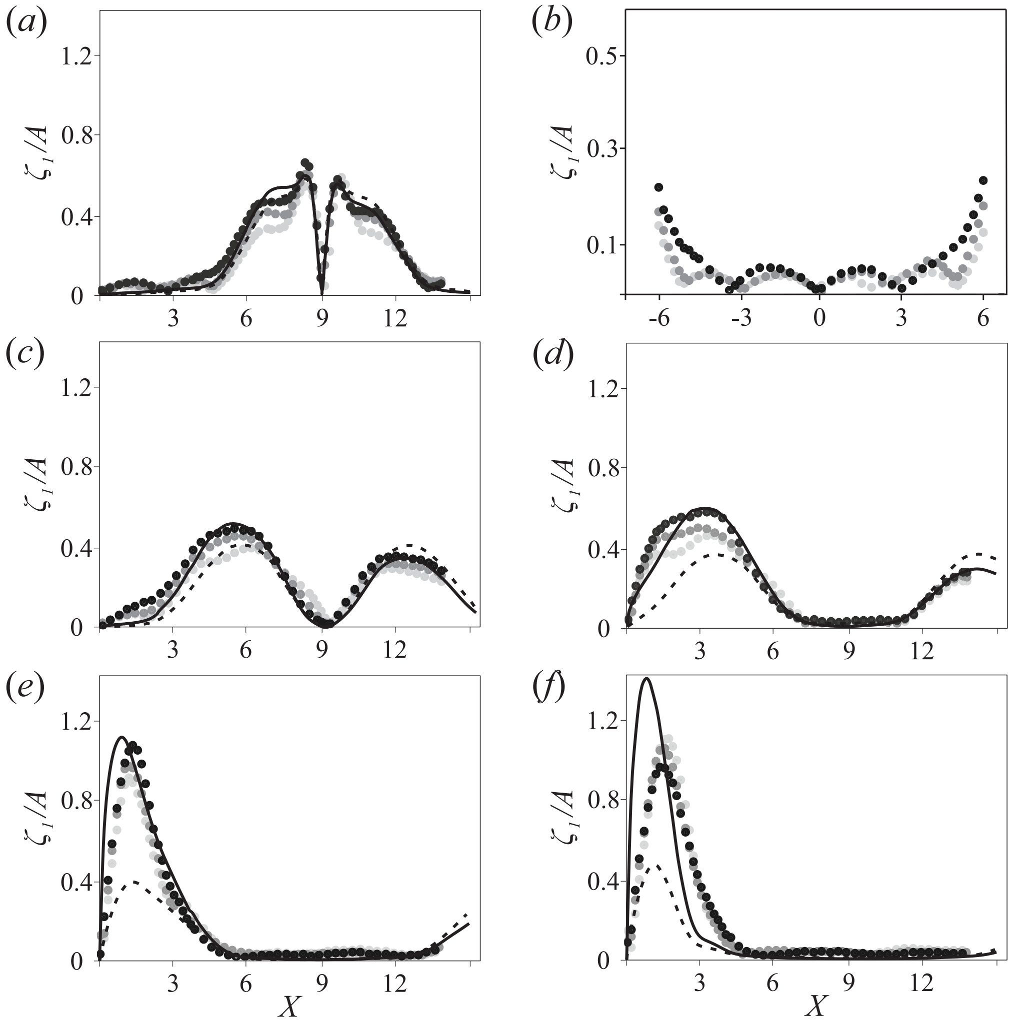

FIGURE 4. Normalized wave amplitude ζ_1/A for Exp A at different heights Z below the centre of the torus, with (a) $Z = -1.84$, (b) $Z = -1.84$ zoomed in including negative values of X (the centre line of the torus is at $X = 0$); (c) $Z = -4.48$; (d) -7.17; (e) -9.84, and (f) -12.51. The focal zone is located at $Z = -11.2$. The dashed and drawn lines represent, respectively, the theoretical profile (eq. (2.4)) obtained for two oscillating cylinders, and the profile corrected for convergence; black, grey and light grey dots correspond respectively to $Ke = 0.19; 0.41$ and 0.65. Data is obtained from LIF experiments.

amplitudes in the focal zone are significantly lower (roughly by 30%) than the theoretical estimate. Indeed the theory presented in §2 neglects the near-field interactions between the wave components in the focal zone, leading to unrealistic infinite wave slopes at the vertical axis Z.

The experimental data presented in figure 4 provide a qualitative information on the non-linear trends in the wave amplitude as function of the oscillation amplitude Ke. With increasing Ke, the normalized wave amplitude of the first harmonic, ζ_1/A typically decreases almost everywhere in the wave field except the focal region: the amplitude profiles marked by light grey and grey symbols are consistently lower than the profiles marked by black symbols. This trend is in agreement with the non-linear trends observed for the two- (Zhang *et al.* 2007) and three-dimensional (Voisin *et al.* 2011; Ermanyuk *et al.* 2011) cases. The opposite trend is seen in figure 4(f) in the focal region at $|Z| = 12.51$ where higher normalized wave amplitudes ζ_1/A correspond to higher Ke. Thus, a linear extrapolation of the low-amplitude experimental data to a high-amplitude case should be done with care: it tends to underestimate the wave amplitudes in localized zones of the focal region and to overestimate the wave amplitudes in all other regions of the wave field. Interestingly, in the middle of the focal region, located around $|Z| = 11.2$, the linear scenario applies in a remarkably wide range of A as discussed below in Section 4.4.

It is worth to make a special remark concerning the data presented in figure 4(b). The low-amplitude standing-wave pattern seen close to the centre of the torus can hardly be interpreted within a linear approach. The whole inner region delimited by the conical wave beams emitted by the torus seems to undergo a weak resonant motion. Its amplitude is typically an order of magnitude smaller than the amplitude of the main wave beams but at high oscillation amplitude A it is high enough to deform the straight wave beams (compare the form of isolines of wave amplitudes in the first column of figure 3 at low and high amplitudes). The mechanism providing the energy flux to this motion is unclear and will be considered elsewhere.

4.3. *Wave pattern in XY-plane*

To study the azimuthal distribution of the wave amplitude, the wave fields in the XY plane were reconstructed from series of images taken particularly in experiments Exp C and Exp D of Table 1. Figures 5 and 6 show the contours of wave amplitudes and the normalized radial distributions of the vertical velocity amplitude of the first harmonic wave, $\zeta_1(R)/(A\cos\phi)$ close to the torus, with ϕ the angle with respect to the plane of symmetry. For this scaling, the data is found to collapse reasonably well on a more or less common curves, for both tori (see figures 5a, 6a). Also we note that the agreement with the linear theory presented in section 2 is within an error of about 10% for both cases. For the thick torus (see figure 6a) the shape of the wave envelope is slightly different due to its bimodal character. Also, here the theoretical prediction is still quite reasonable (note that the original theory of Hurley & Keady (1997), used in section 2 takes bimodality and related viscous effects into account). For larger oscillation amplitudes, the theoretical prediction is systematically higher than the measured values due to nonlinear effects. With increasing azimuthal angle, ϕ , the wave amplitude decreases, and therefore also the energy radiated by the torus. The departure of the observed profiles from the theoretical curve ϕ tending to 90° arises partially due to higher noise-to-signal ratio for these waves, and partially due to the fully three-dimensional nature of the flow. For azimuthal angles close to 90 degrees the cosine variation of wave amplitudes with the azimuthal angle is therefore no longer valid, especially for a thick torus.

4.4. *Nonlinear effects: Maximum wave amplitude and overturning*

The variation of the maximum wave amplitude and maximum slope (measured as in figures 7a, b) with the Keulegan-Carpenter number Ke, are presented in respectively figures 8(a) and (b) for both tori. The overall good agreement between ζ^*_{max}/a and ζ^*_1/a confirms once again the expected dominance of the first harmonic wave for this forcing frequency ($\omega/N > 0.5$). For larger Ke the increasing wave steepness and the increasing difference between S^*_{max} and S^*_1 (see figure 7b) suggest the presence of nonlinear effects. Incipient overturning is observed at $Ke = 0.81$ and $Ke = 1.1$ for tori with $\epsilon = 5$ and $\epsilon = 9$, respectively. From the dye images shown in figure 9, we indeed recognise well-developed overturning regions in the wave pattern. As expected, these regions are located close to

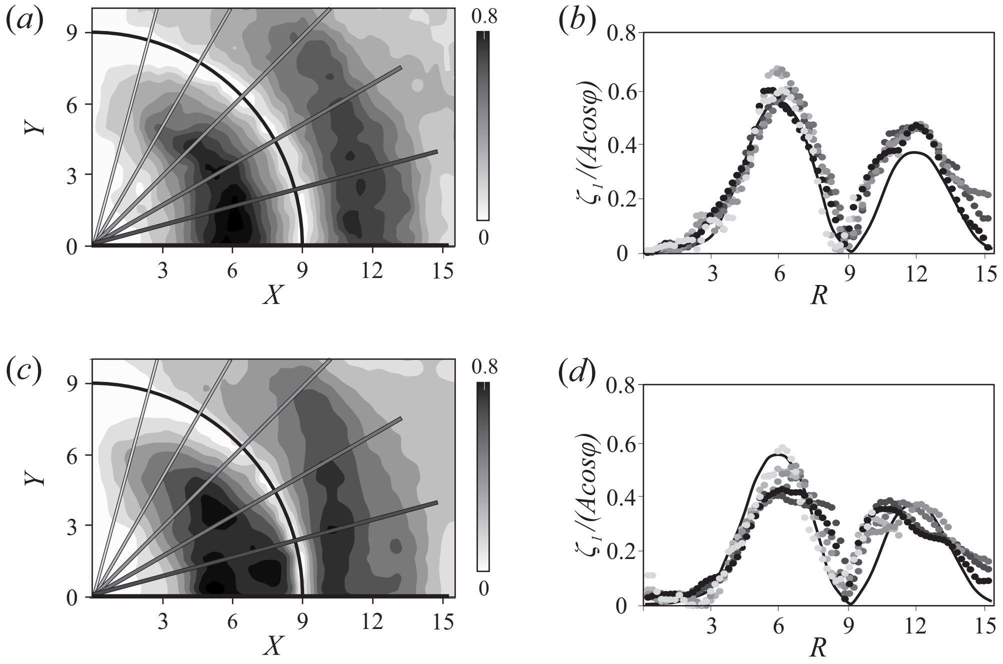

FIGURE 5. Contours of the normalized wave amplitude ζ_1/A (left panel) and the corresponding radial distributions $\zeta_1(R)/(A\cos\varphi)$ (right panel) close to the torus for (a,b) $Ke = 0.17$ and (c,d) $Ke = 0.63$, where $R = r/a$ is the non dimensional radial coordinate. The black lines in (b) and (d) corresponds to eq. (2.4). Exp C in Table 1 ($Z = -3.6$, $\epsilon = 9$). Data is obtained from LIF measurements.

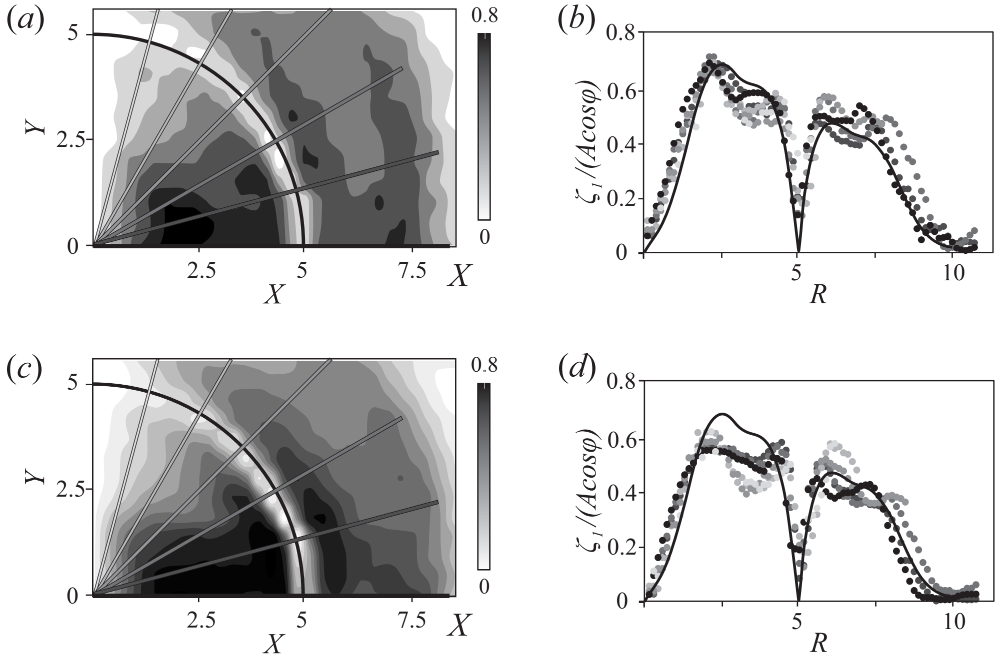

FIGURE 6. As in figure 5 for the thick torus, with (a,b) $Ke = 0.13$ and (c,d) $Ke = 0.29$, where $R = r/a$ is the non dimensional radial coordinate. The black line corresponds to ζ_{corr}. Exp D in Table 1 ($Z = -3.0$, $\epsilon = 5$). Data is obtained from LIF experiments.

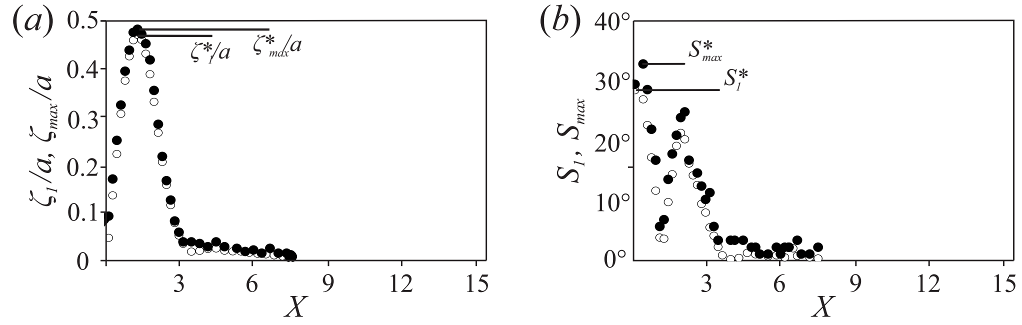

FIGURE 7. LIF measurements of wave amplitude (a) and wave slope (b) in the central plane according to the definitions given in §3.2. Open circles indicate the first harmonic filtered values (ζ_1/a, S_1) and filled circles the unfiltered max-type estimate (ζ_{max}/a, S_{max}). The two represented levels are the focal zone at $Z = -12.51$ for $0 < X < 6$ (open and filled circles). The symbol $*$ refers to the extrema plotted in figure 8. Exp A: $Ke = 0.41$ and $\epsilon = 9$.

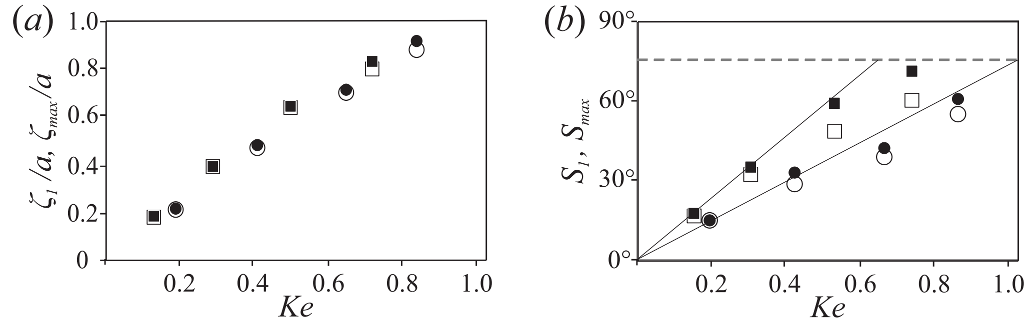

FIGURE 8. Maximum wave amplitude (a) and maximum wave slope (b) against Ke. Filled and open symbols are as in figure 7 with circles for the thin torus with $\epsilon = 9$ (at $Z = -12.51$), and squares for the thick torus with $\epsilon = 5$ (at $Z = -7$). The dashed line at $\theta = 75°$ indicates the slope for which overturning is observed.

the surface of the torus and in the focal region, corresponding to the zones of high local slopes which can be identified in figure 3.

PIV measurements show (see figure 10a) that in the focal region, the horizontal velocity of the first harmonic wave in the direction of oscillation is of the same magnitude as the vertical velocity. With the PIV data in the focal region, the horizontal shear and thus the local Richardson number in the wave can be calculated as

$$Ri = \frac{N^2}{(\partial \hat{u}_1/\partial z)^2},$$

where the stratification N is measured at the start of the experiment; the vertical gradient in velocity is measured from the PIV velocity data over a typical grid distance of $\Delta z =$ 4 pixels (≈ 0.3 cm). The values of the this Ri-number are displayed in grey in figure 10(b). Asymptotically a value of $Ri \approx 0.25$ is reached when Ke approaches a value between 0.8 and 1 for different aspect ratio tori, corresponding for overturning in stratified shear flows (see Miles 1961).

Miles criterion is developed for a flow with vorticity due to the presence of a shear flow, and no baroclinic vorticity in its basic state. For the critical value of $Ri = 0.25$, vorticity of the shear flow is accumulated by the Kelvin Helmholtz instability until breaking occurs. In the present experiments there is no shear flow, and the instability is not of the Kelvin Helmholtz type. However, the amplitude of the waves is here represented by baroclinic vorticity. This amplitude (or baroclinic vorticity) is continuously increased due to focusing of wave energy, until the critical value is reached and breaking occurs. Though the sources of vorticity and mechanism for overturning are essentially different, the present results suggest that the criterion and, as shown below, the critical value are the same.

The LIF method allowed to precisely measure the wave slope of the wave for the different aspect ratio tori. Observations of visualizations showed a nearly linear dependence for $Ke < 0.4$ with the waves remaining linear and passing almost without modification through the focal region. Small changes with respect to the linear regime were found to occur for Ke around 0.6, whereas for approximately $Ke > 0.8$ the onset of wave breaking is observed and waves are hindered to pass through the focal region. From this wave steepness one can derive directly the local wave-Richardson number which can be defined as the ratio between the buoyancy frequency N^2, and the y-component of the baroclinic vorticity of the wave. This yields in the Boussinesq approximation,

$$Ri_{wave} = N^2 \left(\frac{\nabla p \times \nabla \rho}{\rho^2} \right)_y^{-1} \approx \frac{N^2}{-g\rho \frac{\partial \rho}{\partial x}} = \frac{\Delta x}{\Delta z}\Big|_\rho = \frac{1}{\tan S} \tag{4.1}$$

where the index y indicates the y component of the baroclinic vorticity vector. In figure 10(b) the wave Richardson number is displayed as a function of Ke. Even though it is derived in a different manner, it shows also that wave breaking is reached when $Ri_{wave} \approx 0.25$ at $Ke \approx 0.8$ in coherence with the observations and the PIV measurements and shear instability. This local Richardson number indicates the maximum slope which an isopycnal plane may have before it becomes unstable and overturns. This overturning corresponds to a wave slope of $\theta \approx 75^o$ (see figure 8b), the wave slope being measured over a horizontal lengthscale δx (see section 3.1) near X=0 (see figure 11).

5. Conclusions

This paper considers the first experimental results on the geometric focusing of internal waves generated by a horizontally oscillating torus in a linearly stratified fluid. Experiments are conducted in the weakly viscous regime, i.e. for Stokes numbers between 150 and 260. The focusing leads to a strong amplification of the wave amplitude along its ray path with a maximum wave amplitude in the focal point where wave breaking is expected for certain oscillation amplitudes.

A linear wave regime is discerned for $Ke < 0.4$, whereas non-linear effects start to occur at values close to $Ke \approx 0.6$. Incipient wave breaking occurs around $Ke \approx 0.8$, corresponding to a local (shear) Richardson number $Ri = 0.25$, in accordance with classical theory for shear instability. This value coincides with the Richardson number calculated from the wave steepness. Wave breaking occurs for a wave slope of $\theta = 75°$. Nonlinear aspects, as well as the generation of higher harmonics, that occur for these amplitudes, and the effect of higher Stokes numbers are presently under consideration and will be presented elsewhere.

As a first approximation, the focusing wave-field has been approached by making use of the two-dimensional theory of Hurley & Keady (1997) that was adapted by including a term for the wave convergence. This theory shows qualitative agreement with the observed wave field, and gives reasonable quantitative results up to a vertical distance of 5 times the tore radius from the tore centre. However, there is an increasing discrepancy between the data and the theory when approaching the focal zone (see figure 4), for the

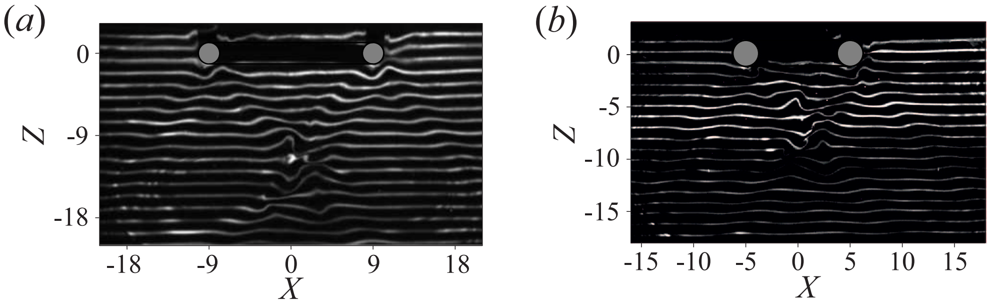

FIGURE 9. Dye visualisation (before data processing) of the overturning of waves profiles in the plane of symmetry for experiments with large-amplitude oscillations. (a) $\epsilon = 9$, $Ke = 0.818$, Exp A in Table 1 and (b) $\epsilon = 5$, $Ke = 1.1$, Exp B in Table 1.

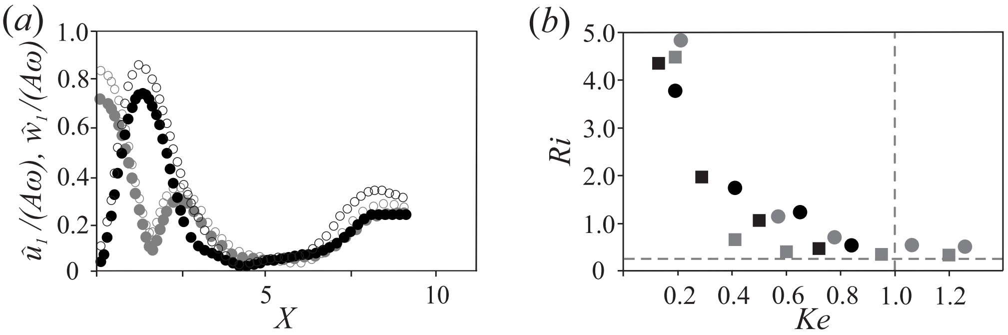

FIGURE 10. PIV measurements results with (a) horizontal and vertical velocity amplitude (respectively grey dots and black dots) along the X-axis in the focal zone at $Z = -4.7$ for $\epsilon = 5$, with $Ke = 0.19$ (filled dots) and $Ke = 0.6$ (open dots); (b) Richardson numbers Ri from PIV data (grey dots) for Exp F, and Ri_{wave} from LIF data (black dots) of experiments A and B in Table 1). The vertical dashed line denotes the $Ke = 1$, and the horizontal line $Ri = 0.25$ corresponding to the onset of overturning.

entire range of wave amplitudes. This difference is about 30% and indicates that the present theory is not satisfactory for the study of the focal region. A three dimensional viscous theory is at present in preparation (Bruno Voisin, personal communications).

Focusing of internal wave energy is a rather recent subject, and opens perspectives to new ways of generating turbulence in the ocean. The overturning in the present experiments has been observed at moderate Reynolds numbers when internal waves are strongly damped by viscous effects. At higher Reynolds numbers the overturning is expected to be more likely to occur. Therefore, internal-wave breaking over other shapes of curved topography (see Bühler & Muller 2007) may serve as an effective mechanism for the generation of 'hot spots' responsible for abyssal mixing. The measurements based on wave steepness allow us to make more precise estimations of the relevance of wave breaking due to wave focusing.

For a realistic bottom topography the effects of viscosity are small. Using the geometric correction for focusing, we may consider whether wave breaking is likely to occur or not. For a M2 tidal oscillation frequency of approximately 12 hours and a typical stratification in the ocean one obtains $\Omega \approx 0.3$ corresponding to an angle of wave propagation of 17 degrees. Considering a large mountain of 2000 m height, and curvature 120 km, i.e. $a = 1$ km, and $b = 60$ km, the oscillation amplitude in the focal region is amplified with a factor $\epsilon^{1/2}$, implying for a typical tidal excursions of $O(100$ m$)$ a wave amplitude of

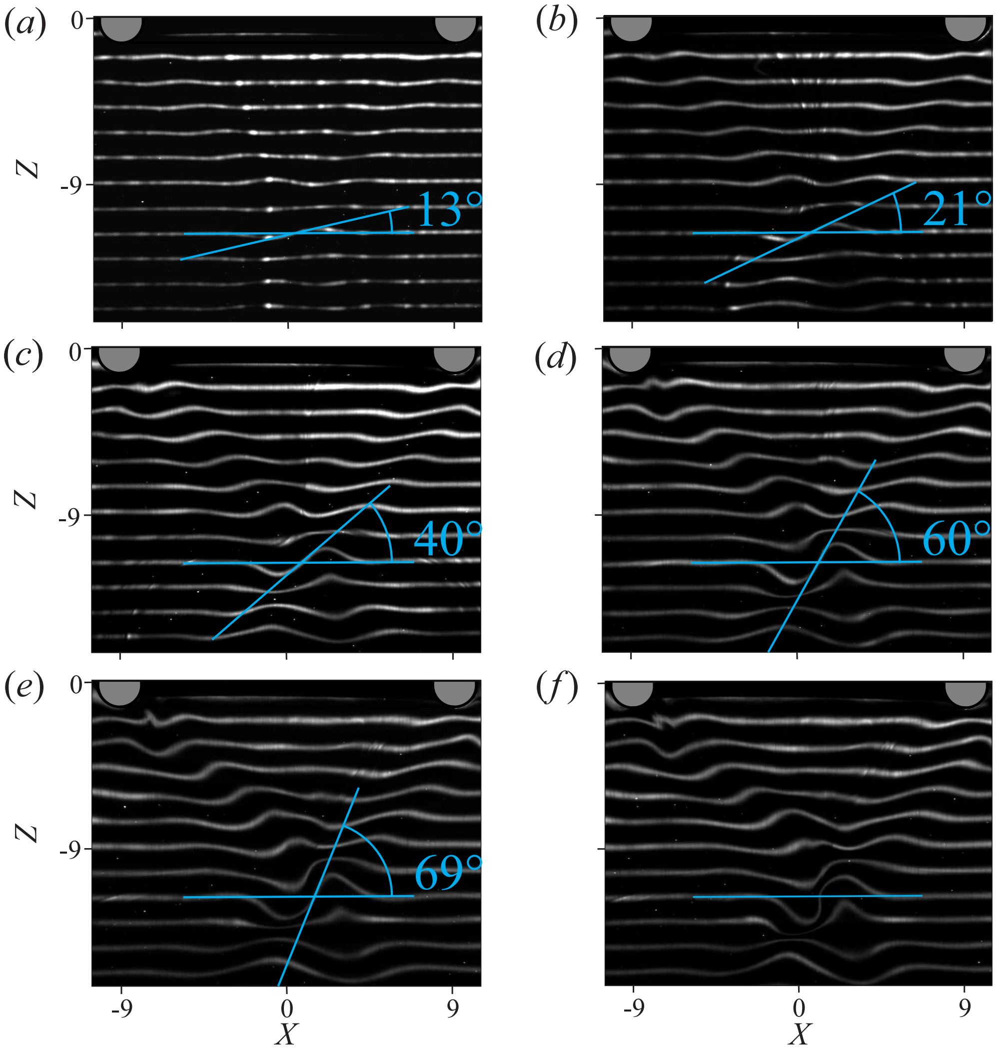

FIGURE 11. Images of dye visualizations of the internal wave field for different oscillation amplitude A: (*a*) 0.19, (*b*) 0.41, (*c*) 0.65, (*d*) 0.84, (*e,f*) 1.1. Images (*a-d*) were taken after 10 periods of oscillation (stable regime), (*e*) and (*f*) were taken after 10 and 12 oscillation periods, respectively.

approximately 800 m. This amplitude is comparable to the size of the generatrix a, which is in turn comparable to the width of internal wave beams. Since the amplitude and the beam width becomes of the same order of magnitude in the focal zone, an overturning can be expected. Note that topographies with nearly-critical local slopes can generate very narrow wave beams, increasing the probability of overturning events even at low Ω typical for the ocean, where $\Omega \approx 0.1$. Thin large ridges as well as thick small ridges of realistic sizes can thus be expected to cause overturning waves due to focusing. Geometric wave focusing could therefore be a candidate for the explanation of recently observed intense mixing regions near spur-shaped mountains (see e.g. Dale & Inall 2015).

The authors acknowledge the referees for a careful reading of the paper, Bruno Voisin for helpful discussions on the theory, and the technical assistance of Pierre-Alain Barraud with the experiments that were conducted at the LEGI. EVE gratefully acknowledges the University of Grenoble Alpes for his appointment as a visiting professor of the at LEGI in February-March 2011. This work has been supported by LabEx Osug@2020 (Investissements d'avenir ANR10LABX56), and grant No.11.G34.31.0035 of Russian Government, by project No. 23.9 of Presidium of RAS and by RFBR grant No. 12-01-00671.

REFERENCES

Bell, T. H. 1975 Lee waves in stratified flows with simple harmonic time dependance. *J. Fluid Mech.* **67**, 705–722.

Bühler, O. 2009 *Waves and Mean Flows*. Cambridge Univ Press.

Bühler, O. & Muller, C. J. 2007 Instability and focusing of internal tides in the deep ocean. *J. Fluid Mech.* **588**, 1–28.

Dale, A. C. & Inall, M. E. 2015 Tidal mixing processes amid small-scale, deep-ocean topography. *Geophys. Res. Lett.* **42**, 484–491.

Dauxois, T. & Young, W. R. 1999 Near-critical reflection of internal waves. *J. Fluid Mech.* **390**, 271–295.

Duran-Matute, M., Flór, J.-B., Godeferd, F. S. & Jause-Labert, C. 2013 Turbulence and columnar vortex formation through inertial-wave focusing. *Phys. Rev. E* **87**, 041001(R).

Echeverri, P., Yokossi, T., Balmforth, N. J. & Peacock, T. 2011 Tidally generated internal-wave attractors between double ridges. *J. Fluid Mech.* **669**, 354–374.

Ermanyuk, E. V. 2000 The use of impulse response functions for evaluation of added mass and damping coefficient of a circular cylinder oscillating in linearly stratified fluid. *Exp. Fluids* **28**, 152–159.

Ermanyuk, E. V., Flór, J.-B. & Voisin, B. 2011 Spatial structure of first and higher harmonic internal waves from a horizontally oscillating sphere. *J. Fluid Mech.* **671**, 364–383.

Ermanyuk, E. V. & Gavrilov, N. V. 2002 Force on a body in a continuously stratified fluid. part 1. circular cylinder. *J. Fluid Mech.* **451**, 421–443.

Ermanyuk, E. V. & Gavrilov, N. V. 2005 Duration of transient processes in the formation of internal-wave beams. *Dokl. Akad. Nauk* **404**, 771–774.

Ermanyuk, E. V. & Gavrilov, N. V. 2008 On internal waves generated by large-amplitude circular and rectilinear oscillations of a circular cylinder in a uniformly stratified fluid. *J. Fluid Mech.* **613**, 329–356.

Ferrari, R. & Wunsch, C. 2008 Ocean circulation kinetic energy: Reservoirs, sources, and sinks. *Annu. Rev. Fluid Mech.* **41**, 253–282.

Fincham, A. & Delerce, G. 2000 Advanced optimization of correlation imaging velocimetry algorithms. *Exp. Fluids* **29**, S013–S022.

Flór, J.-B., Ungarish, M. & Bush, J. W. M. 2002 Spin-up from rest in a stratified fluid: boundary flows. *J. Fluid Mech.* **472**, 51–82.

Flynn, M. R., Onu, K. & Sutherland, B. R. 2003 Internal wave excitation by a vertically oscillating sphere. *J. Fluid Mech.* **494**, 65–93.

Garrett, C. & Kunze, E. 2007 Internal tide generation in the deep ocean. *Annu. Rev. Fluid Mech.* **39**, 57–87.

Gayen, B. & Sarkar, S. 2010 Turbulence during the generation of internal tide on a critical slope. *Phys. Rev. Lett.* **104**, 218502.

Grisouard, N. & Bühler, O. 2012 Forcing of oceanic mean flows by dissipating internal tides. *J. Fluid Mech.* **708**, 250–278.

Guo, Y. & Holmes-Cerfon, M. 2016 Internal wave attractors over random, small-amplitude topography. *J. Fluid Mech.* **787**, 148–174.

Hopfinger, E. J., Flór, J.-B., Chomaz, J. M. & Bonneton, P. 1991 Internal waves generated by a moving sphere and its wake in a stratified fluid. *Exp. Fluids* **11**, 255–261.

Hurley, D. G. 1997 The generation of internal waves by vibrating elliptic cylinders. part 1. inviscid solution. *J. Fluid Mech.* **351**, 105–118.

Hurley, D. G. & Keady, G. 1997 The generation of internal waves by vibrating elliptic cylinders. part 2. approximate viscous solution. *J. Fluid Mech.* **351**, 119–138.

King, B., Zhang, H. P. & Swinney, H. L. 2009 Tidal flow over three-dimensional topography in a stratified fluid. *Phys. Fluids* **21**, 116601.

King, B., Zhang, H. P. & Swinney, H. L. 2010 Tidal flow over three-dimensional topography generates out-of-forcing-plane harmonics. *Geophys. Res. Lett.* **37**, L14606.

Llewellyn Smith, S. G. & Young, W. R. 2002 Conversion of the barotropic tide. *J. Phys. Oceanogr.* **32**, 1554–1566.

Llewellyn Smith, S. G. & Young, W. R. 2003 Tidal conversion at a very steep ridge. *J. Fluid Mech.* **495**, 175–191.

Maas, L. R. M. 2011 Topographies lacking tidal conversion. *J. Fluid Mech.* **684**, 5–24.

Maas, L. R. M., Benielli, D., Sommeria, J. & Lam, F.-P. A. 1997 Observation of an internal wave attractor in a confined, stably stratified fluid. *Nature* **388**, 557–561.

Mathur, M. & Peacock, T. 2009 Internal wave beam propagation in non-uniform stratifications. *J. Fluid Mech.* **639**, 133–152.

Miles, J. W. 1961 On the stability of heterogeneous shear flows. *J. Fluid Mech.* **10**, 496–508.

Morozov, E. G. 1995 Semidiurnal internal wave global field. *Deep-Sea Res. I* **42**, 135–148.

Mowbray, D. E. & Rarity, B. S. H. 1967 A theoretical and experimental investigation of the phase configuration of internal waves of small amplitude in a density stratified liquid. *J. Fluid Mech.* **28**, 1–16.

Newman, J. N. 1977*a* *Marine Hydrodynamics*. MIT Press.

Newman, J. N. 1977*b* The motions of a floating slender torus. *J. Fluid Mech.* **83**, 721–735.

Scolan, H., Ermanyuk, E. & Dauxois, T. 2013 Nonlinear fate of internal wave attractors. *Phys. Rev. Lett.* **110**, 234501.

Sutherland, B. R., Dalziel, S. B., Hughes, G. O. & Linden, P. F. 1999 Visualization and measurement of internal waves by 'synthetic schlieren'. Part 1. Vertically oscillating cylinder. *J. Fluid Mech.* **390**, 93–126.

Sutherland, B. R., Hughes, G. O., Dalziel, S. B. & Linden, P. F. 2000 Internal waves revisited. *Dynam. Atmos. Oceans* **31**, 209–232.

Sutherland, B. R. & Linden, P. F. 2002 Internal wave excitation by a vertically oscillating elliptical cylinder. *Phys. Fluids* **14**, 721–731.

Teoh, S. G., Ivey, G. N. & Imberger, J. 1997 Laboratory study of the interaction between two internal wave rays. *J. Fluid Mech.* **336**, 91–122.

Vlasenko, V., Stashchuk, N. & Hutter, K. 2005 *Baroclinic Tides: Theoretical Modeling and Observational Evidence*. Cambridge University Press.

Vlasenko, V., Stashchuk, N., Inall, M.E., Porter, M. & Aleynik, D. 2016 Focusing of baroclinic tidal energy in a canyon. *J. Geophys. Res. Oceans* **121**, 2824–2840.

Voisin, B. 2003 Limit states of internal wave beams. *J. Fluid Mech.* **496**, 243–293.

Voisin, B., Ermanyuk, E. V. & Flór, J.-B. 2011 Internal wave generation by oscillation of a sphere, with application to internal tides. *J. Fluid Mech.* **666**, 308–357.

Westerweel, J. 1997 Fundamentals of digital particle image velocimetry. *Meas. Sci. Technol.* **8**, 1379–1392.

Wunsch, C. & Ferrari, R. 2004 Vertical mixing, energy, and the general circulation of the oceans. *Annu. Rev. Fluid Mech.* **36**, 281–314.

Xing, J. & Davies, A. M. 2011 On the interaction of internal tides over two adjacent sills in a fjord. *J. Geophys. Res.* **116**, C04022.

Zhang, H.P., King, B. & Swinney, H.L. 2007 Experimental study of internal gravity waves generated by supercritical topography. *Phys. Fluids* **19**, 096602.

Zhang, L. & Swinney, H. L. 2014 Virtual seafloor reduces internal wave generation by tidal flow. *Phys. Rev. Lett.* **112**, 104502.

Appendix C

High Stokes number wave focusing by a circular ridge: Internal, inertial and inertia–gravity waves

High Stokes number wave focusing by a circular ridge: Internal, inertial and inertia–gravity waves

Natalia Shmakova, Jan-Bert Flór, Bruno Voisin, Joel Sommeria and Samuel Viboud

Laboratoire des Écoulements Géophysiques et Industriels (LEGI),
CNRS–Université Grenoble Alpes, F38000, Grenoble, France,
natalia.shmakova@legi.cnrs.fr

Abstract

We consider the focusing and breaking of internal waves generated by the horizontal oscillations of a very large torus mounted at the Coriolis platform, of 13 m diameter. The platform was filled with a linearly stratified fluid and rotated at a constant speed, or stood still to investigate, respectively, inertia–gravity or internal gravity waves. The wave field was measured using 2D or 3D PIV. The large torus size gives access to large Stokes numbers. Nonlinear effects and turbulence are observed in the focal region, but they can be described by linear theory with an eddy viscosity. Spectrum analysis shows the generation of higher harmonics in the focal zone even at low oscillation amplitude. The vertical vorticity field of internal gravity waves exhibits a dipolar structure in the focal zone, which transforms in the rotating case into a "Yin–Yang-shaped" structure. The overall structure of the inertial waves is close to that of internal gravity waves, though the overturning motion in the focal region is relatively intense.

1 Introduction

The generation of internal waves by oscillating objects is a long-standing subject of research in fluid mechanics and has its main applications in the Earth's oceans and atmosphere. In particular, in relation to ocean mixing, internal tides and their overturning have received considerable recent interest (Morozov, 1995; Garrett and Kunze, 2007). Internal tides are believed to transport energy through the ocean interior, and their breaking to cause energy dissipation estimated to be 1 TW .

In the laboratory, generally, waves are generated by two-dimensional objects such as cylinders and ridges, or three-dimensional objects such as spheres and ellipsoids. These are all simply connected objects. We consider a doubly connected object, the torus, which opens up a new possibility: wave focusing, to be considered as a possible scenario for energy concentration in localized zones representing hot spots for incipient overturning in the oceans. Different types of wave focusing exist, for instance when waves reflect on a boundary, in attractors or near density interfaces. Spontaneous geometric focusing may occur for forcing with a specific geometry, like a torus (Bühler and Muller, 2007; Grisouard and Bühler, 2012). Important mixing of stratification due to internal wave focusing of this latter type has been observed by Buijsman et al. (2014) in Luzon Strait, and may be a cause for the mixing observed by Peliz et al. (2009) at Tore seamount.

First experiments on geometric focusing have been conducted by Duran-Matute et al. (2013) who obtained wave turbulence in the focal region for a vertically oscillating torus in a rotating fluid. Ermanyuk et al. (2016) showed with a horizontally oscillating torus in a linearly stratified fluid that at low Stokes numbers $St \approx 200$ the wave amplitude increases toward the focal region, forming one zone of amplitude amplification. In this zone one expects overturning and mixing of waves.

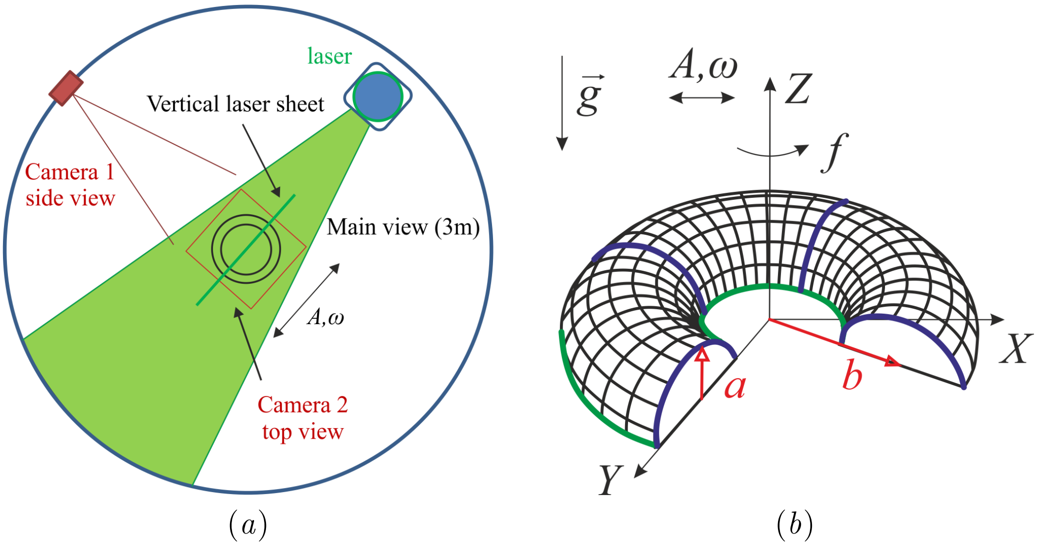

Figure 1: (a) Top view of the experimental setup at the Coriolis platform; (b) geometry of the torus with parameters and notations.

The present experimental results were obtained for a much larger torus of minor radius $a = 15$ cm and major radius $b = 75$ cm, giving access to large Stokes number $St \approx 4500$. They report some new aspects of the dynamics of internal focusing waves in rotating and stratified fluids, and the possibility of wave breaking in the focal region.

2 Experimental setup

Experiments were conducted at the Coriolis platform, a cylindrical tank 13 m in diameter and 1 m of working depth (figure 1a). The platform, which either stood still or rotated, was filled with water linearly stratified in density by salinity to a depth $H = 90$ cm. The stratification was measured with two conductivity probes, moving up and down by a computer-controlled motor. The buoyancy frequency was kept constant for experiments in the stratified fluid at $N = \left(-\frac{g}{\rho}\frac{d\rho}{dz}\right)^{1/2} = 0.5$ rad/s, where $\rho(z)$ is the density profile along the vertical axis, and g is the gravity. In the rotating case the inertial frequency was fixed at $f = 0.2$ rad/s.

In all experiments, waves were generated by the horizontal oscillations of a torus of minor radius $a = 15$ cm and major radius $b = 75$ cm. The oscillations had frequency ω and amplitude A. The torus, made of plexiglas, was cut in half horizontally and fitted upside down on a plexiglas plate kept at the surface of the fluid (see figure 1b). A Cartesian coordinate system is introduced with origin at the centre of the torus, x and y-axes parallel and normal to the direction of oscillations, respectively, and z-axis normal to the free surface. The coordinates X, Y and Z are normalized with the minor radius a.

Waves were visualized with Particle Image Velocimetry (PIV) (Westerweel, 1997) and Volume PIV techniques. For that the fluid was seeded with polystyrene particles of 200 μm in the stratified case, and with Orgasol® 60 μm particles in the rotating case. For a standard PIV measurement the particles were visualised with a vertical laser sheet in the centre plane parallel to the direction of oscillation ($Y = 0$). Images were taken with a 12-bit Dalsa camera of CCD 1024×1024 px. The visualisation of volumes was performed with a horizontal laser sheet moving vertically up and down and the motion of the laser sheet was controlled by a motor. Images in volumes were taken by a Falcon high speed camera with resolution 2432 × 1728 px.

3 Results

Internal waves are generated according to the dispersion relation

$$\omega = \sqrt{f^2 \sin^2 \theta + N^2 \cos^2 \theta}, \tag{1}$$

with θ the angle between the wave beam and the vertical. Depending on whether the fluid is stratified and still ($N \neq 0, f = 0$), or stratified and rotating ($N \neq 0, f \neq 0$), or homogeneous and rotating ($N = 0, f \neq 0$), we shall refer to the waves as internal gravity, inertia–gravity or inertial, respectively. In the present experiments we consider the angle θ to be fixed ($\approx 60°$) for all types of waves for better comparison. In the case of internal gravity waves this angle corresponds to $\omega/N = \arccos\theta = 0.51$, so that all harmonics but the first are evanescent (Mowbray and Rarity, 1967). Measurements are performed at a nondimensional oscillation amplitude $A/a = 0.17$ for all experiments, which is as close as possible given the setup to the tidal oscillation amplitude in the real ocean.

3.1 Vorticity field

The difference between the internal waves generated in stratified and/or rotating fluid is studied by considering the horizontal and vertical vorticity fields. In the presence of rotation (figure 2*b*), inertia–gravity wave motion is found over a bigger region than for internal gravity waves. This is because the waves propagate in beams, with edges at the critical rays tangent to the torus and to its image at the surface. For inertia–gravity waves, these rays turn out to be further apart than for internal gravity waves. The reason for this is unclear, but seems connected with the boundary layer at the mounting plate supporting the torus, since this is where reflection takes place. As a consequence, there are four clearly identifiable separate zones of critical ray intersection in figure 2 (*b*), compared with one single diamond-shaped zone of intersection of wave beams in figure 2 (*a*). The vertical vorticity field of internal gravity waves exhibits a dipolar structure in the focal zone, which transforms for inertia–gravity waves into a "Yin–Yang-shaped" structure (figure 2*d,e*). The overall structure of the inertial wave beams (figure 2*c*) resembles that for internal gravity waves. The overturning motion in the focal region is intense, and results there in a vertically standing inertial wave motion with alternating red-blue vorticity (McEwan, 1973).

The three-dimensional view of the vertical vorticity field was reconstructed from the Volume PIV measurements, and its isosurfaces are presented in figures 3 (*a*) and (*b*) for internal gravity and inertia–gravity waves, respectively. The presence of a dipolar vortex for the nonrotating stratified fluid demonstrates nonlinear effects in the focal zone of internal gravity waves (figure 3*a*). The vorticity structure for inertia–gravity waves reveals that the positive and negative vortices are twisted around each other (figure 3*b*). This motion takes place through 2/3 of the depth. The Rossby radius of deformation was calculated as $R = (Nh)/f$, with $h = 2H/3$, and predicts the size of the vortex to be 150 cm, close to what has been observed.

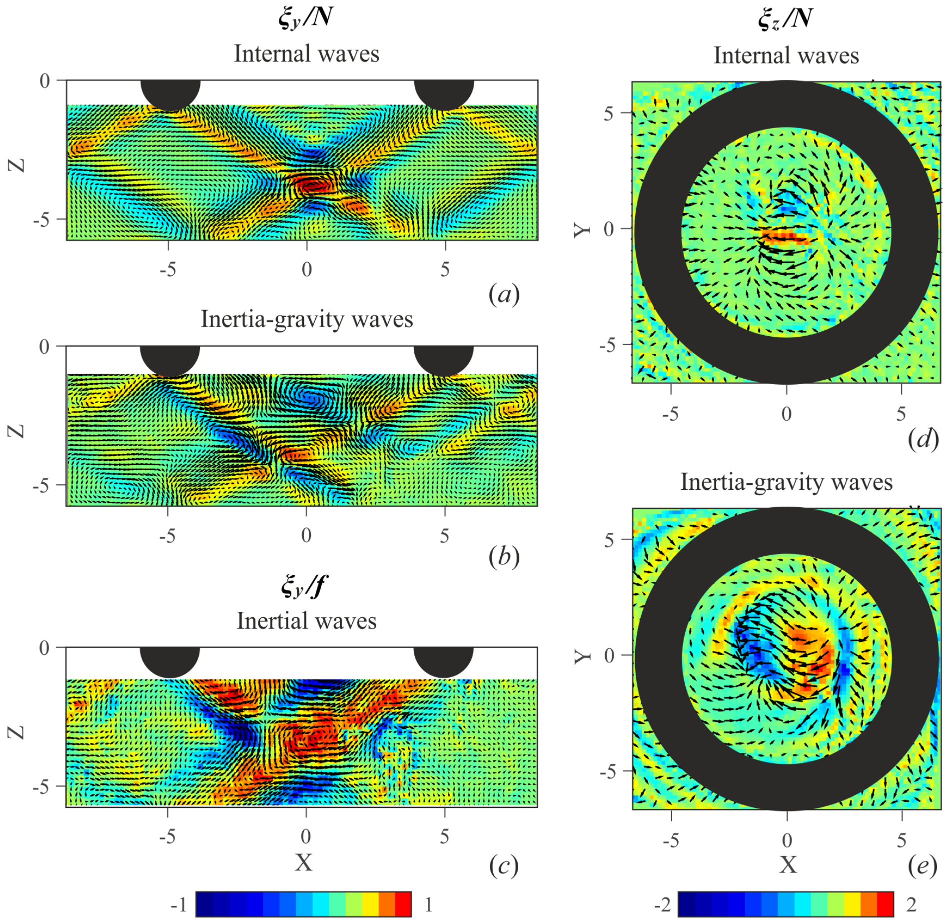

Figure 2: Instantaneous velocity vectors together with (a-c) instantaneous horizontal transverse vorticity, ξ_y/N or ξ_y/f, in the vertical plane of oscillation $Y = 0$ (the color scale is the same in all three images), and (d,e) vertical vorticity, ξ_z/N, in the horizontal plane through the centre $Z = -4$ of the focal zone for internal gravity waves (the color scale is the same in both images).

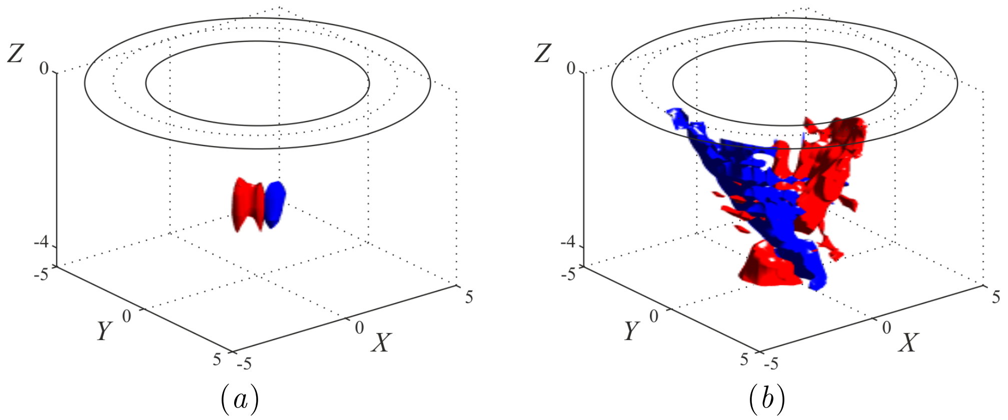

Figure 3: Isosurface of the instantaneous vertical vorticity field $\xi_z/N = \pm 0.6$, reconstructed from the volume PIV measurements for (a) internal gravity waves and (b) inertia–gravity waves. Red and blue colors indicate positive and negative vorticities, respectively. The horizontal section of the torus at $Z = 0$ is shown with black curves.

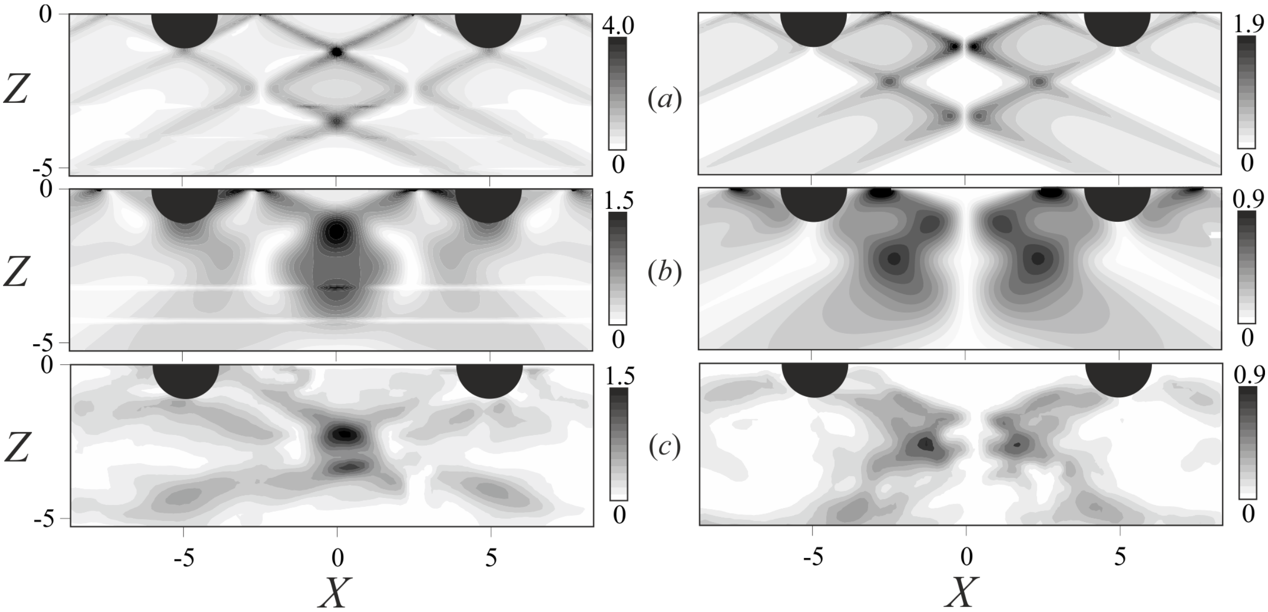

Figure 4: Horizontal velocity amplitude U_1 (left column) and vertical velocity amplitude W_1 (right column) internal gravity waves in the vertical plane of symmetry $Y = 0$: (a) theoretical predictions based on molecular viscosity; (b) theoretical predictions based on eddy viscosity $\nu = 0.4$ m^2/s; (c) experimental results after filtering the first harmonic. The occurrence of spurious maxima at $Z = 0$ in the theory is discussed in Voisin (2016).

3.2 Comparison with the linear theory

The linear theory described in Voisin (2016) allows us to calculate the amplitude of internal gravity waves which may be expected for high Stokes number $St = (\omega a^2)/\nu = 4500$, with $\nu = 0.01$ cm^2/s the molecular viscosity. These results are presented in figure 4 (a) for the horizontal longitudinal U_1 and vertical W_1 velocity components in the vertical plane $Y = 0$, and show the bimodal structure of the wave beams. Comparing this with experimental results in figure 4 (c), one notices a difference in structure. This difference can be caused by mixing in the turbulent boundary layer at the surface of the torus. Theoretical formulas can be therefore recalculated with an eddy viscosity $\nu_{eddy} = 0.4$ cm^2/s $\gg \nu$. These results are presented in figure 4 (b) and show better agreement with the experiment in figure 4 (c). The focal zone is formed of two zones of amplitude amplification in the centre for the horizontal velocity and four zones of amplitude amplification for the vertical velocity. Another specificity of the experimental wave beams is the origin of generation. The upper critical ray delimiting the wave beam is vertically shifted downwards compared with the theoretical calculations, and with the experimental and numerical observations for a hemisphere (King et al., 2009). As a consequence, the upper part of the focal zone is lower than predicted. This shift is caused by the turbulent motion close to the surface of the fluid and to the mounting plate. However the lower part of the focal region is well predicted by the linear theory calculated with eddy viscosity ν_{eddy} (see figure 4b and c at $Z = -3$ for the horizontal longitudinal velocity and $Z = -2.5$ for the vertical velocity).

The internal gravity and inertia–gravity waves are compared in terms of the vertical distribution of the horizontally averaged total kinetic energy. Amplification is observed in the focal zone in the stratified case, and also close to the surface in the rotating stratified case (figure 5a).

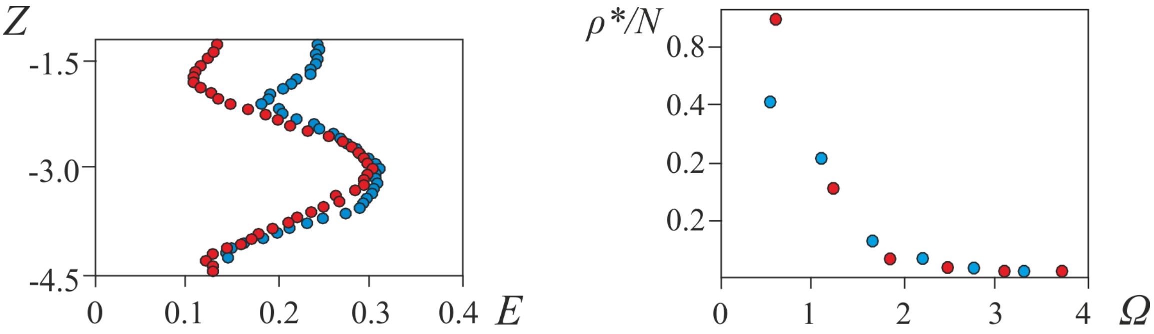

(a) (b)

Figure 5: (a) Vertical distribution of total kinetic energy averaged along the horizontal; (b) Fourier-filtered density amplitude ρ^* against normalized oscillation frequency, $\Omega = \omega/N$, based on conductivity data from the probe in the focal zone. Blue and red dots represent results for internal gravity and inertia–gravity waves, respectively.

3.3 Time-frequency representation

The time–frequency representation (see e.g. Flandrin, 1999) is performed for the horizontal longitudinal velocity u:

$$S(t,\omega) = \left\langle \left| \int_{-\infty}^{+\infty} du\ u \exp^{-i\omega u} h(t-u) \right|^2 \right\rangle_{xy}, \tag{2}$$

where $h(t) = 0.54 - 0.46\cos(\omega t)$ is a Hamming window. Figures 6 (a) and (b) show the result averaged over a small area close to the torus and in the focal zone, respectively. Close to the torus the first two harmonics of internal gravity waves appear. In the focal zone the nonlinear interactions result even for low oscillation amplitude $A/a = 0.17$ in the generation of evanescent higher harmonics after four oscillation periods. From the experimental results we notice that with the present sizes of the object and experimental tank nonlinear effects always take place in the focal region, by contrast with the observations at lower sizes by Ermanyuk et al. (2016). Fourier filtering of the density signal obtained with a conductivity probe in the focal zone (figure 5b) shows that the density amplitude normalised with the buoyancy frequency, ρ^*/N, has a maximum at the fundamental frequency and decreases nearly exponentially with increasing harmonic frequency $n\omega/N$ for internal gravity as well as for inertia–gravity waves. This result is in agreement with that obtained from the velocity field (figure 6b) which also shows qualitatively a decrease in energy with increasing frequency $n\Omega$. Therefore, the energy distribution is similar for internal gravity and inertia–gravity waves.

4 Conclusions

We have measured the 3D wave structure for internal gravity, inertial and inertia–gravity waves. The horizontal vorticity field has a similar structure for internal gravity and inertial waves, though the intensity of the motion is higher for inertial waves and the vorticity spreads through the entire depth due to energy loss by diapycnal mixing. In the case of both rotation and stratification four vortices have been observed in the focal region. The vorticity field demonstrates the presence of nonlinear effects in the focal zone which cause dipolar motion. For inertia–gravity waves this motion is twisted and spreads through

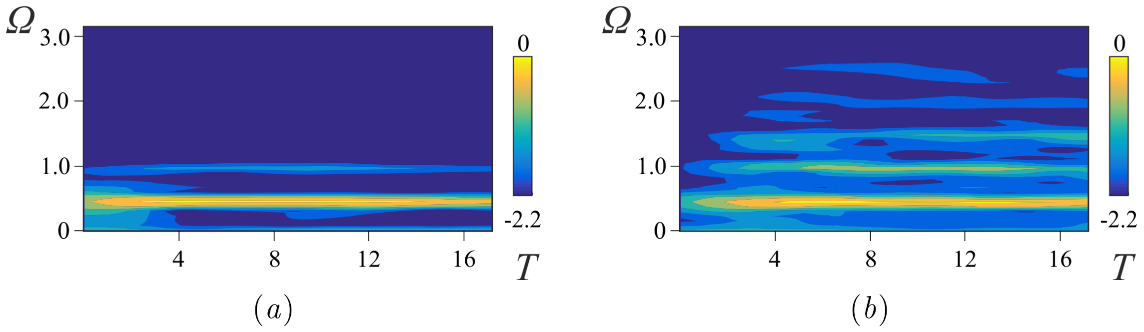

Figure 6: Time–frequency diagram of $\log_{10}(S_U(t,\omega)/S(t,\omega_0))$ for internal gravity waves. The horizontal velocity u is averaged over areas (a) $-5 < X < -4$, $Y = 0$, $-1.7 < Z < -1$ (near field) and (b) $-1 < X < 1$, $Y = 0$, $-4 < Z < -2.6$ (focal zone). The experimental parameters are $N = 0.5$ rad/s, $\omega/N = 0.51$, $A/a = 0.17$ and the normalized variables are $\Omega = \omega/N$ and $T = (\omega t)/2\pi$.

2/3 of the fluid depth. The size of the vortex is well predicted by the Rossby radius of deformation.

Spectral analysis of the velocity and density in the focal zone shows the generation of higher harmonics due to wave beam interaction. Most of the energy is in the fundamental wave, whereas the higher harmonics are evanescent and their energy decreases exponentially.

Our large scale experiment, providing Stokes number of 4500, generates turbulence in the focal region, a source of mean flow generation and mixing. The effect of this turbulence on the wave beam can be taken into account by means of an eddy viscosity.

Acknowledgements

NS, JBF and BV acknowledge funding by LabEx OSUG@2020 (Investissements d'avenir ANR10 LABX56), and BV also by the Del Duca Foundation of the Institut de France.

References

Bühler, O. and Muller, C. (2007). Instability and focusing of internal tides in the deep ocean. *J. Fluid Mech.*, 588:1–28.

Buijsman, M., Klymak, J., Legg, S., Alford, M., Farmer, D., MacKinnon, J., Nash, J., Park, J.-H., Pickering, A., and Simmons, H. (2014). Three-dimensional double-ridge internal tide resonance in Luzon strait. *J. Phys. Oceanogr.*, 44:850–869.

Duran-Matute, M., Flór, J.-B., Godeferd, F. S., and Jause-Labert, C. (2013). Turbulence and columnar vortex formation through inertial-wave focusing. *Phys. Rev. E*, 87:041001(R).

Ermanyuk, E., Shmakova, N., and Flór, J.-B. (2016). Internal wave focusing by a horizontally oscillating torus. *accepted for J. Fluid Mech.*

Flandrin, P. (1999). *Time–Frequency/Time–Scale Analysis.* Academic Press, San Diego.

Garrett, C. and Kunze, E. (2007). Internal tide generation in the deep ocean. *Annu. Rev. Fluid Mech.*, 39:57–87.

Grisouard, N. and Bühler, O. (2012). Forcing of oceanic mean flows by dissipating internal tides. *J. Fluid Mech.*, 708:250–278.

King, B., Zhang, H. P., and Swinney, H. L. (2009). Tidal flow over three-dimensional topography in a stratified fluid. *Phys. Fluids*, 21:116601.

McEwan, A. D. (1973). A laboratory demonstration of angular momentum mixing. *Geophys. Fluid Dyn.*, 5:283–311.

Morozov, E. G. (1995). Semidiurnal internal wave global field. *Deep-Sea Res I*, 42:135–148.

Mowbray, D. E. and Rarity, B. S. H. (1967). A theoretical and experimental investigation of the phase configuration of internal waves of small amplitude in a density stratified liquid. *J. Fluid Mech.*, 28:1–16.

Peliz, A., Le Cann, B., and Mohn, C. (2009). Circulation and mixing in a deep submerged crater: Tore seamount. *Geophysical Research Abstracts*, 11:EGU2009–7567.

Voisin, B. (2016). Internal wave focusing by annular forcing. *This conference.*

Westerweel, J. (1997). Fundamentals of digital particle image velocimetry. *Measurement Science and Technology*, 8:1379–1392.

References

Akylas, T. R. & Karimi, H. H. 2012 Oblique collisions of internal wave beams and associated resonances. *J. Fluid Mech.* **711**, 337–363.

Alford, M. H., MacKinnon, J. A., Nash, J. D., Simmons, H., Pickering, A., Klymak, J. M., Pinkel, R., Sun, O., Rainville, L., Musgrave, R., Beitzel, T., Fu, K.-H. & Lu, C.-W. 2011 Energy flux and dissipation in Luzon Strait: Two tales of two ridges. *J. Phys. Oceanogr.* **41**, 2211–2222.

Allshouse, M. R., Lee, F. M., Morrison, P. J. & Swinney, H. L. 2016 Internal wave pressure, velocity, and energy flux from density perturbations. *Phys. Rev. Fluids* **1**, 014301.

Appleby, J. C. & Crighton, D. G. 1987 Internal gravity waves generated by oscillations of a sphere. *J. Fluid Mech.* **183**, 439–450.

Baines, P. G. 1982 On internal tide generation models. *Deep-Sea Res. A* **29**, 307–338.

Baines, P. G. 1986 Internal tides, internal waves and near-inertial motions. In *Baroclinic Processes on Continental Shelves* (ed. C. N. K. Mooers), pp. 19–31. Wiley.

Baines, P. G. & Fung, X.-H. 1985 Internal tide generation at a continental shelf/slope junction: a comparison between theory and a laboratory experiment. *Dynam. Atmos. Oceans* **9**, 297–314.

Balmforth, N. J., Ierley, G. R. & Young, W. R. 2002 Tidal conversion by subcritical topography. *J. Phys. Oceanogr.* **32**, 2900–2914.

Balmforth, N. J. & Peacock, T. 2009 Tidal conversion by supercritical topography. *J. Phys. Oceanogr.* **39**, 1965–1974.

Bell, T. H. 1975*a* Lee waves in stratified flows with simple harmonic time dependance. *J. Fluid Mech.* **67**, 705–722.

Bell, T. H. 1975*b* Topographically generated internal waves in the open ocean. *J. Geophys. Res.* **80**, 320–327.

Bigot, B., Bonometti, T., Lacaze, L. & Thual, O. 2014 A simple immersed-boundary method for solid–fluid interaction in constant-and stratified-density flows. *Comput. Fluids* **97**, 126–142.

Bourget, B., Dauxois, T., Joubaud, S. & Odier, P. 2013 Experimental study of parametric subharmonic instability for internal plane waves. *J. Fluid Mech.* **723**, 1–20.

Bourget, B., Scolan, H., Dauxois, T., Le Bars, M., Odier, P. & Joubaud, S. 2014 Finite-size effects in parametric subharmonic instability. *J. Fluid Mech.* **759**, 739–750.

Boussinesq, J. 1903 *Théorie Analytique de la Chaleur*, , vol. 2. Gauthier–Villars.

Boyer, D. L. & Zhang, X. 1990*a* The interaction of time-dependent rotating and stratified flow with isolated topography. *Dyn. Atmos. Oceans* **14**, 543–575.

Boyer, D. L. & Zhang, X. 1990*b* Motion of oscillatory currents past isolated topography. *J. Phys. Oceanogr.* **20**, 1425–1448.

Brekhovskikh, L. M. & Goncharov, V. 1994 *Mechanics of Continua and Wave*. Springer.

Brouzet, C., Ermanyuk, E. V., Joubaud, S., Sibgatullin, I. & Dauxois, T. 2016*a* Energy cascade in internal-wave attractors. *Europhys. Lett.* **113**, 44001.

Brouzet, C., Sibgatullin, I. N., Scolan, H., Ermanyuk, E. V. & Dauxois, T. 2016*b* Internal wave attractors examined using laboratory experiments and 3D numerical simulations. *J. Fluid Mech.* **793**, 109–131.

Bühler, O. 2009 *Waves and Mean Flows*. Cambridge Univ Press.

Bühler, O. & Muller, C. J. 2007 Instability and focusing of internal tides in the deep ocean. *J. Fluid Mech.* **588**, 1–28.

Buijsman, M. C., Klymak, J. M., Legg, S., Alford, M. H., Farmer, D., MacKinnon, J. A., Nash, J. D., Park, J.-H., Pickering, A. & Simmons, H. 2014 Three-dimensional double-ridge internal tide resonance in Luzon Strait. *J. Phys. Oceanogr* **44**, 850–869.

Buijsman, M. C., Legg, S. & Klymak, J. 2012 Double-ridge internal tide interference and its effect on dissipation in Luzon Strait. *J. Phys. Oceanogr* **42**, 1337–1356.

Clark, H. A. & Sutherland, B. R. 2009 Schlieren measurements of internal waves in non-Boussinesq fluids. *Exp. Fluids* **47**, 183–193.

Cortet, P.-P., Lamriben, C. & Moisy, F. 2010 Viscous spreading of an inertial wave beam in a rotating fluid. *Phys. Fluids* **22**, 086603.

Dale, A. C. & Inall, M. E. 2015 Tidal mixing processes amid small-scale, deep-ocean topography. *Geophys. Res. Lett.* **42**, 484–491.

Dalziel, S. B., Hughes, G. O. & Sutherland, B. R. 2000 Whole-field density measurements by 'synthetic schlieren'. *Exp. Fluids* **28**, 322–335.

Dauxois, T. & Young, W. R. 1999 Near-critical reflection of internal waves. *J. Fluid Mech.* **390**, 271–295.

Décamp, S., Kozack, C. & Sutherland, B. R. 2008 Three-dimensional schlieren measurements using inverse tomography. *Exp. Fluids* **44**, 747–758.

Dossmann, Y., Paci, A., Auclair, F. & Floor, J. W. 2011 Simultaneous velocity and density measurements for an energy-based approach to internal waves generated over a ridge. *Exp. Fluids* **51**, 1013–1028.

Duran-Matute, M., Flór, J.-B., Godeferd, F. S. & Jause-Labert, C. 2013 Turbulence and columnar vortex formation through inertial-wave focusing. *Phys. Rev. E* **87**, 041001(R).

Echeverri, P., Flynn, M. R., Winters, K. B. & Peacock, T. 2009 Low-mode internal tide generation by topography: an experimental and numerical investigation. *J. Fluid Mech.* **636**, 91–108.

Echeverri, P. & Peacock, T. 2010 Internal tide generation by arbitrary two-dimensional topography. *J. Fluid Mech.* **659**, 247–266.

Echeverri, P., Yokossi, T., Balmforth, N. J. & Peacock, T. 2011 Tidally generated internal-wave attractors between double ridges. *J. Fluid Mech.* **669**, 354–374.

Egbert, G. D. & Ray, R. D. 2000 Significant dissipation of tidal energy in the deep ocean inferred from satellite altimeter data. *Nature* **405**, 775–778.

Egbert, G. D. & Ray, R. D. 2001 Estimates of M2 tidal energy dissipation from TOPEX/Poseidon altimeter data. *J. Geophys. Res.* **106**, 22475–22502.

Ekman, V. W. 1906 On dead water. In *The Norwegian North Polar Expedition 1893–1896. Scientific Results* (ed. F. Nansen), , vol. 5, pp. 1–152. Longmans, Green & Co.

Ermanyuk, E. V. 2002 The rule of affine similitude for the force coefficients of a body oscillating in a uniformly stratified fluid. *Exp. Fluids* **32**, 242–251.

Ermanyuk, E. V., Flór, J.-B. & Voisin, B. 2011 Spatial structure of first and higher harmonic internal waves from a horizontally oscillating sphere. *J. Fluid Mech.* **671**, 364–383.

Ermanyuk, E. V. & Gavrilov, N. V. 2005 Duration of transient processes in the formation of internal-wave beams. *Dokl. Akad. Nauk* **404**, 771–774.

Ermanyuk, E. V. & Gavrilov, N. V. 2008 On internal waves generated by large-amplitude circular and rectilinear oscillations of a circular cylinder in a uniformly stratified fluid. *J. Fluid Mech.* **613**, 329–356.

Ferrari, R. & Wunsch, C. 2008 Ocean circulation kinetic energy: Reservoirs, sources, and sinks. *Annu. Rev. Fluid Mech.* **41**, 253–282.

Fincham, A. & Delerce, G. 2000 Advanced optimization of correlation imaging velocimetry algorithms. *Exp. Fluids* **29**, 13–22.

Flandrin, P. 1998 *Time–Frequency/Time–Scale Analysis*. Academic Press.

Flór, J.-B., Ungarish, M. & Bush, J. W. M. 2002 Spin-up from rest in a stratified fluid: boundary flows. *J. Fluid Mech.* **472**, 51–82.

Flynn, M. R., Onu, K. & Sutherland, B. R. 2003 Internal wave excitation by a vertically oscillating sphere. *J. Fluid Mech.* **494**, 65–93.

Fortuin, J. M. H. 1960 Theory and application of two supplementary methods of constructing density gradient columns. *J. Polym. Sci.* **44**, 505–515.

Franklin, B. 1769 *Experiments and Observations on Electricity*. 4th edn.

Garrett, C. & Kunze, E. 2007 Internal tide generation in the deep ocean. *Annu. Rev. Fluid Mech.* **39**, 57–87.

Gayen, B. & Sarkar, S. 2010 Turbulence During the Generation of Internal Tide on a Critical Slope. *Phys. Rev. Lett.* **104**, 218502.

Gerkema, T., Lam, F.-P. A. & Maas, L. R. M. 2004 Internal tides in the Bay of Biscay: conversion rates and seasonal effects. *Deep Sea Res.* **51**, 2995–3008.

Ghaemsaidi, S.J. & Peacock, T. 2013 3D Stereoscopic PIV visualization of the axisymmetric conical internal wave field generated by an oscillating sphere. *Exp. Fluids* **54**, 1454.

Ghaemsaidi, S. J., Joubaud, S., Dauxois, T., Odier, P. & Peacock, T. 2016 Nonlinear internal wave penetration via parametric subharmonic instability. *Physics of Fluids (1994-present)* **28**, 011703.

Görtler, H. 1943 Über eine Schwingungserscheinung in Flüssigkeiten mit stabiler Dichteschichtung. *Z. Angew. Math. Mech.* **23**, 65–71.

Gostiaux, L., Didelle, H., Mercier, S. & Dauxois, T. 2007 A novel internal waves generator. *Exp. Fluids* **42**, 123–130.

Grisouard, N. & Bühler, O. 2012 Forcing of oceanic mean flows by dissipating internal tides. *J. Fluid Mech.* **708**, 250–278.

Grisouard, N., Leclair, M., Gostiaux, L. & Staquet, C. 2013 Large scale energy transfer from an internal gravity wave reflecting on a simple slope. *Procedia IUTAM* **8**, 119–128.

Guo, Y. & Davies, P. A. 2003 Laboratory modelling experiments on the flow generated by the tidal motion of a stratified ocean over a continental shelf. *Cont. Shelf Res.* **23**, 193–212.

Hazewinkel, J., Maas, L. R. M. & Dalziel, S. B. 2011 Tomographic reconstruction of internal wave patterns in a paraboloid. *Exp. Fluids* **50**, 247–258.

Holloway, P. E. & Merrifield, M. A. 1999 Internal tide generation by seamounts, ridges, and islands. *J. Geophys. Res. Oceans* **104**, 25937–25951.

Hopfinger, E. J., Flór, J.-B., Chomaz, J. M. & Bonneton, P. 1991 Internal waves generated by a moving sphere and its wake in a stratified fluid. *Exp. Fluids* **11**, 255–261.

Hurley, D. G. 1997 The generation of internal waves by vibrating elliptic cylinders. Part 1. Inviscid solution. *J. Fluid Mech.* **351**, 105–118.

Hurley, D. G. & Keady, G. 1997 The generation of internal waves by vibrating elliptic cylinders. Part 2. Approximate viscous solution. *J. Fluid Mech.* **351**, 119–138.

Ivanov, A. V. 1989 Generation of internal waves by an oscillating source. *Izv. Atmos. Ocean. Phys.* **25**, 61–64.

Jiang, C.-H. & Marcus, P. S. 2009 Selection Rules for the Nonlinear Interaction of Internal Gravity Waves. *Phys. Rev. Lett.* **102**, 124502.

Khatiwala, S. 2003 Generation of internal tides in an ocean of finite depth: analytical and numerical calculations. *Deep Sea Res. I* **50**, 3–21.

Killworth, P. D. 1983 Deep convection in the world ocean. *Rev. Geophys.* **21**, 1–26.

King, B., Zhang, H. P. & Swinney, H. L. 2009 Tidal flow over three-dimensional topography in a stratified fluid. *Phys. Fluids* **21**, 116601.

King, B., Zhang, H. P. & Swinney, H. L. 2010 Tidal flow over three-dimensional topography generates out-of-forcing-plane harmonics. *Geophys. Res. Lett.* **37**, L14606.

Klymak, J. M., Buijsman, M., Legg, S. & Pinkel, R. 2013 Parameterizing surface and internal tide scattering and breaking on supercritical topography: The one-and two-ridge cases. *J. Phys. Oceanogr.* **43**, 1380–1397.

Korobov, A. S. & Lamb, K. G. 2008 Interharmonics in internal gravity waves generated by tide–topography interaction. *J. Fluid Mech.* **611**, 61–95.

Kunze, E. 1990 The evolution of salt fingers in inertial wave shear. *J. Marine Res.* **48**, 471–504.

Lam, F.-P. A. & Maas, L. R. M. 2008 Internal wave focusing revisited; a reanalysis and new theoretical links. *Fluid Dyn. Res.* **40**, 95–122.

Lam, F.-P. A, Maas, L. R. M. & Gerkema, T. 2004 Spatial structure of tidal and residual currents as observed over the shelf break in the Bay of Biscay. *Deep Sea Res.* **51**, 1075–1096.

Lamb, K. G. 2004 Nonlinear interaction among internal wave beams generated by tidal flow over supercritical topography. *Geophys. Res. Lett.* **31**, L09313.

Lighthill, J. 1978 *Waves in Fluids*. Cambridge University Press.

Lim, K., Ivey, G. N. & Jones, N. L. 2010 Experiments on the generation of internal waves over continental shelf topography. *J. Fluid Mech.* **663**, 385–400.

Llewellyn Smith, S. G. & Young, W. R. 2002 Conversion of the barotropic tide. *J. Phys. Oceanogr.* **32**, 1554–1566.

Llewellyn Smith, S. G. & Young, W. R. 2003 Tidal conversion at a very steep ridge. *J. Fluid Mech.* **495**, 175–191.

Maas, L. R. M. 2011 Topographies lacking tidal conversion. *J. Fluid Mech.* **684**, 5–24.

Maas, L. R. M., Benielli, D., Sommeria, J. & Lam, F.-P. A. 1997 Observation of an internal wave attractor in a confined, stably stratified fluid. *Nature* **388**, 557–561.

Makarov, S. A., Neklyudov, V. I. & Chashechkin, Yu. D. 1990 Spatial structure of two-dimensional monochromatic internal wave beams in an exponentially stratified liquid. *Izv. Atmos. Ocean. Phys.* **26**, 548–554.

Mathur, M. & Peacock, T. 2009 Internal wave beam propagation in non-uniform stratifications. *J. Fluid Mech.* **639**, 133–152.

Matsuura, T. & Hibiya, T. 1990 An experimental and numerical study of the internal wave generation by tide-topography interaction. *J. Phys. Oceanogr.* **20**, 506–521.

Maurer, P., Joubaud, S. & Odier, P. 2016 Generation and stability of inertia–gravity waves. *J.Fluid Mech.* **808**, 539–561.

McEwan, A. D. 1973 A laboratory demonstration of angular momentum mixing. *Geophys. Fluid Dyn.* **5**, 283–311.

Melet, A., Nikurashin, M., Muller, C., Falahat, S., Nycander, J., Timko, P. G., Arbic, B. K. & Goff, J. A. 2013 Internal tide generation by abyssal hills using analytical theory. *J. Geophys. Res.* **118**, 6303–6318.

Mercier, M. J., Garnier, N. B. & Dauxois, T. 2008 Reflection and diffraction of internal waves analyzed with the Hilbert transform. *Phys. Fluids* **20**, 086601.

Mercier, M. J., Gostiaux, L., Helfrich, K., Sommeria, J., Viboud, S., Didelle, H., Ghaemsaidi, S. J., Dauxois, T. & Peacock, T. 2013 Large-scale, realistic laboratory modeling of M2 internal tide generation at the Luzon Strait. *Geophys. Res. Lett.* **40**, 5704–5709.

Mercier, M. J., Martinand, D., Mathur, M., Gostiaux, L., Peacock, T. & Dauxois, T. 2010 New wave generation. *J. Fluid Mech.* **657**, 308–334.

Messio, L., Morize, C., Rabaud, M. & Moisy, F. 2008 Experimental observation using particle image velocimetry of inertial waves in a rotating fluid. *Exp. Fluids* **44**, 519–528.

Miles, J. W. 1961 On the stability of heterogeneous shear flows. *J. Fluid Mech.* **10**, 496–508.

Morozov, E. G. 1995 Semidiurnal internal wave global field. *Deep-Sea Res. I* **42**, 135–148.

Mowbray, D. E. & Rarity, B. S. H. 1967 A theoretical and experimental investigation of the phase configuration of internal waves of small amplitude in a density stratified liquid. *J. Fluid Mech.* **28**, 1–16.

Munk, W. & Wunsch, C. 1997 The Moon, of Course... *Oceanography* **10**, 132–134.

Munk, W. & Wunsch, C. 1998 Abyssal recipes II: energetics of tidal and wind mixing. *Deep-Sea Res. I* **45**, 1977–2010.

Munroe, J. R. & Lamb, K. G. 2005 Topographic amplitude dependence of internal wave generation by tidal forcing over idealized three-dimensional topography. *J. Geophys. Res.* **110**, C02001.

Nansen, F. 1897 *Farthest North.* Harpers Brothers.

Newman, J. N. 1977*a* *Marine Hydrodynamics*. MIT Press.

Newman, J. N. 1977*b* The motions of a floating slender torus. *J. Fluid Mech.* **83**, 721–735.

Nikurashin, M. & Ferrari, R. 2011 Global energy conversion rate from geostrophic flows into internal lee waves in the deep ocean. *Geophys. Res. Lett.* **38**, L08610.

Nycander, J. 2005 Generation of internal waves in the deep ocean by tides. *J. Geophys. Res.* **110**, C10028.

Onu, K., Flynn, M. R. & Sutherland, B. R. 2003 Schlieren measurement of axisymmetric internal wave amplitudes. *Exp. Fluids* **35**, 24–31.

Oser, Hansjörg 1958 Experimentelle Untersuchung über harmonische Schwingungen in rotierenden Flüssigkeiten. *Z. Angew. Math. Mech.* **38**, 386–391.

Oster, G. & Yamamoto, M. 1963 Density gradient techniques. *Chem. Rev.* **63**, 257–268.

Pairaud, I., Staquet, C., Sommeria, J. & Mahdizadeh, M. M. 2010 Generation of harmonics and sub-harmonics from an internal tide in a uniformly stratified fluid: numerical and laboratory experiments. In *IUTAM Symposium on Turbulence in the Atmosphere and Oceans*, pp. 51–62. Springer.

Peacock, T., Echeverri, P. & Balmforth, N. J. 2008 An experimental investigation of internal tide generation by two-dimensional topography. *J. Phys. Oceanogr.* **38**, 235–242.

Peacock, T. & Weidman, P. 2005 The effect of rotation on conical wave beams in a stratified fluid. *Exp. Fluids* **39**, 32–37.

Peliz, A., Le Cann, B. & Mohn, C. 2009 Circulation and mixing in a deep submerged crater: Tore seamount pp. EGU2009–7567–1.

Peters, F. 1985 Schlieren interferometry applied to a gravity wave in a density-stratified liquid. *Exp. Fluids* **3**, 261–269.

Pétrélis, F., Llewellyn Smith, S. G. & Young, W. R. 2006 Tidal conversion at a submarine ridge. *J. Phys. Oceanogr.* **36**, 1053–1071.

Pingree, R. D. & New, A. L. 1989 Downward propagation of internal tidal energy into the Bay of Biscay. *Deep Sea Res.* **36**, 735–758.

Pingree, R. D. & New, A. L. 1991 Abyssal penetration and bottom reflection of internal tidal energy in the Bay of Biscay. *J. Phys. Oceanogr.* **21**, 28–39.

Ribeiro, A. 2002 *Soft Plate and Impact Tectonics*. Springer.

Rodenborn, B., Kiefer, D., Zhang, H. P. & Swinney, H. L. 2011 Harmonic generation by reflecting internal waves. *Phys. Fluids* **23**, 026601.

Sakai, S. 1990 Visualization of internal gravity wave by Moiré method. *J. Vis. Soc. Japan* **10**, 65–68.

Scolan, H., Ermanyuk, E. & Dauxois, T. 2013 Nonlinear fate of internal wave attractors. *Phys. Rev. Lett.* **110**, 234501.

Scott, R. B., Goff, J. A., Naveira Garabato, A. C. & Nurser, A. J. G. 2011 Global rate and spectral characteristics of internal gravity wave generation by geostrophic flow over topography. *J. Geophys. Res.* **116**, C09029.

Smith, S. & Crockett, J. 2014 Experiments on nonlinear harmonic wave generation from colliding internal wave beams. *Exp. Therm. Fluid Sci.* **54**, 93–101.

Sutherland, B. R., Dalziel, S. B., Hughes, G. O. & Linden, P. F. 1999 Visualization and measurement of internal waves by 'synthetic schlieren'. Part 1. Vertically oscillating cylinder. *J. Fluid Mech.* **390**, 93–126.

Sutherland, B. R., Hughes, G. O., Dalziel, S. B. & Linden, P. F. 2000 Internal waves revisited. *Dynam. Atmos. Oceans* **31**, 209–232.

Sutherland, B. R. & Linden, P. F. 2002 Internal wave excitation by a vertically oscillating elliptical cylinder. *Phys. Fluids* **14**, 721–731.

Tabaei, A., Akylas, T. R. & Lamb, K. G. 2005 Nonlinear effects in reflecting and colliding internal wave beams. *J. Fluid Mech.* **526**, 217–243.

Teoh, S. G., Ivey, G. N. & Imberger, J. 1997 Laboratory study of the interaction between two internal wave rays. *J. Fluid Mech.* **336**, 91–122.

Thomas, L. P., Marino, B. M. & Dalziel, S. B. 2009 Synthetic Schlieren: Determination of the density gradient generated by internal waves propagating in a stratified fluid. *J. Phys. Conf. Ser.* **166**, 012007.

Turner, J. S. 1973 *Buoyancy Effects in Fluids*. Cambridge University Press.

Van Loan, C. 1992 *Computational Frameworks for the Fast Fourier Transform*. SIAM.

Vlasenko, V., Stashchuk, N., Inall, M.E., Porter, M. & Aleynik, D. 2016 Focusing of baroclinic tidal energy in a canyon. *J. Geophys. Res. Oceans* **121**, 2824–2840.

Voisin, B. 2003 Limit states of internal wave beams. *J. Fluid Mech.* **496**, 243–293.

Voisin, B. 2016 Internal wave focusing by annular forcing. *In Proc. 8th Int. Symp. Strat. Flows (San Diego, 29 August-1 September 2016)* .

Voisin, B., Ermanyuk, E. V. & Flór, J.-B. 2011 Internal wave generation by oscillation of a sphere, with application to internal tides. *J. Fluid Mech.* **666**, 308–357.

Westerweel, J. 1997 Fundamentals of digital particle image velocimetry. *Meas. Sci. Technol.* **8**, 1379–1392.

Winters, K. B. & Armi, L. 2013 The response of a continuously stratified fluid to an oscillating flow past an obstacle. *J. Fluid Mech.* **727**, 83–118.

Wunsch, C. & Ferrari, R. 2004 Vertical mixing, energy, and the general circulation of the oceans. *Annu. Rev. Fluid Mech.* **36**, 281–314.

Wyrtki, K. 1981 An estimate of equatorial upwelling in the Pacific. *J. Phys. Oceanogr.* **11**, 1205–1214.

Xing, J. & Davies, A. M. 2011 On the interaction of internal tides over two adjacent sills in a fjord. *J. Geophys. Res.* **116**, C04022.

Yick, K.-Y., Stocker, R. & Peacock, T. 2007 Microscale Synthetic Schlieren. *Exp. Fluids* **42**, 41–48.

Zhang, H.P., King, B. & Swinney, H.L. 2007 Experimental study of internal gravity waves generated by supercritical topography. *Phys. Fluids* **19**, 096602.

Zhang, H. P., King, B. & Swinney, H. L. 2008 Resonant generation of internal waves on a model continental slope. *Phys. Rev. Lett.* **100**, 244504.

Zhang, L. & Swinney, H. L. 2014 Virtual seafloor reduces internal wave generation by tidal flow. *Phys. Rev. Lett.* **112**, 104502.